To the Graduate Council:

I am submitting herewith a dissertation written by Marvin Edward Bennett III entitled "Separating Thermal Metamorphism from Shock Metamorphism in the L Chondrite Asteroidal Parent Body." I have examined the final copy of this dissertation for form and content and recommend that it be accepted in partial fulfillment of the requirements for the degree of Doctor of Philosophy, with a major in Geology.

Harry Y. McSween, Jr., Major Professor

We have read this dissertation
and recommend its acceptance:

Accepted for the Council:

Associate Vice Chancellor
and Dean of the Graduate School

SEPARATING THERMAL METAMORPHISM FROM SHOCK METAMORPHISM IN THE L CHONDRITE ASTEROIDAL PARENT BODY

A Dissertation

Presented for the

Doctor of Philosophy

Degree

The University of Tennessee, Knoxville

Marvin Edward Bennett III

May 1995

This dissertation is dedicated to my parents

Ted and Yvonne Swartz

and to my brother

John Bennett

Acknowledgments

I would like to express my appreciation to the members of my committee for their thoughtful reviews of this manuscript: Theodore C. Labotka, Lawrence A. Taylor, and T. Ffrancon Williams. I would especially like to express my deep gratitude to my dissertation advisor, Harry Y. McSween, Jr., for his guidance and encouragement during the course of this work and for the many hours he spent in reviewing and improving this manuscript.

Ralph Harvey provided a great deal of inspiration for this study by asking all of the right questions at the right time. Allan Patchen was also of enormous assistant in the acquisition and the proper use of electron microprobe data. My thanks go out to both of these good friends.

I would like to thank the Geology Department at the University of Tennessee, Knoxville for providing me with a Teaching Assistantship and travel money through the Departmental Discretionary Fund. Further thanks to Dr. McSween, whose NASA grant provided much of the funding for this research.

I would be remiss not to thank those individuals and committees who curate and apportion meteorites for this type of research: the Meteorite Working Group at the Lunar and Planetary Institute, Houston, Tx; Roy S. Clarke, Jr., Curator for the Division of Meteorites, Smithsonian Institute, Washington D.C.; Martin Prinz, Curator for the Department of Mineral Sciences at the American Museum of Natural History, N.Y.; William C. Metropolis, Assistant Curator for the Harvard University Mineralogical Museum; and Edward Scott at the Planetary Geosciences Department, University of Hawaii at Manoau.

Abstract

The absence of a correlation between petrologic type and shock stage in L-group ordinary chondrites indicates that these metamorphic processes have produced distinct chemical and textural changes in this meteorite class. A petrologic and geochemical study of 63 L chondrites has shown that thermal metamorphism tends to homogenize the Ca component in matrix clinopyroxenes and produces normally zoned Fe-Ni metal and monocrystalline troilite, both of which indicate slow cooling from peak metamorphic temperatures. Shock metamorphism produces brittle deformation features in olivine and pyroxene and metal-sulfide textures, such as homogeneous taenite, polycrystalline kamacite, polycrystalline troilite, sheared troilite, and fizzed troilite, indicative of fast cooling from peak post-shock temperatures. Above shock stage S2 L chondrites may have experienced localized partial melting which produced a series of metal-sulfide melt compositions and melt drop sizes, which appear to correlate with shock stage.

Three geothermometers were applied to a representative group of L chondrites to compare cation-exchange blocking temperatures with petrologic type and shock stage. Olivine + spinel temperatures were found to correlate with shock stage, explaining the extreme homogeneity of major element compositions in L chondrite matrix chromites. Results obtained from the two-pyroxene and metal + sulfide thermometers show an inverse correlation between peak thermal metamorphic temperature and petrologic type, suggesting that the L chondrite asteroid body had an onion-shell internal structure prior to impact disruption. Peak thermal metamorphic temperatures at the core of this body were determined by pyroxene thermometry to be ~1273 K.

Results of this research were combined with recent laboratory measurements of L chondrite physical and thermal properties to produce a revised model of an internally heated body in an attempt to understand the thermal evolution of the L chondrite parent body. With the use of the decay of ^{26}Al as a heat source, model calculations predict that the L chondrite asteroidal parent body accreted 2-4 Ma after Allende CAI formation as a small planetesimal (radius of ~60 km) that was heated to peak temperatures of 1273 K in the core region, and then cooled slowly to the initial surface temperature of 180 K in ~60 Ma. Major impact events at ~4.2 Ga, and again at ~0.5 Ga, formed the shock metamorphic features that now overprint thermal metamorphic features in L chondrites.

TABLE OF CONTENTS

LIST OF TABLES

LIST OF FIGURES

CHAPTER 1

INTRODUCTION AND PURPOSE OF INVESTIGATION

Asteroids are minor planets whose orbits may range from inside the Earth's orbit to beyond Saturn's orbit (Lide, 1991). Approximately 4000 asteroids have been cataloged, most of which are contained in the main belt, the region lying roughly between the orbits of Mars and Jupiter. At a total mass of ~ 0.0004 that of the Earth (Caes, 1988), these planetesimals have until recent years been considered uninteresting planetary dregs by the astronomical community. In the past three decades, numerous studies have pointed to a possible genetic link between asteroids and meteorites (reviewed by Meadows, 1981). The antiquity of meteorites suggests that asteroids actually consist of relict materials that accreted in the solar nebula. Meteorites, therefore, have the potential for recording events that took place during the formation and evolution of their asteroid parent bodies.

Much of the information derived from the study of meteorites can be linked directly to thermal perturbations of their parent bodies. In many meteorites, an early static thermal metamorphic event can be recognized. This event produced petrologic groupings of meteorites whose textures and mineralogies reflect increasing peak metamorphic temperatures (Van Schmus and Wood, 1967). Thermal metamorphism is often overlain by a complex sequence of shock metamorphic textures and mineralogic changes created by hypervelocity collisions among asteroids. These impacts probably occurred throughout the history of the parent body. At intervals they may have partially to totally fragmented the asteroidal parent, producing ejecta that made its way into Earth-crossing orbits to become meteorites.

The meteoritical literature is replete with models that attempt to reconstruct the history of the original meteorite parent body by quantifying these two important metamorphic events. That these models tend to conflict rather strongly with one another is evidence that the database of quantitative information on the thermal history of meteorite parent bodies is incomplete. A systematic petrologic and geochemical study of meteorites from a single parent body, with an emphasis on distinguishing the overlapping effects of these thermal metamorphic and impact events, may provide the information needed to construct models of parent body formation and evolution. By concentrating on a large number of samples from a single chemical group of meteorites with a complex thermal and shock history, the L chondrites, this study is an attempt to provide some of the information necessary to fill this gap.

A Brief Review of Meteorite Classification

Historically, L chondrites have been shown to be an unusual group of meteorites. In order to appreciate how they vary from other meteorite classes, it would be informative to describe their similarities. What follows is a brief description of the meteorite family tree with emphasis on those branches that lead to the classification of the L-group ordinary chondrites.

The broadest classification of meteorites is into stones (composed mainly of silicate minerals), irons (essentially pieces of Fe-Ni metal alloy), and stony-irons (an obvious mixture of the two). This is a very simplistic classification, since it combines meteorite groups of vastly different character and origins. Stony meteorites are further subdivided into two groups based on the presence or absence of chondrules. Chondrules are small (typically 0.1 to 1.0 mm in diameter) round aggregates of minerals that have textures and compositions indicative of fast cooling from a liquid

Table 1. The classification of chondritic meteorites and a listing of some key taxonomic parameters (Wasson and Kallemeyn, 1988).

	Normalized Ratios				Oxygen Isotopes (%)	
GROUP	Al/Si	Mg/Si	Ni/Si	Zn/Si	δ17O	δ18O
CV	1.34	1.00	0.85	0.250	- 3.0	+ 1.0
CO	1.07	0.97	0.87	0.210	- 4.0	+ 0.0
CM	1.10	0.97	0.92	0.480	+ 1.0	+ 7.0
CI	1.00	1.00	1.00	1.000	+ 9.0	+17.0
H	0.80	0.89	0.94	0.092	+ 3.0	+ 4.2
L	0.78	0.84	0.64	0.088	+ 3.5	+ 4.6
LL	0.75	0.84	0.53	0.080	+ 3.8	+ 4.9
EH	0.58	0.68	1.04	0.490	+ 2.9	+ 5.7
EL	0.67	0.81	0.69	0.030	+ 2.9	+ 5.7

state. Chondritic meteorites or chondrites are composed of many chondrules set in a fine-grained matrix of silicates, metals, and sulfides. Sharp differences between the bulk chemistry of chondrules and matrix indicates that these components are not an equilibrium assemblage. Chondrites are, therefore, aggregates of materials which existed independently prior to their accretion and as such have been dubbed cosmic sedimentary rocks. Stony meteorites that lack chondrules have igneous textures or appear to have been derived from igneous rocks.

Chondritic meteorites may be further subdivided into at least nine classes based on major element and oxygen isotope fractionations (Table 1). These classes make up three broad groups of chondrites: carbonaceous chondrites (denote by a prefix 'C' in Table 1), enstatite chondrites (with prefix 'E'), and ordinary chondrites (H, L, and LL). Differences in major element ratios reflect departures from average solar system abundances as expressed by compositionally primitive CI chondrites. Variations in oxygen isotopes may indicate formation of each class within a unique parent body (Clayton et al., 1976).

Table 2. Average mineral norms, standard deviations, and representative meteorites for analyzed ordinary chondrite falls (McSween, et al., 1991).

Mineral	H (27)[1]		L (55)		LL (12)	
apatite	0.65	(7)[2]	0.54	(9)	0.54	(11)
chromite	0.76	(5)	0.78	(5)	0.80	(4)
ilmenite	0.23	(2)	0.24	(2)	0.25	(4)
orthoclase	0.56	(7)	0.64	(7)	0.61	(12)
albite	7.30	(31)	8.07	(44)	8.11	(50)
anorthite	1.70	(43)	1.59	(49)	1.55	(40)
diopside	4.11	(54)	4.97	(66)	5.34	(54)
hypersthene	26.2	(29)	24.2	(26)	21.4	(37)
olivine	35.0	(39)	44.8	(30)	51.9	(56)
metal	18.0	(17)	8.39	(99)	3.59	(165)
troilite	5.47	(38)	5.80	(80)	5.85	(106)
total	100.0		100.0		100.0	

Representative Meteorites[3]

H	Guarena, Sitathali, Dhajala
L	Hallingeberg, Mirzapur
LL	Cherokee Springs

1. Number in ( ) is the number of analyses for each petrologic group
2. Number in ( ) is the standard deviation in terms of the least unit cited, as determined by replicate analyses
3. Meteorites whose bulk composition lie closest to the average norm

The ordinary chondrites are so named because they make up approximately 80% of our current meteorite holdings. There are three groups of ordinary chondrites: H chondrites (high metal content), L chondrites (low metal content), and LL chondrites (low metal - low iron contents). The proportion of iron in silicates and sulfides compared to metals probably reflects a fundamental change in oxidation conditions within the early solar nebula (Fredriksson and Keil, 1964; Keil, 1968; McSween, 1979; McSween and Labotka, 1993). Table 2 lists the normative mineralogy for the three groups of ordinary chondrites calculated from bulk chemical analyses of unweathered meteorite falls (Jarosewich, 1990). From this table it can be readily noted

that there is a systematic decrease in reduced metal (primarily Fe^{0}) with an increase in oxidized metal (Fe^{2+} in olivine). Also listed are individual meteorites with a bulk chemistry typical of that seen in the average norm (McSween et al., 1991).

The textures and mineral compositions of many chondrites indicate that they have undergone post-accretional thermal metamorphism. It has been a matter of much debate whether this thermal metamorphism occurred in small bodies prior to accretion of the parent body (Wasson, 1972) or after the parent body formed (Dodd, 1969). This metamorphism does, however, allow for a final subdivision of chondrites into what are termed petrologic types. Van Schmus and Wood (1967) originally identified six petrologic types for each chondrite class. They divided these groups into type 1 to type 6, in order of increasing metamorphism. These authors used features such as the degree of chemical homogeneity of mineral phases, presence and state of original igneous glasses in chondrules, visibility of chondrules, and several other textural and chemical criteria to place a chondrite into a particular petrologic type. Several modifications were later added to the Van Schmus and Wood classification. Using thermoluminescence sensitivity, Sears et al. (1980) further subdivided type 3 chondrites into types 3.0 to 3.9. McSween (1979) noted that types lower than 3.0 were restricted to carbonaceous chondrites (and a few other relatively rare groups of chondrites), and that a decrease from type 3.0 to type 1 represents an increase in aqueous (not thermal) alteration. All ordinary chondrites (including the L chondrites) are relatively anhydrous and show an increase in thermal metamorphism from type 3.0 to type 6. Dodd et al. (1975) classified the L chondrite Shaw as a type 7 chondrite, based on its crystalline texture. All type 7 chondrites show evidence of melting which may be the result of post-shock metamorphic reheating (Scott and Rajan, 1979). This

would imply that the term type 7 is a misnomer, since type 7 chondrites did not form by the thermal metamorphism of a lower petrologic type.

Shock vs. Thermal Metamorphism - the Purpose for this Study

The first suspicion that L chondrites may have experienced a more complex history than other ordinary chondrites was reported in a study of K-Ar dating by Keil (1964), who noted that many L chondrites had experienced a greater degree of degassing of ^{40}Ar than H-group chondrites. Shortly after this discovery, Anders (1964) observed that K-Ar age dates were bimodal, centering around approximately 4 Ga and 0.52 Ga. He suggested that these age dates may correspond to major impact events resulting in the shock-reheating and degassing of radiogenic ^{40}Ar from the L-chondrite parent body. Heymann (1967) and Taylor and Heymann's (1969) work on over 100 ordinary chondrites of various shock stages provided the firm connection between shocked L chondrites and low gas retention ages. More recent work on the shock-melted L chondrite Point of Rocks has shown it to yield a low-temperature gas plateau in ^{39}Ar-^{40}Ar step-heating measurements (Bogard et al., 1994) and an ^{87}Rb-^{87}Sr isochron (Nakamura et al., 1990) that suggest disruption ages of 500 Ma and 469 +/- 7 Ma, respectively.

The highly shocked nature of L chondrites has led to their use in the calibration of several early shock classification schemes (Carter et al., 1968; Dodd and Jarosewich, 1979). Recent high-pressure shock experiments (for a review of this extensive literature see Stöffler et al., 1991) have led to a further refined shock classification system. Although quantitatively more accurate than the older shock classifications mentioned, the newer scheme nevertheless reaffirms that L chondrites have been shocked to a higher degree than other ordinary chondrite groups.

Table 3. List of blocking temperatures derived from recently calibrated geothermometers.

Meteorite	Type	Geothermometer	Reference	T (°C)
Andreevka	L3	Metal-Sulfide (Ni-T)	Bezmen et al., 1978	440
Bald Mountain	L4	Olivine-Spinel (FeMg-T)	Sack and Ghiorso, 1991	664
Saratov	L4	Metal-Sulfide (Ni-T)	Bezmen et al., 1978	950
Elenovka	L5	Metal-Sulfide (Ni-T)	Bezmen et al., 1978	850
Ergheo	L5	Olivine-Spinel (FeMg-T)	Sack and Ghiorso, 1991	720
Vilna	L5	Metal-Sulfide (Ni-T)	Bezmen et al., 1978	620
Bath Furnace	L6	Opx-Cpx (Ca-T)	Olsen and Bunch, 1984	850-890
Bruderheim	L6	Opx-Cpx (Ca-T)	Olsen and Bunch, 1984	890-900
Colby	L6	Opx-Cpx (Ca-T)	Olsen and Bunch, 1984	810
Harleton	L6	Olivine-Spinel (FeMg-T)	Sack and Ghiorso, 1991	722
Kyushu	L6	Opx-Cpx (Ca-T)	Olsen and Bunch, 1984	890-900
Kyushu	L6	Metal-Sulfide (Ni-T)	Bezmen et al., 1978	840
Kyushu	L6	Olivine-Spinel (FeMg-T)	Sack and Ghiorso, 1991	658
Langhalsen	L6	Opx-Cpx (Ca-T)	Olsen and Bunch, 1984	960-900
Mocs	L6	Opx-Cpx (Ca-T)	Olsen and Bunch, 1984	820
New Concord	L6	Olivine-Spinel (FeMg-T)	Sack and Ghiorso, 1991	663
Pervomaisky	L6	Metal-Sulfide (Ni-T)	Bezmen et al., 1978	825
Walters	L6	Olivine-Spinel (FeMg-T)	Sack and Ghiorso, 1991	714
Shaw	L7	Opx-Cpx (Ca-T)	Scott and Rajan, 1979	1200

Previous studies of shock metamorphism in L chondrites have apparently convinced most researchers that all geothermometers and cooling rate indicators were perturbed sufficiently to render their application useless. Table 3 is a compilation of geothermometry data for non-Antarctic L chondrites spanning the last 30 years. Even considering the brevity of the data in this table, most of it is suspect. Ni blocking temperatures between metal and sulfide were obtained from single mineral pairs within each meteorite sample. Metals and sulfides are highly susceptible to the heterogeneous effects of post-shock reheating, so several pairs should be analyzed throughout the sample in order a provide a more representative range of blocking temperatures (especially in moderately to highly shocked samples). Olivine + spinel temperatures were also obtained by inappropriate means; the data for thermometry

computations was taken by the authors from a number of unrelated publications in the literature spaced several years apart and not from co-existing mineral phases within the same thin sections.

Are the effects of shock metamorphism separable from those of thermal metamorphism in L-group ordinary chondrites? This question is an extremely important one as its answer controls our ability to model the internal physical (and thermal) structure of the L-chondrite parent body prior to shock disruption. Stöffler et al. (1991) stated that there exists a direct correlation between increasing shock metamorphic stage and higher petrologic types. Rubin (1994) has taken this conclusion one step further by suggesting that shock metamorphic reheating and not thermal metamorphism was the primary mechanism for producing the various petrologic types. If either of these studies are correct, than the answer to the above question is: No, the L-chondrite parent body was too heavily shocked to determine its original structure from our current L chondrite collections.

Figure 1 is a summary diagram consisting of all L chondrites of known shock stage subdivided by petrologic type. Stöffler et al. (1991) published a new meteorite shock classification system, employing simple petrographic surveys, which was used to obtain their conclusions concerning the positive correlation between thermal metamorphism and shock stage. They shock classified 27 L chondrites and obtained, according to them, a direct correlation between the two types of metamorphism (Fig. 1a). Rubin (1993), using the same shock classification system, classified 43 additional L chondrites (Fig. 1b) and based his assertions on this data. In this study, we classified 63 L chondrites (Fig. 3c). In all meteorites that overlapped there was good agreement in shock stage assignment. Figure 1d is a composite of all published data excluding samples which overlap between the studies.

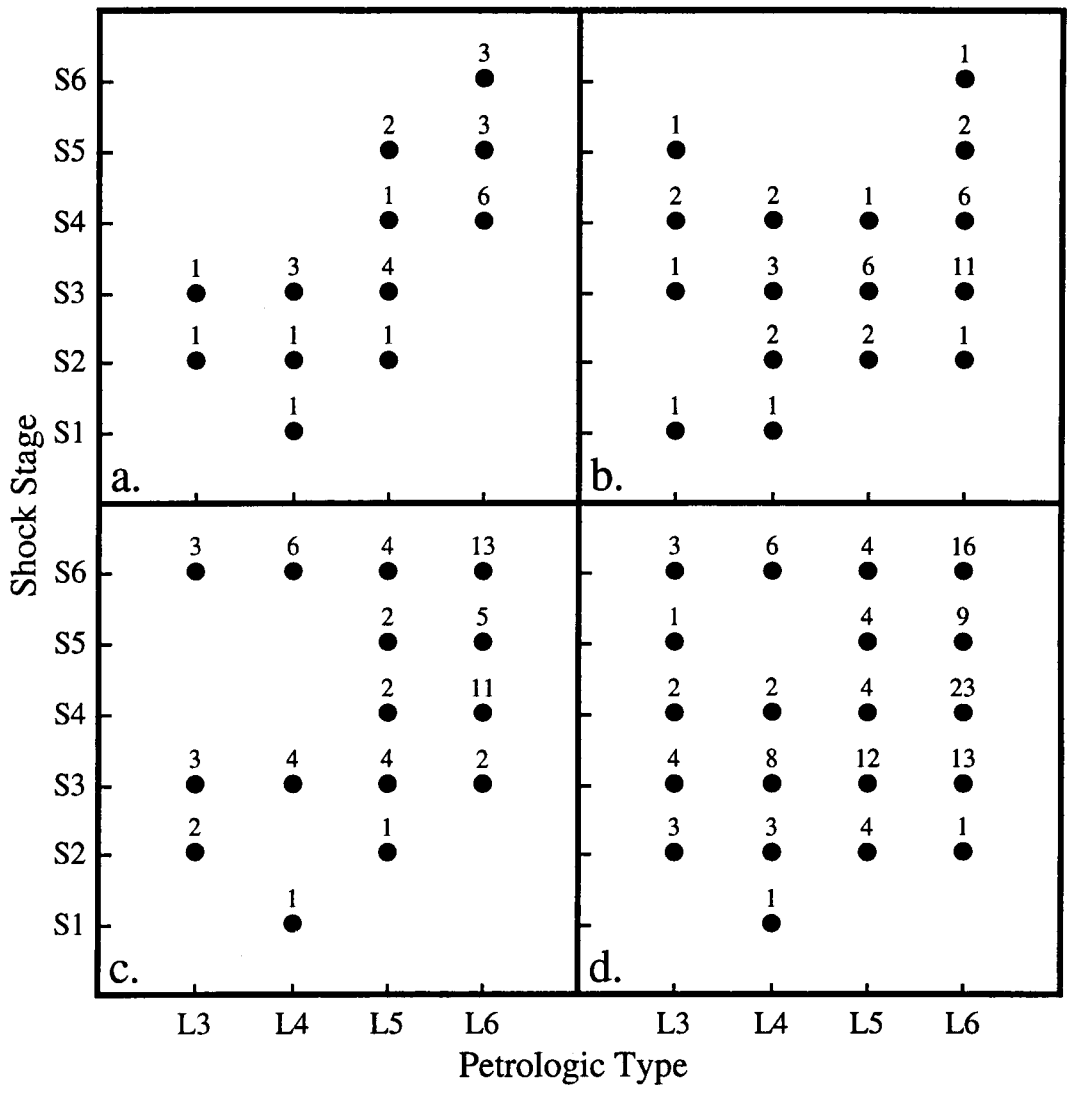

Figure 1. Petrologic type versus shock stage for all recently published shock-classified L chondrites. Small numbers above points give the number of meteorites that fall into each shock stage and petrologic type. Sources for the data are: a) Stöffler et al., 1991, b) Rubin, 1994, c) this study, and d) combination of all 3 sources.

Table 4. Chi-squared test for variable independence between shock stage and petrologic type for all L chondrites shown in Fig. 1.

Data Source	Sample Size	Computed Chi-squared	Degrees of Freedom	Expected Chi-squared *	Cramer V Value
Stöffler et al., 1991	27	25.891	15	30.578	0.5654
Rubin, 1994	43	15.083	15	30.578	0.3419
Bennett and McSween, 1994	63	29.748	15	30.578	0.3967
all data	123	28.584	15	30.578	0.2783

* data for confidence interval = 0.01 taken from tables published in Burlington and May, 1953

A positive correlation between shock stage and petrologic type would indicate that post-shock reheating has completely overprinted thermal metamorphism, thus rendering it impossible to separate the two metamorphic events. In order to test the relationship between shock stage and petrologic type, Fig. 1 was used as a source for contingency tables in order to perform chi-squared analyses on the available shock classified L chondrite data. The chi-squared test for independence uses a null hypothesis which assumes that no relationship exists between the two variables to be tested. If, for a specified confidence interval, the chi-squared value calculated for the data set is less than the expected value (taken from published statistical tables), then the null hypothesis is accepted and a lack of dependence is established. For the calculations presented in Table 4 the confidence interval was set at 0.01 or 99% confidence. There is no apparent correlation between shock stage and petrologic type for any of the four data sets.

Also presented in Table 4 is the Cramer V value, which tests the validity of chi-square analyses (Hale, 1992). This value varies numerically from 0 (an invalid test of association) to +1 (a valid test). The sparse nature of these data sets is revealed in the low Cramer V values for all of the chi-squared calculations. Although these low values

do not invalidate the independence established by chi-squared tests, they do indicate that a measure of caution must be made in their interpretation. Thus, within the limited data set available, there appears to be no correlation between shock stage and petrologic type in L chondrites. This suggests that the two types of metamorphism might be separable if the proper data are collected and analyzed. The purpose of this investigation is to supply petrographic and geochemical information which will aid in distinguishing the effects of each type of metamorphism, with the ultimate goal of using these data to help separate the two metamorphic events. This information will than be used to derive a clearer understanding of the thermal history of the L chondrite parent body.

Methods of Investigation

Polished thin sections of 55 Antarctic L chondrites were examined from the Antarctic meteorite collection (Johnson Space Center, Houston). Based on least-weathered criteria (weathering class A, A/B: Gooding, 1986; Score and Lindstrom, 1990), 11 unbrecciated samples, 2 breccias, and 1 melt inclusion were chosen for study. Sections of 15 non-Antarctic L chondrites were obtained from the American Museum of Natural History. These samples were selected based on a least-shocked criteria as reported from previous shock classifications (Heymann, 1967; Carter et al., 1968; Taylor and Heymann, 1969; Dodd and Jarosewich, 1979; Stöffler et al., 1988). In addition, 2 melt clasts/breccias from the National Institute of Polar Research (Yamato collection, Japan) and a sample of the L7 chondrite Shaw (provided by E.R.D. Scott) were obtained for this study. Table 5 lists all samples examined. Meteorite names in italics were selected for further petrographic and geochemical work.

Table 5. Listing of L chondrites used in this study. Meteorite names in italicizes were selected for petrographic and geothermometry work.

Meteorite	Type	Shock Stage	Source *	Meteorite	Type	Shock Stage	Source
Accalana	L3	S4	AMNH	ALHA77218	L5	S5	MWG
Ausson	L5	S2	AMNH	ALHA77267	L5	S6	MWG
Bjurbole	L4	S1	AMNH	ALHA77277	L6	S5	MWG
Cynthiana	L4	S3	AMNH	ALHA78078	L6	S6	MWG
Fisher	L6	S5	AMNH	*ALHA78106*	L6	S3	MWG
Hallingeberg	L3	S3	AMNH	*ALHA78119*	L3	S3	MWG
Inman	L3	S3	AMNH	ALHA81099	L6	S5	MWG
Jhung	L5	S3	AMNH	*DOM 85503*	L6	S4	MWG
Khohar	L3	S4	AMNH	EET83238	L6	S6	MWG
Kingfisher	L5	S6	AMNH	EET83243	L6	brec.	MWG
Kyushu	L6	S5	AMNH	EET87557	L4	S3	MWG
Long Island	L6	S4	AMNH	*EET87555*	L6	brec.	MWG
McKinney	L4	S6	AMNH	GEO85701	L6	S6	MWG
Tenham	L6	S4	AMNH	GRO85204	L6	S6	MWG
Tennasilm	L4	S3	AMNH	GRO85208	L6	S6	MWG
Y75097	L6	brec.	JIPR	*GRO85209*	L6	S3	MWG
Y793241	L6	brec.	JIPR	LEW85339	L3	S2	MWG
ALH82104	L5	S6	MWG	LEW86011	L6	S6	MWG
ALH82105	L6	S6	MWG	LEW86012	L6	S6	MWG
ALH83101	L6	S5	MWG	*LEW 86024*	L4	S3	MWG
ALH 84005	L5	S3	MWG	LEW86357	L5	S3	MWG
ALH84062	L6	brec.	MWG	LEW87248	L3	S6	MWG
ALH84063	L5	S6	MWG	LEW87284	L3	brec.	MWG
ALH84065	L6	S6	MWG	*LEW88663*	achond.	brec.	MWG
ALH84070	L6	S6	MWG	MAC87302	L4	S6	MWG
ALH85016	L6	S6	MWG	MAC87303	L4	S6	MWG
ALH85017	L6	S6	MWG	MAC87310	L4	S6	MWG
ALH 85026	L6	S4	MWG	*PAT91501*	L7	melt	MWG
ALH85029	L6	S5	MWG	PCA82513	L5	S5	MWG
ALH85033	L4	S6	MWG	*QUE90201*	L5	S3	MWG
ALH85034	L6	S6	MWG	QUE90202	L5	S4	MWG
ALH 85045	L3	S2	MWG	TIL82411	L4	S6	MWG
ALHA76001	L6	S3	MWG	*Shaw*	L7	brec.	Scott
ALHA76003	L6	S4	MWG	*ALHA77297*	L6	S4	SI
ALHA77155	L6	S4	MWG	*ALHA77301*	L6	S4	SI
ALHA77162	L6	S4	MWG	*PCA 82510*	L5	S3	SI

* AMNH American Museum of Natural History
JIPR Japanese Institute of Polar Research
MWG Meteorite Working Group
Scott Collection of E.R.D. Scott
SI Smithsonian Institution

Table 6. Schematics of technique used for shock classification of L chondrites (after Stöffler et al., 1991). Major indicators for each shock stage are in bold text.

Phases Examined	Shock Features	Shock Stage
check 20 to 25 high-birefringent grains of olivine (at least 50 to 100 μm in diameter)	**olivine extinction ≤ 2° rotation** irregular fractures	S1 (unshocked)
	olivine extinction ≥ 2° rotation (undulatory) irregular fractures	S2 (very weakly shocked)
	1 set or 3 or more planar fractures in olivine **2 intersecting sets or 2 or more planar fractures** undulatory extinction	S3 (weakly shocked)
check 10 or more of the largest plagioclases	**weak mosaicism in olivine (domains < 3-5 μm)** olivine extinction not complete planar fractures and undulatory extinction in plagioclase	S4 (moderately shocked)
	plagioclase is maskelynite strong mosaicism in olivine small planar deformation features in olivine	S5 (strongly shocked
check other textural elements	**olivine has recrystallized texture** many irregular melt features ringwoodite may be present in fractures with olivine plagioclase is 'normal melt glass'	S6 (very strongly shocked)

Samples were placed into their appropriate shock stage following the technique of Stöffler et al. (1991). This is a statistical method that can be applied petrographically by noting key deformational features in olivine and plagioclase grains. Table 6 is a synopsis of this classification scheme emphasizing the key elements that were used to separate the various shock stages. Although this procedure utilizes the most recent experimental shock calibrations, it is still a statistical technique. Accuracy (especially between shock stages S3 and S5) is plus or minus one shock stage for repeated surveys

of the same polished thin section (Stöffler, 1992, personnel communication). Also, since shock metamorphic effects are heterogeneously distributed on a very small scale, shock classification of a single thin section may not be representative of the whole meteorite. As an example, the L6 chondrite Tenham was classified as S4 stage in this study (see Table 5), based on the absence of maskelynite in the matrix. It is, however, heavily brecciated on a large scale (Graham et al., 1985) with ringwoodite in some of the veins (Binns et al., 1969). Ringwoodite is a high-pressure polymorph of olivine and the prime indicator of shock stage S6 and above. Because of the strong shock heterogeneity within L chondrites, all polished thin sections used for geothermometry work were carefully placed into their appropriate shock stage. The degree of shock of individual meteorites as reported in the literature (Stöffler et al., 1991; Rubin, 1993) was noted for comparison purposes, but was not taken as representative of the particular thin section of meteorite analyzed in this study.

In addition to shock features that have been experimentally calibrated, there are other possible shock indicators in L chondrites; presence and abundance of silicate-metal-sulfide melt features (Turner, 1969; Dodd and Jarosewich, 1979) and certain Fe-Ni metal textures (Buchwald, 1975; Scott, 1982; Rubin, 1985; Widom et al., 1986).

Willis and Goldstein (1983), while observing Fe-Ni metal microstructures in several ordinary chondrites, noted that many textures did not appear until the samples were etched with a 1 % nital solution (concentrated nitric acid mixed with methyl alcohol) for prolonged periods of time. This was found to be particularly true with the staining effects of nital on some of the taenites that were normally zoned. For this reason, meteorites which have their taenites categorized as incompletely zoned or homogeneous were etched several times with nital (see Appendix A) in order to insure that all features were readily identifiable by optical means.

Geothermometry work was based on spot analyses taken with a Cameca SX-50 electron microprobe. Standard operating conditions were similar for all analyses. Accelerating voltage was 15 kV with a 30 nA beam current and a beam diameter of 1 μm. Counting times were 20 seconds on element peaks and 10 seconds for backgrounds on either side of peaks for each element. Counting times for Ni in Fe-Ni metal and troilite and for P in Fe-Ni metal were raised to 80 seconds to increase statistical counting accuracy on these trace elements. Standards used were a combination of natural and synthetic metals and compounds of appropriate composition. Matrix corrections were based on ZAF procedures incorporated in the Cameca electron microprobe software.

In samples containing the appropriate minerals for geothermometry, 4 to 12 mineral pairs were analyzed. The results were used to calculate blocking temperatures based on three geothermometers: orthopyroxene + clinopyroxene Ca exchange (Lindsley, 1983), Fe-Ni metal + troilite Ni exchange (Bezmen, et al., 1978), and olivine + spinel Fe-Mg exchange (Sack and Ghiorso, 1991). Errors for these thermometers were calculated based on information obtained from these sources. Lower limits of detection at 2 and 3σ were computed for minor and trace elements for each mineral analyzed, which allowed calculation of statistical counting errors and set limits on acceptable data. Problems with secondary fluorescence from adjacent mineral phases were minimized by calculating maximum X-ray excitation volumes for each minor and trace element. This information was used to set minimum distances from grain edges for spot analyses.

Multi-element X-ray maps were acquired for several of the shock-induced melt pockets in order to determine what phases were present. A number of Ni X-ray maps and chemical profiles were also taken in order to distinguish various Fe-Ni metal

phases and to derive Ni cooling profiles. All thin sections were carefully examined with the microprobe set in electron backscatter (BSE) scanning mode at 1000X magnification. This rendered subtle shock textures readily identifiable, making it possible to avoid melt features when acquiring point analyses and profiles. BSE was also used to identify small minerals that contained exsolution features and minerals that were chemically zoned. Minerals such as these are known to give erroneous results when used in geothermometry studies and so were avoided.

Results obtained from the geochemical analyses were combined with the most recent physical parameters from laboratory measurements obtained from the literature and used as a basis to construct a thermal model for the evolution of the L-chondrite parent body.

CHAPTER 2

PETROGRAPHY OF L CHONDRITES

All ordinary chondrites formed from separate components (chondrules, matrix, metals, etc.) within the solar nebula. Evidence for this origin can be found in the variation in chemistry and textures between these components in relatively primitive, unaltered carbonaceous chondrites. Most meteorites, however, display some degree of post-accretional alteration. Thermal metamorphism promotes recrystallization and recombination of the various mineral phases, resulting in eventual mineral homogenization and textural integration. Brittle deformation and brecciation associated with shock metamorphism can mix components that have been reheated to different degrees. Shock metamorphism may also equilibrate portions of the original meteorite by selective melting of low-temperature phases and/or porous regions or through the process of whole-rock melting. What follows is a summary of those textural features and mineralogic changes noted within the samples that have a bearing on their metamorphic history.

Mineralogy of L Chondrites

Ordinary chondrites are composed of different proportions of the same major mineral groups. Olivine and Ca-poor pyroxene are the dominant mineral phases, with Ca-rich pyroxene, sodic plagioclase (in equilibrated chondrites), sulfides, and Fe-Ni metal present in subordinate amounts. These minerals may constitute as much as 99 wt % of an ordinary chondrite (Dodd, 1981; McSween, et al., 1991). In addition, over 100 minor minerals have been identified in these meteorites (Kerridge and Matthews,

1988). Variations in mineralogy and mineral chemistry are due to recrystallization, inversion, and homogenization associated with increasing thermal metamorphism.

In unequilibrated L chondrites (types 3 and 4), plagioclase occurs as microlites within the glassy portions of chondrules and matrix. Increasing thermal metamorphism results in recrystallization and growth of plagioclase, at the expense of glass, until some grains in type L6 chondrites may achieve sizes of several hundred microns. Low-Ca pyroxene (0.2 to 0.6 wt % CaO) in unequilibrated L chondrites is present in the form of polysynthetically twinned clinopyroxene, which is believed to have formed from the inversion of quickly-cooled protoenstatite (Binns, 1970). Ca content in these pyroxene minerals increases with increasing equilibration (up to 1 wt % CaO in type L6 chondrites; Dodd, 1981). In samples that have attained thermal metamorphism above type L3, most low-Ca clinopyroxene inverts to orthopyroxene (either hypersthene or bronzite). High-Ca pyroxene (diopsidic augite) is present as small grains (most are <5 μm) in the matrices of all L chondrites. Augite may be rimmed by or contain lamella of pigeonite (low-Ca clinopyroxene). Most olivine occurs as large (up to several mm) subhedral crystals which range from Fa_{23} (type L3) to Fa_{26} (type L6). The chemical compositions of olivine and pyroxene become more homogeneous with increasing petrologic type.

Fe-Ni metal occurs in all L chondrites. It may be present in one of 5 forms; αFe kamacite (<7.5 wt % Ni), martensite (7.5-25 wt % Ni), γFe taenite (25-50 wt % Ni), tetrataenite (48-57 wt %), or plessite (a mixture of 2 or more Fe-Ni phases). Fe-Ni metal grains are generally zoned, with tetrataenite rims and taenite, martensite, or plessite cores. The occurrence of each phase and the degree of zoning appear to correlate more readily with shock reheating than with thermal metamorphism.

The major sulfide in L chondrites is troilite. It occurs as nearly stoichiometric, hexagonal FeS. Troilite may, however, contain as much as 6 wt % Ni along margins adjacent to high Fe-Ni metals such as tetrataenite. Very small grains (a few microns in diameter) of pentlandite were found in several L chondrite samples, notably Inman and Fisher. Pentlandite occurs in the matrices of these meteorites and is commonly associated with troilite.

Several minor minerals are ubiquitous in L chondrites. Schreibersite $(FeNi)_3P$ was found as small (less than 2 μm) grains in many grains of the kamacite. The early formation of schreibersite may have facilitated the nucleation of the kamacite (Herpfer et al., 1994), making possible the occurrence of large (up to 0.5 cm) grains in some L chondrites, such as in Ausson. Whitlockite is a common accessory mineral in L chondrites. It is present as small (<20 μm) grains in the matrices of most L chondrites. Small, euhedral chromite grains were also found in the matrices (and in a few chondrules) of all L chondrites examined.

Because of the heterogeneous distribution of these minerals among different chondrule types, the difficulty in the optical determination of some of the minerals, and the small sample sizes that are allocated for research, accurate mineral abundances for L chondrites have not been published. Fortunately, it was established as early as the 1950's (Wahl, 1951) that the normative (calculated) mineral abundances in ordinary chondrites correspond closely to what is generally accepted as average modal abundances. This close correspondence between the mode and the norm has been attributed to the evolution of ordinary chondrites in a dry environment (Dodd, 1981). It makes possible the calculation of a set of anhydrous minerals from representative bulk chemical analyses which can serve as a proxy for the modal abundances of minerals. Jarosewich (1990) published several hundred high-quality bulk chemical

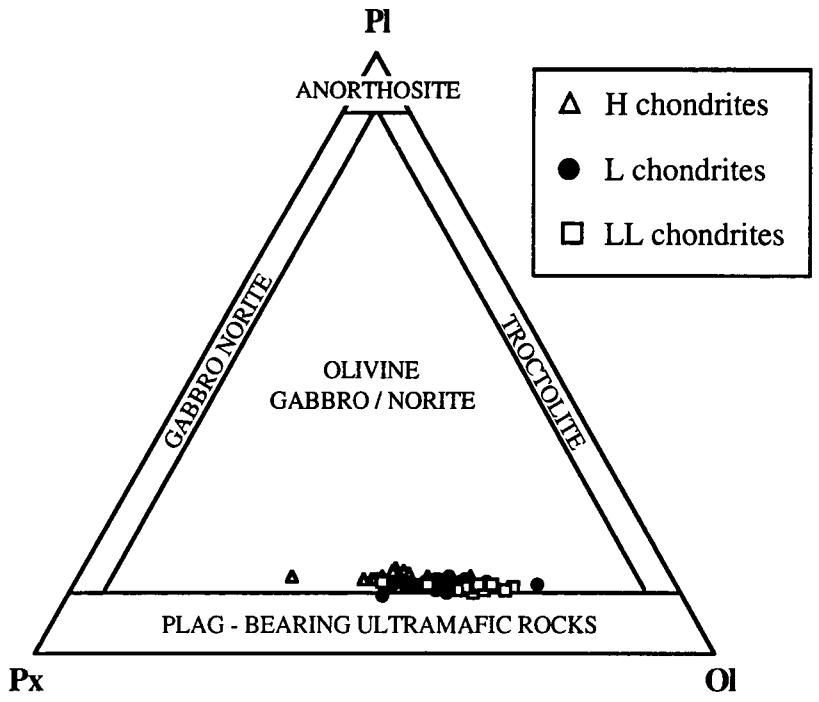

Figure 2. Plot of normative olivine, pyroxene, and plagioclase for H, L, and LL chondrites. Normative data was calculated from bulk analyses of Jarosewich (1990). The three classes of ordinary chondrites form a narrow compositional range within the olivine gabbronorite field.

analyses of ordinary chondrites which were used by McSween et al. (1991) to calculate norms (corrected for metal and sulfide). That study will be used as the source material for the following discussion of L chondrite mineralogy.

As was mentioned previously, the bulk mineral assemblage of L chondrites consists of plagioclase, olivine, and at least two varieties of pyroxene. Plotting these normative components on a mafic igneous triangle (Fig. 2; Streckeisen, 1976) reveals that most ordinary chondrites have a bulk chemistry similar to terrestrial plagioclase-bearing ultramafic rocks and olivine gabbronorites. The nearly uniform plagioclase abundance (9 to 10 wt %) and the relatively uniform ratio of olivine to pyroxene

(~1:1) creates a tight band of compositions that appear to overlap for all three ordinary chondrite classes.

Figure 3 provides a comparison of total pyroxene to olivine contents for the three classes of ordinary chondrites. Although there is a slight overlap between the L and LL classes (notably Manych and Bishunpur, which may belong to the L/LL group), three distinct trends are readily visible in this diagram. The ratio of olivine to pyroxene remains fairly constant for all three groups (1.2:1 to 1.5:1). The absolute abundances of these phases increase with increasing oxidation conditions. L chondrites plot along a linear trend that is intermediate between the more reduced H chondrites and the more oxidized LL chondrites. Differences in the relative abundances of these phases appear to be a function of the composition of the original parent body and are not due to thermal metamorphism. Plotting the compositions of 57 L-chondrite falls from four petrologic types (L3 through L6) reveals no intra-class relationship between them. The linear trend observed might be better understood if Fig. 3 is compared with Fig. 4. In this diagram metallic iron (Fe°) is plotted against iron in troilite and in silicate minerals (both Fe^{2+}). The more reduced H chondrites contain greater quantities of metallic iron as Fe-Ni metal, whereas the oxidized LL chondrites contain more iron in the form of silicate minerals and less as metallic iron. Degree of oxidation is believed to be tied to the location of the parent bodies at different nebular heliocentric distances (McSween et al., 1991). Modern condensation theory predicts the occurrence of higher temperature, more reducing phases closer to the protosun and lower temperature, more oxidizing phases occurring at greater heliocentric distances (Grossman, 1972; Clayton et al, 1985).

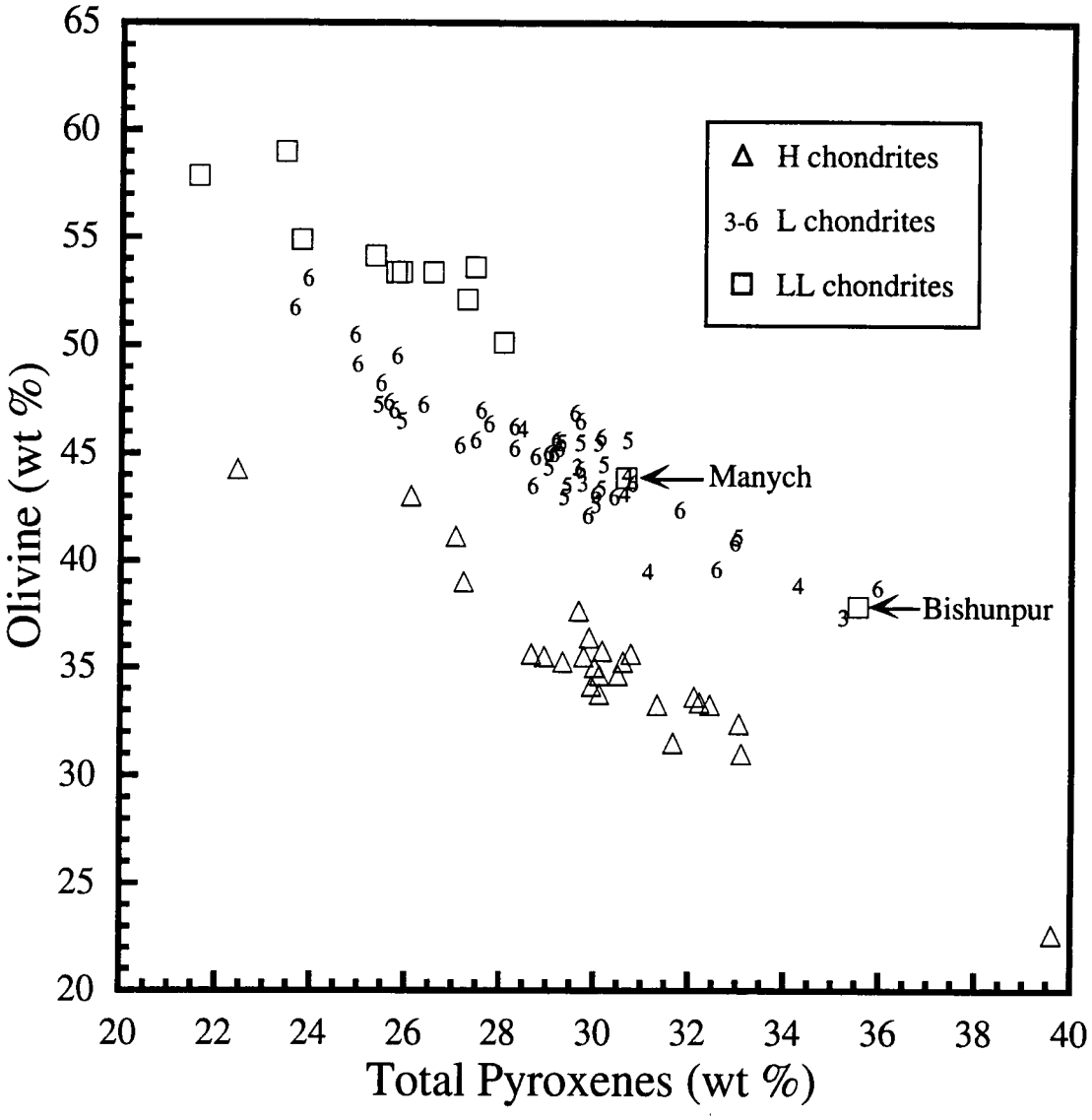

Figure 3. Plot of normative pyroxene (opx + cpx) vs. olivine for the three classes of ordinary chondrites. L chondrites are plotted by petrologic type to illustrate the absence of a trend between types. Only two possible L/LL class samples can be seen to overlap, otherwise the trends are distinct between ordinary chondrite classes.

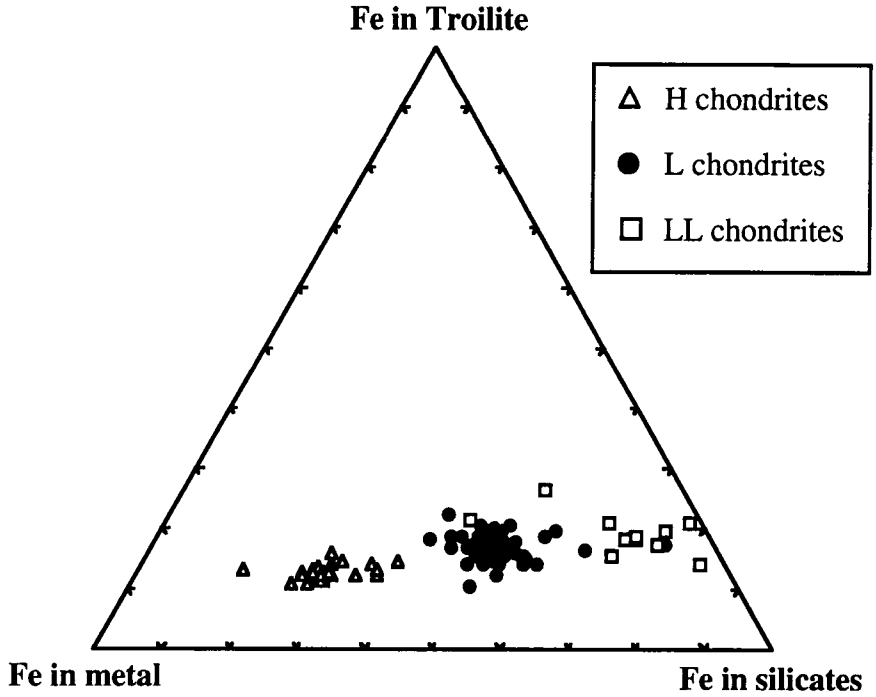

Figure 4. A plot of reduced vs. oxidized Fe reveals three distinct regions for ordinary chondrites. H chondrites contain the highest amount of reduced Fe (at the expense of Fe in silicates) and L chondrites contain the lowest reduced Fe (and a higher proportion of oxidized Fe in silicates). Overlap in the L/LL fields is due to the L/LL chondrite Bishunpur (data is from Jarosewich, 1990).

Thermal Metamorphic Effects

There are several inherent problems with petrographic studies of L chondrites. Samples denoted as finds may be slightly to severely weathered, resulting in oxidation of Fe-Ni metal. Heavy staining by oxy-hydroxides can coat minerals and fill fractures rendering textural observations difficult. It was for this reason that most of the non-Antarctic samples chosen for this study were relatively unweathered falls. This does, however, add a bias to any detailed study of L chondrites as a group. Another difficulty involves the separation of those features formed by static thermal

metamorphism from those formed by the rapid reheating accompanying shock metamorphism. Although shock reheating is a discontinuous, highly transitory process when compared to thermal metamorphism, severely shocked samples may have experienced post-shock temperature increases as high as 1500 °C (Raikes and Ahrens, 1979). It is for this reason that the discussion of thermal metamorphic effects will be limited to those samples which have not been strongly shocked (shock stage S4 and below), where average post-shock temperatures are believed to be <350 °C (Stöffler et al., 1991).

The original division of L chondrites into one of four types (L3-L6) was based on a petrographic assessment of the degree to which thermal metamorphism had altered their original textures (Van Schmus and Wood, 1967). Each petrologic type embodies a range in textures and compositions, making the division between types somewhat arbitrary. Table 5 gives the petrologic classification of all of the samples in this study. Figure 5 shows an example of textures typically assigned to each petrologic type. Figure 5a is a transmitted light photomicrograph of a portion of the L3 chondrite Inman. Type L3 chondrules have sharp, distinct boundaries and often contain clear igneous glass. Matrix is a fine-grained mixture of glass, silicate crystallites and large, irregularly-shaped metals and sulfides. Figure 5b was taken from the L4 chondrite Tennasilm. Chondrule boundaries are less distinct and any glass present within chondrules and matrix is made turbid by the presence of small microlites of olivine, pyroxene, and plagioclase. Jhung, Fig. 5c, is a typical L5 chondrite. Chondrule boundaries are difficult to recognize and all igneous glass has been destroyed by recrystallization. Matrix within Jhung is composed of a coarse-grained mixture of silicates, oxides, metals, and troilite. L6 chondrites contain few distinguishable chondrules. They consist primarily of a coarse equigranular mixture of typical

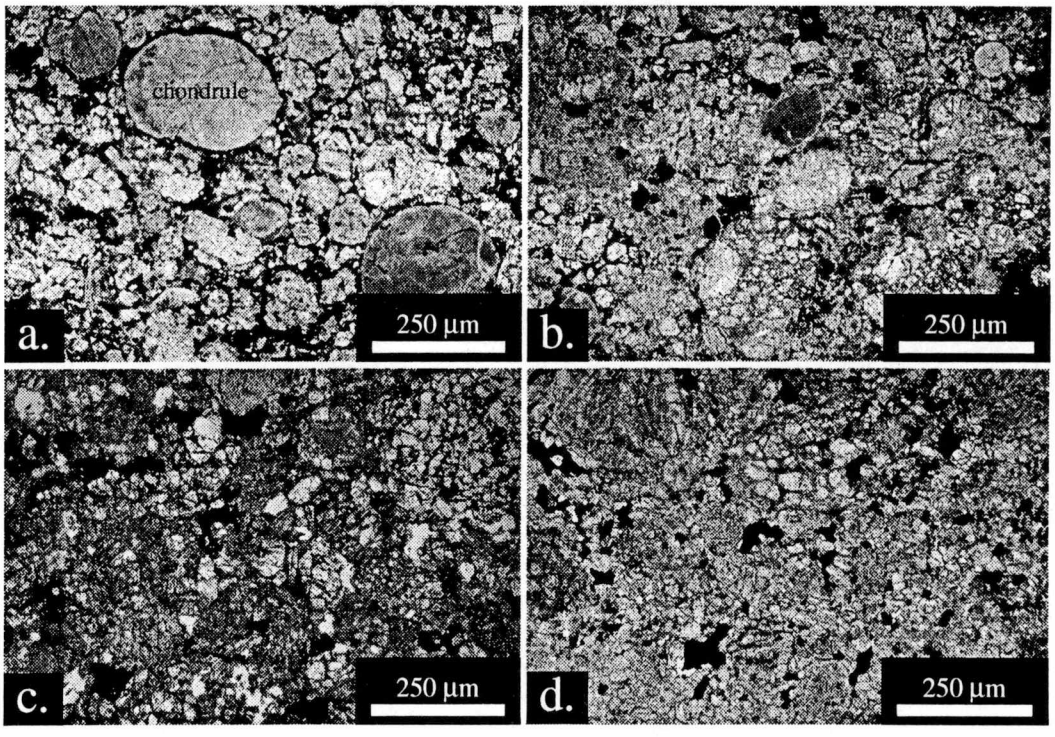

Figure 5. Transmitted light photomicrographs showing textural variations in L3-L6 chondrites resulting from thermal metamorphism. a) Inman (L3) showing large chondrules (many composed of igneous grass and microlites). b) Tennasilm (L4) showing a coarsening of matrix phases and less distinct boundaries between chondrules and matrix. c) Jhung with a coarse matrix and very indistinct chondrules. d) Tenham (L6) which consists almost entirely of matrix with a few relict chondrules.

meteorite mineralogy. Figure 5d was taken from the equilibrated L6 chondrite Tenham. Several relict chondrules are present in this photomicrograph.

Shock Metamorphic Effects

Collisions between meteorite parent bodies in the asteroid belt occur at average speeds of ~ 5 km/sec (Weatherill, 1989). At the point of impact material in the target body is accelerated faster than sound can travel through the body (at hypersonic speeds). This particle acceleration propagates through the body in a period of nanoseconds to microseconds as a compressional wave called a shock front. Material encountering the shock front may undergo strain rates of 10^6/sec, far more than what is necessary to cause permanent deformation (Short, 1966). Shearing occurs at grain boundaries between minerals of different shock impedances. At shock pressures between 4 and 5 GPa, grain-boundary shear begins to produce brittle deformation features in anisotropic minerals (notably olivine and pyroxene) within the target body. At pressures above ~ 55 GPa solid-state recrystallization of minerals and polymorphic phase transformations are possible (Stöffler et al., 1991).

The reduction in material volume is more severe along a shock front than what is generally encountered at slower strain rates, because materials tend to have greater elastic strength at faster strain rates. The difference between a shock-induced dynamic elastic limit and a normal elastic limit represents an increase in entropy in the target material. This increase in entropy manifests itself within shocked material as waste heat or a post-shock temperature increase. The relationship between peak shock pressure and average temperature increase for a given material can be calculated from experimentally derived curves called Hugoniots. A Hugoniot curve is a plot of particle velocity or specific volume (the reciprocal of the average density) versus the pressure

increase. Figure 6a is a plot of the most recent Hugoniot curves calculated for H and L chondrites and the peak-shock pressures derived from these plots (Schmitt et al., 1994). The range of shock pressures for each of the six shock stages is plotted in Fig. 6b (Stöffler et al., 1991). Post-shock temperature increases are on the order of 50 to 250 °C higher for L chondrites than previously reported (Raikes and Ahrens, 1979; Stöffler et al., 1991).

Hugoniot curves form the basis for modern shock classification systems. Peak shock pressures are provided by experiments in which materials of different compositions are shocked to carefully calibrated pressure ranges. The number and type of deformation features are noted at each shock stage and are used to provide a statistical calibration, which is then applied to naturally shocked materials. Once the peak shock pressure is determined for a sample the Hugoniot supplies the average post-shock temperature increase, and with the temperature and pressure known, the degree of shock metamorphism experienced by the sample can be determined. Shock features that may be related by statistical means to peak shock pressures have been termed equilibrium shock effects, because they are believed to represent the final steady shock state that the material achieves prior to decompression (Stöffler et al., 1991). Because chondrites are not uniform in mineral assemblage and density, many shock features are not amenable to simple statistical analyses. Melt pockets and melt veins form in isolated regions where mineralogical heterogeneities create unusually high differences in shock impedance. Meteorites that have reportedly undergone low degrees of shock (peak pressures of 5 to 10 GPa and Hugoniot post-shock temperature increases of ~100 °C) can contain small pockets of shock-induced melt glass. Shock features formed by compositional heterogeneities have been termed disequilibrium

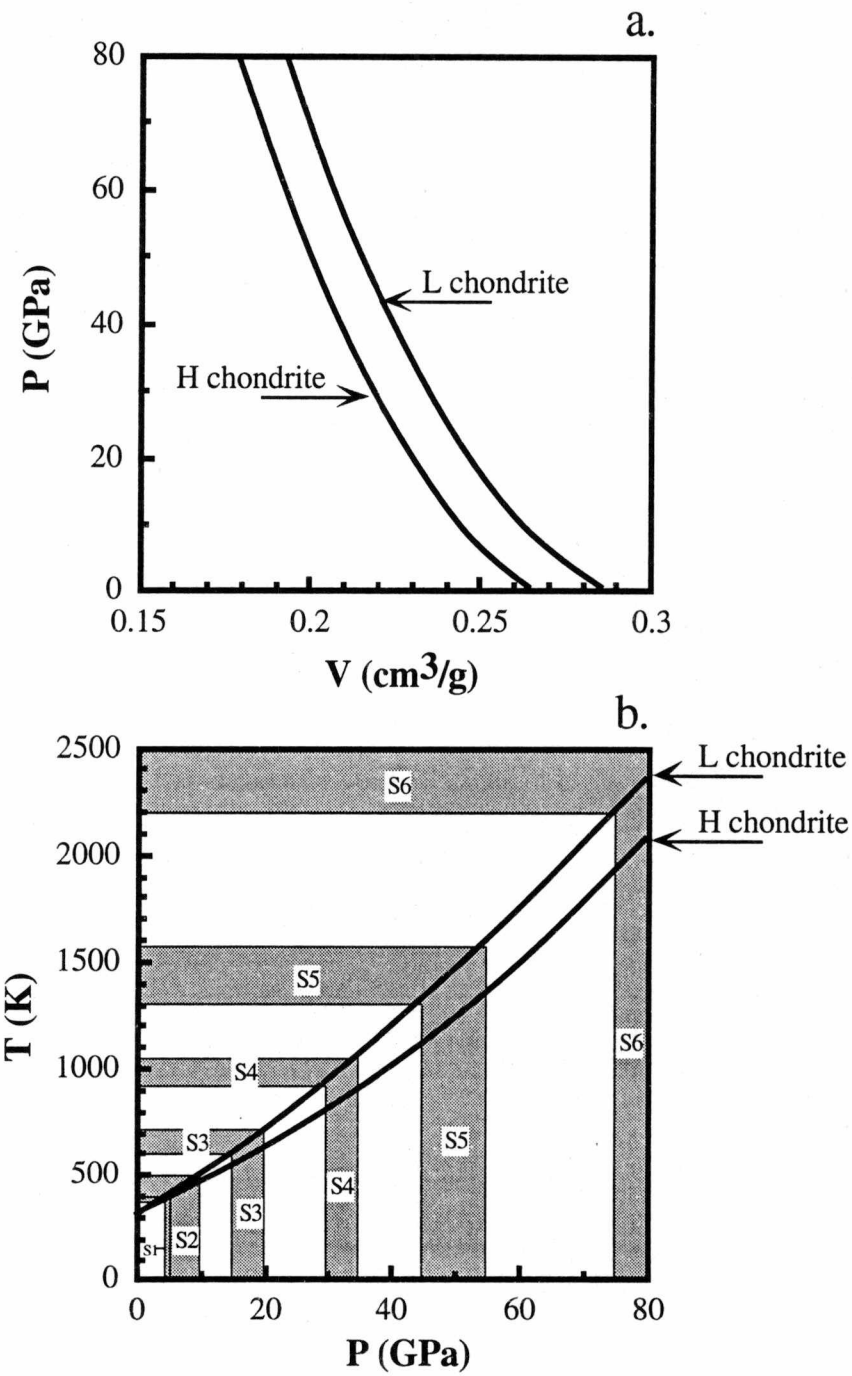

Figure 6. Calculated Hugoniot (a) and Pressure vs. Post-Shock Temperature (b) curves for H and L chondrites (Schmitt et al., 1994). a) L chondrites have a lower metal content and, hence, a higher specific volume than H chondrites. b) Range of shock pressures and post-shock temperatures for the upper limits of each shock stage are shaded in for L chondrites (data from Stöffler et al., 1991).

shock effects, as they do not reflect average or equilibrium temperatures achieved within the bulk of the sample.

Equilibrium Shock Effects in L Chondrites

Equilibrium shock effects form the basis for the shock classification of ordinary chondrites, as outlined by Stöffler et al. (1991). These authors have presented a thorough photo documentation of each feature, along with the shock pressure and post-shock temperature range in which they formed. The following is a brief summary of those equilibrium shock features used to shock classify specific ordinary chondrites. These petrographic features will be discussed in order of increasing shock metamorphism.

L chondrites shocked to S3 and S4 stages appear to dominate the current database of shock-classified samples. It was for this reason that Stöffler et al. (1991 and 1992) considered the L chondrites to be the most severely shocked of the ordinary chondrite groups. This study appears to confirm these findings. Of the thirty samples selected for further chemical and petrographic studies, eleven were found to be shocked to S3 stage and ten to S4 stage. Low-shock L chondrites (below S3) are apparently rare phenomena in our current meteorite holdings. Highly shocked L chondrites (above S4), although not as abundant as moderately shocked samples, are nevertheless more common in L chondrites than in other ordinary chondrite groups.

Virtually every L chondrite examined showed some evidence of shock metamorphism. The only exception found in this study was Bjurböle (L4, S1). The brittle deformation features that dominate the lower shock stages are absent in this sample. Olivine, both in chondrules and matrix, lacks irregular fractures and has

straight extinction under polarized light. Pyroxene grains are also relatively free of fractures and do not show any evidence of mechanical twinning.

What makes Bjurböle such an unusual sample is the consistency with which it has been identified as an unshocked L chondrite. In all three studies that have employed the current shock classification scheme (Stöffler et al., 1991; Rubin, 1993; this study), Bjurböle is the only meteorite that has been classified consistently at an S1 shock stage. All other samples which overlap between studies show some variation in their classification (see Appendix B for a complete list). This variation in shock stage is due either to the statistical nature of the classification (which particular mineral grains were used to determine the shock stage) or actual heterogeneity in peak shock conditions experienced by the samples. Until a thorough study of multiple thin sections from the same meteorite can be undertaken, Bjurböle is, at present, the least-shocked L chondrite reported in the literature.

Two samples selected for further geochemical work were classified at shock stage S2: ALH85045 (L3, S2) and Ausson (L5, S2). Both samples contain olivine that is irregularly fractured and displays undulose extinction under polarized light. In addition, Ausson has numerous olivine grains that show one or more sets of parallel fractures and may be an S3 (as suggested by Stöffler et al., 1991). The section obtained for this study was extremely thin (most olivine has first-order gray birefringence), making it difficult to chose the proper grains for shock classification. Polysynthetic twins in several pyroxene grains of both samples are slightly bent and some twins are offset along fractures. Shock metamorphism in these samples, and in all other samples of higher shock stage, is not uniform. Individual olivine grains may be found that display mosaicism and other features indicative of higher shock levels. Whether these grains represent brecciated clasts or isolated regions of higher shock

impedance contrast is uncertain, but it does emphasize the idea that the peak equilibrium shock pressure given in this shock classification corresponds to the average shock pressure attained in the region of the meteorite from which the thin section was taken.

In all 11 samples classified at S3 stage, olivine grains display a strong undulatory extinction and contain well developed sets of parallel planar fractures. Submicroscopic planar deformation features, originally considered an indicator of shock stage S5 by Stöffler et al. (1991), was found in several olivine grains in Jhung (L5, S3). This is in agreement with similar findings in a continuing study of shock metamorphism by Stöffler et al. (1992). A few of the largest olivine grains exhibited a weak mosaicism (indicative of shock stage S4), but mosaicism was absent in most olivine grains. Pyroxene contains abundant bent or sheared twins in these samples. Plagioclase in the two L6, S3 Antarctic L chondrites (ALHA76001 and GRO85209) is anisotropic and displays a straight to slightly undulatory extinction under polarized light.

Samples shocked to S4 stage are readily distinguishable by the weak mosaicism seen in the larger, high-birefringent olivine grains. Olivine mosaicism has been used as a means of identifying moderately shocked ordinary chondrites since Carter et al. (1968) developed one of the first shock classification schemes. Mosaic domains are very small (<5 μm across) and have independent extinction. This gives olivine grains a slightly mottled appearance and prevents them from going completely extinct under full rotation of the microscope stage. Planar fractures become more numerous in olivine, with at least three distinct sets of fractures visible. Pyroxene grains at S4 shock stage are severely deformed and display undulatory extinction and abundant cross-hachured mechanical twins. Polysynthetic twins are warped and highly fractured. In equilibrated S4 chondrites, such as Long Island and Tenham (both L6,

S4), smaller plagioclase grains (<15 μm) contain finely spaced deformation lamellae and have been partially converted to maskelynite (diaplectic glass after feldspar). Larger plagioclase grains are anisotropic, although they exhibit undulatory extinction and may contain small bent twin lamellae.

In unequilibrated L chondrites the distinction between shock stage S4 and S5 is difficult to determine. There is no apparent difference in the intensity of deformation seen in pyroxene grains. Plagioclase is absent and so can not be used as a shock indicator. The difference between the appearance of weakly mosaicized and strongly mosaicized olivine could, in reality, be the difference between a thick and a thin polished section. Submicroscopic lamellae in olivine, another key indicator of strong shock metamorphism (Grieve et al., 1990), have recently been noted in samples shocked as low as S3 stage (Stöffler et al., 1992). This may be the reason why unequilibrated L chondrites of shock stage S5 appear to be rare in meteorites that have been shock classified to date.

For equilibrated chondrites, the determination of S5 shock grade is a relatively simple matter. Olivine has not been shocked severely enough to recrystallize and all plagioclase grains have been converted to maskelynite. Both Kyushu and Fisher (L6, S5) contain 50 μm size plagioclase grains that have bent deformation lamellae and have been shocked to maskelynite.

Shock stage S6 is the highest stage that can be attained before partial melting takes place (Stöffler et al., 1991). The texture of a sample that has been shocked to S6 stage can only be described as severely crushed. Both olivine and pyroxene contain many submicroscopic planar deformation features. Plagioclase is no longer recognizable, as it has been entirely converted to igneous glass. Olivine has small veinlets and patches of yellowish-colored, strain-free grains that formed as a result of solid-state

recrystallization. All of the original metal and sulfide textures have been completely annealed (or destroyed by partial melting). The recrystallization and subsequent blurring of textural elements is so strong at this stage that it is easy to see why few samples of low petrologic type have been recognized as having been shocked to S6 stage. With average post-shock temperature increases of >1500 °C, however brief they may be, it would be difficult to separate the textural features created by thermal metamorphism from those of shock metamorphism.

Disequilibrium Shock Effects in L Chondrites

The diverse effects of heterogeneous shock reheating and post-shock cooling and annealing are recorded in the metals and sulfides. Shock-induced variations in the textures and chemistries of these phases may be used to augment thermal information derived from studies of equilibrium shock features. A detailed petrographic study of metal-sulfide textures in 20 meteorites, representing the full range of shock stages and most of the petrologic types, was performed in order to quantify those features that may correspond to disequilibrium shock effects. In order to facilitate petrographic identification of Fe-Ni metal phases, all samples were lightly etched in a 1% solution of nital. The results of this petrographic study are summarized in Appendix C.

In addition to nital etching, most of the samples were examined at high magnification (at least 1000X) using a Cameca SX-50 electron microprobe in backscatter electron (BSE) imaging mode. Used in conjunction with energy dispersive spectrometry (EDS) single point analyses, this allowed the rapid identification of textural features too small to be recognizable by optical means.

Scott et al. (1991) proposed two sources of heat that, along with accompanying pressure effects, could produce the metal-sulfide textures present in ordinary

chondrites; residual heat due to equilibrium shock pressure and heat from localized impact melts. Residual heat is responsible for the average shock temperature increases that have been approximated by experimentally derived Hugoniot curves. When residual shock heating is accompanied by normal slow cooling (defined as cooling rates between 1-100 K/My; Wood, 1967; Willis and Goldstein, 1983), Fe-Ni metal (Scott and Rajan, 1981) and troilite (Schmitt et al., 1993) display normal or equilibrium shock textures. With higher initial temperatures and/or at faster cooling rates numerous metastable textures and metal-sulfide compositions can develop (Smith and Goldstein, 1977). Localized impact melting creates disequilibrium shock textures in ordinary chondrites (Scott, et al., 1991; Stöffler et al., 1991). Isolated hotspots can generate a whole series of melt features (Bergmann and Wlotzka, 1969; Scott, 1982; Stöffler et al., 1991) and can lead to annealing of previously formed textural components (Buchwald, 1975). At higher shock stages (above S4) disequilibrium shock features may become the dominant textural elements in portions of some L chondrites.

In L chondrites that have their normal complement of Fe-Ni metal (averaging 7.5 to 9.5 wt %; Jarosewich, 1990), slow cooling from ~700 to 350 °C produces zoned taenite metal grains (Scott, 1973; Willis and Goldstein, 1983). Chemically zoned taenite grains yield a classic M-shaped Ni profile (Wood, 1964) formed by the slow diffusion of Ni toward the center of the grain. Texturally, they have very complex morphologies, as numerous metastable phases may form during slow cooling below 400 °C (Reuter et al., 1989). The outer rim of a zoned taenite grain consists of a thin (1-10 μm), often discontinuous rind of high-Ni metal (48-57 wt % Ni) which becomes bright white upon etching. If optically anisotropic, the metal is referred to as tetrataenite (Clarke and Scott, 1980). Adjacent to the tetrataenite is a thin (several μm

wide) gray rim of cloudy taenite (Scott, 1973) which is a two phase mixture of tetrataenite and martensite (~50 and 11 wt % Ni, respectively; Reuter et al., 1989). The central portion of a zoned taenite grain consists of a dark brown region of martensite, fine-grained plessite, or a combination of the two. Figure 7a shows a normally-zoned Fe-Ni metal grain in Bjurböle (L4, S1) showing a tetrataenite outer rim, a cloudy inner rim, and a plessite core. GRO85209 (L6, S3) has normally zoned Fe-Ni metal grains whose cores have a taenite composition (~35 wt % Ni), but because of normal slow cooling, are probably spinoidal decomposition products consisting of martensite and tetrataenite or high-Ni taenite (Fig. 7b).

Zoned taenite occurs in most of the samples that were shock classified below S4 stage. This is consistent with slow cooling from shock pressures < 20 GPa and average shock temperatures < 100 °C (Stöffler, et al., 1991). Those samples that display incomplete zoning (missing either the tetrataenite or cloudy taenite rims) or homogeneous taenite (grains unaffected by etching) contain evidence that localized reheating has disturbed their original textures. LEW85339 (L3, S2), for instance, has several 100-200 μm patches of a fine-grained mixture of troilite and metal which has been termed fizzed troilite by Scott (1982). These are discrete grains of intermixed phases and should not be mistaken for the finely disseminated metal and sulfide material that commonly occurs within chondrule rims in both shocked and unshocked unequilibrated L chondrites. Although originally considered evidence for eutectic melting at temperatures > 988 °C (Wood, 1967), Scott (1982) theorized that fizzed troilite formed at extremely fast cooling rates (~ 10^6 °C/sec) from peak shock temperature increases of between 100-600 °C. According to Scott, troilite with a fizzed texture may be the low-temperature annealing product of metallic glass. Regardless of how it forms, the presence of fizzed troilite seems to indicate local

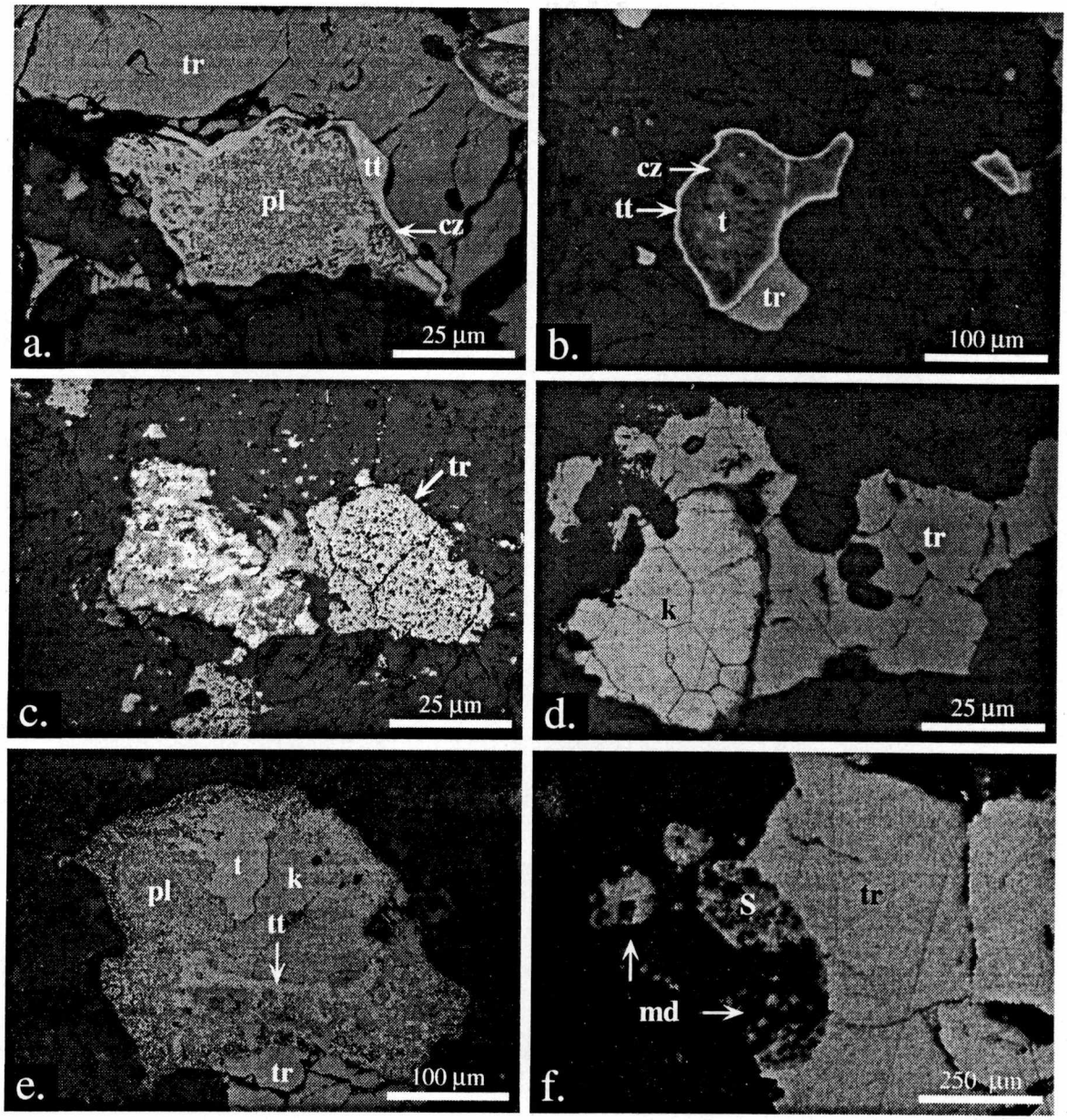

Figure 7. Reflected light photomicrographs of metal-sulfide textures in low- to moderately-shocked L chondrites (<S5). Symbols are: k = kamacite, t = taenite, tt = tetrataenite, cz = cloudy zone, pl = plessite, tr = troilite, and md = melt drops (metal and/or troilite). a) Normal zonation of metal with aplessite core in Bjurböle (L4, S1). b) Normal zonation of metal with a taenite core in GRO85209 (L6, S3). c) Polycrystalline troilite in Khohar (L3, S4; labeled with arrow). d) Polycrystalline kamacite in Jhung (L5, S3). e) Fine-grained, pearlitic plessite in Jhung. F) Troilite melt drops and 'swiss-cheese' texture (labeled with an 'S') in Tenham (L6, S4).

temperature excursions of >100 °C and cooling rates fast enough to prevent the formation of zoned taenite grains.

Several samples which lack both normal zoning of taenite and fizzed troilite contain other evidence for brief periods of localized shock reheating. This evidence includes the presence of polycrystalline troilite (Schmitt et al., 1993), polycrystalline kamacite (Wood, 1967; Taylor and Heymann, 1971; Smith and Goldstein, 1977), and abundant coarse plessite (Taylor and Heymann, 1970 and 1971).

Schmitt et al. (1993) conducted a series of shock-loading experiments with the S1, H6 chondrite Kernouvé and noted that troilite undergoes a series of predictable textural changes under specific shock temperature-pressure conditions. In their experiments, troilite was found to be monocrystalline at pressures below 10 GPa, became twinned between 10-20 GPa, and became polycrystalline at 35-60 GPa. The presence of polycrystalline troilite indicates shock conditions considerably higher than what is predicted to occur in shock stages below S4 (Stöffler et al., 1991, cites 20 GPa as the maximum shock pressure for S3 stage). Inman (L3, S3) and Cynthiana (L4, S3) contain abundant grains of polycrystalline troilite which have 120° angles between grain boundaries. Since both samples are S3 shock stage, this would indicate that they have been undergone localized shock heating, and the absence of zoned taenite indicates a subsequent rapid cooling from peak shock conditions. Khohar (L3, S4) also contains many polycrystalline troilite grains and well as abundant fizzed troilite (Fig. 7c), both indicating fast cooling.

The presence of polycrystalline kamacite in QUE90201 (L5, S3) and Jhung (L5, S3) helps confirm cooling at faster-than-normal rates (Fig. 7d). Polycrystalline kamacite (sometimes called ε-iron) is a very common feature in the fusion crust of unshocked meteorites, where temperatures may undergo rapid fluctuations of several

hundreds of degrees (Buchwald, 1975). Although its formation is still not well understood, polycrystalline kamacite is believed to form when taenite of ~10 wt % Ni is heated to a few hundred degrees and then rapidly cooled (Wood, 1967; Taylor and Heymann, 1971). Instead of converting to Fe-Ni metal with a normal martensitic texture (as predicted by the Fe-Ni phase diagram), polycrystalline kamacite forms by a process known as massive transformation, a form of polymorphic inversion.

Two of the low-shock samples contain many Fe-Ni grains which have coarse plessite in the centers or along the edges of the metal grains (Tennasilm (L4, S3) and Jhung (L5, S3)). Taylor and Heymann (1970), in a study of the coarse-grained plessite in Kingfisher (L5, S6), suggested that the presence of abundant plessite in this sample indicated reheating to ~600 °C with subsequent slow cooling. In Tennasilm, cooling after peak temperature conditions were reached proceeded slowly enough to produce normal metal-sulfide textures. Plessite decomposition products in Tennasilm are closer in size (5-50 μm across) to those of Kingfisher (10-250 μm). In Jhung, cooling was rapid enough that only partial zonation was achieved in many of the taenite grains. Plessite decomposition products are approximately half the size of those in Tennasilm (5-25 μm; Fig. 7e), which also suggests that Jhung cooled at a faster rate.

In samples shocked above S3 stage, melt features become an important addition to the observable disequilibrium shock textures. In two of the three S4 samples, Tenham and Long Island (both are L6), incipient melting of troilite was plainly visible. Since troilite is more compressible than Fe-Ni metal and a poorer conductor of heat (Buchwald, 1975), melting occurs initially at the edges of some of the larger troilite grains and is rare or absent in the Fe-Ni metal. Troilite grain edges closest to the troilite melt droplets commonly take on a bubbly or swiss-cheese appearance. Troilite melt droplets are very small at the S4 stage (the largest are <5 μm in diameter; see Fig.

7f) and are surrounded by a fine-grained mixture of silicate minerals and glass (these are actually small melt pockets from 10 to 40 μm in diameter). Fe-Ni metal melt droplets are present in these samples, but they are very rare (in Tenham they were found adjacent to one metal grain only) and they are much smaller then troilite melt droplets (generally <2 μm in diameter). Although Khohar lacks visible melt droplets, it does contain an abundance of melt features including large patches of fizzed troilite and many anastomosing melt veins of mixed troilite and silicate crystals. The very ragged grain to the left of the polycrystalline troilite grain in Fig. 7c is a typical metal-sulfide mixture found in Khohar. The sulfide component in this grain is fizzed troilite, containing tiny (<1-2 μm metal grains) and the Fe-Ni component has several wt % S.

Of the three S4 samples studied, only Long Island lacked normal zoned taenite. This sample is a find and, as such, it is strongly weathered. Most of the metals are rimmed by a layer of oxidation. Many of the original Fe-Ni metal textures in this sample may have been obliterated (or, at least, were partially obscured) by terrestrial weathering.

In the two L6, S5 stage samples studied (Fisher and Kyushu), metal and sulfide melt droplets occur adjacent to ~10% of all grains present in the samples. Individual droplets are much larger than in the S4 samples (up to 20 μm in diameter) and occur in multiple, partially coalescing melt pockets along individual metal or troilite grains (Fig. 8a). Fizzed troilite is rare in these samples (one grain in Kyushu), but polycrystalline troilite is abundant. Taenite in these samples is not zoned, no tetrataenite or cloudy taenite was observed in either sample. Polycrystalline kamacite is also common, with many of the domains having a polygonal outline (120° intersections). Both samples must have undergone fast cooling from peak shock conditions.

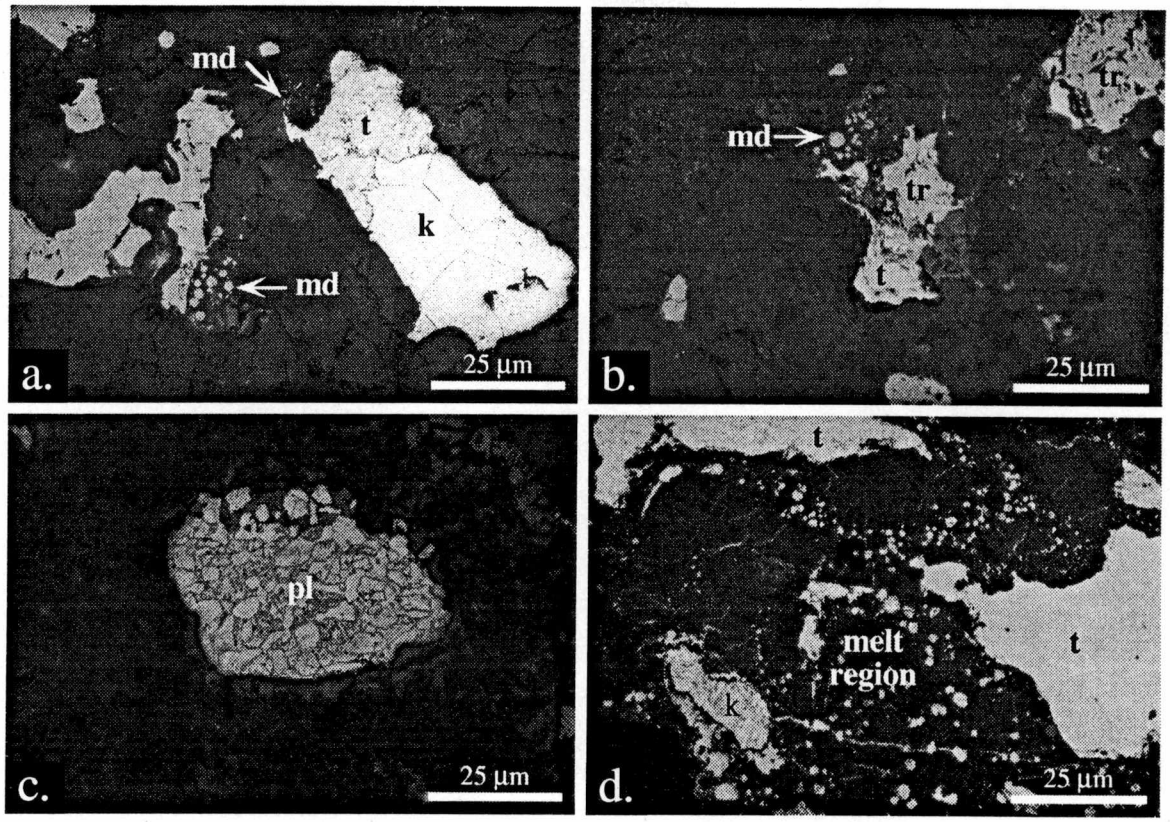

Figure 8. Reflected light photomicrographs of metal-sulfide textures in high-shock (>S4) L chondrites. Symbols are the same as Fig. 7. a) Large troilite melt drops and smaller metal melt drops in Kyushu (L6, S5). b) Melt drops that contain both metal and sulfide in Kingfisher (L5, S6). Coarse-grained plessite in a Kingfisher metal grain. d) All metal and troilite has experienced partial melting in shock-blackened McKinney (L4, S6).

Both of the S6 samples (Kingfisher and McKinney) contain abundant melt features. Metal and sulfide melt droplets occur adjacent to most grains and individual droplets may reach 50 μm in diameter. Figure 8b shows a large melt pocket with melt droplets consisting of mixtures of metal and sulfide in Kingfisher. Both Kingfisher and McKinney have unzoned taenite grains. Kingfisher also contains abundant coarse-grained plessite (Fig. 8c), formed from the decomposition of martensite at ~600 °C and at pressures of ~50 GPa (Taylor and Heymann, 1970). This pressure corresponds to the range of boundary conditions between the S5 and S6 shock stage (Stöffler et al., 1991). McKinney lacks plessite and has the shock-blackened texture of metal and sulfide melt that was injected into adjacent fractures and veins during shock metamorphism. Mixed metal-sulfide melt droplets and melt veins are clearly visible in the dark silicate matrix of McKinney (Fig. 8d). Smith and Goldstein (1977), in a comparison of severely shock-reheated L chondrites, suggested that the presence of metal-sulfide veins represents moderate heating (maximum of 900 °C) with fast cooling. The abundance of fizzed troilite and metal-sulfide melt veins in McKinney and the presence of plessite and absence of fizzed troilite in Kingfisher suggests that Kingfisher had a much slower cooling history than McKinney.

Summary

Equilibrium shock features in silicate minerals have been described and used as a basis to classify 63 L chondrites into their appropriate shock stage. Twenty of these samples, representing the full range of shock metamorphism, were chosen for further petrographic study of equilibrium (homogeneous) and disequilibrium (heterogeneous) shock features. A synopsis of major shock features is presented in Table 7. Samples that are weakly shocked (S3 stage and below) have textures dominated by equilibrium

Table 7. Summary of shock textures observed in metal and troilite. White bars = rare feature (seen in few grains), gray bars = common feature (in <50 % of all grains), and black bars = abundant feature (in >50 % of all grains).

SHOCK FEATURES	S1	S2	S3	S4	S5	S6
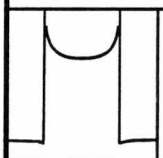 Normal Ni Profile						
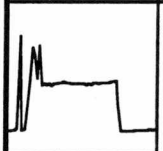 Disturbed Ni Profile						
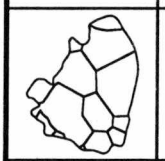 Polygonized Kamacite						
 Fizzed Troilite						
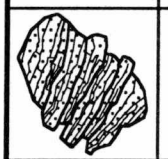 Sheared Troilite						
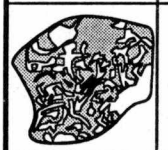 Plessite						
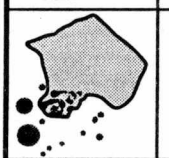 Metal - Sulfide Melt Drops						
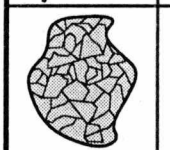 Polycrystalline Troilite						
 Metal - Silicate Melt Veins						

shock features. Normally zoned taenite grains were the most abundant of these features noted and were found in all low-shock L chondrites that experienced slow cooling through 400 °C. The presence of rare polycrystalline kamacite, fizzed troilite, and unzoned taenite in these samples represents quick cooling in isolated regions following heterogeneous, post-shock reheating.

Above shock stage S3, disequilibrium shock effects become abundant. Melting of metal and/or troilite, polygonized kamacite and troilite, fizzed troilite, sheared troilite, and unzoned taenite are among the dominate disequilibrium features above shock stage S3. Melting occurs in troilite at shock stage S3, producing rare, micron-sized melt droplets on the edges of larger grains. Fe-Ni metal joins troilite in melting at shock stage S4. By S5 stage Fe-Ni metal and troilite melt droplets occur adjacent to ~10 % of all metal and sulfide grains. At shock stage S6 all Fe-Ni metal and sulfide grains have experienced some degree of melting.

CHAPTER 3

BULK AND MINERAL CHEMISTRY OF L CHONDRITES

Thermal metamorphism appears to be isochemical for all but the most volatile trace elements. In comparing the bulk chemical compositions of L chondrites with other ordinary chondrite classes, many of the differences noted by previous workers have been attributed to shock metamorphic reheating. The loss of highly volatile noble gases in L chondrites was recognized by Kristen et al. (1963) and Anders (1964) as the result of shock metamorphic reheating accompanying a major impact event. Mobilization of other volatile trace elements (Walsh and Lipschutz, 1982; Huston and Lipschutz, 1984), anomalously low S/Mg and Fe/Mg ratios (Cripe and Moore, 1975; Dodd, 1981), and depletion of certain highly labile trace elements (Lipschutz and Woolum, 1988) have also been suggested to be the result of shock metamorphism in L chondrites.

Since the driving force behind both forms of metamorphism involves the application of heat, the trends mentioned above are not mutually exclusive. Van Schmus and Wood (1967) have shown that trends in certain volatile components in ordinary chondrites (notably C and H_2O) correlate with petrologic type rather than shock state. Likewise, Marti (1967) noticed depletions in certain noble gases which also seem to correlate with petrologic type. Finally, numerous authors (reviewed in Gomes and Keil, 1980) have shown that many of the differences in the bulk chemistry of ordinary chondrites, as expressed by normative mineral compositions, may be related to the original composition of the parent bodies and not to shock-induced element depletions.

The attempt here is to separate the effects of thermal metamorphism from those of shock metamorphism. To accomplish this bulk L chondrite analyses, taken from the literature, and individual mineral analyses, derived from electron microprobe work, were obtained. These analyses were compared by petrologic type and by shock stage in order to determine what, if any, correlations might exist.

Bulk Chemistry of L Chondrites

Element abundances for 87 L chondrites were published by Jarosewich (1990). Nineteen of these L chondrites have been classified by shock stage in this work, or by others, using the Stöffler et al. (1991) classification scheme. Figure 9 shows a summary plot of eighteen of these samples. Inman was not used as it contained an anomalously high amount of Fe^{3+}, possibly due to weathering. Atomic fractions were calculated for each element and then normalized to the CI chondrite Orgueil (also analyzed by Jarosewich) in order to limit the ordinate values. The top two diagrams show relationships between refractory elements, the center diagrams show siderophile elements, and the bottom two diagrams show volatile elements. Average metamorphic temperatures for L chondrite petrologic types were taken from McSween et al. (1988) and average shock temperatures from Stöffler et al. (1991). Goodness-of-fit for each line was determined by calculating a standard regression line and regression error for each data set.

Figure 9 reveals no correlation between either thermal or shock metamorphic temperatures and element abundances. Even the three most volatile elements fail to show any correlation (r^2 values <0.4) with increasing metamorphic temperature. This indicates that element abundances within the L chondrite parent body were established prior to both thermal and shock metamorphism and that both types of metamorphism

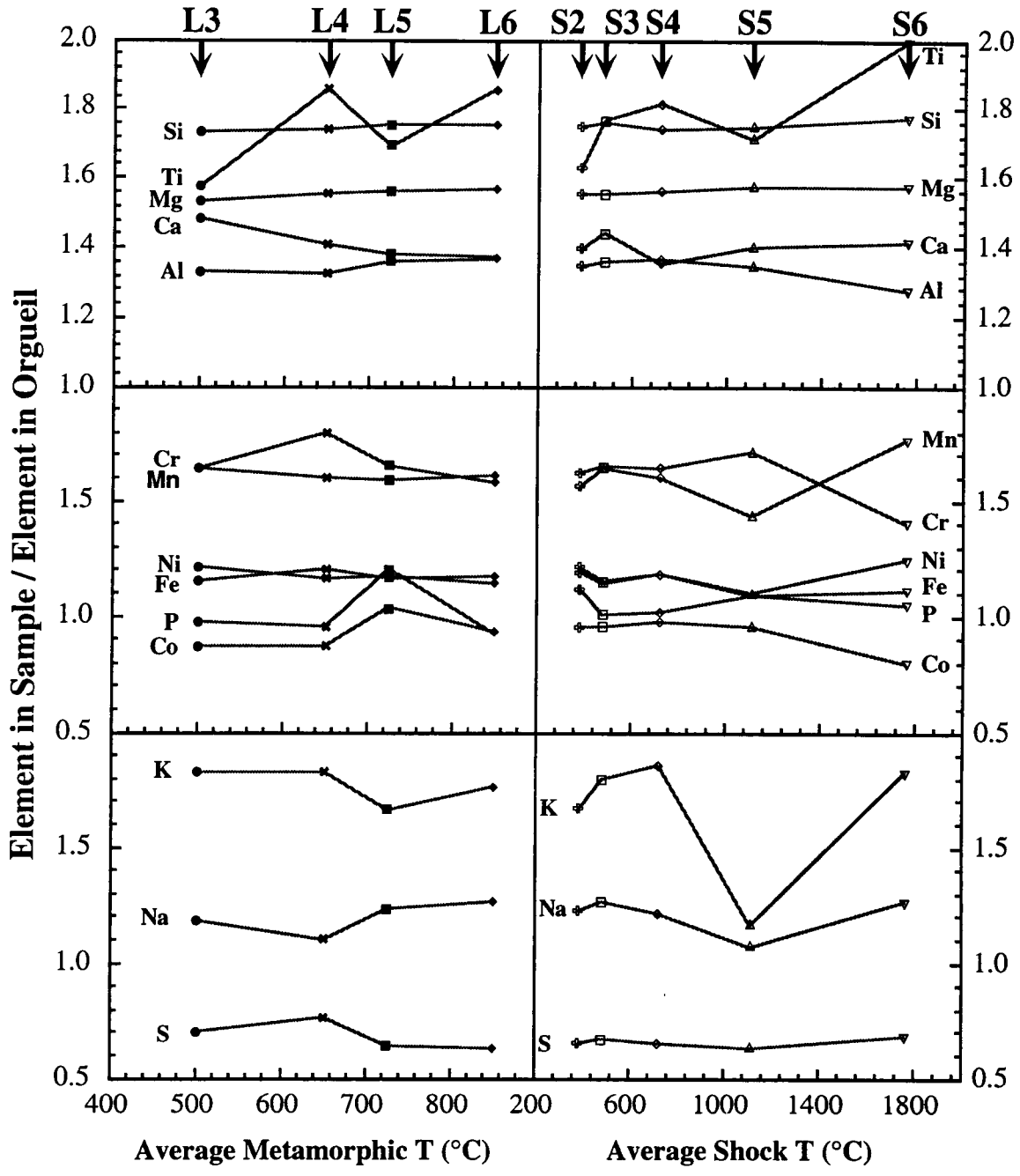

Figure 9. Bulk chemistry of L chondrites vs. average thermal metamorphic and average post-shock temperatures. Absence of any correlation between individual elements and either shock or thermal metamorphism suggests that metamorphism proceeded in a closed system prior to parent body accretion. Chemical data from Jarosewich (1990).

occurred in a closed system with respect to these elements. This does not, however, imply that other, more highly volatile elements could not be mobilized by either type of metamorphism, as evidenced by the chemical trends mentioned above.

Since 18 L chondrites spread over 4 petrologic types and 6 shock stages represents a statistically poor sampling, a similar series of plots was constructed for 14 bulk analyses of H chondrites that also have known shock classifications (Fig. 10). H chondrites have been shown to be less shocked than L chondrites (Stöffler et al., 1991 and 1992), so it was not surprising that a lack of correlation was also found between metamorphic temperatures and element abundances. This comparison also helps to substantiate the validity of any bulk compositional trends in the more highly shocked L chondrites.

Chemistry of Individual Minerals in L Chondrites

Most of the chemical analyses in this work were restricted to matrix phases within L chondrites. Matrix is defined as the fine-grained, low-temperature material found between chondrules in unequilibrated ordinary chondrites (Ashworth, 1977) or the coarser-grained, thermally-recrystallized, inter-chondrule material found in more equilibrated ordinary chondrites (Huss, 1981). Matrix minerals are probably less shielded than chondrule minerals from the effects of thermal metamorphism and, therefore, more susceptible to changes induced by impact heating. Exceptions to the use of matrix phases were in unequilibrated (type L3) and highly equilibrated (types L6 and L7) chondrites. Matrix phases in L3 chondrites consist of glass and submicron-sized mineral clasts (Scott et al., 1982) and, as such, are too fine grained for accurate electron microprobe work. In these samples analyses were restricted to coarser minerals found on the edges of chondrules in order to minimize the affects of

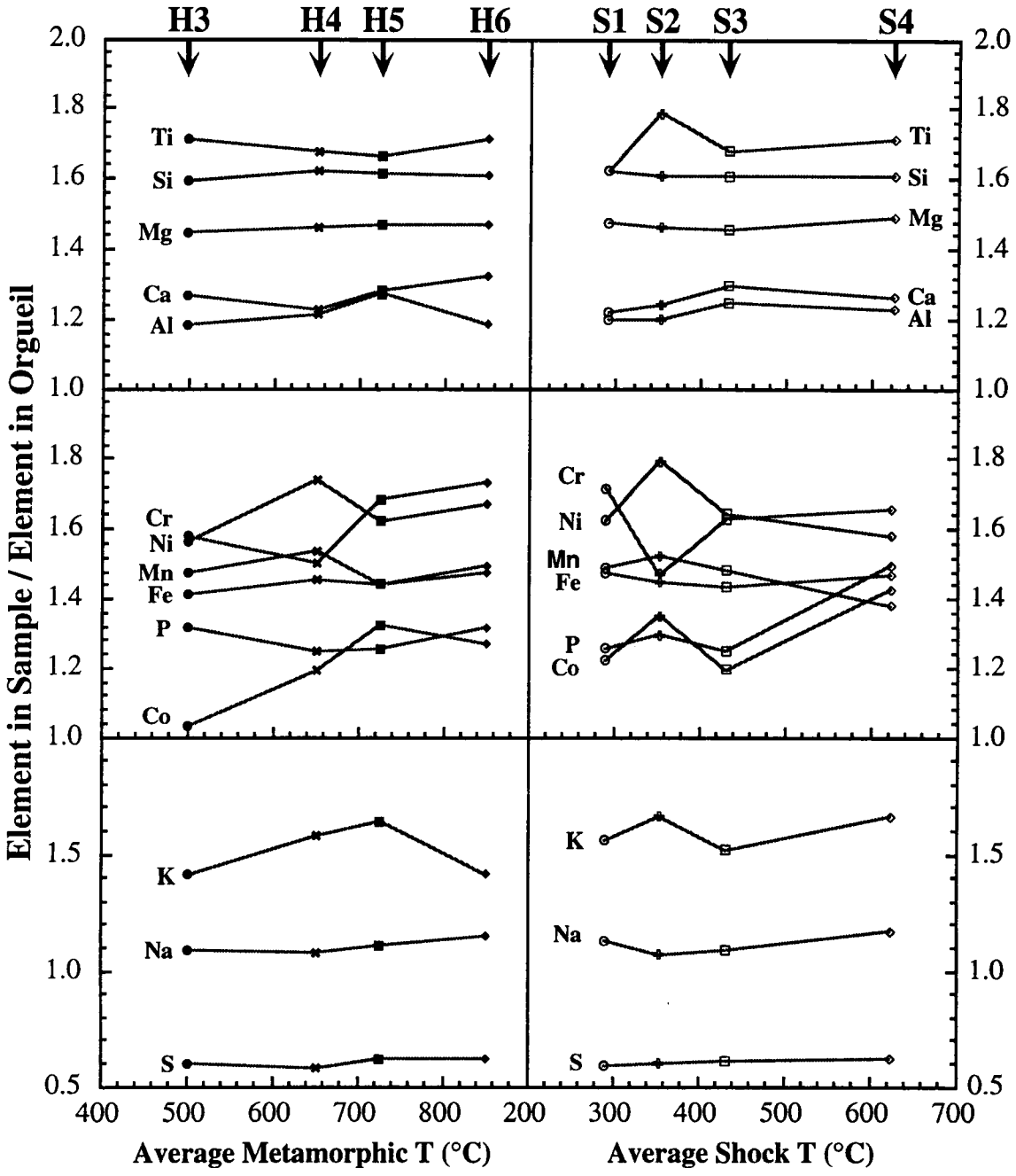

Figure 10. Bulk chemistry of H chondrites vs. average thermal metamorphic and average post-shock temperatures. Absence of any correlation between individual elements and either shock or thermal metamorphism suggests that metamorphism proceeded in a closed system prior to parent body accretion. Chemical data from Jarosewich (1990).

shielding. In type L6 and L7 chondrites, thermal recrystallization makes it nearly impossible to distinguish between matrix and recrystallized chondrules. Relict chondrules in these samples, where recognizable, were avoided.

Chemistry of Silicate Minerals

Three silicate minerals make up nearly 75% of the bulk of all L chondrites; olivine, low-Ca orthopyroxene, and high-Ca clinopyroxene. These minerals play an important role in our understanding of the metamorphic history of the L chondrite parent body. Textural changes occurring within these minerals caused by brittle deformation, and/or partial melting, are the primary tools for determining shock metamorphic stage. Measurements of the extent of chemical homogenization between these silicate minerals also form one of the most widely used discriminators for the assignment of an L chondrite to its appropriate petrologic type (i.e. its degree of thermal metamorphism). Consequently, these minerals appear to contain information related to both types of metamorphism.

If all textural changes in L chondrites were due to shock metamorphism and all chemical changes the result of thermal metamorphism, then these three minerals would provide a perfect Rosetta Stone for understanding metamorphism in L chondrites. However, this is regrettably not the case. There is an apparent overlap in the effects that the two types of metamorphism have on changes in the chemical compositions and textures of these minerals. In nearly every published chemical study of L chondrites in which the sought-after trend was not found, mobilization or even loss of chemical components by shock metamorphism was blamed. In a similar vein, textural changes due to increasing thermal metamorphism form one criterion for

distinguishing petrologic types even though high degrees of shock metamorphism may produce similar textural changes in L chondrites.

Does shock metamorphism alter the chemistry of silicate minerals to the extent that its effects are distinguishable from those of thermal metamorphism? Plots of major and minor elements obtained from electron microprobe analyses are used to answer this question.

To illustrate that thermal metamorphism is a fundamental process in controlling at least the major element compositions of these minerals, Fig. 11 is a plot of the mean Fe content in olivine (Fa) versus the mean Fe content in orthopyroxene (Fs) for over 500 Antarctic L chondrites taken from Score and Lindstrom (1990). The shock stages for these meteorites have not been determined, but they probably span the entire range from S1 to S6 stage. What is important to note is that the L4 chondrites occupy a subset of the L3 chondrites and the more equilibrated L5 and L6 chondrites occupy a subset of the L4 chondrite field. This diagram shows a clear trend toward more restricted (equilibrated) compositions of these mineral components with increasing petrologic type. Also plotted on this diagram are compositions of several of the L chondrites analyzed in this study. Regardless of their shock classification, all meteorites except the L5 chondrite Ausson and the Antarctic L6 chondrite PAT91501 plot in their appropriate fields. Ausson is a low shock (S2) L chondrite that may be misidentified as to its petrologic type. PAT91501 is a unique cumulus melt rock that may have been derived from partial melting of a previous L chondrite (Harvey, 1994).

Figure 12 is a plot of average wt % major and minor oxide components in matrix olivine for a suite of L chondrites. In the upper two diagrams (Fig. 12a), oxides are arranged according to petrologic type. Shaw is a type L7 chondrite that contains a partially melted dike lithology. PAT is the designation for PAT91501, an igneous

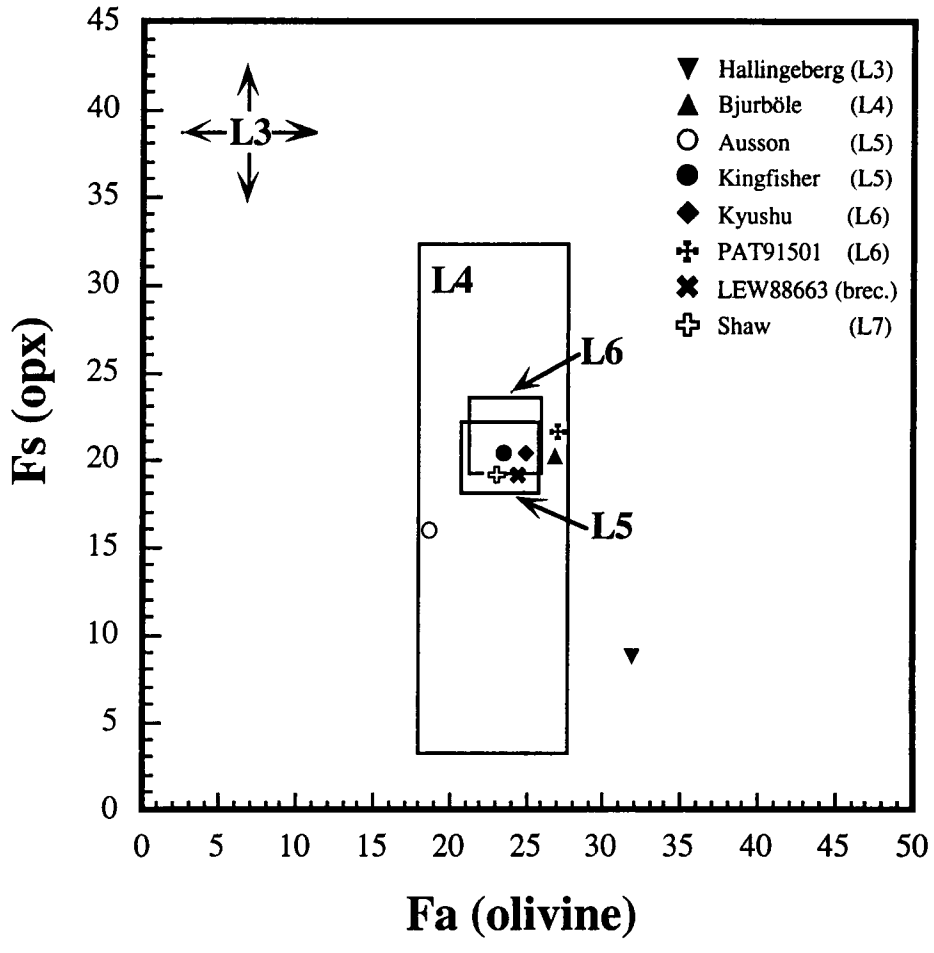

Figure 11. Fe content in olivine (Fa) vs. Fe content in orthopyroxene (Fs) for ~500 Antarctic L chondrites (data from Score and Lindstrom, 1990). L3 chondrite field spans the entire inner portion of the diagram (the full range of olivine and pyroxene compositions possible in L chondrites). Higher petrologic types have more restricted compositional ranges.

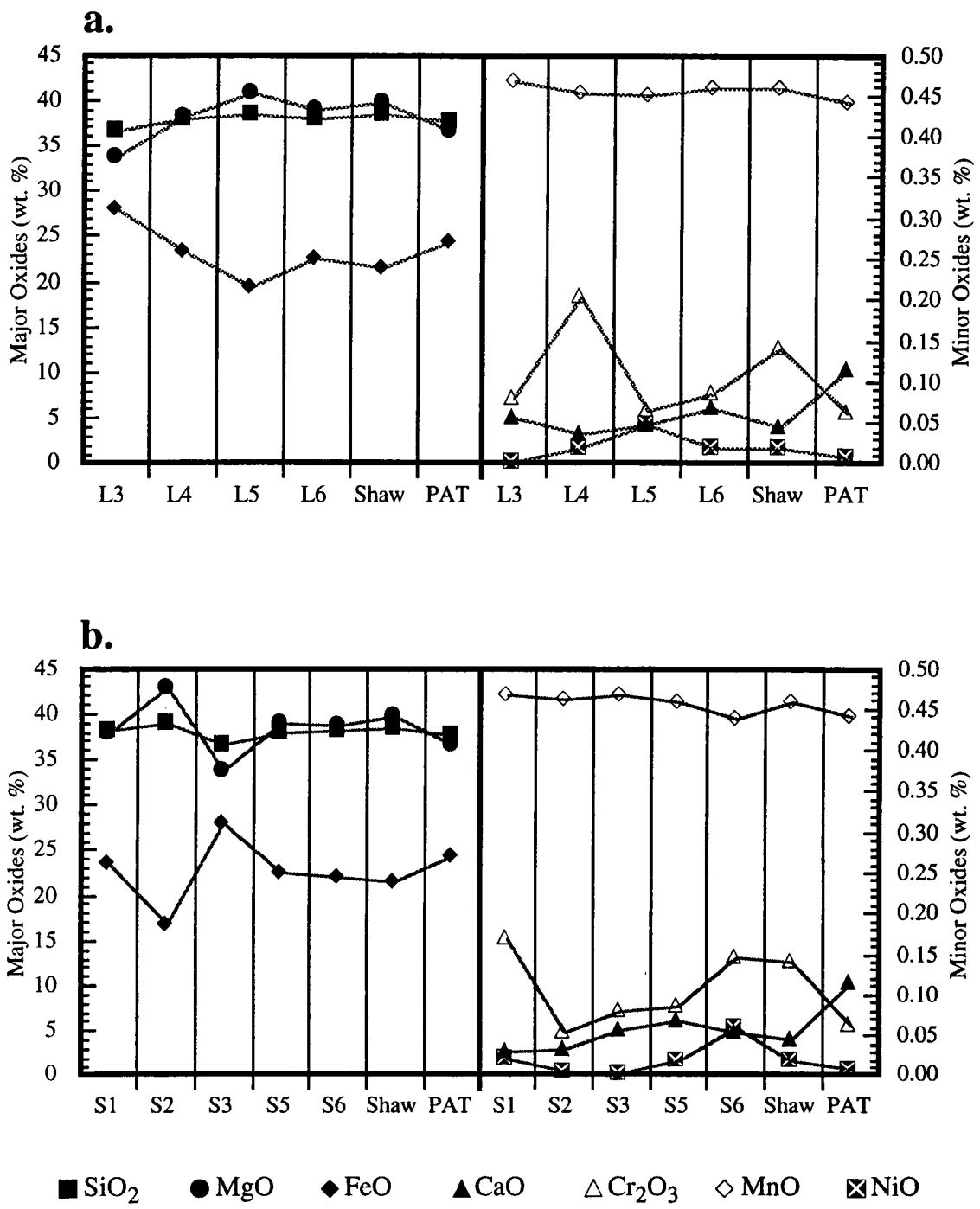

Figure 12. Major and minor oxides for olivine in L chondrites obtained from electron microprobe analyses. Upper two diagrams have data arranged by petrologic type, with major oxides on the left and minor oxides on the right. Lower two diagrams have data arranged by shock stage with major oxides on the left and minor oxides on the right.

cumulate melt rock with L chondrite affinities. These two meteorites were included in both sets of diagrams in order to present the full range of petrologic types and shock stages. The lower two diagrams (Fig. 12b) show the compositional data arranged by shock stage. The general trends in the data between petrologic type and shock stage are remarkably similar for both the major and the minor oxides. Rubin (1994) and Stöffler et al. (1991) have suggested that there is a direct correlation between petrologic type and shock stage in L chondrites. These authors have stated that an increase in petrologic type corresponds to an increase in shock stage in these meteorites. If this correlation is real, than the similarity in the composition trends in Fig. 12 is a simple way of restating a known fact. Table 4, however, supplies convincing information that this correlation is not an accurate one. By applying statistical tests to shock stage versus petrologic type for all L chondrites that have been classified by the Stöffler et al. (1991) method, Table 4 shows that there is no apparent correlation between shock stage and petrologic type in L chondrites in the larger data set. Therefore, the similarity in the compositional trends in Fig.12 can be taken to indicate that shock metamorphism has had no distinguishable affect on the major or the minor element chemistry of olivine. Since textural changes in olivine is one of the most important criteria for deducing the shock stage of all of the chondrite groups, this finding has important implications for the study of the thermal history of chondrite parent bodies. Variations in the mineral chemistry of olivine must reflect fundamental changes in the meteorite parent body prior to shock metamorphism.

Major and minor oxides for L chondrite clinopyroxene and orthopyroxene grains are plotted in Figs. 13 and 14, respectively. Most of the major oxides in both forms of pyroxene show relatively flat patterns when arranged either by petrologic type or by shock stage. The exception to this is a trend of increasing CaO in clinopyroxene with

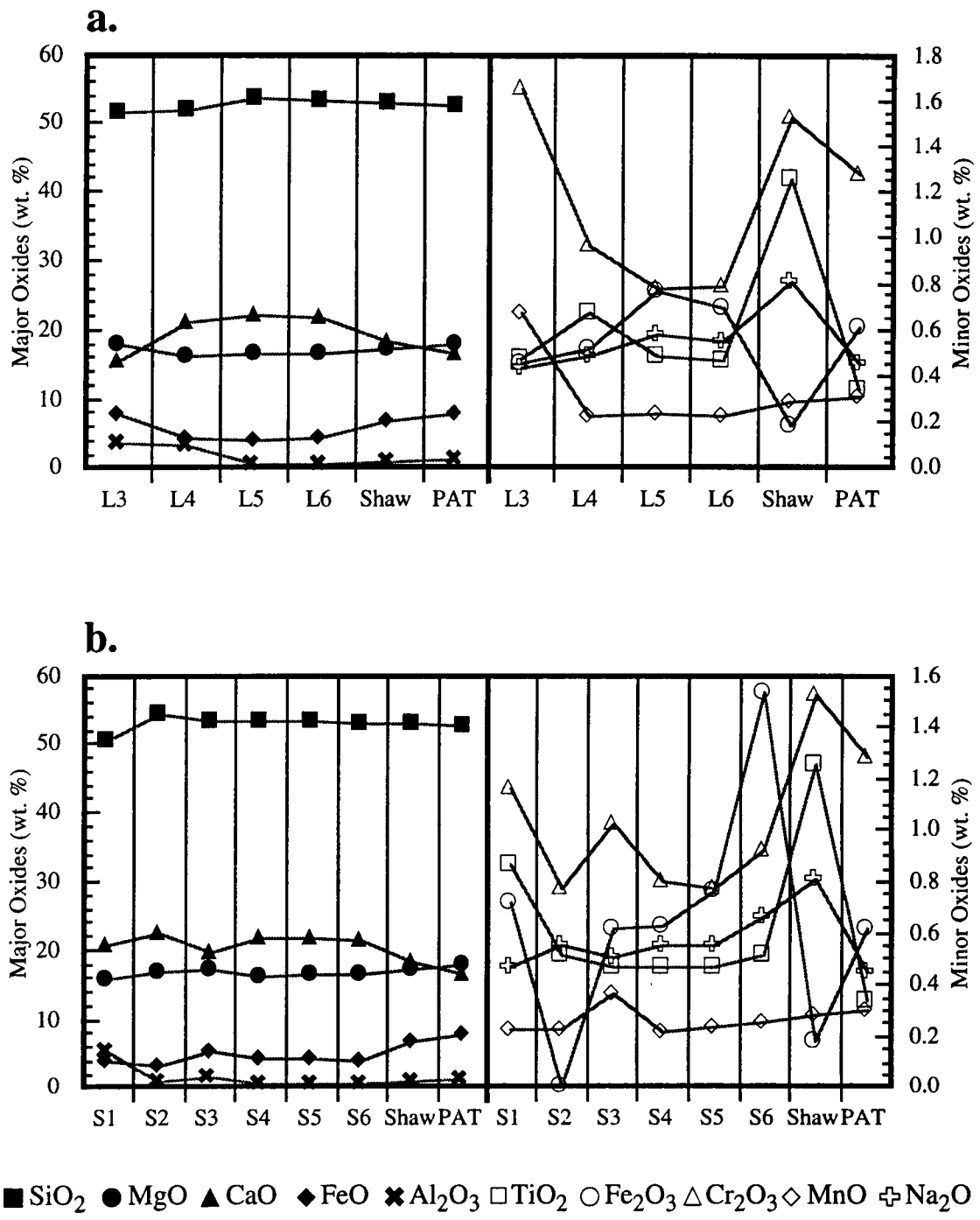

Figure 13. Major and minor oxides for clinopyroxene in L chondrites obtained from electron microprobe analyses. Upper two diagrams have data arranged by petrologic type, with major oxides on the left and minor oxides on the right. Lower two diagrams have data arranged by shock stage with major oxides on the left and minor oxides on the right.

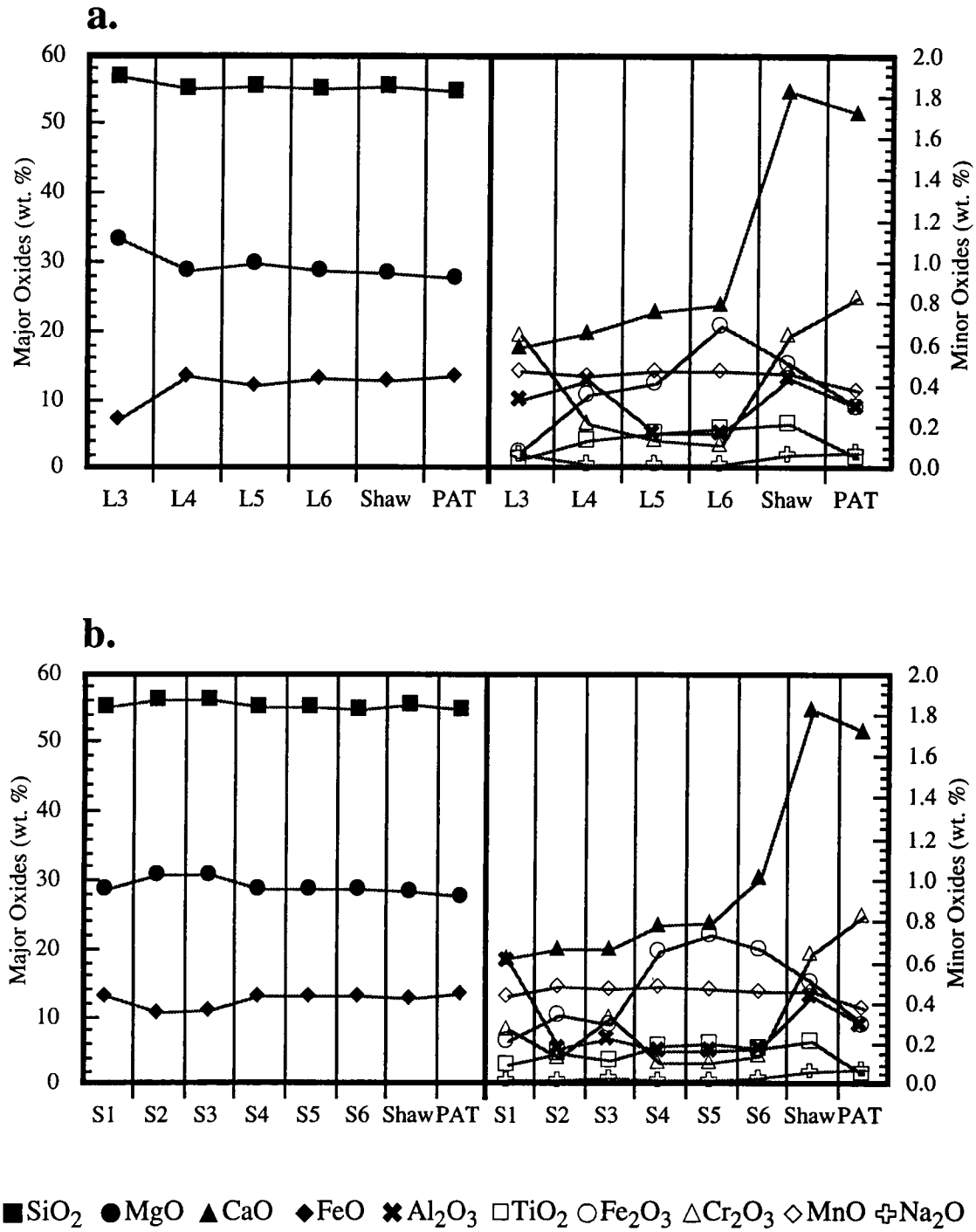

Figure 14. Major and minor oxides for orthopyroxene in L chondrites obtained from electron microprobe analyses. Upper two diagrams have data arranged by petrologic type, with major oxides on the left and minor oxides on the right. Lower two diagrams have data arranged by shock stage with major oxides on the left and minor oxides on the right.

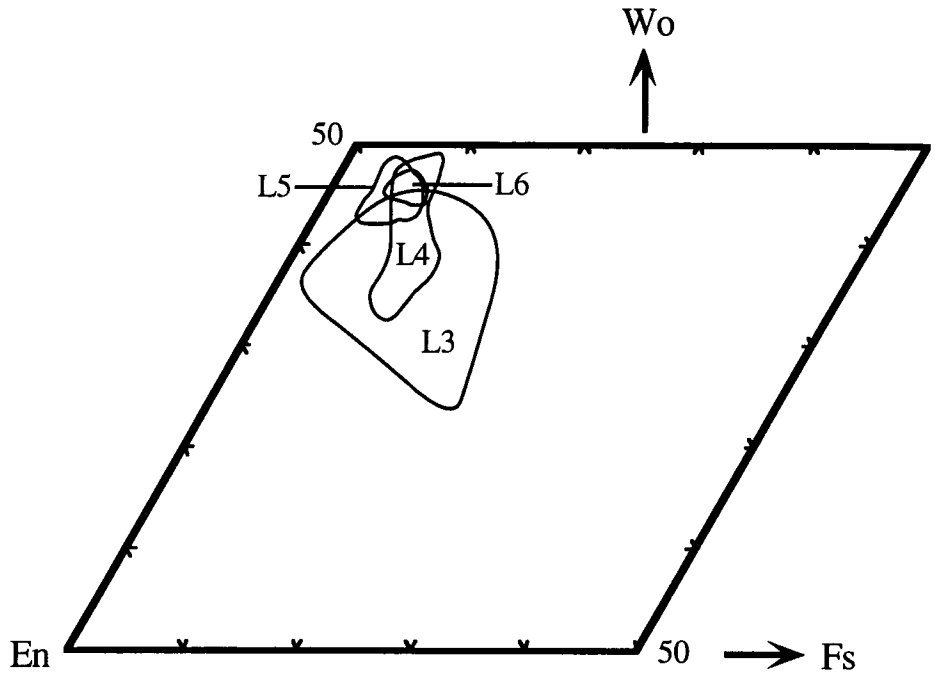

Figure 15. A portion of the pyroxene quadrilateral showing the fields in which clinopyroxene plot. As petrologic type increases Ca in clinopyroxene increases and Fe and Mg decrease. Fields overlap as compositions approach equilibration with increasing metamorphic temperature.

an increase in petrologic type. Plotting pyroxene end member compositions on a standard quadrilateral (Fig. 15) shows that the Ca component in clinopyroxene does increase (equilibrate), with an accompanying restriction in the Fe and Mg components, with an increase in petrologic type. This trend in clinopyroxene compositions has been documented many times by previous workers, as it is the basis for all pyroxene geothermometry studies. This trend of increasing CaO content seems to break down when clinopyroxene grains are plotted against shock stage (Fig. 13b), indicating that shock metamorphism did not seem to affect the pre-shock thermal signature of L chondrite clinopyroxene.

The minor oxides for both clinopyroxene and orthopyroxene also show little variation in the compositional trends between petrologic type and shock stage. CaO in orthopyroxene does, however, show an sharp rise with both increasing petrologic type and increasing shock stage. Like CaO in clinopyroxene, this component is a crucial one for the determination of thermometry in orthopyroxene. This is the first indication that shock metamorphic reheating may have aided parent body metamorphism in establishing a chemical trend in one of these major silicate minerals. This trend will be explored more thoroughly in a later discussion on pyroxene thermometry of L chondrites.

Chemistry of Chromite

The major element compositions of matrix chromite in L chondrites have been shown by several previous studies to be relatively uniform (most around cr# [Cr/Cr + Al] = 0.87 and fm# [Fe/Fe + Mg] = 0.90; Kracher and Kurat, 1980; Wlotzka, 1987). This study is in agreement with these earlier findings. Chromite grains analyzed from eight L chondrites, ranging from low-shock, relatively low petrologic types to high-shock melt rocks, have compositions in the narrow range of cr# = 0.87 ± 0.03 and fm# = 0.85 ± 0.07. This is confirmed graphically in Fig. 16, where all analyses were found to plot in a very narrow portion of the spinel quadrilateral. All of the chromite analyses fall on the extreme ends of three trends established for analyses of spinel in chondrules by Yabukl et al. (1983). Chromite grains of similar composition to those in this study were termed equilibrium chromite by Kracher and Kurat (1980) and were shown to correlate with adjacent equilibrated silicates by Snetsinger et al. (1967).

Figure 17 is a plot of major and minor oxides in matrix chromite, arranged by petrologic type and by shock stage. The slight increase in Al_2O_3 and TiO_2 content was

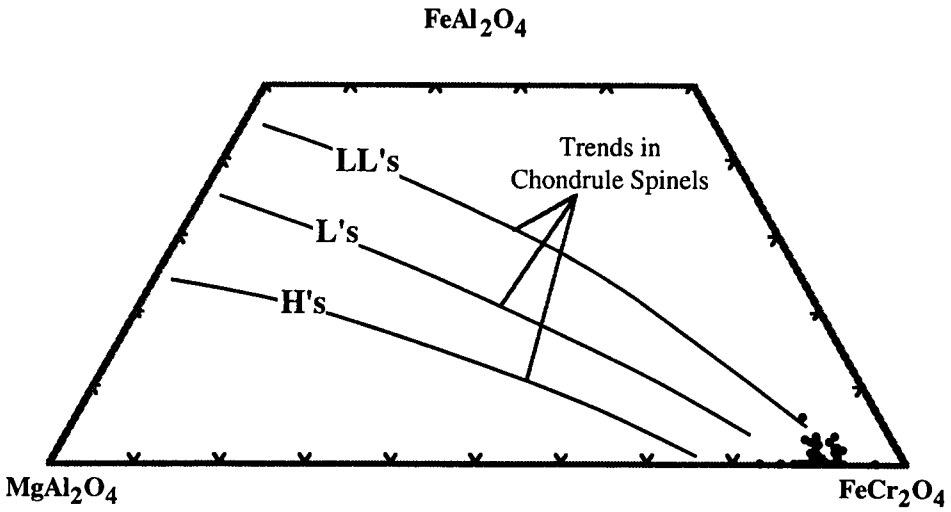

Figure 16. Spinel quadrilateral showing the uniform compositions of matrix chromite in L chondrites. Plots are based on electron microprobe data and include examples from low-shock L chondrites to L chondrite melt rocks. All plots fall within a narrow compositional region at the end of three ordinary chondrite trends established for spinel-bearing chondrules by Yabukl et al. (1983).

shown by Bunch et al. (1967) to be a possible indicator of petrologic type in ordinary chondrites. Since these trends are very slight, rearranging the data according to shock stage has little effect on the overall pattern. The trend of decreasing FeO content with increasing petrologic type, also remains unchanged in the data arranged by shock stage. There are no obvious trends in the minor element data, which is in itself significant since Zn is a highly labile element. It appears from these data that matrix chromite grains in L chondrites do not record any systematic changes in mineral chemistry with either shock or thermal metamorphism. Their overall chemistry, however, is remarkably uniform, which may reflect homogenization by either (or possibly both) metamorphic events.

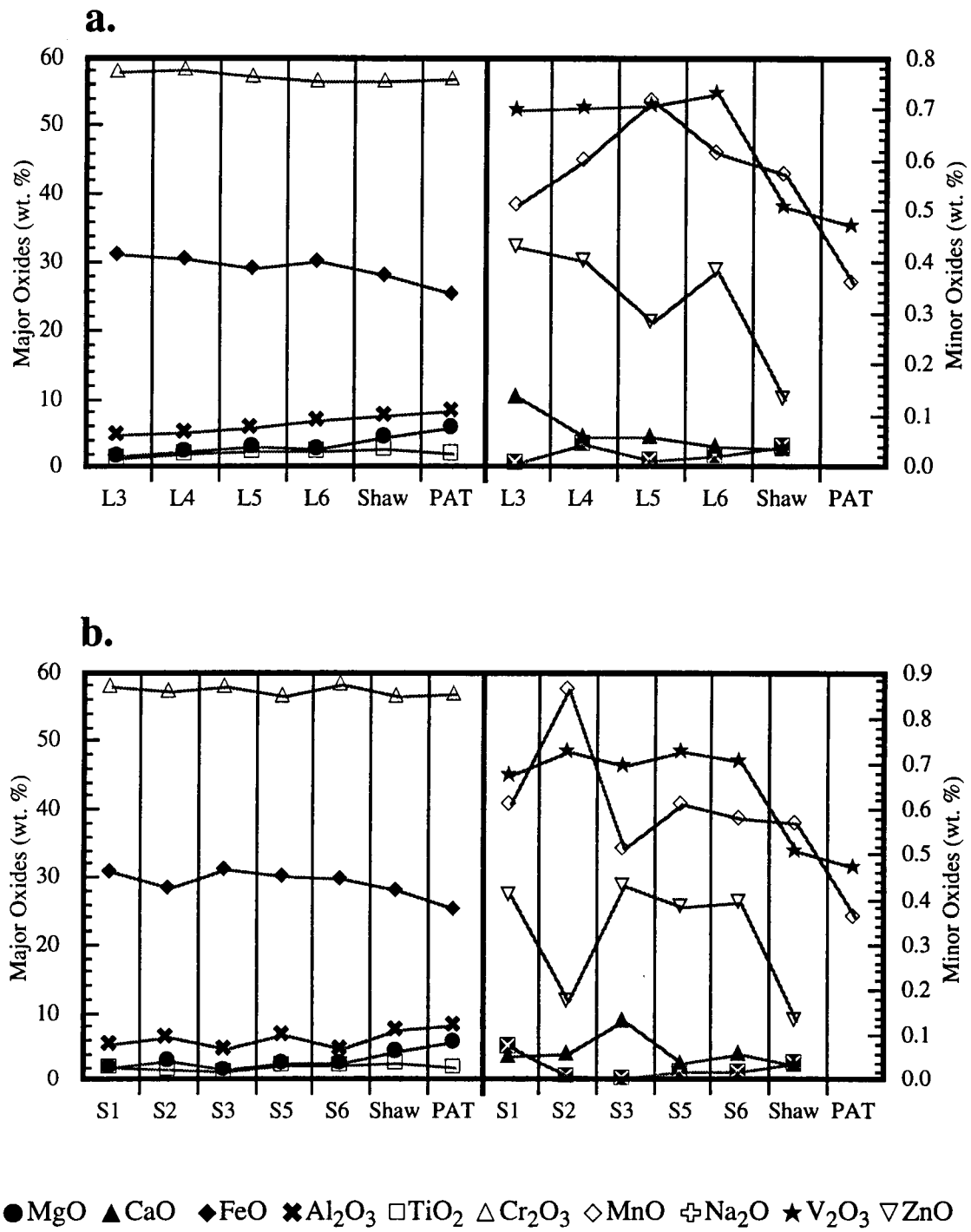

Figure 17. Major and minor oxides for chromite in L chondrites obtained from electron microprobe analyses. Upper two diagrams have data arranged by petrologic type, with major oxides on the left and minor oxides on the right. Lower two diagrams have data arranged by shock stage with major oxides on the left and minor oxides on the right.

Chemistry of Fe-Ni Metal

Metal alloys in L chondrites consist of a solid solution between Fe and Ni. They are generally restricted to ~4 to 54 wt % Ni and 96 to 46 wt % Fe, with only minor to trace amounts of C, P, and other siderophile elements. This simplicity in chemistry can, however, reflect a bewildering array of textures and minerals subject to the thermal history of the individual metal grains. Many of these features occur at the submicron level, making them difficult to impossible to recognize using conventional petrographic techniques.

Figure 18, the latest version of the Fe-Ni phase diagram (Reuter et al., 1989), illustrates the complex subsolidus nature of this binary system. Fe-Ni metal grains that have undergone slow, single-stage cooling histories (cooling rates of 1-100 K/Ma; Wood, 1964; Goldstein and Short, 1967) have textures and chemistries similar to those present in many iron and stony-iron meteorites. At temperatures above 900 °C all metal occurs as γFe or taenite (disordered, paramagnetic Fe-Ni metal). During slow cooling from 900 to 400 °C rapid Ni diffusion within taenite forms low-Ni, αFe, or kamacite. In many iron meteorites kamacite grows parallel to the {111} planes of the host taenite producing an octahedral pattern known as Widmannsträtten structure (Thomson, 1808). In L chondrites kamacite growth is controlled by the impingement of metal-metal or metal-silicate boundaries, producing rims or irregularly-shaped patches of low-Ni metal (Powell, 1969). Slow cooling below 400 °C produces a host of metastable Fe-Ni alloys. Taenite, with <25 wt % Ni, undergoes diffusionless transformation to martensite (α_2Fe) below the M_s or martensite start boundary (Fig. 18). Martensite may further decompose to a mixture of kamacite and ordered (ferromagnetic) taenite, producing an $\alpha + \gamma$ duplex texture known as plessite. Taenite with >25 wt % Ni undergoes spinoidal decomposition producing a submicron-sized

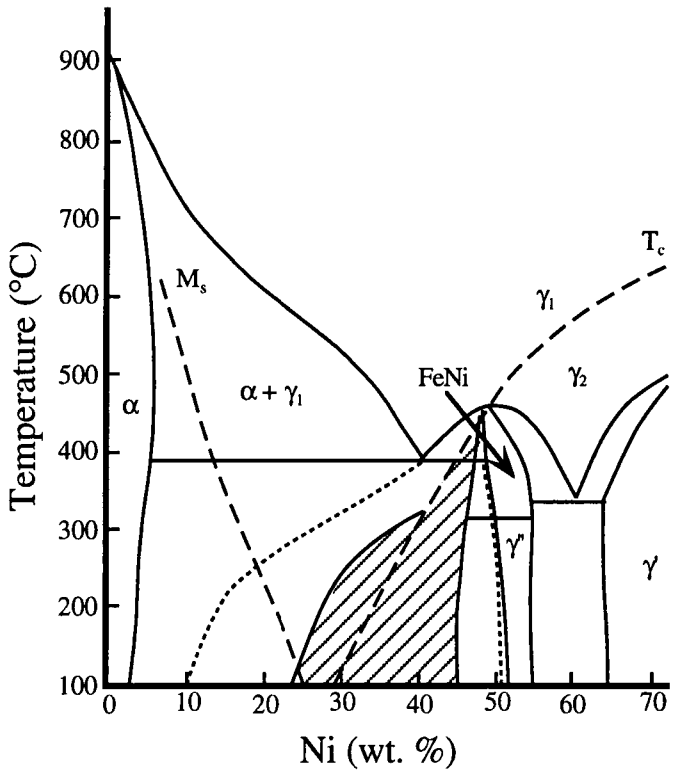

Figure 18. The Fe-Ni phase diagram after Reuter et al., 1989. Symbols are as follows: M_S = martensite start boundary, T_C = taenite Curie temperature, α = kamacite, γ_1 = disordered (paramagnetic) taenite, γ_2 = ordered (ferromagnetic) taenite, FeNi = disordered tetrataenite, γ'' = ordered tetrataenite, and γ' = $FeNi_3$. The striped region represents the area of spinoidal decomposition. The finely dotted lines define a miscibility gap.

intergrowth of tetrataenite (γ'' or ordered tetragonal Fe-Ni) and martensite. This fine-grained mixture is commonly referred to as cloudy taenite (Scott, 1973; Lin et al., 1979; Reuter et al., 1988).

Most of the metal phases mentioned above are metastable at room temperature (Chuang et al., 1986; Reuter et al., 1989). Rapid cooling of metal accompanying shock metamorphic reheating can either create metal alloys with even more complex textures

and compositions or prevent some of these features from forming. In order to determine the degree to which shock reheating has altered Fe-Ni metal in L chondrites, profiles consisting of closely-spaced (<2 μm apart) spot analyses were performed on typical metal grains. Profiles were taken on several suites of L chondrites including: a set of low-shock Antarctic L chondrites (shock stage S3 and below), a set of low- to moderately-shocked non-Antarctic L chondrites (S4 and below), and a set of moderately- to highly-shocked L chondrites (S5 and above).

The following discussion of Fe-Ni textures is based on Ni profiles obtained in 12 low- to high-shock L chondrites. Matching backscatter electron (BSE) images were acquired for each Fe-Ni metal grain profiled. BSE imaging allowed the recognition and documentation of many metal textures that would gone unnoticed by petrographic work.

Chemistry of Low-Shock Antarctic L Chondrites (<S4)

All four of the low-shock Antarctic L chondrites produced profiles that approximate the classic M-shaped curve seen in many iron meteorites (Wood, 1964). These curves were obtained in profiles of all normally-zoned Fe-Ni metal and indicate slow cooling below 400 °C with no appreciable shock reheating (Scott, 1973). All normally-zoned Fe-Ni grains analyzed produced either a symmetric M-shaped profile (indicating a profile taken in a plane perpendicular to the center of the grain) or an asymmetric profile (taken in a plane oblique to the center).

In ALH85045 and LEW86024 metal grains have an outer high-Ni rim of taenite or tetrataenite and centers of cloudy taenite (Figs. 19a and 19b). BSE imaging shows these rims as small (1-5 μm), bright bands surrounding many of the metal grains (Figs. 20a and 20b). Most metal grains in QUE90201 lack a cloudy zone and appear

optically homogeneous, although the profile of the metal grain in Fig. 19c is very similar to those of ALH85045 and LEW86024. The absence of cloudy taenite within these grains could indicate the presence of carbon within the metal; minute quantities of carbon are known to inhibit the formation of martensite in industrial steel (Buchwald, 1975; Lin et al., 1979). Since cloudy taenite is actually a submicroscopic mixture of martensite (which produces the brown nital stain in the cloudy zone) and either tetrataenite or taenite (which is impervious to nital etching), metal grains within QUE90201 may have undergone normal slow cooling and not produced the usual phases present in undisturbed metal.

Metal grains within GRO85209 (Fig. 19d and 20d) contain abundant, irregular patches of isolated tetrataenite (Ni >50 wt %) and martensite (Ni ~20 wt %). The presence of ordered tetrataenite in all of the smaller metal grains within this meteorite is another indicator of normal, slow cooling. During cooling Ni diffusion should take place at a more rapid rate in smaller grains (Willis and Goldstein, 1981), producing regions that are much higher in Ni in smaller metal grains than in larger grains that cooled at similar rates. The calibration of Ni content vs. size of the original grain is the basis for all metallographic cooling curves since Wood's (1964) initial work.

Chemistry of Low- to Moderately-Shocked Non-Antarctic L Chondrites (<S5)

Figure 21 shows a petrologic suite of low- to moderately-shocked non-Antarctic L chondrites. All profiles except Hallingeberg (Fig. 21a) show evidence of reheating. Hallingeberg has a normal, slow-cooled profile. The rim of the grain consists of high-Ni tetrataenite (48 wt % Ni), the central portion contains a fine-grain duplex structure of plessite (which is not clearly visible in the matching BSE image in Fig. 22). The Ni content of the plessite slowly decreases toward the central portion of the grain (to ~33

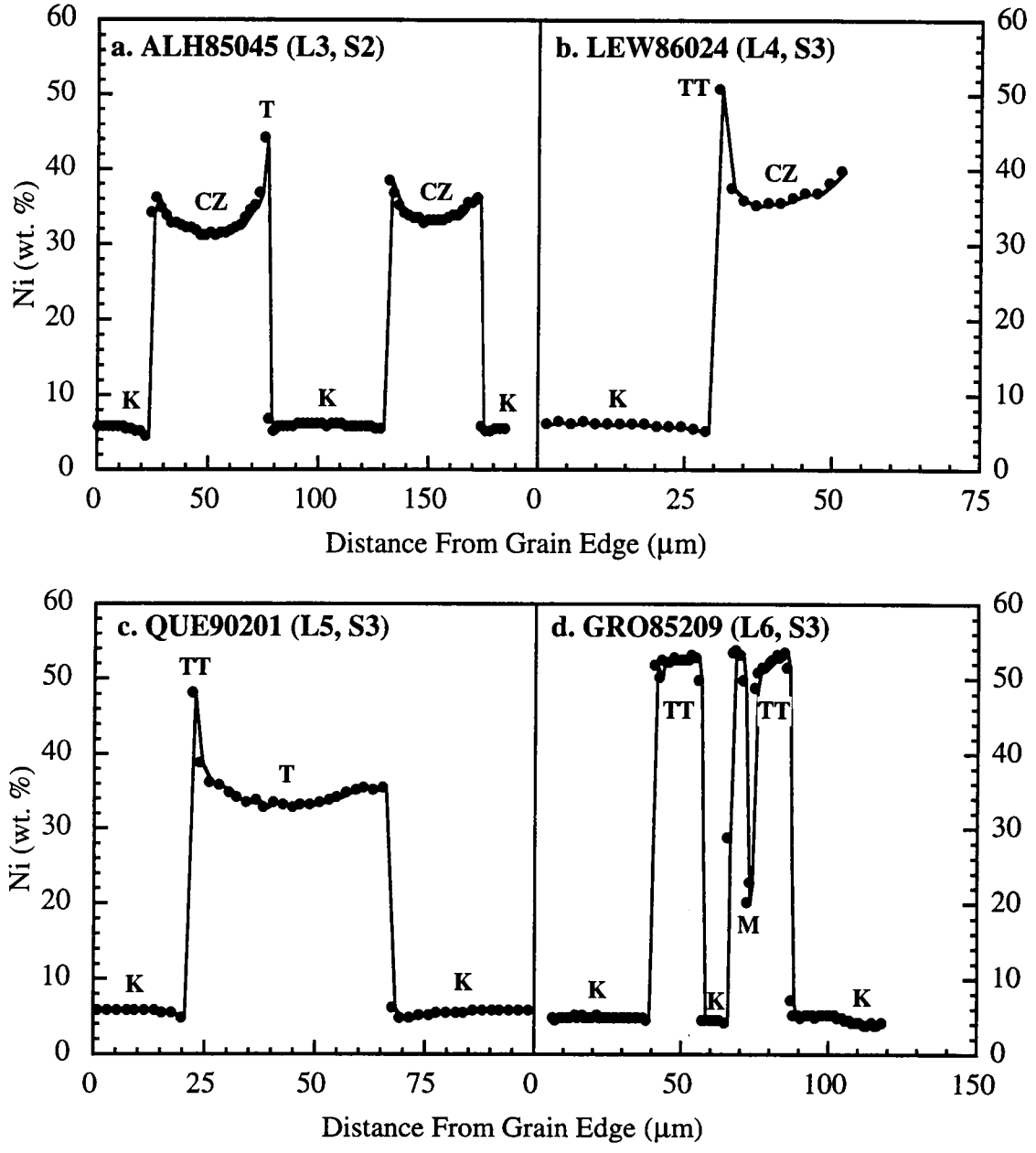

Figure 19. Ni profiles across a petrologic suite of low-shock, Antarctic L chondrites. Symbols for this figure (and Figs. 21, 23) are as follows: K = kamacite, M = martensite, P = plessite, T = taenite, TT = tetrataenite, and CZ = cloudy zone.

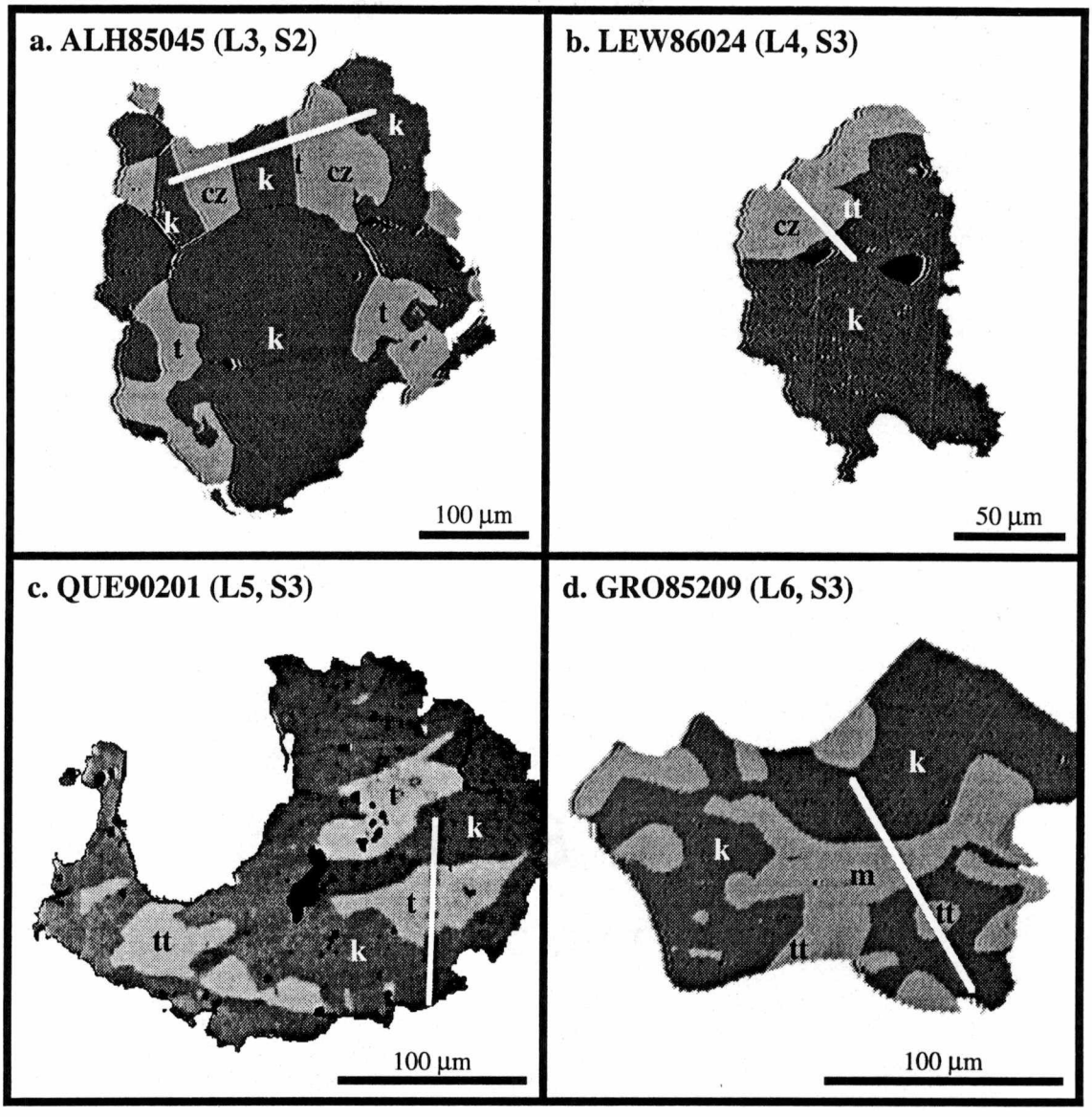

Figure 20. Backscatter electron images for Ni profiles of Fe-Ni metals in Fig. 19 showing the locations where profiles were taken (white lines). Symbols for this figure (and Figs. 22, 24) are as follows: cz = cloudy zone, k = kamacite, m = martensite, pl = plessite, t = taenite, tt = tetrataenite, and tr = troilite.

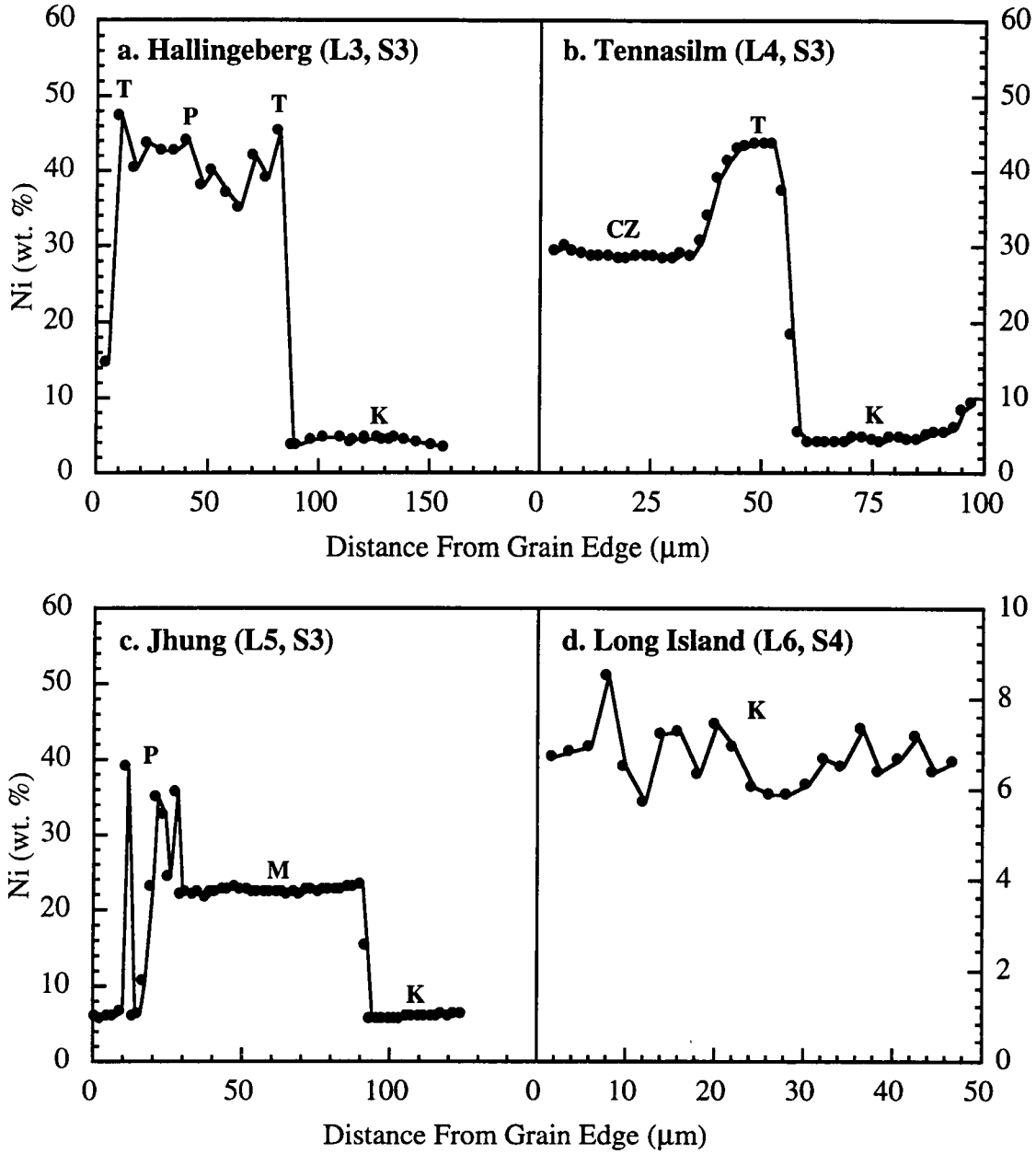

Figure 21. Ni profiles across a petrologic suite of low- to moderately-shocked, non-Antarctic L chondrites. Symbols for this figure correspond to Fig 19.

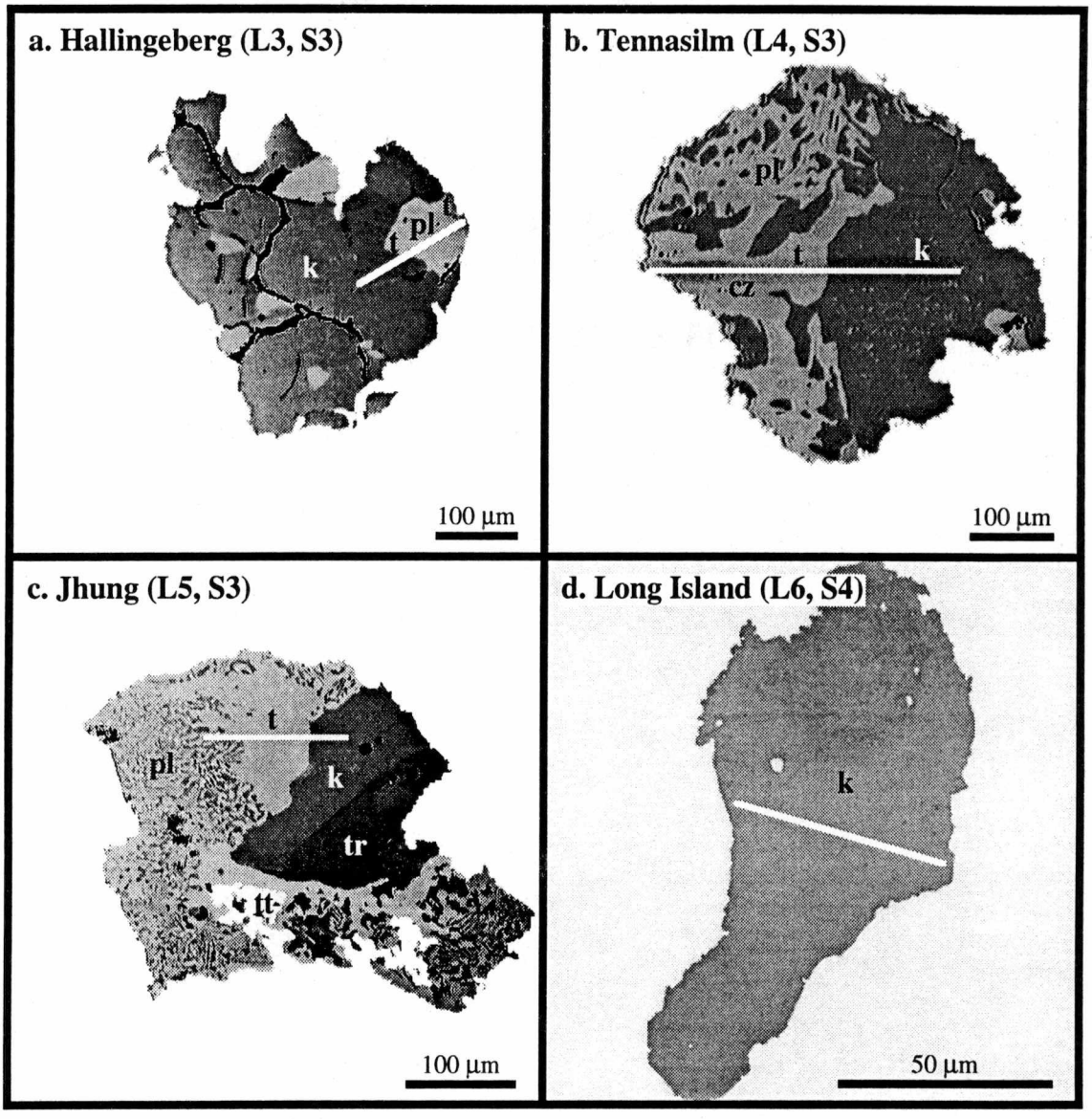

Figure 22. Backscatter electron images for Ni profiles of Fe-Ni metals in Fig. 21 showing the locations where Ni profiles were taken. Symbols are the same as in Fig 20.

wt % Ni), indicating that this was a normally-zoned grain which once had a martensitic core that, through slow cooling, further decomposed into plessite.

Metal grains in Tennasilm (Fig. 21b and 22b) consist of complex intergrowths of taenite and martensite. The cores of these grains are unusual in that they have a constant Ni composition (~30 wt % Ni) generating flat Ni profiles in the centers of these metal grains. This flat central Ni profile seems to be a common feature in all metal grains from samples that display features associated with moderate to strong shock reheating (the initial development of melt pockets and melt veins seen in Tennasilm) and/or quick cooling (as seen by the polygonal kamacite metal grains from other meteorites that share this type of profile). Similar flattening in the central portions of Ni profiles was also seen in Jhung, Kyushu, Shaw, and PAT91501 (Figs. 21c, 23b, 23c, 23d, and matching BSE images). All samples, except Jhung, contain features that are indicative of strong shock reheating. The Jhung profile does, however, lack a significant Agrell effect between the kamacite and the constant martensite (Ni ~21 wt %) portion of the profile. (The Agrell effect is the small dip in Ni content of kamacite at the border between kamacite and a metal grain of higher Ni content. It is readily visible in all of the low-shock Antarctic samples in Fig. 19. Its absence in shock-reheated metal was first noted by Agrell et al. (1963), for whom this feature was based.)

Figure 21d is a Ni profile through the moderately-shocked (S4) L chondrite Long Island. What is unusual about this profile is the higher-than-normal Ni content in the kamacite. Kamacite normally has <7.5 wt % Ni (Buchwald, 1975). The presence of high-Ni kamacite has been previously interpreted as the result of quick cooling of low-Ni taenite (<10 wt % Ni) which undergoes a massive transformation into high-Ni kamacite, rather than converting to martensite as indicated by the Fe-Ni phase diagram

(Wood, 1964). This transformation usually appears as the textural feature known as polygonal kamacite or ε-iron (Buchwald, 1975), which is readily visible optically (see Fig. 7d), but goes unnoticed in BSE imaging (Fig. 22d). The absence of a polygonal texture in this grain may be the result of improper etching as polygonal kamacite was noted in other metal grains in this section.

Chemistry of Highly-Shocked L Chondrites (>S4)

The suite of L chondrites in Fig. 23 all contain features indicative of severe shock reheating. Kyushu has abundant melt droplets of troilite and metal adjacent to sheared and polycrystalline opaque grains (see Fig. 8a). McKinney is a shock-blackened L chondrite whose metal and sulfide textures have been completely disrupted by shock reheating. Shaw and PAT91501 contain shock-melted silicate material indicative of L7 chondrites.

Figure 23a shows a Ni profile across a Kyushu metal grain. Like the lower-shocked Tennasilm and Jhung, Kyushu contains metal grains that have very complex intergrowths of coarse grained plessite and taenite or martensite. Kyushu also has a flat central Ni profile (flattened at ~30 wt % Ni). Plessite is coarser grained than in either Tennasilm or Jhung, and high Ni portions of the plessite tend to contain lower amounts of Ni (30 wt % Ni as opposed to nearly 40 wt % in Jhung). These features may be indicative of faster cooling in Kyushu from the higher post-shock temperatures it encountered.

Shock blackening in L chondrites forms when troilite and metal are melted by the initial shock impulse and then injected into shock-induced fractures formed by dilation after the shock-compressed material relaxes (Stöffler et al., 1991). This process is envisioned to have taken place in a time span of several seconds after impact. The net

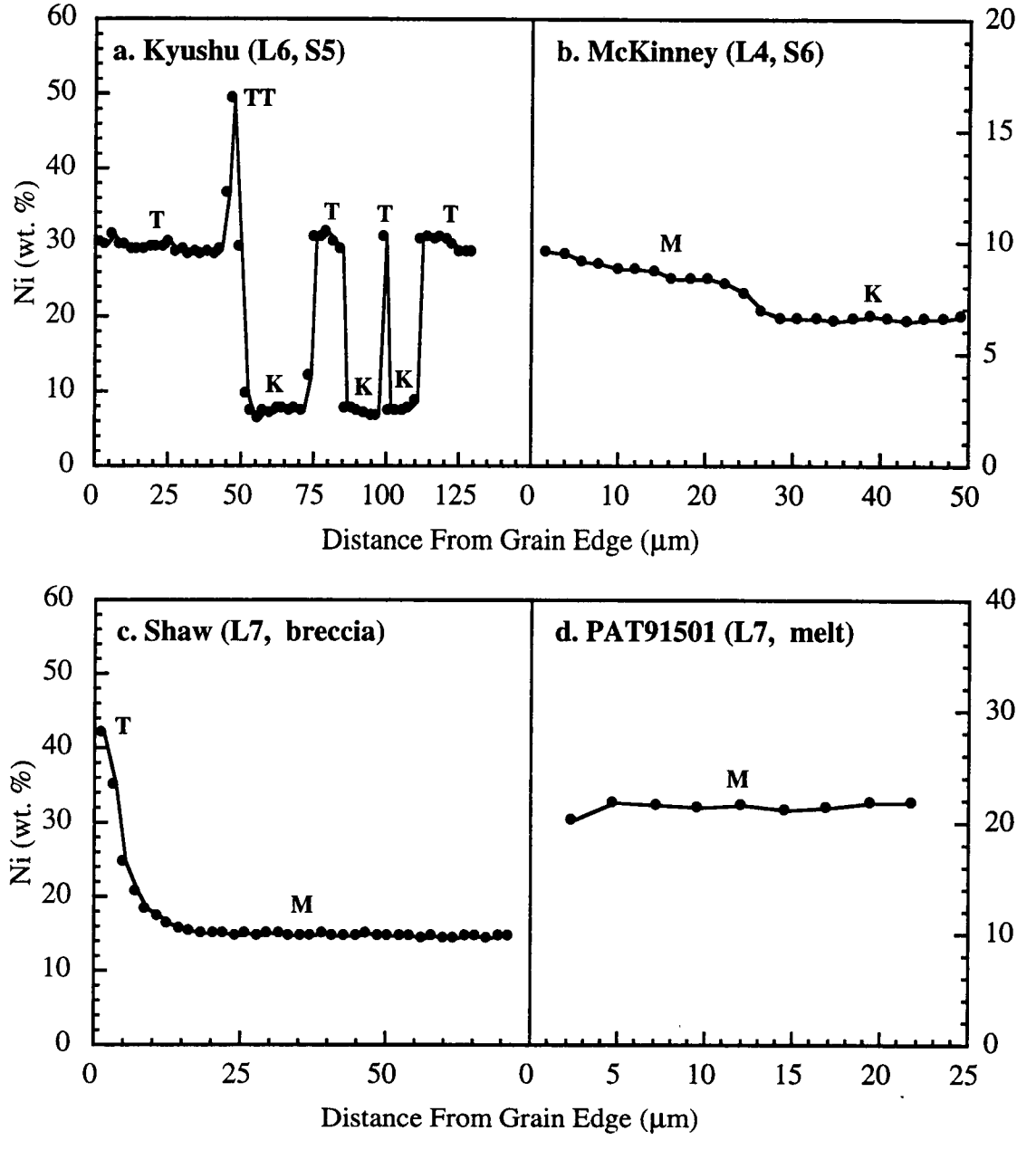

Figure 23. Ni profiles across a petrologic suite of high-shock, L chondrites. Symbols for this figure correspond to those in Fig. 19.

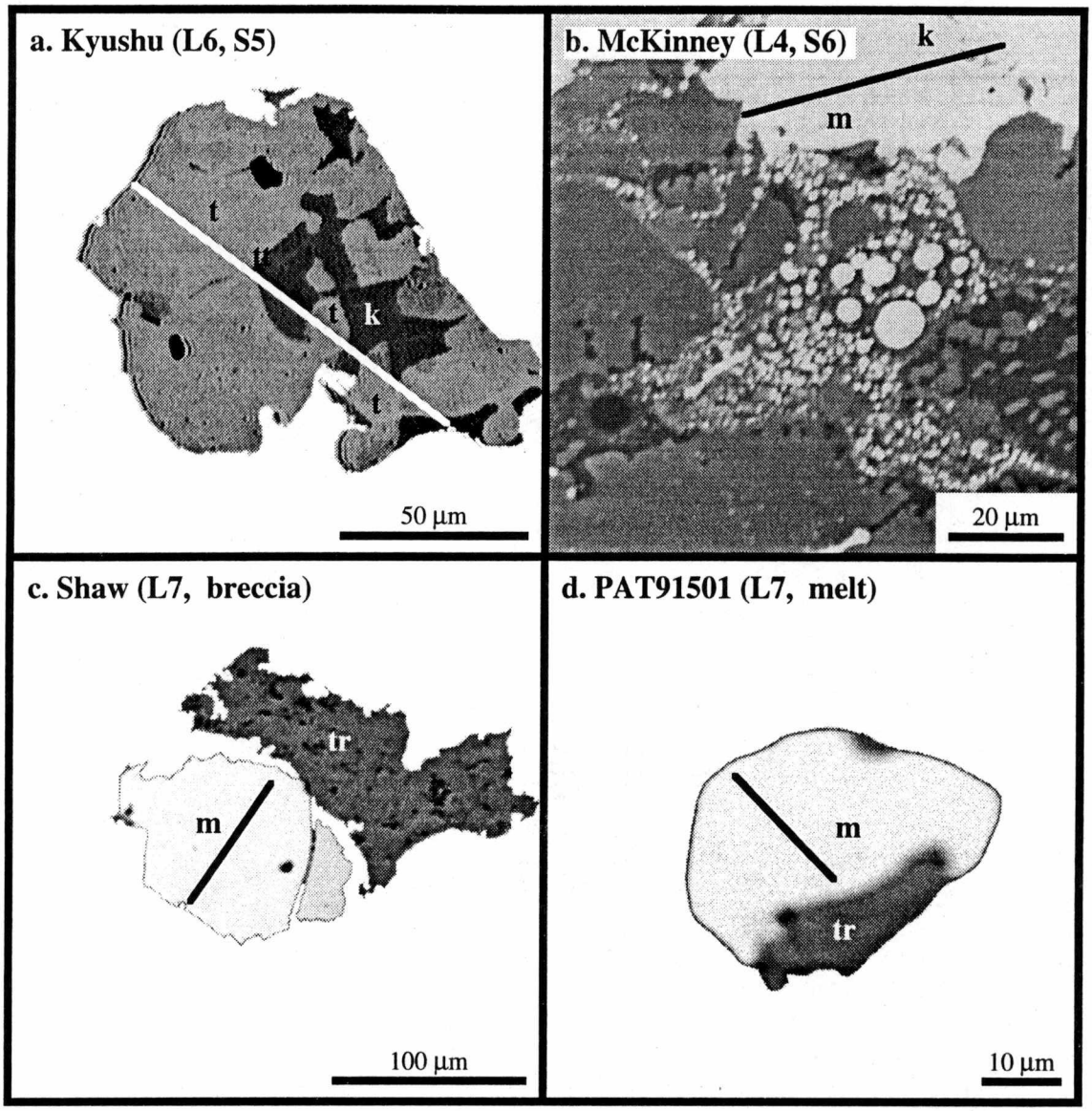

Figure 24. Backscatter electron images for Ni profiles of Fe-Ni metals in Fig. 23 showing the locations where Ni profiles were taken. Symbols are the same as in Fig 20.

effect of shock-induced melting appears to be the homogenization of the original metal content (Wood, 1967; Smith and Goldstein, 1977). This homogenization is readily seen in the Ni profile obtained from McKinney (Fig. 23b), where the average Ni concentration is 7.58 wt % Ni. The BSE imaging reveals the highly melted nature of the metal and sulfide grains in McKinney. Wood (1967) published a Ni profile through the shocked L5 breccia Farmington which bears a strong resemblance to the profile obtained from McKinney. The suggestion was made by Wood that profiles of this shape represent an original kamacite-taenite pair that had been heated to the point of chemical homogenization between the two types of Fe-Ni metal. Ni diffusion during cooling produced a martensite-kamacite pair which appeared optically continuous in reflected light (and are not readily distinguishable in BSE imaging; see position of profile line in Fig. 24b). The lack of an Agrell effect suggests that Ni diffusion did not go to completion, implying relatively fast cooling rates for McKinney metal. Cooling rates for Farmington (Smith and Goldstein, 1977) were estimated at ~0.1 K/y which is on the order of 10^5 faster than cooling rates obtained for normally-zoned taenite (Willis and Goldstein, 1981).

Profiles for the two shock-melted meteorites (Shaw and PAT91501, Figs. 23c and 23d) show nearly flat martensitic compositions. In Shaw, there is a very steep gradient between the taenite rim and the martensite core that is absent in PAT91501. The Ni profile in Shaw was taken from a metal grain adjacent to the light-colored, melt dike portion of the sample. Shock injection of molten silicate material must have heated metal grains to the point of homogenization (at least 650 °C; Willis and Goldstein, 1981). Cooling of the grains proceeded slowly enough to develop a high-Ni rim, but not slowly enough to produce a normal M-shaped profile. Metal grains in PAT are present as rounded nodules in a matrix of cumulate silicates (Harvey, 1994). The

nearly flat profile at 21 wt % Ni indicates reheating at or above 650 °C, with relatively quick cooling in order to prevent the formation of a Ni-rich rim such as seen in Shaw. Homogenization of the Ni content in metal grains of Shaw and PAT90501 can be seen in the uniformity of metal in both samples under BSE mode on the electron microprobe (Figs. 24c and 24d).

Chemistry of Troilite

L chondrites may contain of as much as 6.5 wt % troilite (McSween et al., 1991), and troilite may contain up to 6 wt % Ni (Smith and Goldstein, 1977). This Ni content has been used as an indicator of petrologic type in ordinary chondrites. Van Schmus and Wood (1967) stated that troilite in unequilibrated ordinary chondrites contains1-3 wt % Ni, with equilibrated ordinary chondrites containing <0.5 wt % Ni. Based on experimental work on the Fe-Ni-S system by Kullerud (1963), Smith and Goldstein (1977) proposed that the abundance of Ni in troilite was a function of the peak-shock temperature and post-shock cooling rate. When peak-shock temperature exceeds 1050 °C the solubility of Ni in troilite can exceed 6 wt % (Kullerud, 1963). Upon cooling, Ni diffuses out of the troilite into the adjacent metal, eventually establishing a final Ni composition which is dependent on the post-shock cooling rate. In their study of severely shock-reheated L chondrites, Smith and Goldstein (1977) concluded that those meteorites with high-Ni troilite (~0.3 wt % Ni) cooled very rapidly (in the range of ~ 25 °C/hr). Troilite that was either not reheated by shock metamorphism, or that cooled at much slower rates, had lower Ni contents (as low as 0.02 wt % Ni).

Ni profiles were obtained across metal-sulfide pairs in a petrologic suite of low-shock Antarctic L chondrites to see what effect, if any, thermal metamorphism may have had on the Ni content in troilite. Profiles were obtained by spot analyses taken at

2-3 μm steps using an electron microprobe and are presented in Figs. 25 and 26. The central Ni content of troilite in all four profiles is below the lower limit of detection for the spot analyses (<0.04 wt % Ni). Since these metal-sulfide pairs reside in meteorites whose peak-shock conditions were ≤S3, this low central Ni content is in agreement with Smith and Goldstein's (1977) values for Ni in unreheated chondrites. However, several patterns do emerge when comparing the shape of each profile. Maximum Ni content in troilite increases with an increase in petrologic type. The unequilibrated L3 and L4 chondrites have a maximum of 0.07 to 0.30 wt %. Ni, whereas the equilibrated L5 and L6 chondrites have maxima between 0.35 to 0.50 wt % Ni. The range of Ni content may be somewhat higher for the L6 chondrite, since surface irregularities between the metal-sulfide pair prevented good analyses from being obtained close to the contact between the two phases. The other pattern which emerged was that the Ni profiles tend to broaden with an increase in petrologic type. The profile in the L3 chondrite (Fig. 25a) extends for only a few microns before concentrations drop below the lower limit of detection of Ni, but that in the L6 chondrite (Fig. 26b) is approximately 20 μm wide.

If the assumption is made that these troilite grains had similar (order of magnitude) quantities of Ni prior to thermal metamorphism, then there are two possible explanations for the systematic variation in the shape of the profiles. One explanation is that all of these meteorites were at one time raised to a similar peak temperature and the differences in the profiles reflect different rates of cooling. In this scenario, the equilibrated chondrites would have cooled the fastest, thus retaining broader Ni profiles with higher peak Ni concentrations. The unequilibrated chondrites would have cooled at a much slower rate, allowing most of the Ni to diffuse from troilite into the metal. The obvious flaw with this explanation is that it implies an inverse onion-shell

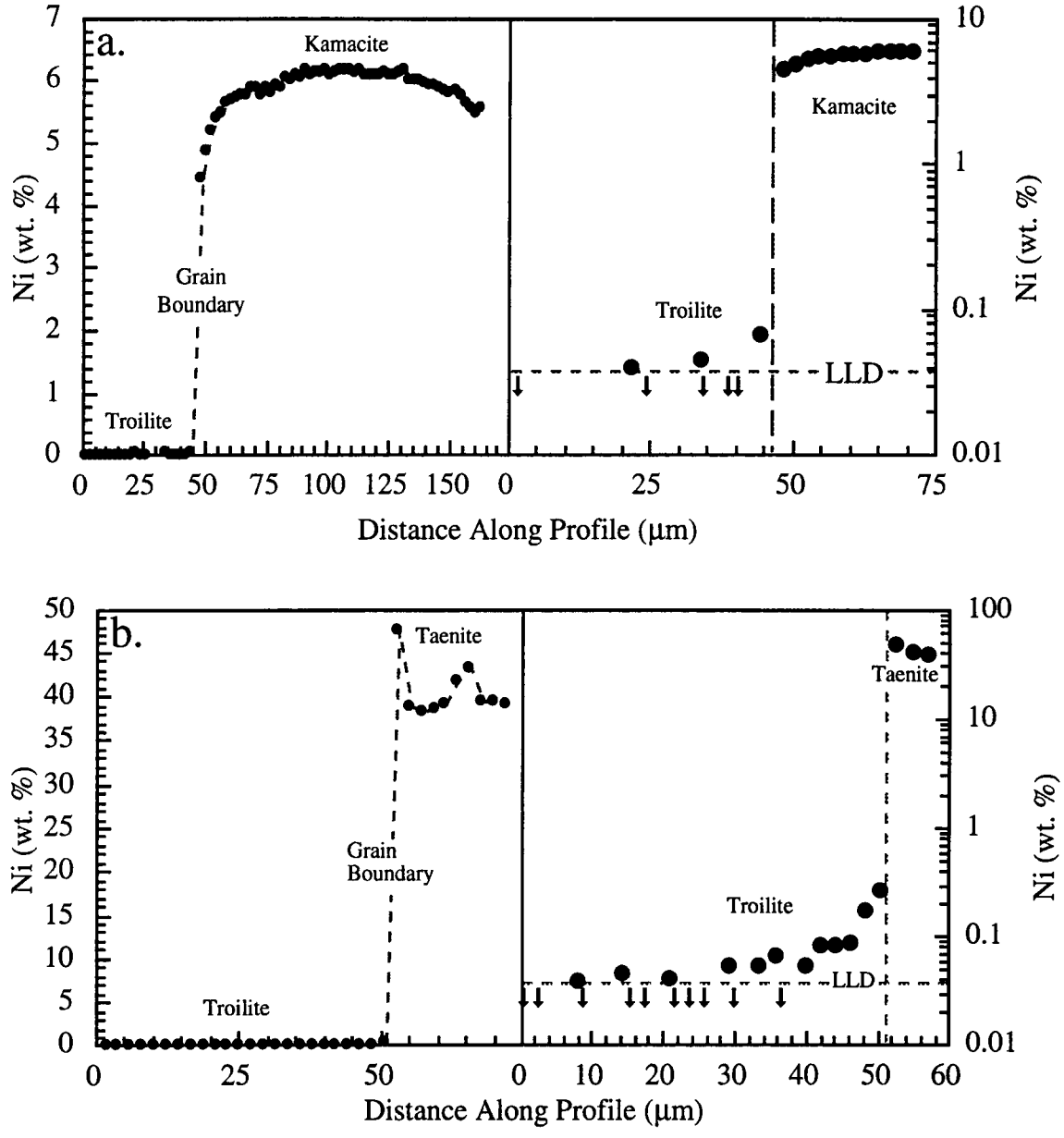

Figure 25. Ni profiles across a metal-troilite pair in a) ALH85045 (L3, S3) and b) LEW86024 (L4, S3). The left diagrams show the full profile. The right diagrams show closeups at the contact between the two phases. Arrows across the profile indicate analyses below the lower limit of detection (LLD) of Ni in troilite.

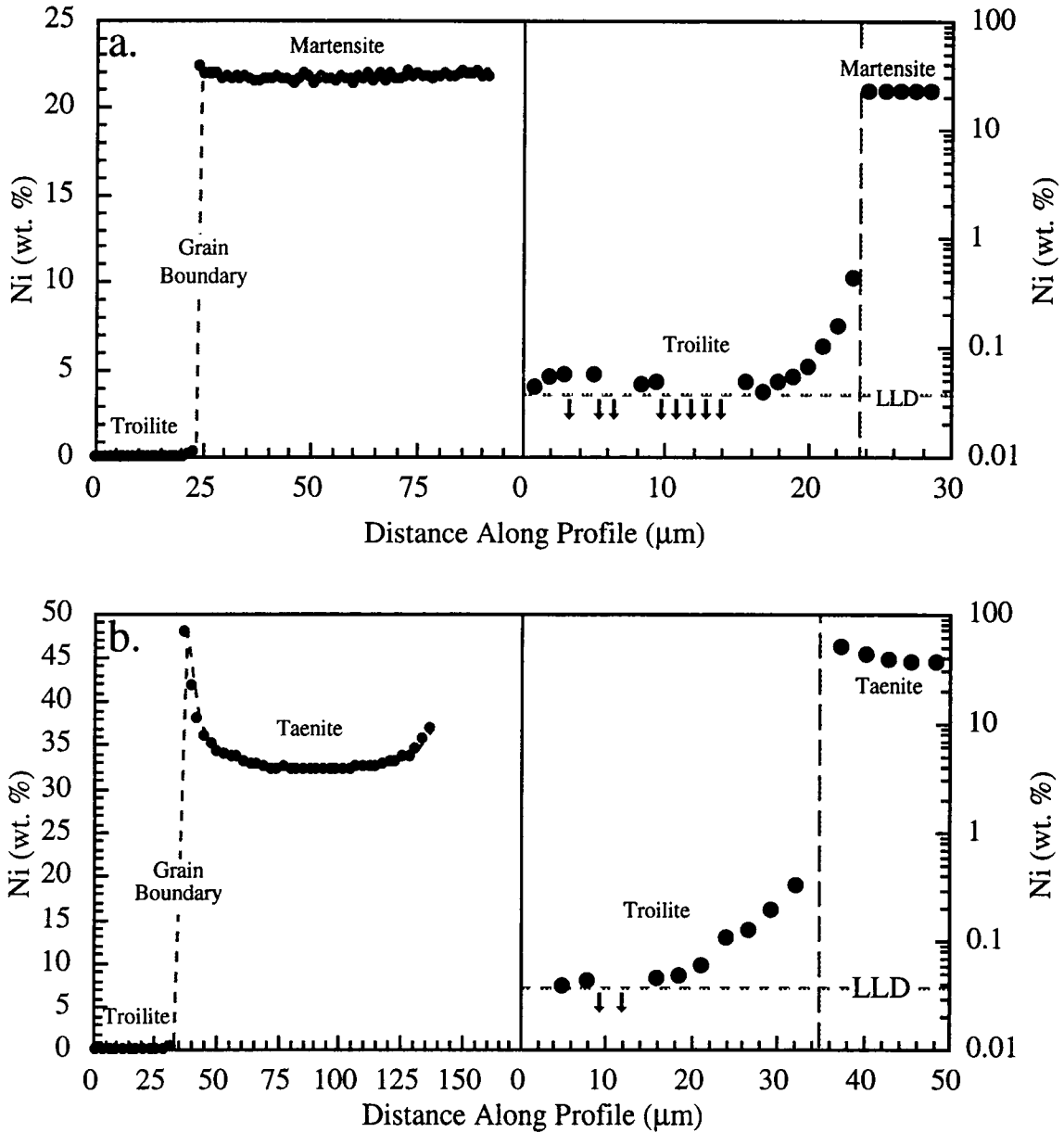

Figure 26. Ni profiles across a metal-troilite pair in a) QUE90201 (L5, S3) and b) GRO85209 (L46 S3). The left diagrams show the full profile. The right diagrams show closeups at the contact between the two phases. Arrows across the profile indicate analyses below the lower limit of detection (LLD) of Ni in troilite.

thermal history for the L chondrite parent body. Fast cooling on the inside of a parent body and slow cooling on the outside is not an acceptable model for the thermal history of the parent body.

The second possible explanation for these Ni profiles is that the equilibrated chondrites were raised to a higher peak temperature than the unequilibrated chondrites, following which all four samples underwent cooling at approximately the same rates. This reasoning holds greater possibilities than the previous idea, since several authors (Scott and Rajan, 1981; Grimm, 1985) have suggested that disruption of the L chondrite parent body might have occurred while it was still a relatively hot mass. Cooling rates, prior to reaccretion of the parent body, might have resumed at relatively uniform rates in the disrupted fragments, freezing in the current Ni profiles.

Profiles across two high-shock L chondrites (Shaw and McKinney) are shown in Fig. 27. The metal-sulfide pair that was profiled in the Shaw L7 chondrite was located adjacent to a large, cm-sized, silicate melt dike. Shock injection of the dike caused rapid reheating of the metal-sulfide pair, but no melting was in evidence. The Ni profile across the Shaw troilite documents the injection of this dike and the relatively quick cooling that followed. Peak Ni content of the profile is an order of magnitude higher then in the previous low-shock L chondrites (~4 wt % Ni). Also, the profile is considerably broader than even the L6 chondrite Ni profile.

The metal-sulfide pair profiled in the shock-blackened L chondrite McKinney displayed abundant petrographic evidence of having been at least partially melted. Melt droplets and melt veins of mixed metal and sulfide were found adjacent to the pair. The profile in Fig. 27b shows a history of rapid, heterogeneous intake of Ni in troilite during shock reheating. This heterogeneous distribution of Ni would be expected of troilite that was partially melted and then cooled too rapidly to allow a

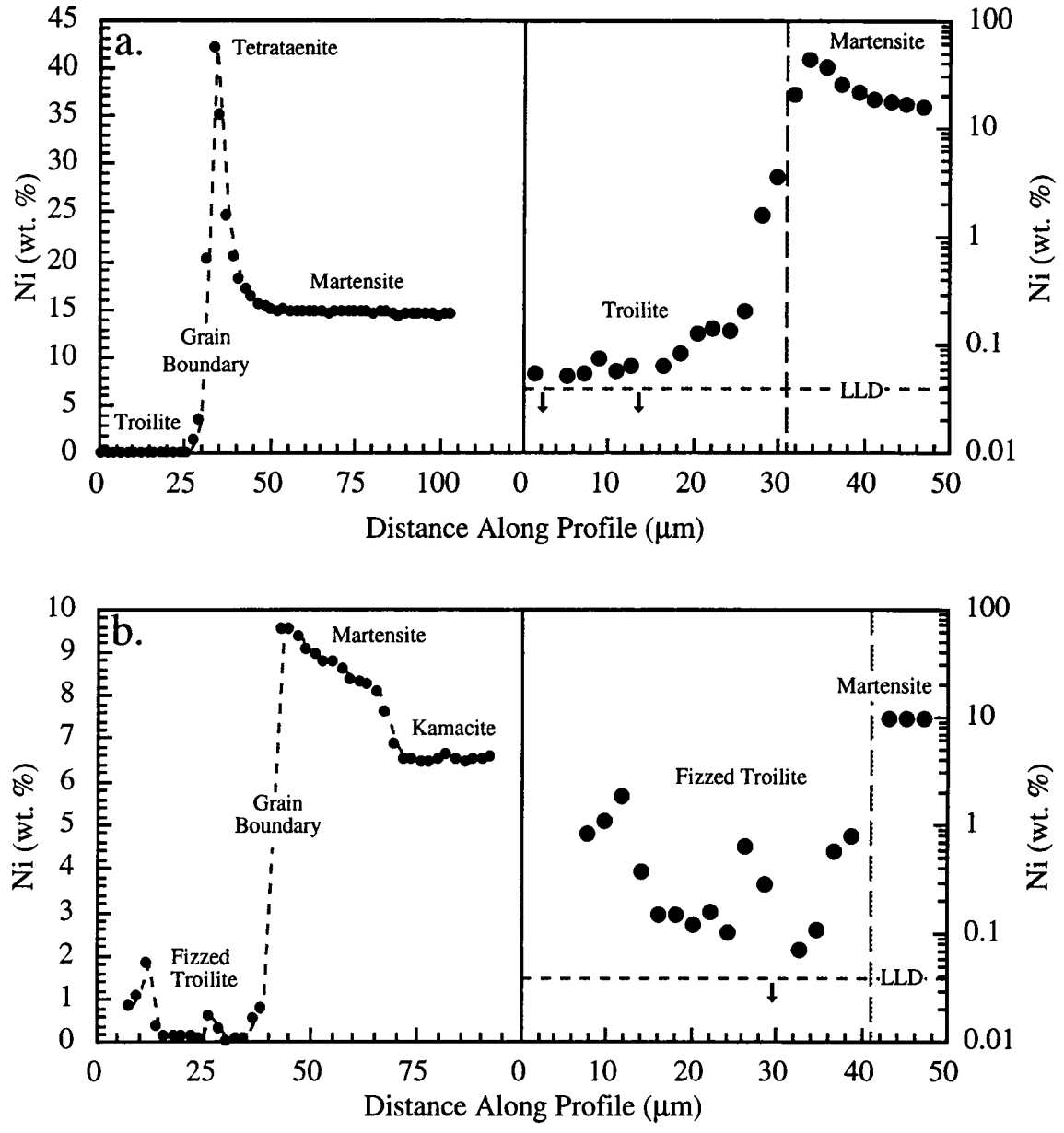

Figure 27. Ni profiles across a metal-troilite pair in a) Shaw (L7, melt) and b) McKinney (L4, S6). The left diagrams show the full profile. The right diagrams show closeups at the contact between the two phases. Arrows across the profile indicate analyses below the lower limit of detection (LLD) of Ni in troilite. Note that the Ni diffusion profile peaks at ~10 times the Ni content that was present in the two previous figures. In McKinney, post-shock cooling proceded too rapidly for regular Ni diffuion profile to form.

normal Ni diffusion profile to develop. Note that the Ni content in the central part of the troilite ranges between 0.1 to 1.0 wt %, values that fall well within the range of Smith and Goldstein's (1977) Ni values for severely shock reheated, rapidly cooled troilite.

What these data suggest is that the width of the Ni profile and the peak Ni content in troilite may be correlated to petrologic type in low shock (S3 and below) L chondrites. At higher stages of shock metamorphism, but below the point of partial melting of troilite, the width and peak Ni content in the diffusion profile increases with an increase in shock stage. This would suggest that peak Ni content in troilite may also correlate with an increase in shock metamorphism. Such a correlation is seen in Fig. 28. In this diagram, spot analyses of troilite were taken adjacent to Fe-Ni metal grains in eleven L chondrites of known shock stage. Within each shock stage, peak Ni in troilite was found in troilite grains that were adjacent to Fe-Ni metal with the highest Ni concentration (usually in troilite adjacent to tetrataenite). For all but the one S5 L chondrite (Kyushu), peak Ni values do tend to increase with an increase in shock stage. Since troilite was not found adjacent to tetrataenite in the Kyushu thin section, the full range of Ni values was not sampled in this meteorite. Finally, partially melted troilite in highly shocked L chondrites have diffusion profiles that have been totally disrupted by the rapid reheating, heterogeneous intake of Ni, and rapid cooling after the injection of the melt material that, in the case of McKinney, resulted in a shock-blackened texture.

Summary

Bulk chemical analyses of L chondrites show no trends in major or minor oxides when compared with degree of thermal or shock metamorphism. Both types of

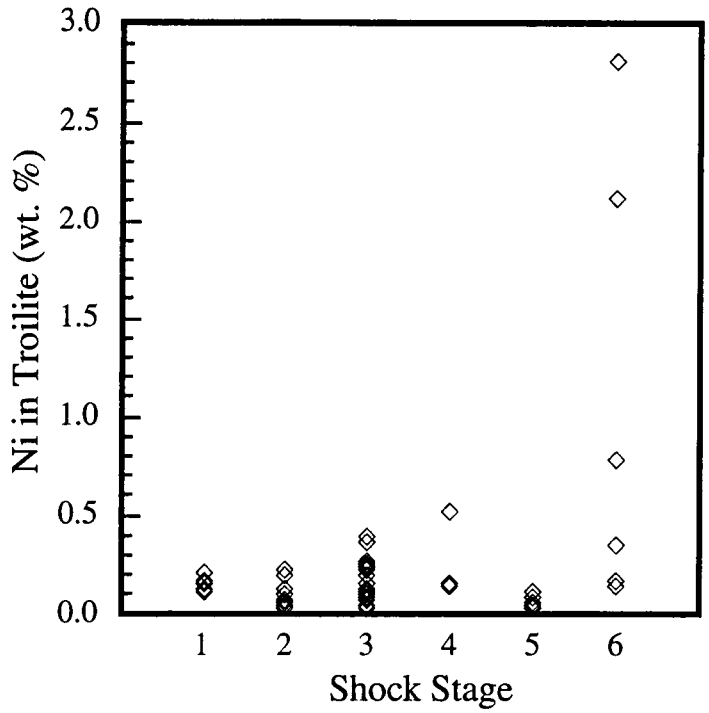

Figure 28. Shock stage vs. Ni content in matrix troilite showing an increase in peak Ni content with an increase in shock stage. Peak values were obtained at the boundaries of troilite grains adjacent to the high-Ni metal tetrataenite (contacts of this type were absent from the S5 L chondrite Kyushu).

metamorphism must have taken place in a closed system (with respect to these oxides) after accretion of the L chondrite parent body.

Although textural changes in olivine and pyroxene are important shock metamorphism indicators, there appears to be no progressive alteration in the composition of these minerals with an increase in shock stage.

The CaO content in clinopyroxene, and to a lesser extent in orthopyroxene, correlates with an increase in thermal metamorphism, but not shock metamorphism. This is an important observation when considering a geothermometer to use in interpreting peak thermal metamorphic temperatures of shocked L chondrites.

Matrix chromite grains in L chondrites of all shock stages are remarkably homogeneous in their chemistry. This may represent chemical equilibration following shock or thermal metamorphism, or both.

Most low-shock Fe-Ni metal grains (<S4) have Ni profiles that suggest slow cooling though 400 °C. Metal grains shocked higher than S3 stage tend to have flat central Ni profiles suggesting post-shock cooling rates several orders in magnitude faster than low-shock metal.

In low-shock L chondrites (<S4), an increase in the width of the Ni profile in troilite and the peak Ni content seem to correspond to an increase in petrologic type. This could either be the result of slower cooling at increasing depths within the L chondrite parent body or from uniform cooling rates that began at higher temperatures with an increase in petrologic type. For moderately- to highly-shocked L chondrites, the peak Ni content in troilite adjacent to high-Ni tetrataenite correlates directly with the relative post-shock cooling rate.

CHAPTER 4

THERMOMETRY OF L CHONDRITES

Whether induced by shock or purely thermal processes, metamorphism resulted in the reheating of meteorites. Pressure effects on meteorites were considered negligible, since all research to date indicates that asteroid parent bodies were less than a few thousand kilometers in diameter. If the peak temperature attained was greater than the blocking temperature for cation diffusion between two adjacent minerals, then these minerals may have exchanged certain of their more mobile components. If the sample was held at the peak temperature for a sufficiently long time, cation diffusion ceased when the mineral pair achieves equilibrium. Slow cooling following metamorphism (at normal asteroidal cooling rates of 1 to 100 K/My) resulted in further cation diffusion, allowing the minerals to adjust their chemical compositions to lower temperature conditions. If, however, the assumption was made that rapid cooling (ie. instantaneous) followed metamorphic reheating, such that cation diffusion was prevented from taking place, then the final compositions of the mineral pair reflect equilibrium at the peak metamorphic temperature conditions. If cation exchange altered the chemistry of the mineral pair in a readily quantifiable fashion and if all of the thermodynamic parameters of the exchange are known, then laboratory calibrations can be used to derive cation-exchange thermometers.

Since cation-exchange reactions for various mineral pairs occur over different temperature intervals and block at different temperatures, it is often advantageous to use several cation-exchange thermometers when dealing with materials that have experienced more than one metamorphic event. L chondrites appear to have

experienced such polymetamorphism, with each metamorphic event subjecting the meteorites to distinct peak temperature and cooling-rate histories. Three cation-exchange thermometers were employed in an attempt to derive peak metamorphic temperatures for 14 L chondrites: olivine + spinel Fe-Mg exchange (Sack and Ghiorso, 1991a), orthopyroxene + clinopyroxene Ca exchange (Lindsley, 1983), and Fe-Ni metal + troilite Ni exchange (Bezmen et al., 1978). In samples that contained the appropriate mineralogies for use with a specific thermometer, 4 to 12 mineral pairs were analyzed. Results of the thermometric calculations are presented in light of their potential use in separating temperatures attained during shock metamorphism and thermal metamorphism.

Olivine + Spinel Thermometry

The olivine + spinel thermometer of Sack and Ghiorso (1991a) is based on the low-pressure (down to several bars) and variable-temperature (400 to 1400 °C) exchange of Fe and Mg between coexisting olivine and spinel. It is a mathematically complex thermometer that attempts to take into account the co-diffusion of other components (such as Cr and Al), as well as relevant features from recent spinel phase diagram research (reviewed by the authors). Temperatures were obtained from compositions of coexisting olivine + spinel pairs using algorithms provided by the authors. Results were cross-checked by entering analyses into a Fortran program (OL-SP GEOTHERM) provided by the authors. There is a reported error of ± 50 °C in the temperatures obtained using this thermometer. This error is viewed as a minimum, provided that there is a minimal amount of Fe^{3+} in analyzed spinel, as should be the case for reduced ordinary chondrites. Calculating Fe^{3+}, by stoichiometry, revealed a range in all L chondrites sampled of 0-0.84 wt % Fe_2O_3, with most spinel grains

having 0 wt % of this cation. Using cation concentrations with recalculated Fe^{3+} values produced variations in the resulting temperatures of only 2-5 °C; thus, the ± 50 °C error seems to apply to these L chondrite samples.

Figure 29 illustrates the ranges and average temperatures obtained from this thermometer for each analyzed L chondrite. These values are arranged into three groups: normal L chondrites of shock stage S1 through S6, L chondrite breccias, and L chondrite melt rocks. Notice that a distinction has been made between the Shaw host and Shaw melt dike. The host is the brecciated, chondrule-bearing portion of Shaw that Taylor et al. (1979), designated the gray lithology. This region of Shaw lacks evidence of silicate or metal-sulfide melt textures. The melt dike in Shaw was designated as the light lithology by Taylor et al. (1979), and contains mineral textures indicative of injection as molten to partially-molten material.

For S1-S6 chondrites (averages labeled with squares), all temperatures fall within the range of 707 ± 48 °C. This is very similar to the temperature range of 720 ± 40 °C that Sack and Ghiorso (1991b) obtained for all ordinary chondrites (H, L, and LL classes) by applying their thermometer to olivine and spinel compositions taken from the literature (chromite data was taken from Bunch et al., 1967, and olivine data from Keil and Fredriksson, 1964). There are several interesting points to note from this figure. One point is the unusual difference in the range of temperatures recorded by unequilibrated chondrites (650-700 °C), as opposed to equilibrated chondrites (650-800 °C). This suggests that the olivine + spinel thermometer has been partially reset. Wlotzka (1987) has stated that matrix chromite grains of constant composition, such as these, record cooling-history information and not peak equilibration temperatures. Rapid cooling from higher post-shock temperatures could explain why the three high-

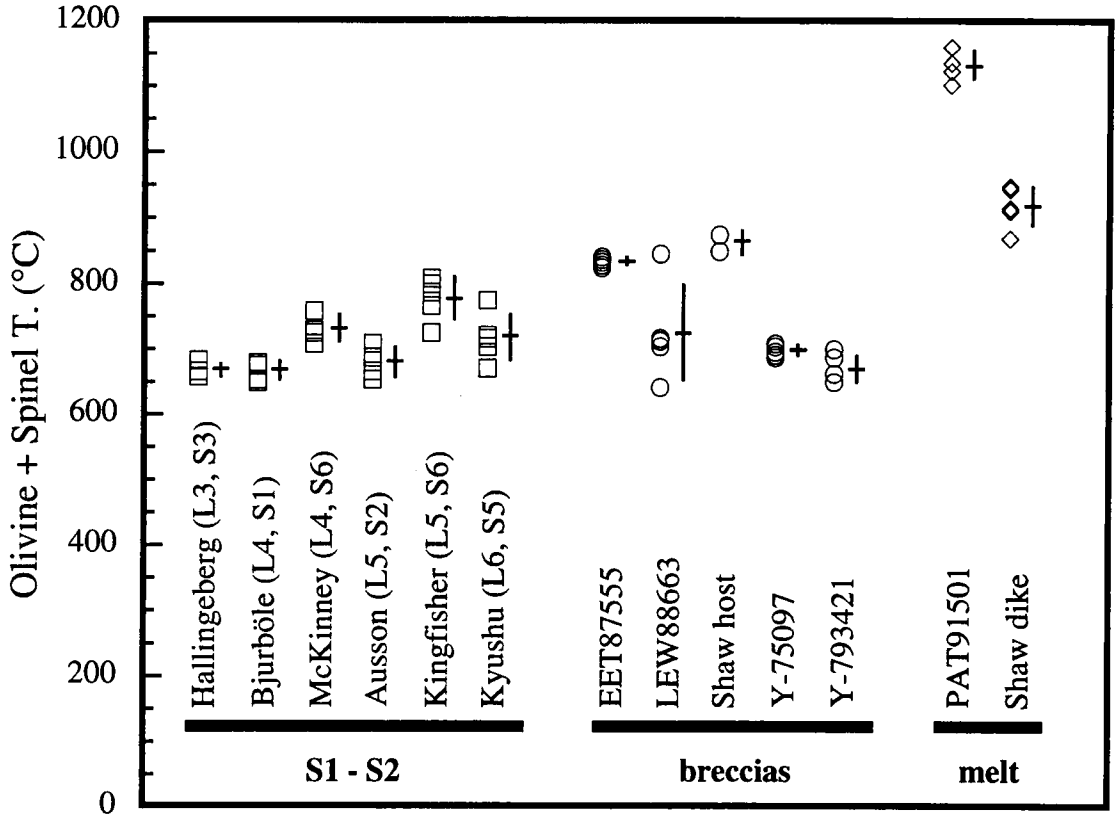

Figure 29. Plot of the range of temperatures obtained for individual L chondrites using the olivine + spinel thermometer of Sack and Ghiorso (1991a). Cross-bars to the right of each data set represent mean temperature (horizontal line) and standard deviation (vertical line). A similar format will be used to represent statistical calculations in Figs. 30-34.

shock L chondrites shown in Fig. 29 have a wider temperature span and record higher peak temperatures then the three less-shocked L chondrites.

Supporting the possible shock-metamorphic influence on these olivine + spinel temperatures is the range of values recorded in the L chondrite breccias. Samples that show evidence of severe shock reheating (Shaw and EET87555) record the highest peak temperatures, while samples that lack significant shock textures (the two Yamato meteorites) record lower peak temperatures and smaller temperature ranges. LEW88663 is an unusual breccia that contains small igneous inclusions in a strongly-shocked matrix. Slow cooling of these igneous melt drops could explain the wide temperature range seen in Fig. 29.

Both the PAT91501 L chondrite melt rock and the Shaw melt dike have extremely high olivine + chromite temperatures (1050 and 900 °C, respectively), which have been taken to indicate shock reheating to the point of partial melting (as suggested by Taylor et al., 1979 and Harvey et al., 1994, respectively). Metal textures in PAT91501 (this work) and in Shaw (Scott and Rajan, 1979) suggest that both meteorites cooled rapidly through 450 °C. This could explain both the high peak temperatures and the narrow range of temperatures obtained from olivine + chromite pairs in these meteorites.

In Fig. 30, olivine + chromite temperatures have been grouped and arranged according to petrologic type (Fig. 30a) and shock stage (Fig. 30b). Here, the relationship between shock stage and peak temperatures is clear. As was implied by comparing temperatures of individual L chondrites, the higher peak temperatures are associated with L chondrites that have preserved a record of higher post-shock reheating. Widening of the temperature range appears to correspond to the faster cooling rates associated with higher shock stages. This work helps to confirm the

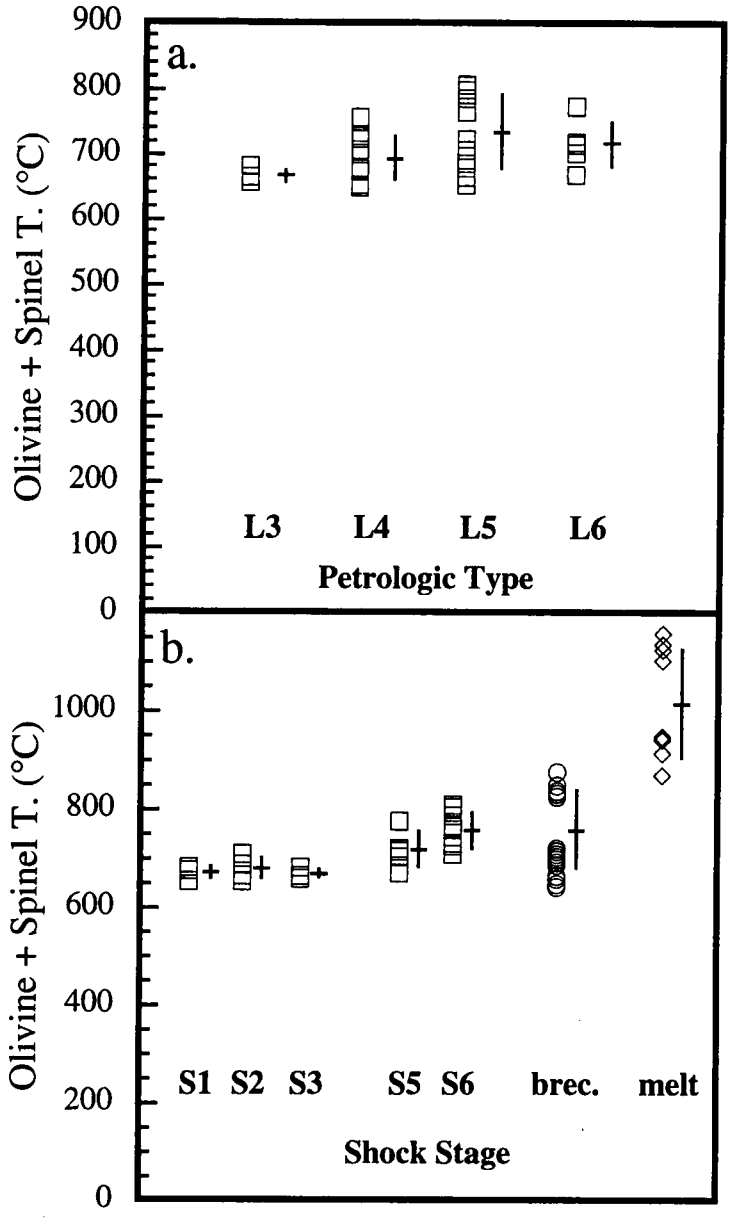

Figure 30. Temperatures derived from the olivine + spinel thermometer arranged by: a) petrologic type and b) shock stage. Cross-bars indicate mean and standard deviation for each data set.

findings of Wlotzka (1987). Shock metamorphism has partially reset this thermometer, making it a poor choice for use as a thermal metamorphic indicator.

Pyroxene Thermometry

The two-pyroxene thermometer of Lindsley (1983) utilizes the Ca content in coexisting low-Ca orthopyroxene and high-Ca clinopyroxene to derive equilibration temperatures. Temperatures for this thermometer are obtained by optimizing the Ca content of pyroxene, in effect, by removing the nonquadrilateral components (cations other than Ca, Mg, and Fe^{2+}) through a sequence of calculations similar to standard normative computations. Corrected quadrilateral end-member components are then plotted onto a graph containing experimentally derived isotherms, and temperatures are read directly from the graph. The standard error reported for this thermometer is $\pm$ 50 °C, although the error increases systematically with an increase in the amount of nonquadrilateral components. The orthopyroxene grains analyzed in 14 L chondrites from this study have average nonquadrilateral components of 1.4 ± 0.7 mole proportions, corresponding to an error of 50 °C. Clinopyroxene grains had higher mole proportions of nonquadrilateral components (5.2 ± 2.5) which produced a slightly larger error range (66 °C).

Temperature ranges obtained from this thermometer are plotted in Figs. 31a and 31b. One conclusion that is immediately apparent from these diagrams is that clinopyroxene temperatures are consistently higher (by as much as 200 °C) than orthopyroxene temperatures. This trend was noted in two recent studies of ordinary chondrites (McSween and Patchen, 1989, and Harvey et al., 1993) and in many previous terrestrial studies. McSween and Patchen (1989) gave two possible explanations for this discrepancy in pyroxene temperatures: orthopyroxene re-equilibration problems, or the unusual phase transformation history of chondritic

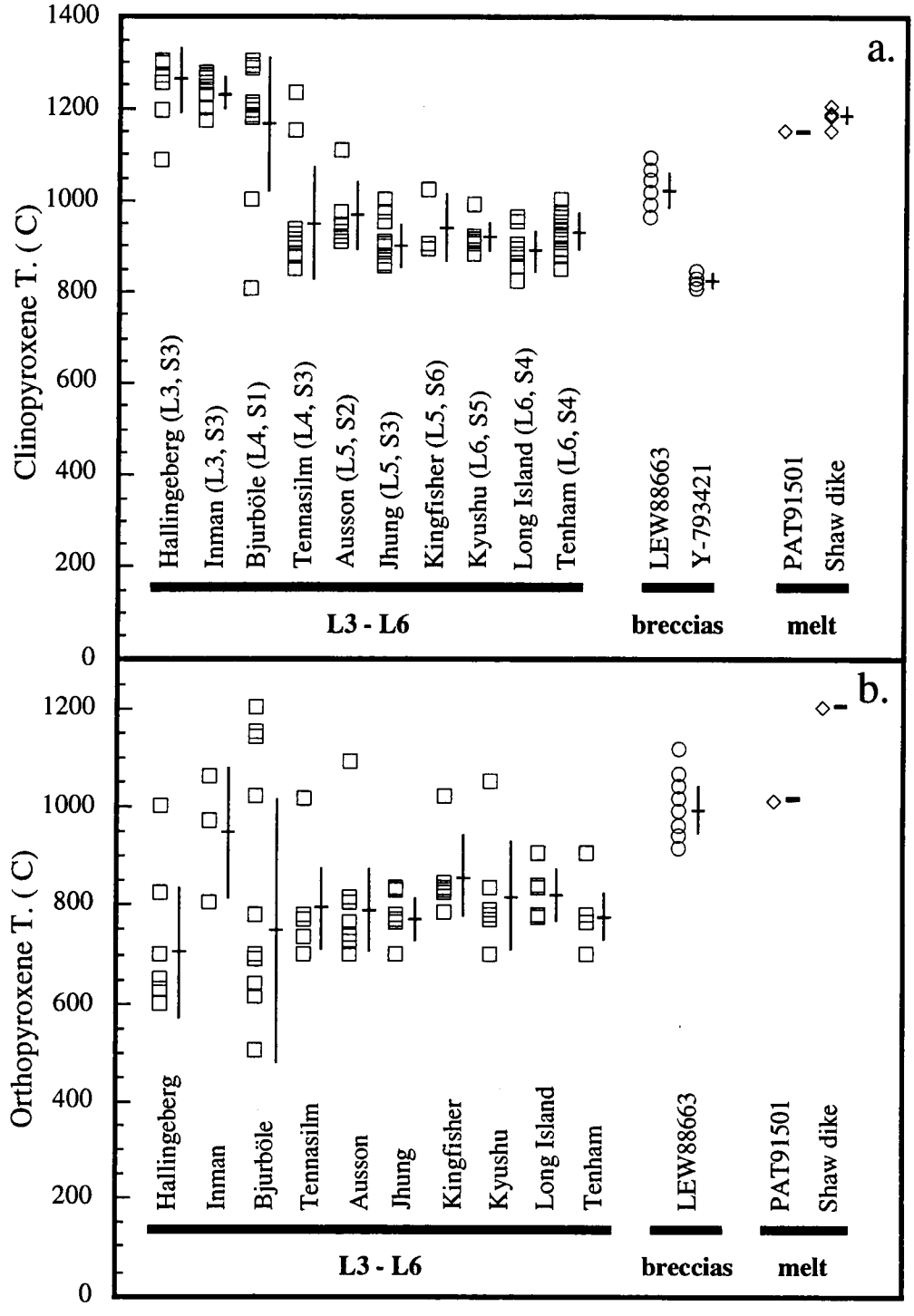

Figure 31. Plot of the range of temperatures obtained for individual L chondrites using the two-pyroxene thermometer of Lindsley (1983). a) Plots of clinopyroxene temperatures and b) orthopyroxene temperatures.

orthopyroxene. Due to differences in the slopes of solvus limbs in the orthopyroxene-clinopyroxene system, orthopyroxene may equilibrate more readily upon slow cooling than clinopyroxene. It is also possible that the Ca contents of orthopyroxene were inherited through its polymorphic transition, upon cooling, from protoenstatite (or protohypersthene) to monoclinic low-Ca pyroxene to orthopyroxene (Binns, 1970). Regardless of the reason for the discrepancy, orthopyroxene temperatures in meteorites appear to be suspect and will not be used to extract conclusions about L chondrite metamorphism in this study. Orthopyroxene temperatures are, however, summarized in Table 8 for comparison with the results obtained from the other thermometers.

Four of the L chondrites plotted in Fig. 31a gave igneous clinopyroxene temperatures (>1200 °C, subliquidus temperatures for materials of chondrule composition; Nagahara, 1983). These unequilibrated chondrites (Hallingeberg and Inman are type L3 chondrites, Bjurböle and Tennasilm are type L4 chondrites) have clinopyroxene grains that retained the high igneous-crystallization temperatures from their chondrule melt origins. The equilibrated type L5 and L6 chondrites yielded clinopyroxene temperatures lower than igneous values (913 ± 53 °C), indicating resetting by metamorphism. Blocking temperatures for clinopyroxene in these L chondrites were 800 to 850 °C, 100 to 200 °C higher than olivine + chromite blocking temperatures. This observation is consistent with the fact that, during cooling, Ca exchange reactions between coexisting pyroxenes block at higher temperatures than Fe-Mg reactions between olivine and spinel (Sack and Ghiorso, 1991b).

Clinopyroxene grains in the two L chondrite breccias also display higher blocking temperatures than their olivine + spinel equivalents. Notice, however, that LEW88663 displays a wide range in temperatures, similar to the wide span in its olivine +

Table 8. Summary of thermometry data for L chondrites analyzed in this study. All temperatures are given in °C.

Olivine + Spinel Thermometry

Type	N	Max T	Min T	Avg T	Stdev	Shock	N	Max T	Min T	Avg T	Stdev
L3	4	677	651	662	(11)	S1	5	674	646	662	(14)
L4	9	752	646	690	(36)	S2	4	701	650	674	(22)
L5	9	803	650	729	(59)	S3	4	677	651	662	(11)
L6	5	768	665	711	(37)	S4	0	•	•	•	•
breccia	24	870	643	760	(81)	S5	5	768	665	711	(37)
melt	14	1155	636	905	(175)	S6	9	803	702	751	(37)

Pyroxene Thermometry (clinopyroxene)

Type	N	Max T	Min T	Avg T	Stdev	Shock	N	Max T	Min T	Avg T	Stdev
L3	19	1300	1083	1243	(58)	S1	11	1300	800	1165	(146)
L4	26	1300	800	1038	(171)	S2	6	1108	905	961	(75)
L5	29	1108	850	918	(58)	S3	47	1300	845	1052	(179)
L6	23	1000	819	907	(47)	S4	23	1000	819	907	(47)
breccia	24	1087	800	952	(101)	S5	7	987	876	914	(35)
melt	6	1205	1150	1181	(18)	S6	3	1021	888	936	(74)

Pyroxene Thermometry (orthopyroxene)

Type	N	Max T	Min T	Avg T	Stdev	Shock	N	Max T	Min T	Avg T	Stdev
L3	12	1060	600	760	(167)	S1	14	1200	500	744	(269)
L4	24	1200	500	763	(210)	S2	18	1088	700	786	(85)
L5	41	1088	700	797	(84)	S3	32	1060	600	772	(113)
L6	19	900	700	794	(55)	S4	19	900	700	794	(55)
breccia	29	1112	912	988	(50)	S5	7	1050	700	814	(111)
melt	5	1200	1010	1162	(85)	S6	6	1020	785	855	(83)

Metal + Sulfide Thermometry

Type	N	Max T	Min T	Avg T	Stdev	Type	N	Max T	Min T	Avg T	Stdev
L3	14	768	458	585	(93)	S1	8	488	431	471	(18)
L4	17	733	402	504	(94)	S2	12	768	469	597	(90)
L5	17	672	403	529	(73)	S3	27	672	402	505	(71)
L6	6	540	411	467	(60)	S4	0	•	•	•	•
breccia	19	856	403	600	(133)	S5	4	635	403	484	(103)
melt	4	606	432	531	(79)	S6	3	733	665	688	(39)

chromite temperatures, and Y-793421 shows a corresponding narrow range of temperatures for both thermometers. Clinopyroxene in these breccias seem to have been affected by shock metamorphism in a manner similar to that of the olivine + chromite pairs. The higher blocking temperatures recorded in the clinopyroxene grains apparently reflect their higher closure temperatures during cooling following post-shock reheating.

Temperatures obtained from clinopyroxenes in the two melt samples, Shaw and PAT91501, have very uniform, igneous values of 1200 and 1175 °C, respectively. This supports information obtained from Fe-Ni textures that the Shaw melt dike was shock-melted, injected into the host breccia, and then cooled rapidly from melt temperatures to at least 400 °C. It also confirms the relatively fast cooling rates obtained from the flat, martensitic metal profiles in PAT91501.

A comparison of clinopyroxene temperatures with petrologic type (Fig. 32a) produces a clear correlation. Peak temperatures and temperature ranges decrease with increasing thermal metamorphism in response to progressive resetting of high (igneous) temperatures to lower (metamorphic) temperatures. This trend is in agreement with an onion-shell internal structure for the L chondrite parent body, where higher petrologic types form at increasing depth in the parent body, allowing them to cool over longer periods of time. Rearranging the temperature data by shock stage (Fig. 32b) results in a significant decrease in the correlation among peak temperatures. Clinopyroxene in L chondrites, excluding breccias and melt rocks, does not appear to have been affected by shock metamorphism. They seem to see through post-shock reheating to reveal younger, thermal metamorphic temperature conditions.

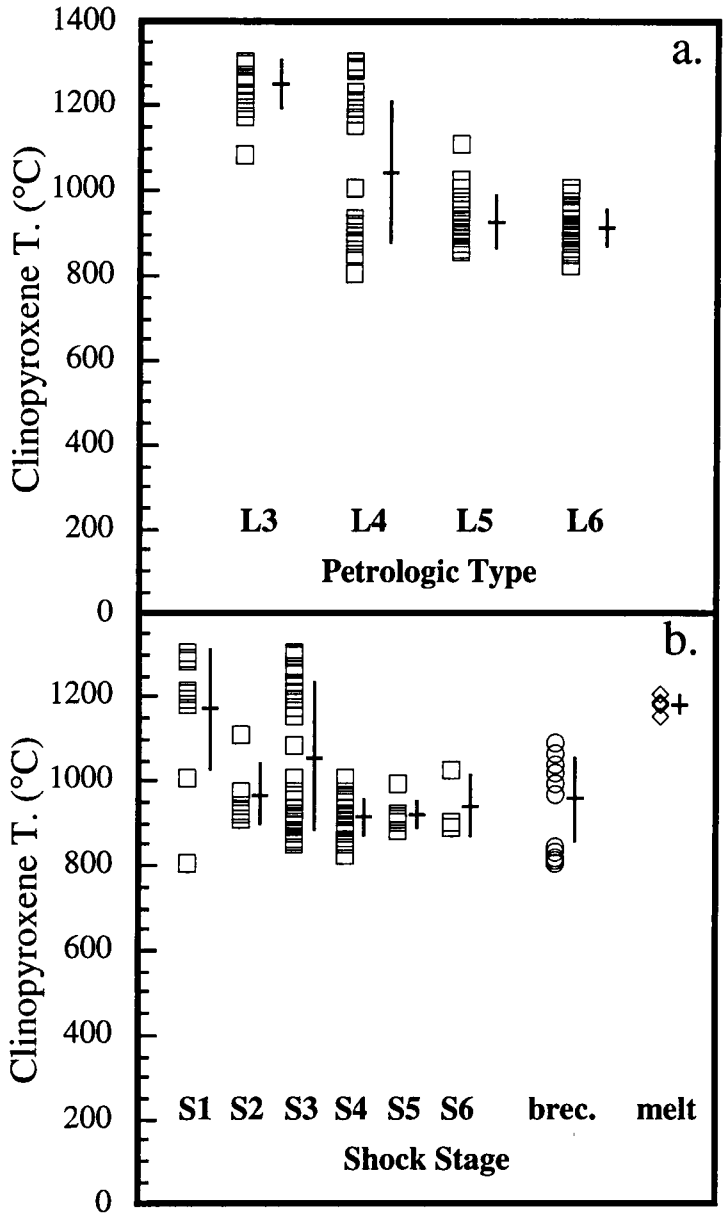

Figure 32. Temperatures obtained from the two-pyroxene thermometer arranged by: a) petrologic type and b) shock stage. Peak temperatures recorded in clinopyroxenes seem to change systematically with petrologic type and not with shock stage.

Metal + Sulfide Thermometry

Unlike the previous thermometers, the metal + sulfide thermometer of Bezmen et al. (1978) has not been used extensively in the study of meteorites. This thermometer is based on the equilibrium distribution of Ni between Fe-Ni metal and troilite. Separate calibrations were experimentally derived by the authors for coexisting kamacite + troilite and taenite + troilite, in the temperature range of 700-900 °C. Its effective range was extrapolated from 980 °C (the melting temperature of nickeliferous troilite) to 400 °C (the blocking temperature of Ni diffusion in Fe-Ni metal). No method was provided by the authors to determine the error associated with this thermometer.

Figure 33 is a plot of the range of temperatures derived for various L chondrites using this thermometer. Metal + sulfide temperatures for types L3 through L6 display a wide range of temperatures (400-770°C) and, at first glance, there appears to be no relationship between temperature range (or peak temperatures) and either petrologic type or shock stage. For example, Bjurböle (an L4, S1) metal + sulfide temperatures span a range of 420-490 °C, comparable with Kyushu (an L6, S5) which yielded a temperature range of 400-530 °C, and vastly different from McKinney (an L4, S6) whose range falls between 660-720 °C. The only systematic trend in the L3-L6 chondrites is that the thermometer gave blocking temperatures for all samples of ~400-480 °C, corresponding roughly with the blocking temperature for Ni diffusion in Fe-Ni metal (400-450 °C; Reuter et al., 1989).

Metal + sulfide temperatures in the breccias seem to be more predictable than those of the L3-L6 chondrites. Both of the Yamato meteorites yielded narrow temperature ranges, similar to the narrow ranges obtained in these samples by the olivine + spinel thermometer. Peak temperatures for the Yamato samples are ~200 °C

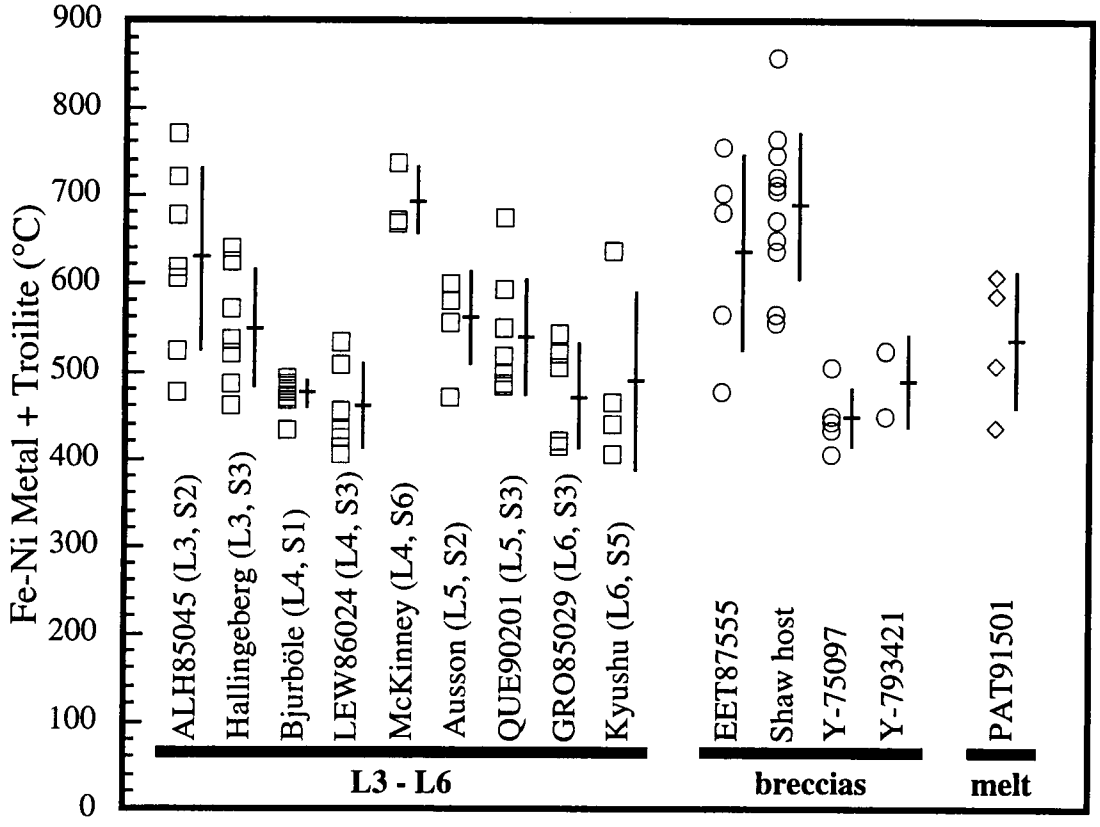

Figure 33. Plot of the range of temperatures obtained for individual L chondrites using the metal + sulfide thermometer of Bezmen et al. (1978).

lower than those obtained from the olivine + spinel thermometer, showing the greater ease of sulfide mineral reequilibration. Both thermometers seem to indicate that the Yamato samples underwent relatively slow cooling prior to shock brecciation. In Shaw and EET87555, metal + sulfide temperatures correspond directly with shock textures. Both meteorites have metal- and sulfide-free shock-melt regions surrounded by brecciated host material. In Shaw, the melt portion appears as a large (several mm wide) melt dike, while in EET87555, the melt consists of an isolated region (~1 cm wide) with a clear igneous fabric. Temperatures obtained in host material adjacent to the melt regions are consistently high (up to 860 °C in Shaw) and decrease rapidly away from the melt. Faster cooling of the Shaw melt dike may have been the reason that the Shaw metal + sulfide temperatures are higher than those of EET87555.

Temperatures derived for the PAT91501 meteorite appear to be surprisingly low for a melted L chondrite. Most of the metal and sulfide in PAT91501 is present as large (cm sized) nodules, formed from metal-silicate separation due to immiscibility. The mineral pairs analyzed for this thermometer came from tiny (mm sized) droplets of mixed metal and sulfide, widely scattered among the silicate minerals. It is possible that the silicate minerals insulated these small droplets, allowing them to cool at slow rates.

The diagrams in Fig. 34 show plots of metal + sulfide temperatures arranged according to petrologic type and shock stage. The high correlation between petrologic type and peak temperature among these analyses was a surprising discovery. It has already been shown in this work that many of the textures in Fe-Ni metal grains owe their existence to Ni redistribution following post-shock reheating. Also, Ni diffusion profiles in troilite, for at least high-shock L chondrites, were established by an increase in Ni abundance in troilite due to progressive shock reheating. If Ni distribution in

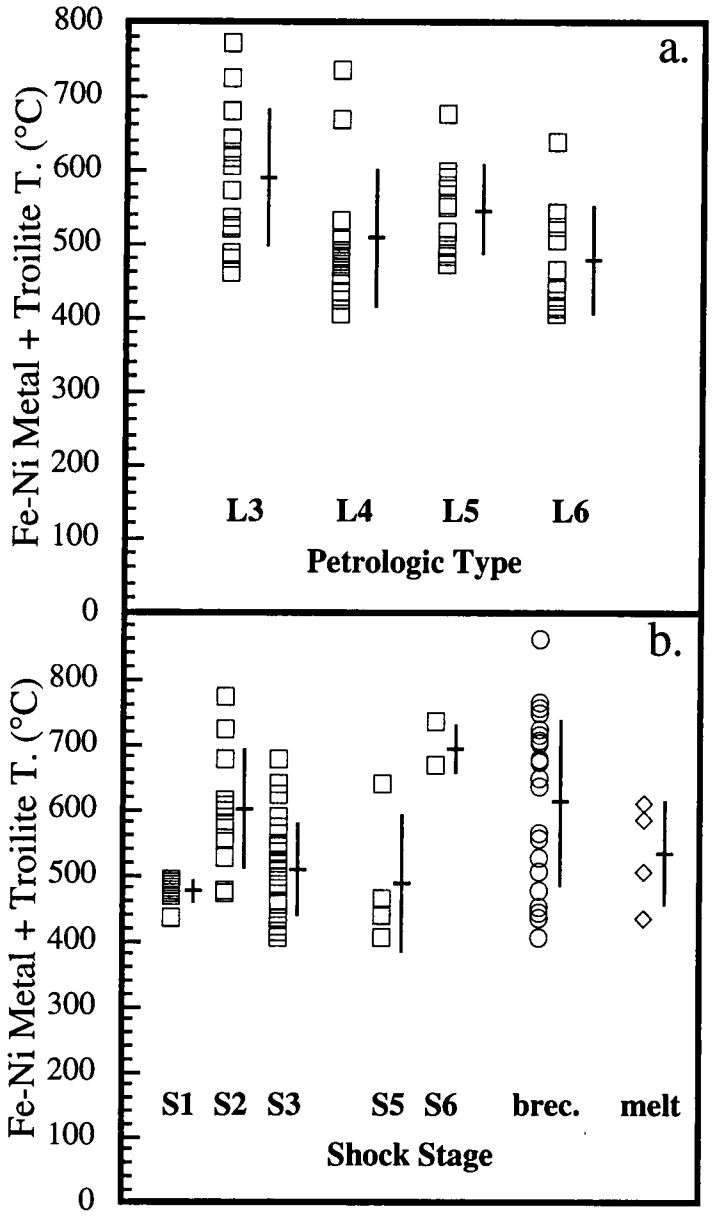

Figure 34. Temperatures obtained from the metal + sulfide thermometer arranged by a) petrologic type and b) shock stage. Peak temperatures correspond to petrologic type in a manner similar to clinopyroxene grains.

metals and sulfides were controlled by shock metamorphism, then a correlation would be expected in Ni equilibration temperatures between the mineral pair and increasing shock stage. This correlation is absent in Fig. 34b. The correlation between peak metamorphic temperatures with petrologic type and the decrease in the temperature range recorded with increasing petrologic type is very similar to that seen in the clinopyroxene temperatures derived from the Lindsley thermometer (although temperatures obtained from this thermometer are ~400 °C lower than corresponding clinopyroxene temperatures). This suggests that the equilibrium distribution of Ni between troilite and Fe-Ni metal, at least near the edges of the mineral pair, was established by thermal metamorphism and was not seriously perturbed by post-shock reheating.

Summary

The correlation between shock stage and olivine + spinel peak temperatures suggests that this thermometer is recording post-shock cooling rates; higher peak temperatures correspond to variable rates of cooling from higher peak-shock temperatures. Shock metamorphism appears to be responsible for the homogenization of the major element chemistry in matrix chromite.

Clinopyroxene grains in nonbrecciated, unmelted L chondrites yielded peak temperatures that correlate with petrologic type. Thermal metamorphism has reset clinopyroxene from initial igneous temperatures (in unequilibrated L chondrites) to increasingly more uniform metamorphic temperatures (in equilibrated L chondrites). Results obtained from this thermometer support the theory that the L chondrite parent body formed an early onion-shell internal structure which achieved peak metamorphic temperatures (in the interior) of ~1000 °C.

Despite evidence that textures in metal and in troilite are strongly perturbed by shock metamorphism, peak temperatures obtained from the metal+ sulfide thermometer correspond to an increase in petrologic type and not shock stage. The results obtained from this thermometer lend support to the initial onion-shell nature of the L chondrite parent body.

CHAPTER 5

THE L CHONDRITE PARENT BODY - AN INTERNAL HEATING MODEL

Textural and geochemical evidence from this study support the idea that thermal metamorphism alone is capable of producing the full range of petrologic types (L3-L6) within a single L chondrite parent body. Other L chondrites, such as type L7 chondrites, breccias, and melt rocks, are later, shock-induced derivatives of these four basic petrologic types. Thermal modeling of the source of L chondrites, therefore, can be restricted to (but is not necessarily limited to) the study of a single parent body. In order to model the thermal history of this L chondrite parent body, prior to impact disruption, two additional parameters must be determined: the internal structure of the parent body and the heat source for thermal metamorphism.

Data presented in this study indicate that pyroxene thermometry is capable of seeing through younger shock metamorphic events. The inverse correlation between petrologic type and peak metamorphic temperature is consistant with a parent body that developed an internally heated, onion-shell-type thermal structure prior to shock metamorphism. Type L3 chondrites contain chondrule pyroxene grains that have retained their pre-accretional igneous temperatures (as high as 1300 °C), whereas higher petrologic types have pyroxene grains that were reheated and partially re-equilibrated to lower temperatures, corresponding to their original depth within the parent body. Those materials that were buried to greater depths experienced more severe reheating and slower cooling, thus yielding more equilibrated (i.e. producing a narrower range of) temperatures. L6 chondrites record peak metamorphic temperatures within the central portion of the parent body as high as 1000 °C. A similar correlation

was noted between metal + sulfide temperatures and petrologic type. The peak temperature of L6 chondrites, using metal + sulfide pairs, was found to be ~220 °C lower than that obtained from clinopyroxene analyses, reflecting the lower blocking temperature of Ni between Fe-Ni metal and troilite. This is also consistent with slower rates of cooling from higher peak temperatures at increasing depths within the parent body; this observation is additional evidence for an onion-shell internal structure.

Wasson (1974) proposed three possible heat sources for an internally heated parent body: release of gravitational energy, decay of long-lived radionuclides, and decay of short-lived radionuclides. Previous heating models (Fujii et al., 1979; Minster and Allégre, 1979; Miyamoto and Fujii, 1980; Miyamoto et al., 1981) have proposed a range in theoretical radii of 10 to 175 km for the L chondrite parent body, far less than the >500 km radius necessary for the first two heat sources to be considered effective (Miyamoto et al., 1981). This leaves heating by decay of an extinct radionuclide as the only viable option of the three proposed for an internal heat source. Of the several possible extinct radionuclides predicted to exist in the primitive solar nebula, ^{26}Al has been used as an internal heat source since the discovery of an excess of its decay product, ^{26}Mg, in Allende CAI's (Lee et al., 1976). ^{26}Al is a high-energy, short-lived radionuclide which may havebeen present in sufficient quantities (the canonical value of $^{26}Al/^{27}Al = 5 \times 10^{-5}$; Lee et al., 1977) within the nebula to have heated small bodies (radii $\cong 5$ km) to temperatures of 1800 K (Herndon and Herndon, 1977). Internal heating by decay of ^{26}Al has been shown to be an efficient method for melting ice in volatile-rich asteroids, thus providing a fluid source for the hydrothermal alteration of carbonaceous chondrites (Grimm and McSween, 1989). It has also been successfully employed in modeling the compositional zoning (or variation in observed asteroid spectral classes) within the asteroid belt (Grimm and McSween, 1993).

Using the constraints of a single parent body with an onion-shell structure internally heated by decay of ^{26}Al, Miyamoto et al. (1981) derived a mathematical formulation for the time-temperature-depth relations within the L chondrite parent body. Since this model was based on measurable physical parameters in meteorites and the equations that formed its basis were amenable to computer manipulation, it was readily modified to incorporate more recent information about the nature of the L chondrite parent body. The following sections describe the original Miyamoto et al. (1981) thermal model and show how its modification, in light of more recent laboratory measurements, may be used to place reasonable constraints on the formation time and thermal evolution of the L chondrite parent body.

Description of the Model

The mathematical formulation for the proposed thermal model was derived by modifying the equation for a sphere of an initial temperature T_o, heated internally, and radiating the heat outward into the surrounding medium (Carslaw and Jaeger, 1959). The equation used for the model is as follows:

$$T = T_o + \frac{2hR^2A}{rK} \sum_{n=1}^{\infty} \frac{1}{1-\lambda/\kappa\alpha_n^2} \frac{\left[\exp(-\lambda t) - \exp(-t\kappa\alpha_n^2)\right] \sin(r\alpha_n)}{\alpha_n^2\left[R^2\alpha_n^2 + R * h(R * h - 1)\right] \sin(R\alpha_n)}$$

This formula differs from the one published in the Miyamoto et al. (1981) paper in that the time variable (t) was inadvertently left out of the second exponential in the original paper. Definitions for the variables used in this model are as follows:

α_n (n = 1, 2,...) are the roots of the equation	$R\alpha\cot(R\alpha) + R * h - 1 = 0$
T_o = initial temperature	180 K
K = thermal conductivity	1×10^5 erg / cm s K
A = heat generation	115 erg / cm^3 s
λ = decay constant of ^{26}Al	9.63×10^{-7} y^{-1}
κ = thermal diffusivity	5×10^{-3} cm^2 / s
R = parent body radius	85 km
h = emissivity	0.01 cm^{-1}
t = time	converted to seconds
r = radial distance from the center of body	in kilometers
ρ = parent body density	3.2 g / cm^3.

Figure 35 is a plot of the time-temperature-depth calculations for the L chondrite body taken from the Miyamoto et al. (1981) thermal model. This plot was produced by modifying the original Fortran subroutine, generously provided by Professor Miyamoto, for use on a microcomputer. Each major physical parameter that went into the calculation of these curves has important ramifications for the final thermal model and will be discussed below, along with the changes to the original model.

The Radius (R) and Density (ρ) of the Parent Body

Calculations derived from thermal modeling produce curves that are sensitive to the duration of thermal metamorphism at the center of the parent body. The duration of thermal metamorphism may be estimated from the time difference between the formation of type 3 and type 6 L chondrites. This time difference was estimated on the

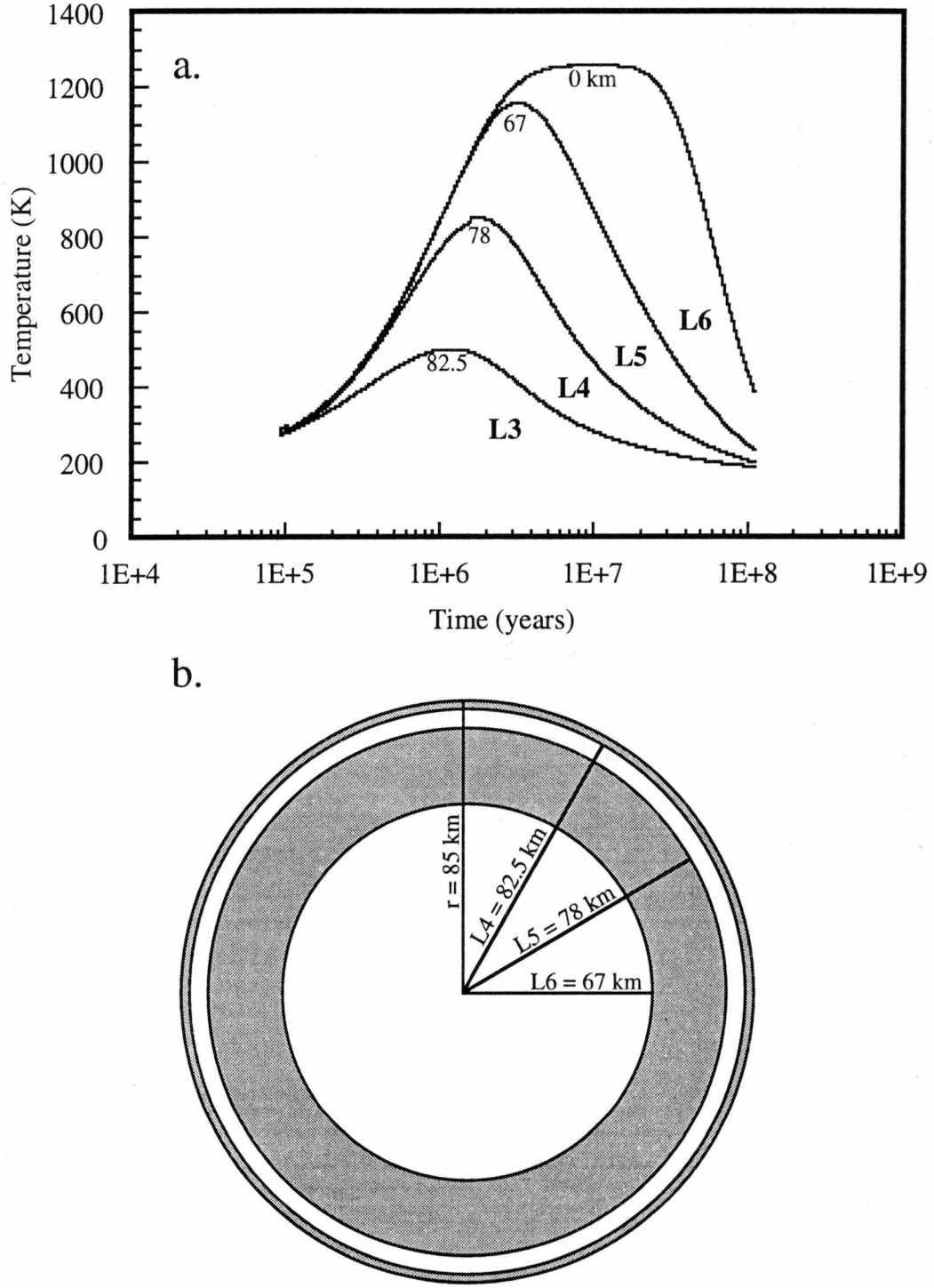

Figure 35. Original thermal model from Miyamoto et al. (1981). a) Time-temperature-depth curves calculated from Fortran program. Each curve in this plot (and all subsequent plots) was generated from 2500 iterations spaced at even time intervals. b) Scaled diagram of an onion-shell internal structure for the L chondrite parent body calculated from the original model.

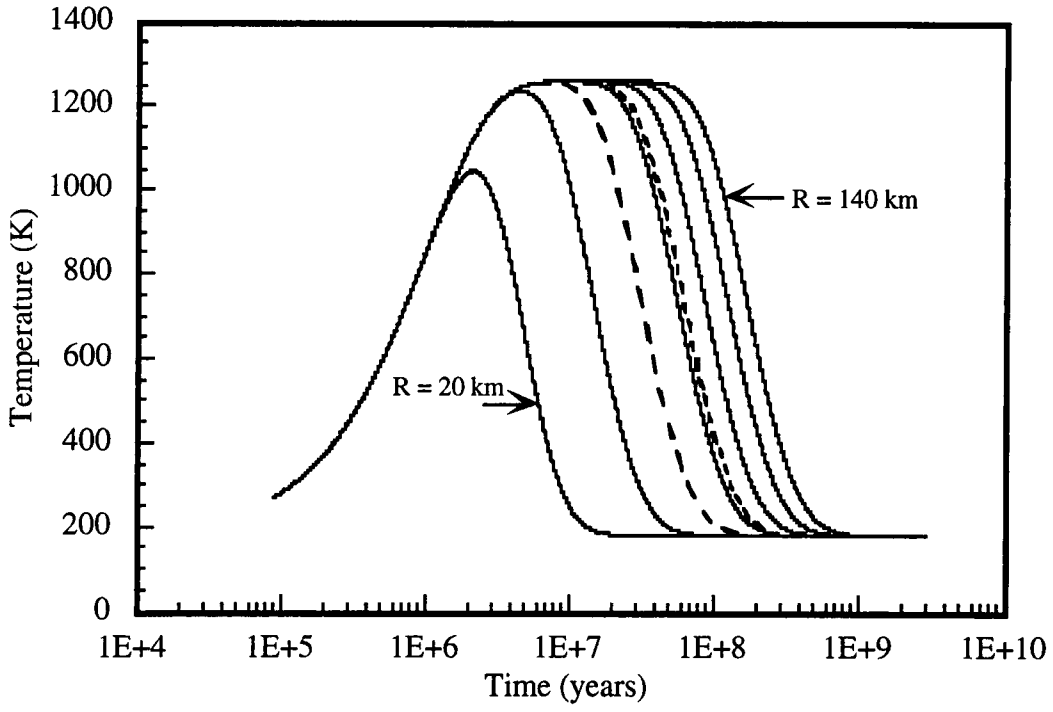

Figure 36. The relationship between the radius of the parent body (R) and the duration of thermal metamorphism can be seen in this set of time-temperature-depth curves. Each curve shows a stepped increase in radius of 20 km. Short dashed curve represents the 85 km radius used in the original Miyamoto et al. (1981) model. Long dashed curve represents a radius of 60 km used in the updated model.

basis of Rb-Sr radiochronometry of ordinary chondrites as ~100 Ma (Wasserburg et al., 1969; Gray et al., 1973) .

Figure 36 shows the relationship between duration of thermal metamorphism and radius of the parent body. When all other physical parameters are set constant, the peak temperature attained by the central portion of the parent body persists for a longer time span with an increase in radius. Using a formation interval of 100 Ma, Miyamoto et al. (1981) established the radius of the L chondrite parent body at ~ 85 km (short dashed line in Fig. 36).

Göpel et al. (1994), using U-Pb radiochronometry in phosphate separates, obtained a concordant age for equilibrated H chondrites and a near concordant age for equilibrated L chondrites of ~ 60 Ma. Since this value was obtained from both U-Pb systems (^{235}U and ^{238}U), with a published resolution of 1 Ma, it was incorporated in the updated thermal model. Using a formation interval of 60 Ma, the proposed radius of the parent body decreases from 85 km to 60 km (long dashed line in Fig. 36).

Not only does this new value for the radius represent more precise age dating, but it helps to offset the underestimation of another physical parameter used in the original model; the density of the parent body. Miyamoto et al. (1981) used a value of 3.2 g/cm^3 as the L chondrite density in their original calculations. This value is much lower than that cited by Gomes and Keil (1981), (density range of 3.26 - 3.75 g/cm^3, average of 3.52) or measured from bulk samples (3.61 g/cm^3; Yomogida and Matsui, 1983). Since density is one of the controls on the amount of bulk Al present in the original body (which in turn controls the ^{26}Al abundance), it is an important component in the heat source portion of the calculation. A denser body of smaller radius would be able to generate and retain heat comparable to a larger, less dense body. The value that was used in this model is 3.61 g/cm^3, the average bulk density of L chondrites measured by Yomogida and Matsui (1983).

The Initial Temperature (T_o)

The initial temperature forms the baseline from which the thermal evolution of the body begins. It is both the temperature of the body prior to internal heating and the temperature of the surrounding medium. The original formulation of T_o was based on the assumption that L chondrite petrologic types are present in the source region (presumably the asteroid belt) in the same proportions as are maintained in our

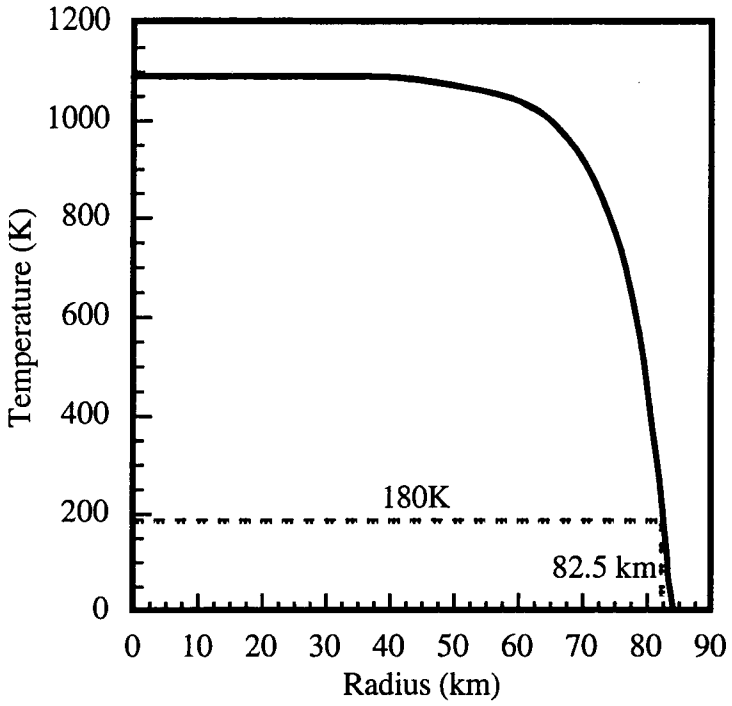

Figure 37. Calculation of the initial temperature (T_o) from the original thermal model of Miyamoto et al. (1981). Assuming that L3 chondrites comprise 8.6 vol % (equivalent to a central radius of 82.5 km in a parent body of radius = 85 km), T_o is read directly from the radius vs. peak temperature curve.

meteorite collections. By setting the proportion of L3 chondrites at 8.6 vol. %, Miyamoto et al. calculated a T_o = 180 K. This valve of T_o was based on a central radial distance (or 'r' parameter) of L3 chondrites set at 82.5 km and a peak metamorphic temperature for L3 chondrites of 500 K (see Fig. 37). By using these parameters, Miyamoto et al. were able to produce final L chondrite abundances in similar proportions to those present in our meteorite holdings (values used were from Wasson, 1974).

Statistical analyses of meteorite falls (Harvey and Cassidy, 1989) have shown that there is no basis for assuming that our present meteorite holdings reflect a non-biased

sampling of the meteorite source region. Rather, the overabundance of certain meteorite types (notably H5 and L6 chondrites) suggests a time-dependent shift in the types of parent bodies that have supplied our meteorite flux. There is, therefore, no reason to constrain the model to produce petrologic types in proportion to the mass of each type found in chondrite fall statistics.

Although the method of obtaining the initial temperature may have been inaccurate, we believe that the value of 180 K is, nonetheless, a reasonable initial temperature for the L chondrite parent body. Starting at 180 K a body of the size of our proposed parent would achieve peak temperatures of 1073 to 1273 K at distances between ~ 2.2 and 2.6 AU from the protosun (Grimm and McSween, 1993). Since this distance falls near the proposed boundary between differentiated igneous asteroids and undifferentiated metamorphic asteroids (roughly 2.7 AU; Gaffey et al., 1989), it places the nebular formation of the parent body in the correct region of space for accretion of anhydrous, silicate-metal bodies.

Thermal Conductivity (K) and Thermal Diffusivity (κ)

The thermal properties of L chondrites are important parameters in controlling the peak temperature obtained from the time-temperature-depth plot. Decreasing either thermal conductivity (K) or thermal diffusivity (κ) by even a small amount vastly increases the parent body's potential to retain heat. Figure 38 illustrates that a decrease in either parameter (by an order of magnitude) can increase the peak temperature to absurdly high levels. The Miyamoto et al. model originally used values of these parameters obtained from measurements of four Yamato Antarctic ordinary chondrites (Matsui and Osako, 1979). Yomogida and Matsui (1983) have since increased this

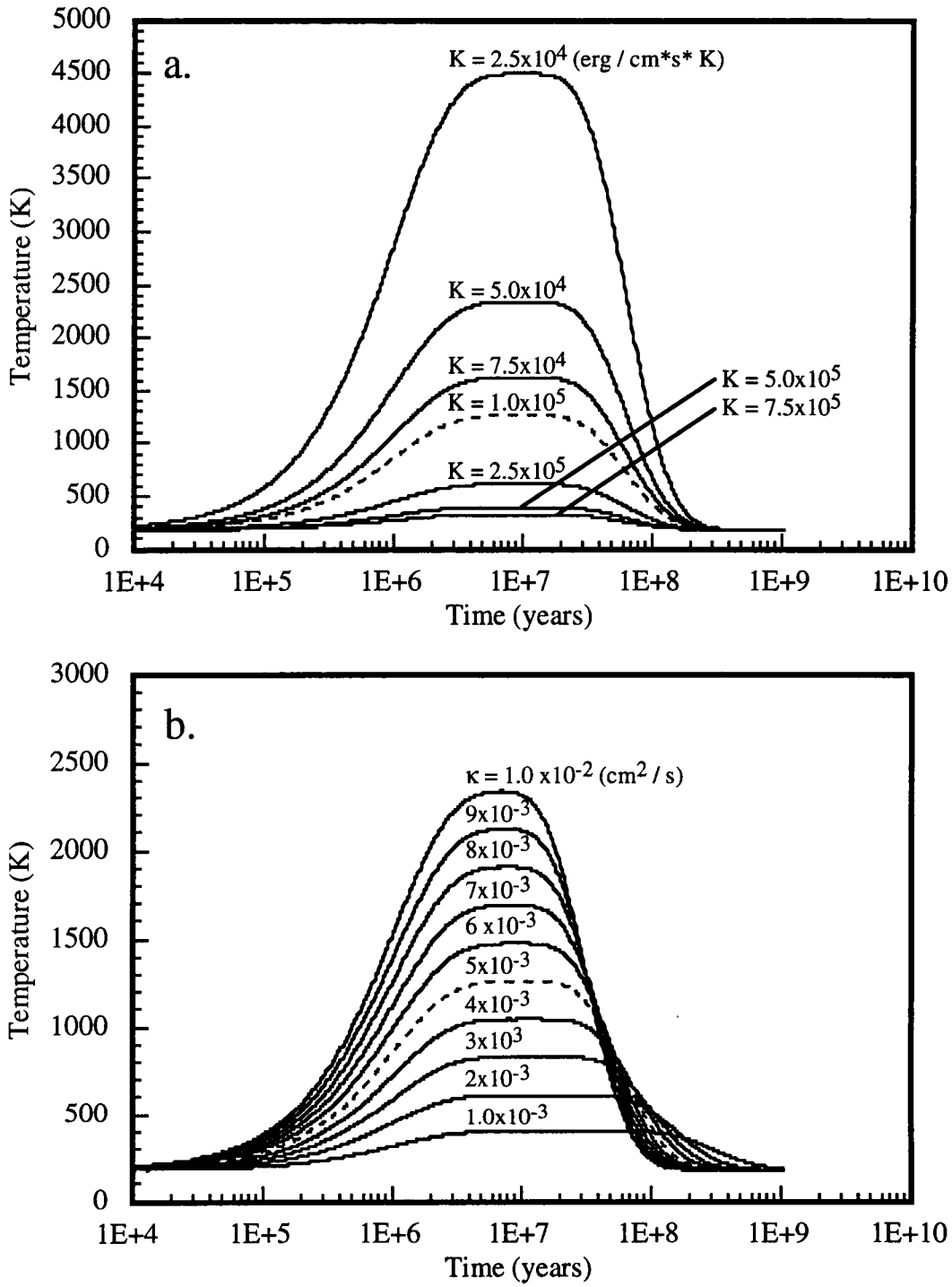

Figure 38. Time-temperature-depth curves using a) variable conductivity and b) variable thermal diffusivity in the original model. Both physical parameters exert strong controls on peak metamorphic temperatures achieved in the central portion of the parent body. Dashed curves show values used in the original model.

database of measurements by twelve more chondrites (including six non-Antarctic, L chondrite falls).

In order to chose the thermal parameters that most closely represent average L chondrite composition, silicate normative minerals were calculated for each of the six measured L chondrite falls. Normative mineralogy, metal, and sulfide content of each of these falls were then compared with similar values derived from average L chondrite compositions obtained from the high-precision bulk chemical analyses published by Jarosewich (1990). Of the 6 L chondrites whose thermal properties are known, the one which most closely matched the computed average composition was the L6 chondrite Kunasak. Kunasak has a thermal conductivity of ~1.98 X 10^5 erg / cm s K and a thermal diffusivity that varies with temperature by the formula:

$$\kappa \cong 3.77 \text{ X } 10^{-3} + 1.16/T \text{ cm}^2 / \text{s}$$

These values were chosen for incorporation into the updated thermal model. It might be noted that the original model used a fixed value for κ, which created a further source of error in this model.

The Updated Thermal Model

The list presented below is a summary of the physical parameters used to construct the thermal model presented in this study:

T_o = initial temperature of body	180 K
K = thermal conductivity	1.98 X 10^5 erg / cm K
A = heat generation	115 erg / cm^3 s
λ = decay constant of 26Al	9.63 X 10^{-7} y^{-1}
κ = thermal diffusivity	3.77 X 10^{-3} + 1.16/T cm^2 / s (T in K)

R = parent body radius	60 km
h = emissivity	0.01 cm^{-1}
ρ = parent body density	3.61 g / cm^3.

Figure 39 illustrates the final model calculated with the modified physical parameters presented above. Peak thermal metamorphic temperatures for each petrologic type were taken from McSween et al. (1988), except for the peak temperature of L6 chondrites, which was based on pyroxene thermometry from this work. This model represents a departure from the original Miyamoto et al. (1981) calculations in several important aspects. In the original model the metamorphic temperature ranges which produced each petrologic type were thought to be nearly uniform (600 - 700 °C for L4, 700 - 750 °C for L5, and 750 - 1000 °C for L6). These values resulted in the generation of nearly symmetrical curves in their model (Fig. 35). Values used in this study, based on the more recent temperature-range information cited above, show these divisions to be less uniform (600 - 700 °C for L4, 700 - 850 °C for L5, and 850 - 1000 °C for L6). Using these temperature ranges as the major constraint in the model, instead of the original model's constraint of matching abundances of petrologic types with peak temperatures, produced curves (or radii of petrologic shells) which are less uniformly spaced (Fig. 39b). Another important difference between the two models is that Miyamoto et al. (1981) treated thermal diffusivity as a constant value. Figure 38b shows that small variations in thermal diffusivity can have large effects on the overall shape of the calculated curve, as it is an important component in the heat generation portion of the computations. The model presented here treated thermal diffusivity as a variable, and using the appropriate

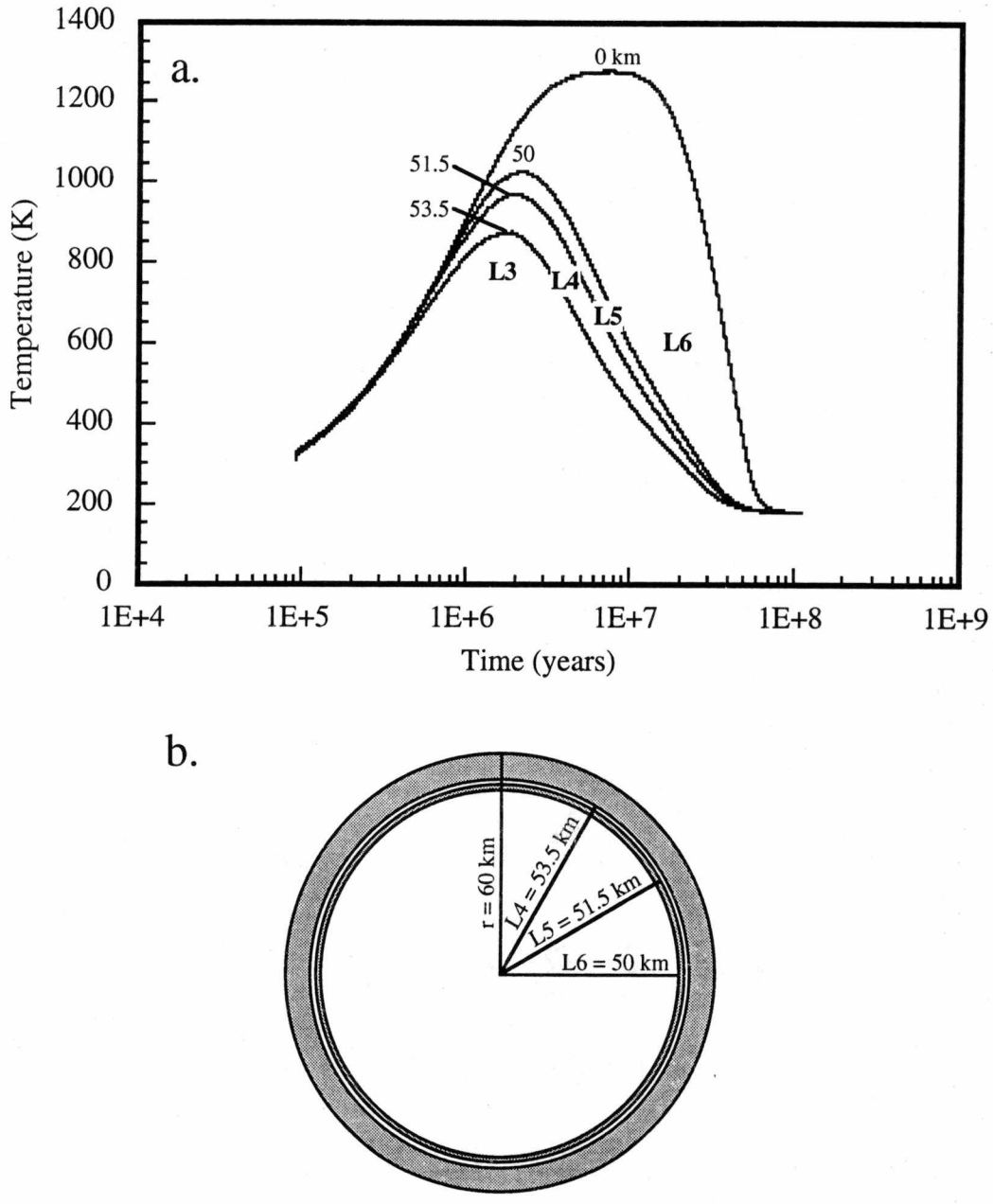

Figure 39. Updated thermal model presented in this study. a) Time-temperature-depth curves calculated from revised Fortran program. b) Scaled diagram of an onion-shell internal structure for the L chondrite parent body calculated from the updated thermal model.

diffusivity equation published in Yomogida and Matsui (1983), recalculated a new value for thermal diffusivity with each incremental temperature increase.

In order to achieve peak metamorphic temperatures for each petrologic type a value for $^{26}Al/^{27}Al$ was chosen at 1×10^{-5}. This value represents a minimum accretion age of roughly 2 million years after the formation of Allende CAI's (assuming that the zeroth year for Allende CAI formation is equal to an Al ratio of 5×10^{-5}). Minimum peak temperatures for each petrologic type (as reported in McSween et al., 1988) were used to bracket the maximum accretion age for the L chondrite parent body. By varying the Al ratio minimum peak temperatures for the four petrologic types were obtained when $^{26}Al/^{27}Al$ was set at 7.35×10^{-6}, yielding an accretion age of ~4 million years after Allende CAI formation. This brackets the accretion age of the L chondrite body between 2-4 million years after Allende CAI's, well within the time span of 10^7 yr reported by Podosek and Cassen (1994) as the most reasonable time interval in which accretion could take place in the protostellar nebula, based on a host of meteorite isotopic data.

Besides providing a possible range of accretion times for the L chondrite parent body, this model also allows the estimation of the volume of each petrologic type (Table 9). These quantities are dependent on the peak temperature achieved within each shell (petrologic type) in the parent body and not upon amounts present in meteorite falls or museum collections. One important conclusion to note in Fig. 39 is that the present model suggests that the L chondrite parent body was coated by a thick outer shell of relatively unmetamorphosed L3 chondrite material. A thick mantle of cooler, insulating material surrounding a hotter core region would more readily explain the prolonged time span of central peak temperatures of both models (2 to 3

Table 9. Calculated volume fractions for the four L chondrite petrologic types.

Model presented in this study

	inner radius (km)	outter radius (km)	ΔV	volume %
L6	0.0	50.0	523598.8	57.87
L5	50.0	51.5	48551.7	5.37
L4	51.5	53.5	69280.5	7.66
L3	53.5	60.0	263347.7	29.11
total volume	0.0	60.0	904778.7	100.00

Miyamoto et al. (1981), the original model

	inner radius (km)	outter radius (km)	ΔV	volume %
L6	0.0	67.0	1259833.1	48.97
L5	67.0	78.0	727965.7	28.30
L4	78.0	82.5	364272.4	14.16
L3	82.5	85.0	220369.6	8.57
total volume	0.0	85.0	2572440.8	100.00

Ma), than would the relatively thin, less insulating layer calculated from the original model.

One final component of the model presented in this study is that, like the original Miyamoto et al. (1981) model, it seems to accurately reproduce average cooling rates recorded in relatively undisturbed (unshocked) meteoritic FeNi metal. Since the pioneering work of Wood (1964), normal cooling rates in chondritic metal have been reported to fall in a range of from 1 to 100 K/My. Using a peak metal + sulfide temperature value of 760 °C in unequilibrated L3 chondrites and Ni blocking temperatures in L4 through L6 chondrites of 400 °C (see Fig. 34), cooling rates obtained from calculated time-temperature-depth curves range from 20 to 30 K/Ma. The lack of coherence between metal cooling rates in L chondrites must, therefore, be due to secondary shock effects, even in those meteorites that seem to be relatively unshocked.

Summary

Using the most recent L chondrite physical parameters derived from the literature and this study, modeling the thermal evolution of the L chondrite parent body has provided some important constraints concerning its origin and thermal history.

U-Pb age differences between type L3 and L6 chondrites of 60 Ma limit the radius of the L chondrite parent body to ~60 km.

Peak temperature ranges achieved by each petrologic type suggest accretion ages of 2-4 million years after the formation of Allende CAI's. These ages are in agreement with current calculations of nebular accretion time.

Cooling rates obtained from model calculations are comparable with those obtained unshocked ordinary chondrites.

Peak temperatures ranges also constrain the volume of each petrologic type formed in the parent body to be approximately the same. This is in sharp contrast to the volume of material calculated from museum collections or L chondrite fall statistics.

CHAPTER 6

SUMMARY OF THE THERMAL AND SHOCK HISTORY OF THE L CHONDRITE PARENT ASTEROID

Of the 63 L chondrites investigated in this study only one, Bjurböle (an unusual L/LL4 ordinary chondrite), was found to lack features indicative of shock metamorphism. This observation alone emphasizes the complex history of L chondrites and raises the intriguing question, Are shock metamorphic effects separable from those of thermal metamorphism? If these effects can be separated and quantified then this information could serve as a theoretical basis for reconstructing the source region of this complex class of ordinary chondrites. The results of this study indicate that the two types of metamorphism can be separated and provide the following evidence to support this conclusion.

A comparison of recently shock-classified L chondrites (123 total) revealed no statistical correlation between shock metamorphism and petrologic type. Such a correlation would be expected if shock metamorphism had completely reset all previous thermal metamorphic indicators. This was the first evidence to suggest that the two types of metamorphism were separable.

A detailed petrographic study of 28 L chondrites was performed in order to better define the extent of shock metamorphic overprinting on original thermal textures and minerals. It was determined that weakly-shocked L chondrites (stage S3 and below) have textures which are dominated by equilibrium shock features, such as zoned taenite, and monocrystalline kamacite and troilite. Above shock stage S3 L chondrite textures are overprinted by disequilibrium shock features: homogenous taenite, fizzed

and polycrystalline troilite, and polycrystalline kamacite. A systematic change in the size and mineralogy of metal-sulfide melt droplets was noted and presented as a method that could potentially augment the current shock metamorphic classification of ordinary chondrites.

Although no systematic changes were seen between bulk L chondrite chemistry and thermal or shock metamorphism, several important trends were noted in individual mineral chemistry. Olivine and pyroxene geochemistry seemed to be unaffected by shock stage, making these minerals potential thermal metamorphic indicators. Matrix chromite grains, regardless of shock stage or petrologic type, were found to be extremely homogenous, indicating metamorphic resetting. Ni abundance in low-shock troilite correlated with petrologic type; in high-shock troilite Ni abundance correlated with shock state.

Three cation-exchange thermometers were chosen for this study, based on the individual mineral trends mentioned above. These thermometers provided the final evidence needed for establishing the separation of thermal and shock metamorphism. Blocking temperatures obtained from matrix clinopyroxene displayed an inverse correlation with petrologic type. Since no trends were observed between clinopyroxene chemistry and shock stage, this inverse correlation suggests an early onion-shell internal structure for the L chondrite source region, presumably an asteroid parent body. Although they did not block at peak temperatures, results of the metal-sulfide thermometer help to confirm this inverse correlation. Blocking temperatures obtained from the olivine-spinel thermometer showed a direct correlation with shock state, suggesting that matrix chromite grains in L chondrites were homogenized by post-shock reheating.

Postulating an onion-shell internal structure for the L chondrite parent body, as suggested by geothermometry, provided a method for placing the textural and mineralogic observations from this study into an evolutionary framework. Using an internal heating model driven by the decay of ^{26}Al, model calculations supplied the following constraints on the L chondrite parent body. The radius of the body, based on an age difference of 60 Ma between type L3 and type L6 chondrites, was ~60 km. The rate of decay of 26Al confines the time of accretion to 2-4 Ma after the formation of Allende CAI's (which formed ~4.55 Ga; Göpel et al, 1994). Pyroxene thermometry of type L6 chondrites suggest that the core of the body achieved peak metamorphic temperatures of 1000 °C. Cooling from peak metamorphic temperatures proceeded at a rate of 20-30 K/Ma, allowing normal metal and sulfide profiles to form.

U-Th-He and K-Ar ages for L chondrites (Loeken, et al, 1992) indicate initial impact disruption of the parent body occurred at ~4.2 Ga. Model calculations show that this is sufficient time for an onion-shell parent body to have formed and to have cooled to its initial temperature (~180K). Geochemical evidence for a second major impact event at ~0.5 Ga (Nakamura et al., 1990 and Bogard et al., 1994) suggests that the early disruption was incomplete. It is possible that the L chondrite gravitationally reassembled as a rubble-pile following the initial impact disruption. If reassembly occurred before the fragments had cooled to below 500 °C (as suggested by Taylor et al., 1987), then the absence of a correlation between metallographic cooling rates and petrologic types in L chondrites would be expected. Much of the information about the second disruption event comes from shock-melted L chondrites (such as the Point-of-Rocks melt rock). This fact and the observation that higher L chondrite petrologic types (L5 and L6) are the most abundant meteorite falls, suggest the second major impact event might have totally disrupted the L chondrite parent body.

REFERENCES CITED

REFERENCES CITED

Agrell S.O., Long J.V.P., and Oglive R.E. (1963) Nickel content of kamacite near the interface with taenite in iron meteorites. *Nature* **198**, 749-750.

Anders E. (1964) Origin, age, and composition of meteorites. *Space Sci. Rev.* **3**, 583-714.

Ashworth J.R. (1977) Matrix textures in unequilibrated ordinary chondrites. *Earth Planet. Sci. Lett.* **35**, 25-34.

Bergmann F. and Wlotzka F. (1969) Shock induced thermal metamorphism and mechanical deformations in the Ramsdorf chondrite. *Geochim. Cosmochim. Acta* **33**, 1351-1370.

Bezmen N.I., Lutov V.S., and Osadchiy Y.G. (1978) Distribution of nickel between troilite and metallic iron as a mineralogical thermometer. *Geochem. Intern.* **15**, 120-127.

Binns R.A. (1970) Pyroxenes from non-carbonaceous chondritic meteorites. *Mineral. Mag.* **37**, 649-669.

Binns R.A., Davis R.J., and Reed S.J.B. (1969) Ringwoodite, natural $(Mg,Fe)_2SiO_4$ spinel in the Tenham meteorite. *Nature* **221**, 943-944.

Bogard D.D., Garrison D.H., Norman M.D., Scott E.R.D., and Keil K. (1994) ^{40}Ar-^{39}Ar age and petrology of Chico: Large-scale impact melting on the L chondrite parent body. *Geochim. Cosmochim. Acta* **58**, (submitted).

Buchwald V.F. (1975) Handbook of Iron Meteorites: Their History, Distribution, Composition, and Structure. Univ. of California Press, Berkley, Ca.

Bunch T.E., Keil K., and Snetsinger K.G. (1967) Chromite composition in relation to chemistry and texture of ordinary chondrites. *Geochim. Cosmochim. Acta* **31**, 1569-1582.

Burington R.S. and May D.C. (1953) Probability and statistics with tables. Handbook Publishers, Sandusky, Oh., 332 p.

Caes C.J. (1988) Studies in Starlight: Understanding Our Universe. TAB Books, Blue Ridge Summit, Pa., 227 p.

Carslaw H.S. and Jaeger J.C. (1959) Conduction of heat in solids. Oxford Univ., New York, N.Y., 510 p.

Carter N.L., Raleigh C.B., and DeCarli P.S. (1968) Deformation of olivine in stony meteorites. *J. Geophys. Res.* **73**, 5439-5461.

Chuang Y.Y., Chang Y.A., Schmid R., and Lin J.C. (1986) Magnetic contribution to the thermodynamic functions of alloys and the phase equilibria of the Fe-Ni system below 1200 °K. *Met. Trans.* **17A**, 1361-1372.

Clarke R.S., Jr. and Scott E.R.D. (1980) Tetrataenite-ordered FeNi, a new mineral in meteorites. *Am. Mineral.* **65**, 624-630.

Clayton R.N., Mayeda T.K., and Molini-Velsko C.A. (1985) Isotopic variations in solar system material: Evaporization and condensation of silicates. In *Protostars and Planets II* (eds. D. C. Black and M. S. Matthews), pp. 755-771, Univ. Arizona Press.

Clayton R.N., Onuma N., and Mayeda T.K. (1976) A classification of meteorites based on oxygen isotopes. *Earth Planet. Sci. Lett.* **30**, 10-18.

Cripe J.D. and Moore C.B. (1975) Total sulphur content of ordinary chondrites (abstract). *Meteoritics* **10**, 387-388.

Dodd R.T., Jr (1969) Metamorphism of the ordinary chondrites: a review. *Geochim. Cosmochim. Acta* **33**, 161-203.

Dodd R.T., Jr. (1981) Meteorites: A Petrologic-Chemical Synthesis. Cambridge University Press, New York, N.Y., 368 p.

Dodd R.T., Jr. and Jarosewich E. (1979) Incipient melting in and shock classification of L-group chondrites. *Earth Planet. Sci. Lett.* **44**, 335-340.

Dodd R.T., Jr., Grover J.E., and Brown G.E. (1975) Pyroxenes in the Shaw (L-7) chondrite. *Geochim. Cosmochim. Acta* **39**, 1585-1594.

Dodd R.T., Jr., Van Schmus W.R., and Koffman D.M. (1967) A survey of the unequilibrated ordinary chondrites. *Geochim. Cosmochim. Acta* **31**, 921-951.

Fredriksson K. and Keil K. (1964) The iron, magnesium, and calcium distribution in coexisting olivines and rhombic pyroxenes in chondrites. *J. Geophys. Res.* **69**, 3487-3515.

Fujii N., Miyamoto M., and Ito K. (1979) The role of external heating and thermal metamorphism of chondritic parent body. *Planet. Sci.* **1**, 84.

Gaffey M.J., Bell J.F., and Cruikshank D.P. (1989) Reflectance spectroscopy and asteroid surface mineralogy. In *Asteroids II* (eds. R. P. BinzelT. Gehrels and M. G. Matthews), pp. 98-127, Univ. of Arizona Press.

Goldstein J.I. and Short J.M. (1967) The iron meteorites, their thermal history and parent bodies. *Geochim. Cosmochim. Acta* **31**, 1733-1770.

Gomes C.B. and Keil K. (1980) Brazilian Stone Meteorites. Univ. Of New Mexico Press, Albuquerque, NM, 162 p.

Gooding J.L. (1986) Weathering of stoney meteorites in Antarctica. In *Workshop on Antarctic Meteorites* (ed. J. Annexsted), pp. 48-54, Lunar and Planetary Institute.

Göpel C., Manhès G., and Allègre C.J. (1994) U-Pb systematics of phosphates from equilibrated ordinary chondrites. *Earth Planet. Sci. Lett.* **121**, 153-171.

Graham A.L., Bevan A.W.R., and Hutchison R. (1985) Catalogue of Meteorites. The University of Arizona Press, Tucson, Ar., 460 p.

Gray C., Papanastassiou D.A., and Wasserburg G.J. (1973) The identification of early condensates from the solar nebula. *Icarus* **20**, 213-239.

Grieve R.A.F., Sharpton V.L., and Stöffler D. (1990) Shocked minerals and the K/T controversy. *Eos* **71**, 1792.

Grimm R.E. (1985) Penecontemporaneous metamorphism, fragmentation, and reassembly of ordinary chondrite parent bodies. *J. Geophys. Res.* **90**, 2022-2028.

Grimm R.E. and McSween H.Y., Jr. (1989) Water and the thermal evolution of carbonaceous chondrite parent bodies. *Icarus* **82**, 244-280.

Grimm R.E. and McSween H.Y., Jr. (1993) Heliocentric zoning of the asteroid belt by aluminum-26 heating. *Science* **259**, 653-655.

Grossman L. (1972) Condensation in the primative solar nebula. *Geochim. Cosmochim. Acta* **38**, 47-64.

Hale R.L. (1992) Mystat statistical applications: MacIntosh edition. Course Technology, Cambridge, Ma., 184 p.

Harvey R.P. (1994) PAT91501 and similar olivine-rich lithologies: Crystallization from L-chondrite impact melts. *Submitted to Meteoritics* .

Harvey R.P. and Cassiday W.A. (1989) A statistical comparison of Antarctic finds and modern falls: Mass frequency distributions and relative abundances by type. *Meteoritics* **24**, 9-14.

Herndon J.M. and Herndon M.A. (1977) Aluminum-26 as a planetoid heat source in the early solar system. *Meteoritics* **12**, 459-465.

Herpfer M.C., Larimer J.W., and Goldstein J.I. (1994) A comparison of metallographic cooling methods used in meteorites. *Geochim. Cosmochim. Acta* **58**, 1353-1365.

Heymann D. (1967) On the origin of hypersthene chondrites: Ages and shock effects of black chondrites. *Icarus* **6**, 189-221.

Huss G.R., Keil K., and Taylor G.J. (1981) The matrices of unequilibrated ordinary chondrites: Implications for the origin and history of chondrites. *Geochim. Cosmochim. Acta* **45**, 33-51.

Huston T.J. and Lipschutz M.E. (1984) Chemical studies of L chondrites - III. Mobile elements and $^{40}Ar/^{39}Ar$ ages. *Geochim. Cosmochim. Acta* **48**, 1319-1329.

Jarosewich E. (1990) Chemical analyses of meteorites: A compilation of stony and iron meteorite analyses. *Meteoritics* **25**, 323-337.

Keil K. (1964) Possible correlation between classifications and potassium-argon ages of chondrites. *Nature* **203**, 511.

Kerridge J.R. and Matthews M.S. (1988) Meteorites and the Early Solar System. Univer. of Arizona Press, Tuscon, Az.

Kirsten T., Krankowsky D., and Zähringer J. (1963) Edelgas- und Kaliumbestimmungen an einer größeren Zahl von Steinmeteoriten. *Geochim. Cosmochim. Acta* **27**, 13-42.

Kracher A. and Kurat G. (1980) Ordinary chondrites: The spinel problem (abstract). *Meteoritics* **15**, 319-320.

Kullerud G. (1963) The Fe-Ni-S system. Carnegie Institute, Washington, 175-189.

Lee T., Papanastassiou D.A., and Wasserburg G.J. (1976) Demonstration of ^{26}Mg excess in Allende and evidence for ^{26}Al. *Geophys. Res. Lett.* **3**, 41-44.

Lee T., Papanastassiou D.A., and Wasserburg G.J. (1977) ^{26}Al in the early solar system: Fossil or fuel? *Astrophys. J. Lett.* **211**, L107-L110.

Lide D.R. (1991) CRC Handbook of Chemistry and Physics. CRC Press, Inc., Ann Arbor, Mi.

Lin L.S., Goldstein J.I., and Williams D.B. (1979) Analytical electron microscopy study of the plessite structure in four IIICD iron meteorites. *Geochim. Cosmochim. Acta* **43**, 725-737.

Lindsley D.H. (1983) Pyroxene thermometry. *Am. Mineral.* **68**, 477-493.

Lipschutz M.E. and Woolum D.S. (1988) Highly labile elements. In *Meteorites and the early solar system* (eds. J. F. Kerridge and M. S. Matthews), pp. 462-487, The Univ. of Arizona Press.

Marti K. (1967) Trapped xenon and the classification of meteorites. *Earth Planet. Sci. Lett.* **2**, 193-196.

Matsui T. and Osako M. (1979) Thermal property measurement of Yamato meteorites. *Mem. Natl. Inst. Polar Res., Spec. Issue* **15**, 243-252.

McSween H.Y., Jr. (1979) Are carbonaceous chondrites primative or processed? A review. *Rev. Geophys. Space Phys.* **17**, 1059-1078.

McSween H.Y., Jr. and Labotka T.C. (1993) Oxidation during metamorphism of the ordinary chondrites. *Geochim. Cosmochim. Acta* **57**, 1105-1114.

McSween H.Y., Jr. and Patchen A.D. (1989) Pyroxene thermobarometry in LL-group chondrites and implications for parent body metamorphism. *Meteoritics* **24**, 219-226.

McSween H.Y., Jr., Bennett M.E., III, and Jarosewich E. (1991) The mineralogy of ordinary chondrites and implications for asteroid spectrophotometry. *Icarus* **90**, 107-116.

McSween H.Y., Jr., Sears D.W.G., and Dodd R.T., Jr. (1988) Thermal metamorphism. In *Meteorites and the Early Solar System* (eds. J. R. Kerridge and M. S. Matthews), pp. 102-113, Univ. of Arizona Press.

Meadows A.J. (1981) Links between meteorites and asteroids. *Proc. R. Soc. Lond.* **A 374**, 271-279.

Minster P.M. and Allègre C.J. (1979) ^{87}Rb-^{87}Sr dating of L chondrites: Effects of shock and brecciation. *Meteoritics* **14**, 235-248.

Miyamoto M., Fujii N., and Takeda H. (1980) A model of the ordinary chondrite parent body (abstract). *Lunar Planet. Sci.* **11**, 737-739.

Miyamoto M., Fujii N., and Takeda H. (1981) Ordinary chondrite parent body: An internal heating model. *Proc. Lunar Planet. Sci. Conf.* **12th**, 1145-1152.

Nagahara H. (1983) Texture of chondrules. *Mem. Natl. Inst. Polar Res., Spec. Issue* **30**, 61-108.

Nakamura N., Fujiwara T., and Nohda S. (1990) Young asteroid melting event indicated by Rb-Sr dating of the Points of Rock meteorite. *Nature* **345**, 51-52.

Olsen E.J. and Bunch T.E. (1984) Equilibrium temperatures of the ordinary chondrites: A new evaluation. *Geochim. Cosmochim. Acta* **48**, 1363-1365.

Podosek F.A. and Cassen P. (1994) Theoretical, observational, and isotopic estimates of the lifetime of the solar nebula. *Meteoritics* **29**, 6-25.

Powell B.N. (1969) Petrology and chemistry of mesosiderites - I. Textures and composition of nickel-iron. *Geochim. Cosmochim. Acta* **33**, 789-810.

Raikes S. and Ahrens T.J. (1979) Post-shock temperatures in minerals. *Geophys. J. R. Astron. Soc.* **58**, 717-747.

Reuter K.B., Williams D.B., and Goldstein J.I. (1988) Low temperature phase transformations in the metallic phases of iron and stony-iron meteorites. *Geochim. Cosmochim. Acta* **52**, 617-626.

Reuter K.B., Williams D.B., and Goldstein J.I. (1989) Determination of the Fe-Ni phase diagram below 400 °C. *Met. Trans.* **20A**, 719-725.

Rubin A.E. (1985) Impact melt products of chondritic material. *Rev. Geophys.* **23**, 277-300.

Rubin A.E. (1993) Metallic copper in ordinary chondrites. *Meteoritics* **29**, 94-98.

Rubin A.E. (1994) Contact metamorphism in ordinary chondrite impact breccias: Implications for the impact heating of chondrite parent bodies (abstract). *Lunar Planet. Sci.* **25**, 1169-1170.

Sack R.O. and Ghiorso M.S. (1991a) Chromian spinels as petrogenetic indicators: Thermodynamics and petrological applications. *Am. Mineral.* **76**, 827-847.

Sack R.O. and Ghiorso M.S. (1991b) Chromite as a petrogenetic indicator. In *Oxide Minerals: Petrologic and Magnetic Significance* (eds. D. H. Lindsley), pp. 323-354, Mineralogical Society of America.

Schmitt R.T., Deutsch A., and Stöffler D. (1993) Shock effects in experimentally shocked samples of the H6 chondrite Kernouvé (abstract). *Meteoritics* **28**, 431-432.

Schmitt R.T., Deutsch A., and Stöffler D. (1994) Calculation of Hugoniot curves and post-shock temperatures for H- and L-chondrites (abstract). *Lunar Planet. Sci.* **25**, 1209-1210.

Score R. and Lindstrom M.M. (1990) Guide to the U.S. Collection of Antarctic meteorites 1976-1988. *Antarctic Meteorite Newsletter* **13/1**, 135 p.

Scott E.R.D. (1973) The nature of dark-etching rims in meteoritic taenite. *Geochim. Cosmochim. Acta* **37**, 2283-2294.

Scott E.R.D. (1982) Origin of rapidly solidified metal-troilite grains in chondrites and iron meteorites. *Geochim. Cosmochim. Acta* **46**, 813-823.

Scott E.R.D. and Rajan R.S. (1979) Thermal history of the Shaw chondrite. *Proc. Lunar Planet. Sci. Conf.* **10th**, 1031-1043.

Scott E.R.D. and Rajan R.S. (1981) Metallic minerals, thermal histories, and parent bodies of some xenolithic, ordinary chondrites. *Geochim. Cosmochim. Acta* **45**, 53-67.

Scott E.R.D., Keil K., and Stöffler D. (1991) Impact heating of shocked chondrites (abstract). *Meteoritics* **26**, 393.

Sears D.W.G., Grossman J.N., Melcher C.L., Ross L.M., and Mills A.A. (1980) Measuring metamorphic history of unequilibrated ordinary chondrites. *Nature* **287**, 791-795.

Short N.M. (1966) Shock processes in geology. *J. Geol. Ed.* **14**, 149-166.

Smith B.A. and Goldstein J.I. (1977) The metallic microstructures and thermal histories of severely reheated chondrites. *Gochimica et Cosmochimica Acta* **41**, 1061-1072.

Snetsinger K.G., Keil K., and Bunch T.E. (1967) Chromite from "equilibrated" chondrites. *Am. Mineral.* **52**, 1322-1331.

Stöffler D., Bischoff A., Buchwald A., and Rubin A.E. (1988) Shock effects in meteorites. In *Meteorites and the Early Solar System* (eds. J. F. Kerridge and M. S. Matthews), pp. 165-202, Univ. of Arizona Press.

Stöffler D., Keil K., and Scott E.R.D. (1991) Shock metamorphism of ordinary chondrites. *Geochim. Cosmochim. Acta* **55**, 3845-3867.

Stöffler D., Keil K., and Scott E.R.D. (1992) Shock classification of ordinary chondrites; new data and interpretations (abstract). *Meteoritics* **27**, 292-293.

Streckeisen A.L. (1976) To each plutonic rock its proper name. *Earth-Sci. Rev.* **12**, 1-33.

Taylor G.J. and Heymann D. (1969) Shock, reheating, and the gas retention ages of chondrites. *Earth Planet. Sci. Lett.* **7**, 151-161.

Taylor G.J. and Heymann D. (1970) Electron microprobe study of metal particles in the Kingfisher meteorite. *Geochim. Cosmochim. Acta* **34**, 677-687.

Taylor G.J. and Heymann D. (1971) Postshock thermal histories of reheated chondrites. *J. Geophys. Res.* **76**, 1879-1893.

Taylor G.J., Keil K., Berkley J.L., Lange D.E., Fodor R.V., and Fruland R.M. (1979) The Shaw meteorite: History of a chondrite consisting of impact-melted and metamorphic lithologies. *Geochim. Cosmochim. Acta* **43**, 323-337.

Thomson G. (1808) Saggio de G.: Thomson, Sul Ferro malleabile trovota de Pallas in Siberia. Tradotto dal Manoscritto Ingelse del medesimo. *Atti. Accad. Sci. Siena* **9**, 37-57.

Turner G. (1969) Thermal histories of meteorites by the ^{39}Ar-^{40}Ar method. In *Meteorite Research* (eds. P. M. Millman), pp. 407-417, D. Reidel.

Van Schmus W.R. and Wood J.A. (1967) A chemical-petrologic classification for the chondritic meteorites. *Geochim. Cosmochim. Acta* **31**, 747-765.

Wahl W. (1951) The statement of chemical analyses of stony meteorites and the interpretation of the analyses in terms of minerals. *Mineral. Mag.* **29**, 416-426.

Walsh T.M. and Lipschutz M.E. (1982) Chemical studies of L chondrites - II. Shock-induced trace element mobilization. *Geochim. Cosmochim. Acta* **46**, 2491-2500.

Wasserburg G.J., Papanastassiou D.A., and Sanz H.G. (1969) Initial Sr for a chondrite and the determination of a metamorphism or formation interval. *Earth Planet. Sci. Lett.* **7**, 33-43.

Wasson J.A. (1972) Formation of ordinary chondrites. *Rev. Geophys. Space Phys.* **10**, 711-759.

Wasson J.T. (1974) Meteorites: Classification and Properties. Springer-Verlag, New York, N.Y.

Wasson J.T. and Kallemeyn G.W. (1988) Compositions of chondrites. *Phil. Trans. R. Soc. London* **A325**, 535-544.

Weatherill G.W. (1989) Origin of the asteroid belt. In *Asteroids II* (eds. R. P. Binzel, T. Gehrels, and M. S. Matthews), pp. 1258, Univ. of Arizona Press.

Widom E., Rubin A.E., and Wasson J.T. (1986) Composition and formation of metal nodules and veins in ordinary chondrites. *Geochim. Cosmochim. Acta* **50**, 1989-1995.

Willis J. and Goldstein J.I. (1981) A revision of metallographic cooling rate curves for chondrites. *Proc. Lunar Planet. Sci. Conf.* **12th**, 1135-1143.

Willis J. and Goldstein J.I. (1983) A three-dimensional study of metal grains in equilibrated, ordinary chondrites. *Proc. Lunar Planet. Sci. Conf.* **14th**, B287-B292.

Wlotzka F. (1987) Equilibration temperatures and cooling rates of chondrites: A new approach (abstract). *Meteoritics* **22**, 529-530.

Wood J.A. (1964) The cooling rates and parent planets of several iron meteorites. *Icarus* **3**, 429-459.

Wood J.A. (1967) Chondrites: Their metallic minerals, thermal histories, and parent bodies. *Icarus* **6**, 1-49.

Yabukl H., El Goresy A., and Ramdohr P. (1983) A petrologic microprobe survey of coexisting olivines, Pyroxenes, and spinels in L- and LL-chondrites (abstract). *Meteoritics* **18**, 426-427.

Yomogida K. and Matsui T. (1983) Physical properties of ordinary chondrites. *J. Geophys. Res.* **88**, 9513-9533.

APPENDICES

Appendix A: Procedure for Etching Polished Thin Sections

When working with Fe-Ni metal in polished thin sections it is sometimes necessary to etch the surfaces of the metals so that textures not easily visible by optical means will stand out more clearly. The standard etchant for meteoritical work is a called nital, a solution of nitric acid and ethyl alcohol. Nital preferentially dissolves low Ni metal, making grain boundaries between different Fe-Ni metal phases more distinct when using reflected light microscopy. Nital also stains certain features making them more readily recognizable. After treatment, cloudy taenite is stained dark brown to black and fine grained plessite is stained dark brown to a deep blue. Kamacite and martensite will develop deep etch pits and a rough surface texture. Taenite and tetrataenite will not be affected by etching unless the solution is too strong.

To prepare a 1% solution of nital pipette and mix 2ml of concentrated nitric acid (assay 60 to 70% HNO_3) into 200 ml of ethanol. Ethanol used may be standard reagent-grade alcohol (95% ethanol with a small amount of methyl and isopropyl alcohol added). Apply the etchant to the surface of the sample with a small, soft brush rapidly 'painting' the solution over the portion of the slide that is to be etched. Apply the solution for 5 to 10 seconds and then thoroughly rinse the sample with ethanol. In thin sections with a large number of cracks and/or very-fine grained metals, ultrasonic cleaning in ethanol is required to remove the excess etchant. If the samples are not adequately cleaned, the nital may eventually destroy all of the kamacite in the thin section (it is especially reactive on the kamacitic or martensitic components in plessite). After work on the sample is completed, the etched surface should be repolished using 1 μm diamond paste on a clean buffing pad.

Appendix B: Shock-Classified L Chondrites

Meteorite	Fall?	Group	Shock Stage	Author*	Meteorite	Fall?	Group	Shock Stage	Author
Accalana	find	L3	S4	1	Bjurböle	fall	L4	S1	1
Alfianello	fall	L6	S5	2	Bjurböle	fall	L4	S1	2
Alfianello	fall	L6	S5	3	Bjurböle	fall	L4	S1	3
ALH 82104	find	L5	S6	1	Borkut	fall	L5	S3	2
ALH 82105	find	L6	S6	1	Bruderheim	fall	L6	S4	3
ALH 83101	find	L6	S5	1	Chico	find	L6	S6	2
ALH 84005	find	L5	S3	1	Chico	find	L6	S6	3
ALH 84062	find	L6	brec.	1	Colby (Wisc.)	fall	L6	S3	2
ALH 84063	find	L5	S6	1	Cynthiana	fall	L4	S3	1
ALH 84065	find	L6	S6	1	Cynthiana	fall	L4	S3	2
ALH 84070	find	L6	S6	1	Denver	fall	L6	S4	2
ALH 85016	find	L6	S6	1	DOM 85503	find	L6	S4	1
ALH 85017	find	L6	S6	1	Dubrovnik	fall	L5	S3	3
ALH 85026	find	L6	S4	1	EET 83238	find	L6	S6	1
ALH 85029	find	L6	S5	1	EET 83243	find	L6	brec.	1
ALH 85033	find	L4	S6	1	EET 87557	find	L4	S3	1
ALH 85034	find	L6	S6	1	EET87555	find	L6	brec.	1
ALH 85045	find	L3	S2	1	Elenovka	fall	L5	S3	2
ALHA76001	find	L6	S3	1	Elenovka	fall	L5	S2	3
ALHA76003	find	L6	S4	1	Etter	find	L5	S5	3
ALHA77155	find	L6	S4	1	Fisher	fall	L6	S5	1
ALHA77162	find	L6	S4	1	Floyd	find	L4	S3	3
ALHA77218	find	L5	S5	1	Fukutomi	fall	L5	S3	2
ALHA77267	find	L5	S6	1	GEO 85701	find	L6	S6	1
ALHA77277	find	L6	S5	1	Gifu	fall	L6	S4	3
ALHA77297	find	L6	S4	1	Glanerbrug	fall	L5	S2	2
ALHA77301	find	L6	S4	1	GRO 85204	find	L6	S6	1
ALHA78078	find	L6	S6	1	GRO 85208	find	L6	S6	1
ALHA78106	find	L6	S3	1	GRO 85209	find	L6	S3	1
ALHA78119	find	L3	S3	1	Guangnan	fall	L6	S3	2
ALHA81099	find	L6	S5	1	Guangrao	fall	L6	S3	2
Armel	find	L5	S5	3	Gunlock	fall	L3	S5	2
Ausson	fall	L5	S2	1	Hallingeberg	fall	L3	S3	1
Ausson	fall	L5	S3	3	Hedjaz	fall	L3	S4	2
Bald Mountain	fall	L4	S4	2	Homestead	fall	L5	S4	2
Barratta	find	L4	S4	2	Inman	find	L3	S3	1
Barwell	fall	L6	S3	2	Inman	find	L3	S1	2
Beaver-Harrison	find	L6	S5	3	Inman	find	L3	S2	3

Appendix B: (continued)

Meteorite	Fall?	Group	Shock Stage	Author	Meteorite	Fall?	Group	Shock Stage	Author
Innisfree	fall	L5	S2	2	Nan Yang Pao	fall	L6	S3	2
Jartai	fall	L6	S4	2	Neenach	find	L6	S3	2
Jhung	fall	L5	S3	1	Nikolskoe	fall	L4	S2	2
Julesburg	find	L3	S3	2	Paranaiba	fall	L6	S6	3
Jumapalo	fall	L6	S3	2	PAT91501	find	L7	melt	1
Kendleton	fall	L4	S3	3	PCA 82510	find	L5	S3	1
Khohar	fall	L3	S4	1	PCA 82513	find	L5	S5	1
Kingfisher	find	L5	S6	1	Pierceville	find	L5	S3	3
Knyahinya	fall	L5	S3	2	Pinto Mtns	find	L6	S5	3
Kramer Creek	find	L4	S2	3	QUE 90201	find	L5	S3	1
Kyushu	fall	L6	S5	1	QUE 90202	find	L5	S4	1
La Criolla	fall	L6	S4	2	Ramsdorf	fall	L6	S4	3
La Lande	find	L5	S4	3	Roy (1933)	find	L5	S3	3
Lanxi	fall	L6	S3	2	Saratov	fall	L4	S2	2
Leedey	fall	L6	S3	2	Shaw	find	L7	brec.	1
LEW 85339	find	L3	S2	1	Sixiangkou	fall	L6	S5	2
LEW 86011	find	L6	S6	1	Stratford	fall	L6	S4	2
LEW 86012	find	L6	S6	1	Suizhou	fall	L6	S4	2
LEW 86024	find	L4	S3	1	Taiban	find	L6	S6	3
LEW 86357	find	L5	S3	1	Tathlith	fall	L6	S3	2
LEW 87248	find	L3	S6	1	Tenham	fall	L6	S4	1
LEW 87284	find	L3	brec.	1	Tennasilm	fall	L4	S3	1
LEW88663	find	achond	brec.	1	Tennasilm	fall	L4	S3	2
Lishui	fall	L5	S3	2	TIL 82411	find	L4	S6	1
Long Island	find	L6	S4	1	Trysil	fall	L6	S3	2
MAC 87302	find	L4	S6	1	Umbarger	find	L6	S4	3
MAC 87303	find	L4	S6	1	Waconda	find	L6	S4	3
MAC 87310	find	L4	S6	1	Walters	fall	L6	S4	3
Mafra	fall	L4	S3	3	Xi Ujimgin	fall	L6	S2	2
Manych	fall	L3	S4	2	Y75097	find	L6	brec.	1
McKinney	find	L4	S6	1	Y793241	find	L6	brec.	1
Monte Milone	fall	L5	S3	2	Zhaodong	fall	L4	S3	2
Naiman	fall	L6	S4	2	Zulu Queen	fall	L3	S3	3

* Source for the shock classification
1. this work
2. Rubin, 1993
3. Stöffler et al., 1991

Appendix C: Petrography of Disequilibrium Shock Features

The information below provides a key to the 'notes' column within this appendix.

1. All sizes are given in terms of microns.
2. The quantity given for each shock feature is in terms of the percentage of all grains observed that contained the feature where:

   rare: indicates < 10% of all grains observed contained this feature

   common: indicates 10 - 50%

   abundant: indicates > 50%

3. Polygonized kamacite is a form of polycrystalline kamacite with subgrain boundaries that intersect at ~120°.
4. Zonation is described as:

   normal: contains all of the features found in slow-cooled taenite as defined by Scott (1973)

   incomplete: is missing one or more zones (usually the tetrataenite or the cloudy taenite rim)

   homogeneous: shows not zonation upon repeated nitah etching.

5. Parallel fractures/shear defines the shock condition of the troilite

   fractured: irregular fractures with no preferred orientation

   slight shear: parallel fractures with a slight offset between them

   strong shear: parallel fractures with a significant offset between them.

6. Abundance of melt veins is given in terms of the percent area of the slide in which they are visible. Note that for many samples melt veins are an indication of fusion crust and not of shock.

meteorite petrologic type shock stage	notes	Bjurböle L4 S1	Ausson L5 S2	LEW85339 L3 S2	ALH85045 L3 S2	Inman L3 S3
KAMACITE						
size range	1	500-20	1000-10	20-2	350-10	50-10
Neumann bands	2	•	•	•	•	•
polycrystalline	2	rare	•	•	rare	•
polycrystalline (polygonized)	3	•	•	•	•	•
TAENITE						
size range	1	400-10	40-10	80-2	80-10	10-5
zonation	4	normal	normal	incomplete	normal	homogenous
plessite abundance	2	rare	•	•	rare	•
plessite grain size	1	20-5	•	•	~5	•
cloudy taenite abundance	2	abundant	abundant	rare	abundant	•
tetrataenite rims/grains	2	abundant	abundant	rare	abundant	rare
TROILITE						
size range	1	500-10	350-5	300-1	600-2	150-1
polycrystalline	2	rare	•	rare	•	abundant
parallel fractures/shearing	5	fractured	fractured	fractured	fractured	slight shear
abundance of twinned grains	2	•	•	•	rare	abundant
abundance of fizzed grains	2	•	•	present	•	•
size of fizzed grains	1	•	•	200-100	•	•
OTHER FEATURES						
abundance of melt pockets	2	•	•	rare	•	•
size of melt droplets	1	•	•	<2	•	•
composition of melt droplets		•	•	troilite	•	•
abundance of melt veins	6	•	•	•	•	•
composition of melt veins		•	•	•	•	•

meteorite petrologic type shock stage	notes	LEW86024 L4 S3	Tennasilm L4 S3	Cynthiana L4 S3	QUE90201 L5 S3	ALH84005 L5 S3
KAMACITE						
size range	1	1000-5	250-5	700-2	500-5	500-2
Neumann bands	2	•	•	•	•	•
polycrystalline	2	•	rare	•	common	•
polycrystalline (polygonized)	3	•	•	•	•	•
TAENITE						
size range	1	100-50	120-10	160-40	75-10	120-10
zonation	4	normal	normal	homogeneous	most homogen.	normal
plessite abundance	2	rare	abundant	rare	•	rare
plessite grain size	1	16-5	50-5	10	•	10-1
cloudy taenite abundance	2	abundant	present	•	rare	abundant
tetrataenite rims/grains	2	abundant	abundant	rare	rare	abundant
TROILITE						
size range	1	200-10	300-10	1000-2	500-2	550-2
polycrystalline	2	rare	rare	abundant	rare	rare
parallel fractures/shearing	5	fractured	fractured	fractured	slight shear	slight shear
abundance of twinned grains	2	common	rare	•	abundant	•
abundance of fizzed grains	2	•	•	•	•	•
size of fizzed grains	1	•	•	•	•	•
OTHER FEATURES						
abundance of melt pockets	2	•	rare	•	•	•
size of melt droplets	1	•	<2	•	•	•
composition of melt droplets		•	troilite	•	•	•
abundance of melt veins	6	•	•	•	•	•
composition of melt veins		•	•	•	•	•

meteorite petrologic type shock stage	notes	Jhung L5 S3	GRO85209 L6 S3	ALHA76003 L6 S3	Khohar L4 S4	Long Island L6 S4
KAMACITE						
size range	1	1000-5	400-10	1000-10	300-1	1600-10
Neumann bands	2	•	•	•	common	•
polycrystalline	2	abundant	•	rare	abundant	•
polycrystalline (polygonized)	3	rare	•	•	•	•
TAENITE						
size range	1	50-20	100-50	300-30	50-1	60-10
zonation	4	most homogen.	normal	normal	most homogen.	homogenous
plessite abundance	2	abundant	rare	common	abundant	•
plessite grain size	1	25-5	10	10-5	5-1	•
cloudy taenite abundance	2	rare	abundant	abundant	rare	•
tetrataenite rims/grains	2	rare	abundant	abundant	rare	•
TROILITE						
size range	1	500-5	200-10	500-5	500-<1	300-10
polycrystalline	2	abundant	•	•	abundant	abundant
parallel fractures/shearing	5	fractured	•	slight shear	•	fractured
abundance of twinned grains	2	•	•	•	•	•
abundance of fizzed grains	2	•	•		abundant	•
size of fizzed grains	1	•	•	•	500-100	•
OTHER FEATURES						
abundance of melt pockets	2	•	•	•	•	rare
size of melt droplets	1	•	•	•	•	<3.5
composition of melt droplets		•	•	•	•	troilite-metal
abundance of melt veins	6	•	•	•	abundant	•
composition of melt veins		•	•	•	troilite-metal	•

meteorite petrologic type shock stage	notes	Tenham L6 S4	Fisher L6 S5	Kyushu L6 S5	Kingfisher L5 S6	McKinney L4 S6
KAMACITE						
size range	1	600-10	400-2	1100-10	650-20	300-20
Neumann bands	2	•	•	•	•	•
polycrystalline	2	•	•	•	•	•
polycrystalline (polygonized)	3	•	abundant	abundant	abundant	abundant
TAENITE						
size range	1	500-20	40-10	80-10	60-30	50-10
zonation	4	normal	homogeneous	homogeneous	homogenous	normal
plessite abundance	2	abundant	rare	•	abundant	•
plessite grain size	1	10-1	10-5	•	30-20	•
cloudy taenite abundance	2	rare	•	•	•	abundant
tetrataenite rims/grains	2	abundant	•	•	•	abundant
TROILITE						
size range	1	650-15	750-20	400-10	200-10	250-<1
polycrystalline	2	abundant	abundant	abundant	rare	abundant
parallel fractures/shearing	5	•	strong shear	fractures	strong shear	strong shear
abundance of twinned grains	2	•	•	•	•	•
abundance of fizzed grains	2	•	rare	rare	•	abundant
size of fizzed grains	1	•	200	150	•	300-20
OTHER FEATURES						
abundance of melt pockets	2	rare	common	common	•	abundant
size of melt droplets	1	<5	<20	<10	•	<50
composition of melt droplets		troilite-metal	troilite-metal	troilite-metal	•	metal-troilite
abundance of melt veins	6	rare	rare	rare	abundant	abundant
composition of melt veins		troilite,silicate	troilite,silicate	troilite,silicate	troilite,silicate	met,troil,silicate

Appendix D: Procedure Used for Calculating the Lower Limit of Detection of an Element

The lower limit of detection (LLD) for an element is obtained from electron microprobe analyses. A plot is made of weight percent of the element of interest versus the peak counting rate (see Figure A-1 below). The peak counting rate is given as total counts (peak + background) in counts per second (cps). A standard linear regression line is obtained for the data and the slope and y-intercept of this regression line is used in the calculation of the LLD. Data for this plot should be limited to analyses that contain <0.5 wt % of the element of interest. In this range peak counts should be proportional to element wt. % (Henry's Law behavior), as seen by a high correlation coefficient (>0.9) of the regression line.

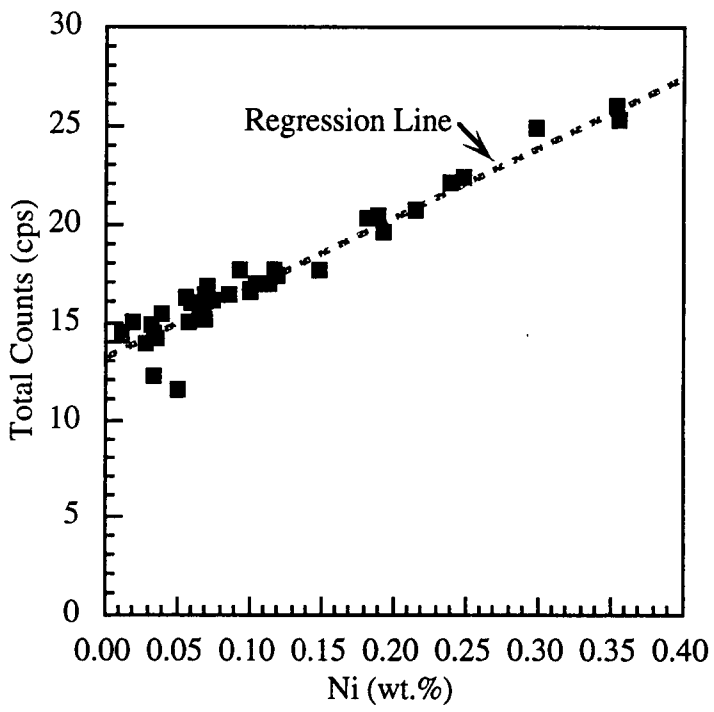

Figure 40. Plot of Ni vs. Total Counts for 38 high-quality electron microprobe analyses of troilite grains in several different L chondrites.

The slope and y-intercept of the regression line is applied to the following equation to calculate the LLD:

$$LLD = \left(\frac{\varphi\sqrt{2}}{m}\right)\sqrt{\frac{b}{c}}$$

where LLD = lower limit of detection (in wt.%)

φ = confidence interval

$\varphi = 3$ yields 3σ of confidence (99%)

$\varphi = 2$ yields 2σ of confidence (95%)

$\varphi = 1$ yields 1σ of confidence (65%)

m = slope of the regression line (in the regression form: $y = mx + b$)

b = y-intercept of the regression line

c = counting time (in seconds) for the element of interest.

LLD's for minor elements are presented in the following table. All microprobe analyses throughout this work employ 2σ values when used with thermometry calculations or when presented in a tabular form.

Appendix D: (continued)

element in phase	# of data points	'm' for calibration	'b' for calibration	correlation coefficient	count time (secs)	LLD 3 sigma (99%)	LLD 2 sigma (95%)
Ni in Troilite	38	31.5	13.6	0.88	80	0.06	0.04
S in Metal	38	87.8	5.42	0.53	20	0.03	0.02
P in Metal	63	25.1	5.45	0.58	80	0.04	0.03
Co in Metal	35	43.8	19.6	0.92	20	0.10	0.06
Mn in Spinel	29	52.8	15.9	0.99	20	0.07	0.05
Ni in Spinel	19	31.4	18.8	0.61	20	0.13	0.09
V in Spinel	29	36.1	6.65	0.93	20	0.07	0.05
Zn in Spinel	29	36.9	22.5	0.96	20	0.12	0.08
Ca in Spinel	27	190.6	19.7	0.98	20	0.02	0.01
Ti in Cpx	21	199.0	31.1	0.96	20	0.03	0.02
Al in Cpx	21	466.9	32.7	1.00	20	0.01	0.01
Cr in Cpx	21	45.0	5.02	0.99	20	0.05	0.03
Mn in Cpx	21	33.4	9.22	0.85	20	0.09	0.06
Na in Cpx	21	188.4	16.7	1.00	20	0.02	0.01
Ca in Opx	22	202.6	15.8	1.00	20	0.02	0.01
Ti in Opx	22	188.8	29.7	0.97	20	0.03	0.02
Cr in Opx	22	46.8	4.53	0.97	20	0.04	0.03
Na in Opx	22	129.7	13.5	0.89	20	0.03	0.02
Mn in Opx	22	43.6	8.65	0.94	20	0.06	0.04
Al in Opx	22	379.0	33.1	0.98	20	0.01	0.01

Appendix E: Paired Mineral Analyses Used in Thermometry

The following tables present paired mineral analyses used in the calculation of blocking temperatures for the three cation-exchange thermometers described in this study. Notations used in the tables are as follows:

- n.d. = oxides not determined
- number in () in 'Points' heading denotes the number of analyses used to calculate average compositions
- number in () adjacent to oxide values indicates standard deviation in terms of least units cited for replicate analyses
- Fe_2O_3 in chromite was calculated based on stoichiometry
- Total Fe in silicates was calculated as FeO

Meteorite Type/Shock Mineral Point	Ausson L5, S2 chromite SP1	Ausson L5, S2 olivine OL1	Ausson L5, S2 chromite SP2	Ausson L5, S2 olivine OL2	Ausson L5, S2 chromite SP3	Ausson L5, S2 olivine OL3	Ausson L5, S2 chromite SP5	Ausson L5, S2 olivine OL5a	Ausson L5, S2 olivine OL5b
SiO_2	0.00	38.6	<0.03	38.9	0.06	39.4	0.06	38.4	38.5
TiO_2	2.06	n.d.	1.52	n.d.	2.19	n.d.	1.75	n.d.	n.d.
Fe_2O_3	0.00	n.d.	0.00	n.d.	0.00	n.d.	0.00	n.d.	n.d.
Al_2O_3	5.89	0.00	6.66	0.00	6.67	0.00	6.48	0.00	0.01
V_2O_3	0.75	n.d.	0.73	n.d.	0.72	n.d.	0.74	n.d.	n.d.
Cr_2O_3	57.5	0.12	57.6	0.00	57.2	0.03	57.4	0.04	0.12
MgO	2.72	42.7	2.59	43.0	2.40	42.9	3.01	43.4	42.7
CaO	0.04	0.02	0.08	0.03	0.06	0.04	0.06	0.04	0.04
MnO	0.87	0.44	0.91	0.50	0.99	0.48	0.82	0.43	0.47
FeO	28.9	16.7	28.8	16.7	28.3	16.9	28.2	16.6	17.0
NiO	0.00	0.00	0.00	0.00	0.00	0.00	<0.04	0.00	<0.04
ZnO	0.20	n.d.	0.18	n.d.	0.17	n.d.	0.17	n.d.	n.d.
Total	98.88	98.58	99.05	99.04	98.73	99.72	98.61	98.86	98.88
# of Oxygens	4	4	4	4	4	4	4	4	4
Si	0.000	0.994	0.000	0.996	0.002	1.001	0.002	0.987	0.991
Ti	0.056	-------	0.041	-------	0.059	-------	0.047	-------	-------
Fe^{3+}	0.000	-------	0.000	-------	0.000	-------	0.000	-------	-------
Al	0.249	0.000	0.280	0.000	0.280	0.000	0.273	0.000	0.000
V	0.022	-------	0.021	-------	0.021	-------	0.021	-------	-------
Cr	1.628	0.002	1.622	0.000	1.612	0.001	1.619	0.001	0.002
Mg	0.145	1.638	0.137	1.641	0.128	1.627	0.160	1.659	1.636
Ca	0.002	0.000	0.003	0.001	0.002	0.001	0.002	0.001	0.001
Mn	0.027	0.010	0.028	0.011	0.030	0.010	0.025	0.009	0.010
Fe^{2+}	0.864	0.359	0.860	0.356	0.845	0.359	0.840	0.355	0.367
Ni	0.000	0.000	0.000	0.000	0.000	0.000	0.001	0.000	0.000
Zn	0.005	-------	0.005	-------	0.004	-------	0.005	-------	-------
Total	2.996	3.003	2.997	3.005	2.983	2.999	2.995	3.012	3.007
mg#	14.4	82.0	13.8	82.2	13.1	81.9	16.0	82.4	81.7
cr#	86.7	-------	85.3	-------	85.2	-------	85.6	-------	-------
Fo	-------	81.6	-------	81.7	-------	81.5	-------	82.0	81.3
Fa	-------	18.4	-------	18.3	-------	18.5	-------	18.0	18.7

Meteorite	Ausson	Bjurböle	Bjurböle	Bjurböle	Bjurböle	Bjurböle	Bjurböle	Bjurböle	Bjurböle
Type/Shock	L5, S2	L4, S1	L4, S1	L4, S1	L4, S1	L4, S1	L4, S1	L4, S1	L4, S1
Mineral	olivine	chromite	olivine	chromite	olivine	chromite	olivine	chromite	olivine
Point	OL5c	SP1	OL1	SP2	OL2	SP3	OL3	SP4	OL4
SiO_2	38.9	0.00	38.3	0.00	37.9	<0.03	38.5	0.00	37.8
TiO_2	n.d.	1.57	n.d.	2.10	n.d.	1.60	n.d.	1.57	n.d.
Fe_2O_3	n.d.	0.21	n.d.	0.00	n.d.	0.77	n.d.	0.21	n.d.
Al_2O_3	0.01	5.25	0.07	5.28	0.04	5.47	0.00	5.25	0.02
V_2O_3	n.d.	0.67	n.d.	0.69	n.d.	0.68	n.d.	0.67	n.d.
Cr_2O_3	<0.03	58.1	0.06	58.3	0.18	57.4	0.62	58.1	0.22
MgO	42.9	1.86	37.8	1.90	37.5	1.72	38.3	1.86	37.8
CaO	0.03	0.10	0.06	0.03	<0.02	0.02	<0.02	0.10	0.06
MnO	0.44	0.62	0.47	0.59	0.45	0.62	0.49	0.62	0.48
FeO	16.9	29.9	23.3	30.9	23.6	30.1	23.2	29.9	23.2
NiO	0.00	0.00	0.00	0.05	<0.04	0.40	0.07	0.00	<0.04
ZnO	n.d.	0.43	n.d.	0.36	n.d.	0.43	n.d.	0.43	n.d.
Total	99.13	98.73	99.96	100.20	99.66	99.12	101.25	98.73	99.53
# of Oxygens	4	4	4	4	4	4	4	4	4
Si	0.997	0.000	1.001	0.000	0.997	0.000	0.995	0.000	0.993
Ti	-------	0.043	-------	0.056	-------	0.044	-------	0.043	-------
Fe^{3+}	-------	0.006	-------	0.000	-------	0.021	-------	0.006	-------
Al	0.000	0.224	0.002	0.222	0.001	0.233	0.000	0.224	0.001
V	-------	0.020	-------	0.020	-------	0.020	-------	0.020	-------
Cr	0.000	1.665	0.001	1.646	0.004	1.638	0.013	1.665	0.005
Mg	1.635	0.101	1.473	0.101	1.469	0.093	1.477	0.101	1.482
Ca	0.001	0.004	0.002	0.001	0.000	0.001	0.000	0.004	0.002
Mn	0.009	0.019	0.010	0.018	0.010	0.019	0.011	0.019	0.011
Fe^{2+}	0.361	0.908	0.508	0.924	0.519	0.908	0.502	0.908	0.510
Ni	0.000	0.000	0.000	0.000	0.000	0.012	0.001	0.000	0.001
Zn	-------	0.012	-------	0.009	-------	0.012	-------	0.012	-------
Total	3.003	3.000	2.997	2.998	3.000	3.000	2.999	3.000	3.005
mg#	81.9	10.0	74.3	9.9	73.9	9.3	74.6	10.0	74.4
cr#	-------	88.1	-------	88.1	-------	87.5	-------	88.1	-------
Fo	81.5	-------	74.0	-------	73.5	-------	74.2	-------	74.0
Fa	18.5	-------	26.0	-------	26.5	-------	25.8	-------	26.0

Meteorite	Bjurböle	Bjurböle	Bjurböle	Bjurböle	Bjurböle	Hallingeberg	Hallingeberg	Hallingeberg	Hallingeberg
Type/Shock	L4, S1	L4, S1	L4, S1	L4, S1	L4, S1	L3, S3	L3, S3	L3, S3	L3, S3
Mineral	chromite	olivine	chromite	olivine	olivine	chromite	olivine	chromite	olivine
Point	SP5	OL5	SP7	OL7a	OL7b	SP2	OL2	SP3	OL3
SiO_2	0.06	37.9	<0.03	38.4	38.2	0.25	36.4	0.21	36.6
TiO_2	1.96	n.d.	1.75	n.d.	n.d.	1.73	n.d.	1.44	n.d.
Fe_2O_3	0.27	n.d.	0.05	n.d.	n.d.	1.03	n.d.	0.28	n.d.
Al_2O_3	5.50	0.00	5.62	0.00	0.01	4.79	0.01	2.01	0.02
V_2O_3	0.64	n.d.	0.68	n.d.	n.d.	0.77	n.d.	0.72	n.d.
Cr_2O_3	57.2	0.03	57.7	0.04	0.03	56.4	0.09	61.2	0.09
MgO	1.88	37.6	1.76	38.0	38.0	1.49	33.5	1.31	33.7
CaO	0.04	0.04	0.05	0.03	<0.02	0.12	0.04	0.17	0.06
MnO	0.65	0.45	0.58	0.46	0.46	0.51	0.48	0.62	0.47
FeO	30.6	24.0	30.6	23.8	23.8	30.9	28.4	30.4	27.9
NiO	0.00	0.00	0.00	0.00	<0.04	<0.04	<0.04	0.00	0.00
ZnO	0.41	n.d.	0.40	n.d.	n.d.	0.42	n.d.	0.37	n.d.
Total	99.12	99.98	99.19	100.60	100.47	98.37	99.02	98.74	98.81
# of Oxygens	4	4	4	4	4	4	4	4	4
Si	0.002	0.995	0.001	0.999	0.996	0.009	0.990	0.008	0.994
Ti	0.053	-------	0.048	-------	-------	0.048	-------	0.040	-------
Fe^{3+}	0.007	-------	0.001	-------	-------	0.028	-------	0.008	-------
Al	0.234	0.000	0.239	0.000	0.000	0.206	0.000	0.088	0.001
V	0.019	-------	0.020	-------	-------	0.023	-------	0.021	-------
Cr	1.630	0.001	1.644	0.001	0.001	1.630	0.002	1.787	0.002
Mg	0.101	1.472	0.095	1.474	1.478	0.081	1.358	0.072	1.363
Ca	0.001	0.001	0.002	0.001	0.000	0.005	0.001	0.007	0.002
Mn	0.020	0.010	0.018	0.010	0.010	0.016	0.011	0.019	0.011
Fe^{2+}	0.922	0.526	0.923	0.517	0.518	0.943	0.646	0.940	0.633
Ni	0.000	0.000	0.000	0.000	0.001	0.000	0.000	0.000	0.000
Zn	0.011	-------	0.011	-------	-------	0.011	-------	0.010	-------
Total	3.000	3.005	3.000	3.002	3.004	3.000	3.008	3.000	3.006
mg#	9.9	73.7	9.3	74.0	74.0	7.9	67.8	7.1	68.3
cr#	87.5	-------	87.3	-------	-------	88.8	-------	95.3	-------
Fo	-------	73.3	-------	73.7	73.7	-------	67.4	-------	67.9
Fa	-------	26.7	-------	26.3	26.3	-------	32.6	-------	32.1

Meteorite	Hallingeberg	Hallingeberg	Hallingeberg	Hallingeberg	Kingfisher	Kingfisher	Kingfisher	Kingfisher	Kingfisher
Type/Shock	L3, S3	L3, S3	L3, S3	L3, S3	L5, S6	L5, S6	L5, S6	L5, S6	L5, S6
Mineral	chromite	olivine	chromite	olivine	chromite	olivine	chromite	olivine	chromite
Point	SP4	OL4	SP5	OL5	SP1	OL1	SP2	OL2	SP3
SiO_2	0.20	36.9	0.20	36.2	<0.03	38.3	0.00	38.4	0.03
TiO_2	0.87	n.d.	1.03	n.d.	2.91	n.d.	2.98	n.d.	2.55
Fe_2O_3	1.17	n.d.	0.45	n.d.	0.00	n.d.	0.00	n.d.	<0.04
Al_2O_3	5.84	0.01	6.00	0.00	5.20	0.00	5.23	0.00	4.74
V_2O_3	0.63	n.d.	0.67	n.d.	0.63	n.d.	0.61	n.d.	0.74
Cr_2O_3	57.0	0.06	57.0	0.08	56.5	0.00	56.7	0.07	57.1
MgO	1.57	34.3	1.62	33.6	3.10	39.0	3.04	39.6	2.45
CaO	0.13	0.07	0.11	0.06	0.00	0.08	0.08	0.04	0.06
MnO	0.49	0.48	0.43	0.44	0.59	0.44	0.55	0.41	0.61
FeO	30.1	27.1	30.1	28.1	29.2	21.1	29.1	20.6	30.0
NiO	0.00	0.00	<0.04	0.00	<0.04	<0.04	0.05	<0.04	0.00
ZnO	0.43	n.d.	0.48	n.d.	0.39	n.d.	0.39	n.d.	0.36
Total	98.43	98.86	98.14	98.49	98.58	98.94	98.78	99.13	98.65
# of Oxygens	4	4	4	4	4	4	4	4	4
Si	0.007	0.997	0.008	0.988	0.001	1.002	0.000	1.000	0.001
Ti	0.024	-------	0.028	-------	0.079	-------	0.080	-------	0.070
Fe^{3+}	0.032	-------	0.012	-------	0.000	-------	0.000	-------	0.000
Al	0.250	0.000	0.257	0.000	0.220	0.000	0.221	0.000	0.202
V	0.018	-------	0.019	-------	0.018	-------	0.018	-------	0.022
Cr	1.637	0.001	1.640	0.002	1.606	0.000	1.609	0.001	1.635
Mg	0.085	1.380	0.088	1.368	0.166	1.520	0.163	1.537	0.132
Ca	0.005	0.002	0.004	0.002	0.000	0.002	0.003	0.001	0.002
Mn	0.015	0.011	0.013	0.010	0.018	0.010	0.017	0.009	0.019
Fe^{2+}	0.914	0.611	0.917	0.641	0.879	0.462	0.874	0.449	0.908
Ni	0.000	0.000	0.000	0.000	0.001	0.000	0.000	0.001	0.000
Zn	0.012	-------	0.013	-------	0.011	-------	0.010	-------	0.010
Total	3.000	3.002	3.000	3.011	2.999	2.996	2.994	2.998	3.000
mg#	8.5	69.3	8.8	68.1	15.9	76.7	15.7	77.4	12.7
cr#	86.7	-------	86.4	-------	87.9	-------	87.9	-------	89.0
Fo	-------	68.9	-------	67.8	-------	76.3	-------	77.0	-------
Fa	-------	31.1	-------	32.2	-------	23.7	-------	23.0	-------

Meteorite Type/Shock Mineral Point	Kingfisher L5, S6 olivine OL3	Kingfisher L5, S6 chromite SP4	Kingfisher L5, S6 olivine OL4	Kingfisher L5, S6 chromite SP6	Kingfisher L5, S6 olivine OL6a	Kingfisher L5, S6 olivine OL6b	Kingfisher L5, S6 olivine OL6c	Kyushu L6, S5 chromite SP1	Kyushu L6, S5 olivine OL1a
SiO_2	38.6	<0.03	38.4	0.00	38.3	38.4	37.6	0.31	38.2
TiO_2	n.d.	2.73	n.d.	2.37	n.d.	n.d.	n.d.	1.90	n.d.
Fe_2O_3	n.d.	0.00	n.d.	0.00	n.d.	n.d.	n.d.	0.00	n.d.
Al_2O_3	0.01	5.07	0.01	4.86	0.05	0.03	0.03	9.22	0.00
V_2O_3	n.d.	0.70	n.d.	0.71	n.d.	n.d.	n.d.	0.74	n.d.
Cr_2O_3	0.08	57.0	<0.03	57.9	0.11	0.23	0.03	55.0	0.04
MgO	39.9	2.99	38.8	2.71	38.2	39.2	37.8	2.28	38.8
CaO	0.06	0.07	0.05	0.08	0.07	0.04	0.06	0.05	0.22
MnO	0.48	0.53	0.44	0.57	0.43	0.43	0.47	0.63	0.42
FeO	20.6	29.5	21.5	29.1	22.4	21.3	23.1	29.0	22.6
NiO	<0.04	<0.04	<0.04	0.00	0.30	0.06	0.16	0.00	<0.04
ZnO	n.d.	0.40	n.d.	0.41	n.d.	n.d.	n.d.	0.35	n.d.
Total	99.68	98.94	99.19	98.78	99.80	99.77	99.17	99.47	100.22
# of Oxygens	4	4	4	4	4	4	4	4	4
Si	0.999	0.000	1.003	0.000	1.000	0.998	0.993	0.011	0.993
Ti	-------	0.074	-------	0.064	-------	-------	-------	0.050	-------
Fe^{3+}	-------	0.000	-------	0.000	-------	-------	-------	0.000	-------
Al	0.000	0.214	0.000	0.206	0.002	0.001	0.001	0.380	0.000
V	-------	0.020	-------	0.020	-------	-------	-------	0.021	-------
Cr	0.002	1.618	0.000	1.651	0.002	0.005	0.001	1.521	0.001
Mg	1.540	0.160	1.513	0.146	1.488	1.520	1.486	0.119	1.505
Ca	0.002	0.003	0.001	0.003	0.002	0.001	0.002	0.002	0.006
Mn	0.011	0.016	0.010	0.017	0.009	0.009	0.011	0.019	0.009
Fe^{2+}	0.447	0.884	0.469	0.878	0.489	0.464	0.510	0.847	0.492
Ni	0.000	0.001	0.001	0.000	0.006	0.001	0.003	0.000	0.000
Zn	-------	0.011	-------	0.011	-------	-------	-------	0.009	-------
Total	3.001	3.000	2.997	2.997	2.998	2.999	3.007	2.978	3.006
mg#	77.5	15.3	76.3	14.2	75.3	76.6	74.5	12.3	75.4
cr#	-------	88.3	-------	88.9	-------	-------	-------	80.0	-------
Fo	77.1	-------	76.0	-------	74.9	76.3	74.0	-------	75.0
Fa	22.9	-------	24.0	-------	25.1	23.7	26.0	-------	25.0

Meteorite Type/Shock Mineral Point	Kyushu L6, S5 olivine OL1b	Kyushu L6, S5 chromite SP2	Kyushu L6, S5 olivine OL2	Kyushu L6, S5 chromite SP3	Kyushu L6, S5 olivine OL3	Kyushu L6, S5 chromite SP4	Kyushu L6, S5 olivine OL4	Kyushu L6, S5 chromite SP8	Kyushu L6, S5 olivine OL8
SiO_2	37.6	0.12	37.9	0.00	38.4	0.05	37.7	<0.03	38.0
TiO_2	n.d.	2.91	n.d.	2.03	n.d.	2.56	n.d.	2.12	n.d.
Fe_2O_3	n.d.	<0.04	n.d.	0.05	n.d.	0.00	n.d.	0.00	n.d.
Al_2O_3	0.00	5.57	0.00	6.10	0.01	6.09	0.02	6.02	0.00
V_2O_3	n.d.	0.70	n.d.	0.82	n.d.	0.67	n.d.	0.71	n.d.
Cr_2O_3	0.04	56.2	0.03	57.4	0.00	56.1	0.35	57.1	0.05
MgO	38.8	2.83	39.4	2.35	39.1	2.31	38.9	2.33	38.6
CaO	0.02	<0.02	0.05	0.00	0.03	0.07	0.02	0.07	0.06
MnO	0.49	0.68	0.48	0.54	0.43	0.63	0.44	0.58	0.49
FeO	22.9	30.3	22.1	30.4	22.4	30.5	22.0	29.8	22.8
NiO	0.00	0.00	<0.04	<0.04	0.00	0.05	<0.04	0.04	0.08
ZnO	n.d.	0.39	n.d.	0.38	n.d.	0.41	n.d.	0.38	n.d.
Total	99.92	99.73	99.86	100.10	100.30	99.46	99.42	99.20	100.01
# of Oxygens	4	4	4	4	4	4	4	4	4
Si	0.985	0.004	0.987	0.000	0.995	0.002	0.987	0.000	0.991
Ti	-------	0.078	-------	0.054	-------	0.069	-------	0.057	-------
Fe^{3+}	-------	0.001	-------	0.001	-------	0.000	-------	0.000	-------
Al	0.000	0.233	0.000	0.255	0.000	0.256	0.001	0.254	0.000
V	-------	0.020	-------	0.023	-------	0.019	-------	0.020	-------
Cr	0.001	1.581	0.001	1.612	0.000	1.585	0.007	1.617	0.001
Mg	1.515	0.150	1.531	0.125	1.512	0.123	1.519	0.125	1.503
Ca	0.001	0.001	0.001	0.000	0.001	0.003	0.001	0.003	0.002
Mn	0.011	0.021	0.011	0.016	0.009	0.019	0.010	0.018	0.011
Fe^{2+}	0.502	0.901	0.481	0.903	0.486	0.912	0.483	0.893	0.498
Ni	0.000	0.000	0.000	0.001	0.000	0.000	0.000	0.000	0.002
Zn	-------	0.010	-------	0.010	-------	0.011	-------	0.010	-------
Total	3.015	3.000	3.012	3.000	3.003	2.998	3.008	2.996	3.008
mg#	75.1	14.3	76.1	12.1	75.7	11.9	75.9	12.2	75.1
cr#	-------	87.1	-------	86.3	-------	86.1	-------	86.4	-------
Fo	74.7	-------	75.7	-------	75.3	-------	75.5	-------	74.7
Fa	25.3	-------	24.3	-------	24.7	-------	24.5	-------	25.3

Meteorite Type/Shock Mineral Point	McKinney L4, S6 chromite SP1	McKinney L4, S6 olivine OL1	McKinney L4, S6 chromite SP3	McKinney L4, S6 olivine OL3	McKinney L4, S6 chromite SP4	McKinney L4, S6 olivine OL4	McKinney L4, S6 chromite SP5	McKinney L4, S6 olivine OL5	Shaw Host L7, brec chromite SP1
SiO_2	0.34	37.4	0.00	37.7	0.00	38.0	0.00	37.1	0.03
TiO_2	2.14	n.d.	2.13	n.d.	2.13	n.d.	2.09	n.d.	4.63
Fe_2O_3	0.00	n.d.	0.00	n.d.	0.00	n.d.	0.00	n.d.	0.00
Al_2O_3	4.61	0.01	4.61	0.02	4.61	0.01	4.60	0.01	5.22
V_2O_3	0.71	n.d.	0.80	n.d.	0.74	n.d.	0.71	n.d.	0.72
Cr_2O_3	58.7	0.41	59.6	0.44	59.2	0.08	58.8	0.14	56.1
MgO	2.51	38.5	2.21	38.0	2.29	38.7	2.12	38.2	3.71
CaO	0.23	0.05	0.02	0.05	0.03	0.06	0.02	0.03	<0.02
MnO	0.60	0.38	0.65	0.46	0.63	0.40	0.50	0.48	0.66
FeO	29.4	22.1	29.8	23.1	29.9	22.5	29.7	22.5	29.7
NiO	0.00	0.00	0.05	0.00	0.00	0.00	<0.04	0.05	0.05
ZnO	0.32	n.d.	0.48	n.d.	0.39	n.d.	0.44	n.d.	0.12
Total	99.59	98.87	100.27	99.75	99.82	99.75	98.97	98.51	100.93
# of Oxygens	4	4	4	4	4	4	4	4	4
Si	0.012	0.988	0.000	0.990	0.000	0.993	0.000	0.985	0.001
Ti	0.058	-------	0.057	-------	0.057	-------	0.057	-------	0.122
Fe^{3+}	0.000	-------	0.000	-------	0.000	-------	0.000	-------	0.000
Al	0.194	0.000	0.194	0.001	0.195	0.000	0.196	0.000	0.214
V	0.020	-------	0.023	-------	0.021	-------	0.021	-------	0.020
Cr	1.660	0.009	1.680	0.009	1.676	0.002	1.681	0.003	1.545
Mg	0.134	1.514	0.118	1.487	0.123	1.509	0.114	1.512	0.193
Ca	0.009	0.001	0.001	0.002	0.001	0.002	0.001	0.001	0.001
Mn	0.018	0.008	0.020	0.010	0.019	0.009	0.015	0.011	0.020
Fe^{2+}	0.880	0.487	0.888	0.507	0.895	0.491	0.897	0.501	0.867
Ni	0.000	0.000	0.000	0.000	0.000	0.000	0.000	0.001	0.000
Zn	0.009	-------	0.013	-------	0.010	-------	0.012	-------	0.003
Total	2.994	3.007	2.993	3.006	2.997	3.006	2.994	3.014	2.986
mg#	13.2	75.7	11.7	74.6	12.0	75.4	11.3	75.1	18.2
cr#	89.5	-------	89.7	-------	89.6	-------	89.6	-------	87.8
Fo	-------	75.4	-------	74.2	-------	75.1	-------	74.7	-------
Fa	-------	24.6	-------	25.8	-------	24.9	-------	25.3	-------

Meteorite Type/Shock	Shaw Host L7, brec	Shaw Host L7, brec	Shaw Host L7, brec	Shaw Dike melt rock	Shaw Dike melt rock	Shaw Dike melt rock	Shaw Dike melt rock	Shaw Dike melt rock	Shaw Dike melt rock
Mineral	olivine	chromite	olivine	chromite	olivine	chromite	olivine	chromite	olivine
Point	OL1	SP2	OL2	SP1	OL1	SP2	OL2	SP3	OL3
SiO_2	38.4	0.04	38.6	0.07	38.4	0.05	38.3	0.07	38.1
TiO_2	n.d.	2.98	n.d.	3.09	n.d.	2.52	n.d.	1.10	n.d.
Fe_2O_3	n.d.	0.00	n.d.	0.00	n.d.	0.00	n.d.	0.00	n.d.
Al_2O_3	0.00	7.66	0.00	6.82	0.01	7.68	0.00	7.66	0.01
V_2O_3	n.d.	0.58	n.d.	0.53	n.d.	0.41	n.d.	0.46	n.d.
Cr_2O_3	0.22	55.4	0.04	55.0	0.07	57.7	0.08	59.7	0.14
MgO	39.8	4.11	39.6	3.96	39.7	4.59	39.7	4.73	39.6
CaO	0.04	0.00	0.05	0.09	0.03	0.02	0.06	0.03	0.03
MnO	0.46	0.64	0.41	0.52	0.44	0.68	0.47	0.49	0.48
FeO	21.5	28.5	21.3	28.9	21.3	27.1	21.0	26.0	21.5
NiO	0.00	0.14	<0.04	<0.04	0.04	<0.04	<0.04	<0.04	<0.04
ZnO	n.d.	0.18	n.d.	0.12	n.d.	0.13	n.d.	0.12	n.d.
Total	100.41	100.20	99.95	99.02	99.92	100.90	99.68	100.32	99.93
# of Oxygens	4	4	4	4	4	4	4	4	4
Si	0.991	0.002	0.999	0.002	0.995	0.002	0.995	0.002	0.990
Ti	-------	0.078	-------	0.082	-------	0.065	-------	0.029	-------
Fe^{3+}	-------	0.000	-------	0.000	-------	0.000	-------	0.000	-------
Al	0.000	0.313	0.000	0.284	0.000	0.310	0.000	0.311	0.000
V	-------	0.016	-------	0.015	-------	0.011	-------	0.013	-------
Cr	0.004	1.520	0.001	1.534	0.001	1.565	0.002	1.627	0.003
Mg	1.533	0.213	1.529	0.208	1.535	0.235	1.538	0.243	1.536
Ca	0.001	0.000	0.001	0.003	0.001	0.001	0.002	0.001	0.001
Mn	0.010	0.019	0.009	0.016	0.010	0.020	0.010	0.014	0.011
Fe^{2+}	0.466	0.827	0.461	0.852	0.462	0.778	0.457	0.750	0.468
Ni	0.000	0.004	0.000	0.001	0.001	0.000	0.000	0.000	0.000
Zn	-------	0.005	-------	0.003	-------	0.003	-------	0.003	-------
Total	3.005	2.996	3.000	3.000	3.005	2.990	3.004	2.993	3.009
mg#	76.7	20.5	76.8	19.6	76.8	23.2	77.1	24.5	76.6
cr#	-------	82.9	-------	84.4	-------	83.5	-------	83.9	-------
Fo	76.3	-------	76.5	-------	76.5	-------	76.7	-------	76.2
Fa	23.7	-------	23.5	-------	23.5	-------	23.3	-------	23.8

Meteorite Type/Shock Mineral Point	Shaw Dike melt rock chromite SP4	Shaw Dike melt rock olivine OL4	Shaw Dike melt rock chromite SP5	Shaw Dike melt rock olivine OL5	PAT91501 melt rock chromite SP1	PAT91501 melt rock chromite SP2	PAT91501 melt rock chromite SP3	PAT91501 melt rock chromite SP4	PAT91501 melt rock olivine OL (14)
SiO_2	0.12	38.1	0.10	38.3	n.d.	n.d.	n.d.	n.d.	37.7 (1)
TiO_2	2.95	n.d.	1.85	n.d.	1.15	1.83	0.86	3.58	n.d.
Fe_2O_3	0.00	n.d.	0.00	n.d.	0.00	0.00	0.00	0.00	n.d.
Al_2O_3	9.28	0.01	8.23	0.00	7.57	11.09	6.27	7.78	0.02 (0)
V_2O_3	0.38	n.d.	0.46	n.d.	0.51	0.35	0.60	0.42	n.d.
Cr_2O_3	53.4	0.07	57.5	0.36	58.9	54.8	60.6	52.3	0.06 (1)
MgO	4.60	39.1	4.98	40.2	5.57	6.66	5.37	5.50	36.5 (2)
CaO	0.04	0.06	0.07	0.05	n.d.	n.d.	n.d.	n.d.	0.11 (2)
MnO	0.49	0.52	0.51	0.43	0.34	0.35	0.39	0.36	0.44 (2)
FeO	28.5	22.1	26.5	20.9	24.8	24.5	24.3	26.6	24.3 (2)
NiO	0.00	<0.04	0.04	0.04	n.d.	n.d.	n.d.	n.d.	<0.04 (0)
ZnO	0.09	n.d.	0.16	n.d.	n.d.	n.d.	n.d.	n.d.	n.d.
Total	99.83	99.92	100.35	100.26	98.79	99.50	98.35	96.50	99.10
# of Oxygens	4	4	4	4	4	4	4	4	4
Si	0.004	0.992	0.003	0.990	-------	-------	-------	-------	1.000
Ti	0.077	-------	0.048	-------	0.030	0.047	0.023	0.096	-------
Fe^{3+}	0.000	-------	0.000	-------	0.000	0.000	0.000	0.000	-------
Al	0.377	0.000	0.333	0.000	0.311	0.442	0.260	0.326	0.001
V	0.011	-------	0.013	-------	0.014	0.010	0.017	0.012	-------
Cr	1.455	0.001	1.560	0.007	1.621	1.463	1.687	1.471	0.001
Mg	0.236	1.519	0.255	1.546	0.289	0.335	0.282	0.292	1.445
Ca	0.001	0.002	0.003	0.001	-------	-------	-------	-------	0.003
Mn	0.014	0.012	0.015	0.009	0.010	0.010	0.012	0.011	0.010
Fe^{2+}	0.820	0.482	0.761	0.451	0.722	0.691	0.715	0.792	0.539
Ni	0.000	0.000	0.000	0.001	-------	-------	-------	-------	0.000
Zn	0.002	-------	0.004	-------	-------	-------	-------	-------	-------
Total	2.998	3.008	2.995	3.005	2.997	2.997	2.995	3.000	2.999
mg#	22.4	75.9	25.1	77.4	28.6	32.7	28.3	26.9	72.8
cr#	79.4	-------	82.4	-------	83.9	76.8	86.6	81.8	-------
Fo	-------	75.5	-------	77.1	-------	-------	-------	-------	72.5
Fa	-------	24.5	-------	22.9	-------	-------	-------	-------	27.5

Meteorite	Y75097	Y75097	Y75097	Y75097	Y793241	Y793241	Y793241	Y793241	Y793241
Type/Shock	breccia	breccia	breccia	breccia	breccia	breccia	breccia	breccia	breccia
Mineral	chromite	chromite	chromite	olivine	chromite	chromite	chromite	chromite	chromite
Point	SP1	SP2	SP3	OL (17)	SP1	SP2	SP3	SP4	SP5
SiO_2	n.d.	n.d.	n.d.	37.8 (6)	n.d.	n.d.	n.d.	n.d.	n.d.
TiO_2	3.68	2.63	3.21	n.d.	2.89	2.88	4.22	3.00	3.80
Fe_2O_3	0.72	0.22	0.73	n.d.	0.60	0.34	0.44	0.11	0.24
Al_2O_3	6.33	6.63	6.85	n.d.	7.18	7.67	6.61	6.99	6.50
V_2O_3	0.80	0.84	0.73	n.d.	0.90	0.88	0.81	0.87	0.90
Cr_2O_3	51.8	53.3	52.0	n.d.	51.8	51.2	50.2	52.7	51.8
MgO	2.38	2.20	2.39	38.7 (4)	2.25	2.37	2.02	2.07	2.09
CaO	n.d.	n.d.	n.d.	0.02 (1)	n.d.	n.d.	n.d.	n.d.	n.d.
MnO	0.59	0.60	0.53	0.46 (3)	0.59	0.60	0.61	0.60	0.66
FeO	31.4	30.6	31.0	22.5 (4)	30.9	30.5	32.4	31.4	32.1
NiO	n.d.	n.d.	n.d.	<0.04 (2)	n.d.	n.d.	n.d.	n.d.	n.d.
ZnO	n.d.	n.d.	n.d.	n.d.	n.d.	n.d.	n.d.	n.d.	n.d.
Total	97.75	96.94	97.45	99.42	97.09	96.51	97.29	97.70	98.08
# of Oxygens	4	4	4	4	4	4	4	4	4
Si	-------	-------	-------	0.992	-------	-------	-------	-------	-------
Ti	0.100	0.072	0.088	-------	0.079	0.079	0.116	0.082	0.103
Fe^{3+}	0.020	0.006	0.020	-------	0.016	0.009	0.012	0.003	0.007
Al	0.271	0.286	0.293	-------	0.308	0.330	0.284	0.299	0.277
V	0.023	0.025	0.021	-------	0.026	0.026	0.024	0.025	0.026
Cr	1.486	1.539	1.491	-------	1.491	1.477	1.449	1.510	1.483
Mg	0.129	0.120	0.129	1.512	0.122	0.129	0.110	0.112	0.113
Ca	-------	-------	-------	0.001	-------	-------	-------	-------	-------
Mn	0.018	0.019	0.016	0.010	0.018	0.019	0.019	0.018	0.020
Fe^{2+}	0.954	0.934	0.942	0.492	0.939	0.932	0.987	0.952	0.970
Ni	-------	-------	-------	0.000	-------	-------	-------	-------	-------
Zn	-------	-------	-------	-------	-------	-------	-------	-------	-------
Total	3.000	3.000	3.000	3.007	3.000	3.000	3.000	3.000	3.000
mg#	11.9	11.4	12.1	75.4	11.5	12.2	10.0	10.5	10.4
cr#	84.6	84.3	83.6	-------	82.9	81.8	83.6	83.5	84.3
Fo	-------	-------	-------	75.1	-------	-------	-------	-------	-------
Fa	-------	-------	-------	24.9	-------	-------	-------	-------	-------

Meteorite	Y793241	Y793241	LEW87555	LEW87555	LEW87555	LEW87555	LEW87555	LEW87555	EET87555
Type/Shock	breccia	breccia	breccia	breccia	breccia	breccia	breccia	breccia	breccia
Mineral	chromite	olivine	chromite	chromite	chromite	chromite	chromite	olivine	chromite
Point	SP6	OL (11)	SP1	SP2	SP3	SP4	SP5	OL (32)	SP1
SiO_2	n.d.	37.7 (1)	n.d.	n.d.	n.d.	n.d.	n.d.	37.7 (2)	n.d.
TiO_2	2.97	n.d.	2.81	3.00	1.70	2.86	2.76	n.d.	0.76
Fe_2O_3	0.64	n.d.	0.00	0.15	0.12	0.00	0.00	n.d.	0.05
Al_2O_3	6.93	n.d.	5.57	5.46	6.06	5.57	5.52	n.d.	29.4
V_2O_3	0.84	n.d.	0.60	0.48	0.71	0.62	0.61	n.d.	0.68
Cr_2O_3	52.0	n.d.	56.6	55.2	56.5	56.3	56.3	n.d.	33.8
MgO	1.98	38.9 (2)	2.28	3.36	1.81	2.36	2.38	38.6 (3)	6.92
CaO	n.d.	0.02 (1)	n.d.	n.d.	n.d.	n.d.	n.d.	0.03 (1)	n.d.
MnO	0.54	0.46 (4)	0.50	0.48	0.66	0.51	0.48	0.40 (3)	0.35
FeO	31.4	22.5 (2)	30.5	29.2	30.5	30.6	30.6	22.0 (3)	25.7
NiO	n.d.	0.00 (1)	n.d.	n.d.	n.d.	n.d.	n.d.	<0.04 (3)	n.d.
ZnO	n.d.	n.d.	n.d.	n.d.	n.d.	n.d.	n.d.	n.d.	n.d.
Total	97.27	99.61	98.84	97.31	98.02	98.85	98.61	98.74	97.75
# of Oxygens	4	4	4	4	4	4	4	4	4
Si	-------	0.988	-------	-------	-------	-------	-------	0.993	-------
Ti	0.081	-------	0.076	0.082	0.047	0.077	0.075	-------	0.018
Fe^{3+}	0.018	-------	0.000	0.004	0.003	0.000	0.000	-------	0.001
Al	0.298	-------	0.236	0.234	0.260	0.236	0.235	-------	1.098
V	0.025	-------	0.017	0.014	0.021	0.018	0.018	-------	0.017
Cr	1.497	-------	1.609	1.585	1.623	1.601	1.605	-------	0.847
Mg	0.108	1.520	0.122	0.182	0.098	0.127	0.128	1.519	0.327
Ca	-------	0.001	-------	-------	-------	-------	-------	0.001	-------
Mn	0.017	0.010	0.015	0.015	0.020	0.016	0.015	0.009	0.009
Fe^{2+}	0.957	0.493	0.917	0.885	0.928	0.921	0.923	0.484	0.682
Ni	-------	0.000	-------	-------	-------	-------	-------	0.001	-------
Zn	-------	-------	-------	-------	-------	-------	-------	-------	-------
Total	3.000	3.012	2.993	3.000	3.000	2.995	2.997	3.007	3.000
mg#	10.1	75.5	11.8	17.0	9.6	12.1	12.2	75.8	32.4
cr#	83.4	-------	87.2	87.2	86.2	87.1	87.2	-------	43.5
Fo	-------	75.1	-------	-------	-------	-------	-------	75.5	-------
Fa	-------	24.9	-------	-------	-------	-------	-------	24.5	-------

Meteorite	EET87555	EET87555	EET87555	EET87555	EET87555	EET87555	EET87555	EET87555	EET87555
Type/Shock	breccia	breccia	breccia	breccia	breccia	breccia	breccia	breccia	breccia
Mineral	chromite	chromite	chromite	chromite	chromite	chromite	chromite	chromite	chromite
Point	SP2	SP3	SP4	SP5	SP6	SP7	SP8	SP9	SP10
SiO_2	n.d.	n.d.	n.d.	n.d.	n.d.	n.d.	n.d.	n.d.	n.d.
TiO_2	0.98	0.63	0.72	0.85	0.83	0.73	0.56	0.86	0.96
Fe_2O_3	<0.04	0.35	0.58	0.31	0.00	0.00	0.22	0.30	0.43
Al_2O_3	28.4	29.5	29.5	27.6	27.7	28.1	28.7	26.8	25.2
V_2O_3	0.68	0.60	0.55	0.63	0.70	0.68	0.71	0.68	0.67
Cr_2O_3	34.5	33.6	33.5	35.0	35.2	35.3	34.5	36.1	37.5
MgO	6.69	6.96	6.93	6.55	6.52	6.62	6.72	6.39	5.95
CaO	n.d.	n.d.	n.d.	n.d.	n.d.	n.d.	n.d.	n.d.	n.d.
MnO	0.35	0.35	0.38	0.33	0.35	0.31	0.33	0.28	0.39
FeO	26.1	25.4	25.7	26.0	25.9	26.0	25.7	26.3	26.7
NiO	n.d.	n.d.	n.d.	n.d.	n.d.	n.d.	n.d.	n.d.	n.d.
ZnO	n.d.	n.d.	n.d.	n.d.	n.d.	n.d.	n.d.	n.d.	n.d.
Total	97.71	97.37	97.85	97.23	97.24	97.77	97.39	97.63	97.82
# of Oxygens	4	4	4	4	4	4	4	4	4
Si	-------	-------	-------	-------	-------	-------	-------	-------	-------
Ti	0.024	0.015	0.017	0.021	0.020	0.018	0.014	0.021	0.023
Fe^{3+}	0.000	0.008	0.014	0.008	0.000	0.000	0.005	0.007	0.010
Al	1.067	1.104	1.101	1.046	1.049	1.058	1.078	1.015	0.965
V	0.017	0.015	0.014	0.016	0.018	0.017	0.018	0.018	0.017
Cr	0.868	0.843	0.838	0.889	0.894	0.890	0.872	0.919	0.961
Mg	0.318	0.330	0.327	0.314	0.312	0.315	0.320	0.307	0.288
Ca	-------	-------	-------	-------	-------	-------	-------	-------	-------
Mn	0.010	0.009	0.010	0.009	0.010	0.008	0.009	0.008	0.011
Fe^{2+}	0.696	0.676	0.680	0.698	0.696	0.694	0.685	0.707	0.725
Ni	-------	-------	-------	-------	-------	-------	-------	-------	-------
Zn	-------	-------	-------	-------	-------	-------	-------	-------	-------
Total	3.000	3.000	3.000	3.000	2.999	3.000	3.000	3.000	3.000
mg#	31.3	32.8	32.5	31.0	31.0	31.2	31.8	30.3	28.4
cr#	44.9	43.3	43.2	45.9	46.0	45.7	44.7	47.5	49.9
Fo	-------	-------	-------	-------	-------	-------	-------	-------	-------
Fa	-------	-------	-------	-------	-------	-------	-------	-------	-------

Appendix E: (continued)

Meteorite	EET87555	EET87555
Type/Shock	breccia	breccia
Mineral	chromite	olivine
Point	SP11	OL (35)
SiO_2	n.d.	37.6 (2)
TiO_2	0.94	n.d.
Fe_2O_3	0.25	n.d.
Al_2O_3	25.5	n.d.
V_2O_3	0.69	n.d.
Cr_2O_3	37.1	n.d.
MgO	5.89	36.8 (4)
CaO	n.d.	0.03 (1)
MnO	0.35	0.45 (4)
FeO	26.8	24.5 (3)
NiO	n.d.	<0.04 (10)
ZnO	n.d.	n.d.
Total	97.58	99.42
# of Oxygens	4	4
Si	------	0.996
Ti	0.023	------
Fe^{3+}	0.006	------
Al	0.977	------
V	0.018	------
Cr	0.953	------
Mg	0.285	1.454
Ca	------	0.001
Mn	0.010	0.010
Fe^{2+}	0.728	0.543
Ni	------	0.001
Zn	------	------
Total	3.000	3.005
mg#	28.1	72.8
cr#	49.4	------
Fo	------	72.4
Fa	------	27.6

Meteorite	Hallingeberg	Hallingeberg	Hallingeberg	Hallingeberg	Hallingeberg	Hallingeberg	Hallingeberg	Hallingeberg	Hallingeberg
Type/Shock	L3, S3	L3, S3	L3, S3	L3, S3	L3, S3	L3, S3	L3, S3	L3, S3	L3, S3
Mineral	augite	opx	augite	pigeonite	augite	pigeonite	augite	opx	augite
Point	cpx1	opx1	cpx2	opx2	cpx3	opx3	cpx4	opx4	cpx5
SiO_2	51.1	56.9	49.2	54.4	50.4	54.6	51.1	57.6	51.2
TiO_2	0.37	0.04	0.58	0.16	0.74	0.13	0.32	0.03	1.00
Al_2O_3	2.37	0.24	8.66	1.15	4.55	0.77	4.45	0.26	3.22
Cr_2O_3	1.34	0.45	1.93	1.11	2.29	1.45	1.08	0.55	0.56
MgO	13.7	33.1	16.8	26.0	15.5	26.4	20.0	34.4	19.0
CaO	17.8	0.15	15.4	3.9	19.9	2.8	14.4	0.23	11.5
MnO	0.38	0.31	0.86	1.22	0.83	1.41	0.26	0.34	0.32
FeO	10.9	7.82	5.81	10.5	4.22	11.1	8.59	5.57	12.8
Na_2O	0.96	0.06	0.80	0.15	0.59	0.04	0.01	0.05	<0.01
Total	98.90	99.00	100.11	98.50	99.06	98.68	100.21	99.02	99.72
# of Oxygens	6	6	6	6	6	6	6	6	6
Si	1.937	1.995	1.792	1.975	1.868	1.981	1.865	2.000	1.897
Ti	0.010	0.001	0.016	0.004	0.021	0.003	0.009	0.001	0.028
Al	0.106	0.010	0.371	0.049	0.199	0.033	0.191	0.011	0.140
Cr	0.040	0.012	0.056	0.032	0.067	0.042	0.031	0.015	0.016
Mg	0.771	1.729	0.912	1.407	0.857	1.429	1.086	1.779	1.050
Ca	0.724	0.005	0.601	0.150	0.790	0.109	0.563	0.009	0.457
Mn	0.012	0.009	0.026	0.037	0.026	0.043	0.008	0.010	0.010
Fe^{2+}	0.345	0.229	0.177	0.320	0.131	0.337	0.262	0.162	0.397
Na	0.070	0.004	0.056	0.011	0.043	0.002	0.001	0.004	0.000
Total	4.015	3.994	4.007	3.985	4.000	3.979	4.016	3.990	3.995
Calculated WoEnFs									
Wo	39.1	0.25	35.0	7.84	43.8	5.68	29.3	0.43	23.9
En	41.6	87.7	53.1	73.5	47.5	74.5	56.6	90.8	54.9
Fs	19.3	12.1	11.8	18.7	8.71	19.8	14.1	8.78	21.3
Lindsley WoEnFs									
Wo	35.6	0.26	21.9	11.4	35.0	9.00	22.3	0.44	20.2
En	45.8	88.1	66.2	72.2	56.4	73.6	64.1	91.2	57.9
Fs	18.7	11.7	11.9	16.4	8.60	17.4	13.6	8.31	21.9

Meteorite	Hallingeberg	Hallingeberg	Hallingeberg	Hallingeberg	Hallingeberg	Hallingeberg	Hallingeberg	Hallingeberg	Hallingeberg
Type/Shock	L3, S3	L3, S3	L3, S3	L3, S3	L3, S3	L3, S3	L3, S3	L3, S3	L3, S3
Mineral	opx	augite	opx	augite	opx	opx	opx	opx	opx
Point	opx5	cpx6	opx6	cpx7	opx7	opx8	opx9	opx10	opx11
SiO_2	57.4	51.0	57.6	52.3	56.5	58.6	56.8	57.8	57.5
TiO_2	0.04	0.66	0.03	0.57	0.05	0.02	0.05	0.02	<0.02
Al_2O_3	0.29	5.14	0.30	4.45	0.64	0.10	0.44	0.22	0.29
Cr_2O_3	0.63	3.08	0.72	2.39	0.66	0.35	0.45	0.38	0.36
MgO	34.0	18.9	35.3	19.8	32.7	37.6	34.0	36.4	32.4
CaO	0.35	16.9	0.22	15.7	0.46	0.12	0.28	0.13	1.05
MnO	0.46	1.29	0.40	1.49	0.45	0.25	0.39	0.28	0.40
FeO	6.24	2.42	5.05	2.62	7.04	2.71	6.09	4.17	7.37
Na_2O	0.03	0.23	0.05	0.35	0.12	0.02	0.12	0.04	0.07
Total	99.39	99.68	99.67	99.75	98.64	99.79	98.59	99.38	99.41
# of Oxygens	6	6	6	6	6	6	6	6	6
Si	1.994	1.850	1.984	1.887	1.986	1.993	1.987	1.986	2.008
Ti	0.001	0.018	0.001	0.016	0.001	0.001	0.001	0.001	0.001
Al	0.012	0.220	0.012	0.189	0.027	0.004	0.018	0.009	0.012
Cr	0.017	0.088	0.020	0.068	0.018	0.009	0.012	0.010	0.010
Mg	1.758	1.023	1.816	1.066	1.716	1.905	1.774	1.863	1.683
Ca	0.013	0.658	0.008	0.606	0.017	0.004	0.010	0.005	0.040
Mn	0.013	0.040	0.012	0.045	0.013	0.007	0.012	0.008	0.012
Fe^{2+}	0.181	0.073	0.146	0.079	0.207	0.077	0.178	0.120	0.215
Na	0.002	0.016	0.004	0.025	0.008	0.001	0.008	0.002	0.005
Total	3.991	3.986	4.003	3.981	3.993	4.001	4.000	4.004	3.984
Calculated WoEnFs									
Wo	0.66	36.7	0.40	33.7	0.87	0.20	0.51	0.25	2.05
En	89.5	57.0	91.6	59.3	87.9	95.6	89.9	93.3	86.3
Fs	9.87	6.30	7.97	6.94	11.3	4.21	9.63	6.41	11.6
Lindsley WoEnFs									
Wo	0.67	25.8	0.41	24.3	0.89	0.20	0.51	0.25	2.08
En	90.1	69.3	92.2	70.5	88.4	95.9	90.5	93.9	86.8
Fs	9.27	4.94	7.41	5.25	10.7	3.88	8.98	5.85	11.1

Appendix E: (continued)

Meteorite	Hallingeberg	Inman	Inman	Inman	Inman	Inman	Inman	Inman	Inman
Type/Shock	L3, S3	L3, S3	L3, S3	L3, S3	L3, S3	L3, S3	L3, S3	L3, S3	L3, S3
Mineral	opx	augite	pigeonite	augite	opx	augite	opx	pigeonite	opx
Point	opx12	cpx1	opx1	cpx2	opx2	cpx3	opx3	cpx4	opx4
SiO_2	56.7	52.3	54.5	53.1	55.6	53.2	54.6	53.9	56.1
TiO_2	0.08	0.22	0.13	0.17	0.06	0.12	0.08	0.13	0.05
Al_2O_3	0.56	1.07	0.37	0.78	0.25	0.46	0.45	0.63	0.19
Cr_2O_3	0.90	1.35	1.01	1.07	0.88	1.39	1.05	1.06	0.94
MgO	33.3	17.5	26.1	18.4	28.3	17.7	27.2	23.3	30.1
CaO	0.67	14.5	3.2	13.6	1.53	13.1	1.66	6.11	0.78
MnO	0.67	0.36	0.70	0.38	0.67	0.53	0.88	0.76	0.59
FeO	6.47	11.0	12.5	11.0	11.9	12.0	12.9	12.7	11.0
Na_2O	0.05	0.37	0.13	0.48	0.07	0.48	0.07	0.20	0.04
Total	99.36	98.71	98.76	99.03	99.29	99.00	98.93	98.78	99.87
# of Oxygens	6	6	6	6	6	6	6	6	6
Si	1.978	1.962	1.986	1.978	1.996	1.990	1.982	1.983	1.989
Ti	0.002	0.006	0.004	0.005	0.002	0.004	0.002	0.004	0.001
Al	0.023	0.048	0.016	0.034	0.011	0.020	0.019	0.027	0.008
Cr	0.025	0.040	0.029	0.032	0.025	0.041	0.030	0.031	0.026
Mg	1.733	0.979	1.418	1.023	1.512	0.985	1.472	1.279	1.592
Ca	0.025	0.583	0.127	0.543	0.059	0.527	0.065	0.241	0.030
Mn	0.020	0.011	0.022	0.012	0.020	0.017	0.027	0.024	0.018
Fe^{2+}	0.189	0.345	0.382	0.342	0.358	0.375	0.391	0.390	0.327
Na	0.003	0.027	0.009	0.034	0.005	0.035	0.005	0.014	0.003
Total	3.998	4.001	3.992	4.002	3.987	3.993	3.994	3.992	3.994
Calculated WoEnFs									
Wo	1.27	30.4	6.50	28.3	3.02	27.7	3.30	12.5	1.51
En	88.1	51.0	72.8	53.3	77.6	51.8	75.3	66.1	81.0
Fs	10.6	18.6	20.7	18.4	19.4	20.6	21.4	21.4	17.5
Lindsley WoEnFs									
Wo	1.30	27.3	8.56	25.8	3.10	24.3	3.40	15.0	1.54
En	89.0	53.9	72.0	55.8	78.3	54.9	76.3	65.1	81.7
Fs	9.71	18.9	19.4	18.4	18.6	20.9	20.3	19.9	16.8

Appendix E: (continued)

Meteorite	Inman	Inman	Bjurböle	Bjurböle	Bjurböle	Bjurböle	Bjurböle	Bjurböle	Bjurböle	Bjurböle
Type/Shock	L3, S3	L3, S3	L4, S1	L4, S1	L4, S1	L4, S1	L4, S1	L4, S1	L4, S1	L4, S1
Mineral	pigeonite	pigeonite	augite	opx	augite	opx	augite	opx	opx	augite
Point	cpx5	opx5	cpx1	opx1	cpx2	opx2	cpx3	opx3	opx3	cpx4
SiO_2	54.8	54.6	49.3	55.5	46.7	54.9	47.0	55.0	48.0	
TiO_2	0.12	0.11	0.60	0.05	0.91	0.25	1.53	0.16	1.58	
Al_2O_3	0.38	0.41	6.44	0.14	11.05	0.41	9.83	0.18	9.82	
Cr_2O_3	1.13	1.20	1.74	0.15	1.04	0.59	0.83	0.15	0.80	
MgO	25.7	26.4	16.9	29.9	13.5	27.1	14.0	27.6	15.1	
CaO	4.44	3.23	16.9	0.29	20.1	1.50	23.0	0.56	23.9	
MnO	0.72	0.65	0.21	0.35	0.26	0.41	<0.06	0.50	<0.06	
FeO	11.7	12.5	7.19	12.2	5.14	13.6	2.45	14.3	0.81	
Na_2O	0.14	0.12	0.37	<0.02	0.52	0.05	0.36	<0.02	0.01	
Total	99.07	99.23	99.71	98.69	99.22	98.73	99.02	98.52	99.96	
# of Oxygens	6	6	6	6	6	6	6	6	6	
Si	1.989	1.980	1.816	1.995	1.727	1.993	1.735	2.002	1.742	
Ti	0.003	0.003	0.017	0.001	0.025	0.007	0.042	0.004	0.043	
Al	0.016	0.018	0.280	0.006	0.482	0.018	0.427	0.008	0.419	
Cr	0.032	0.034	0.051	0.004	0.030	0.017	0.024	0.004	0.023	
Mg	1.389	1.427	0.930	1.602	0.743	1.464	0.769	1.498	0.814	
Ca	0.173	0.126	0.669	0.011	0.798	0.058	0.908	0.022	0.927	
Mn	0.022	0.020	0.006	0.011	0.008	0.013	0.001	0.016	0.001	
Fe^{2+}	0.355	0.379	0.222	0.369	0.159	0.412	0.076	0.434	0.025	
Na	0.010	0.009	0.026	0.001	0.037	0.003	0.026	0.000	0.001	
Total	3.989	3.995	4.017	4.000	4.009	3.985	4.008	3.988	3.995	
Calculated WoEnFs										
Wo	8.90	6.44	36.6	0.56	46.7	2.98	51.8	1.12	52.5	
En	71.6	73.1	50.9	80.4	43.5	75.2	43.8	76.0	46.1	
Fs	19.5	20.5	12.5	19.1	9.78	21.8	4.39	22.8	1.47	
Lindsley WoEnFs										
Wo	11.2	7.98	27.3	0.57	29.8	3.04	37.4	1.13	37.2	
En	70.7	72.7	60.2	80.8	59.2	75.7	58.4	76.7	60.9	
Fs	18.1	19.3	12.5	18.6	11.0	21.3	4.18	22.2	1.87	

Meteorite	Bjurböle	Bjurböle	Bjurböle	Bjurböle	Bjurböle	Bjurböle	Bjurböle	Bjurböle	Bjurböle
Type/Shock	L4, S1	L4, S1	L4, S1	L4, S1	L4, S1	L4, S1	L4, S1	L4, S1	L4, S1
Mineral	opx	augite	opx	augite	opx	augite	opx	augite	opx
Point	opx4	cpx5	opx5	cpx6	opx6	cpx7	opx7	cpx8	opx8
SiO_2	55.5	47.9	55.5	53.0	54.6	52.5	55.5	52.2	54.8
TiO_2	0.05	1.53	<0.02	0.54	0.09	0.44	0.04	0.55	0.07
Al_2O_3	0.08	9.60	0.21	2.31	0.09	1.67	0.06	1.78	0.09
Cr_2O_3	0.10	0.81	0.27	1.38	0.24	1.69	0.05	2.11	0.06
MgO	29.0	15.5	29.3	16.5	28.5	16.3	28.7	16.7	29.1
CaO	0.15	23.6	0.47	18.4	0.35	18.0	0.16	18.2	0.20
MnO	0.40	<0.06	0.53	0.27	0.45	0.52	0.49	0.42	0.45
FeO	13.8	0.97	12.6	5.77	14.5	7.59	13.9	6.27	13.7
Na_2O	<0.02	0.05	<0.02	0.75	0.03	0.73	<0.02	0.95	<0.02
Total	99.02	99.88	98.85	98.95	98.80	99.40	98.79	99.12	98.55
# of Oxygens	6	6	6	6	6	6	6	6	6
Si	1.999	1.738	1.996	1.955	1.984	1.949	2.004	1.937	1.988
Ti	0.001	0.042	0.000	0.015	0.002	0.012	0.001	0.015	0.002
Al	0.003	0.411	0.009	0.100	0.004	0.073	0.003	0.078	0.004
Cr	0.003	0.023	0.008	0.040	0.007	0.050	0.001	0.062	0.002
Mg	1.556	0.840	1.570	0.908	1.542	0.902	1.543	0.922	1.574
Ca	0.006	0.917	0.018	0.729	0.014	0.714	0.006	0.722	0.008
Mn	0.012	0.001	0.016	0.008	0.014	0.016	0.015	0.013	0.014
Fe^{2+}	0.415	0.029	0.379	0.178	0.441	0.235	0.419	0.194	0.415
Na	0.001	0.004	0.000	0.053	0.002	0.053	0.001	0.068	0.000
Total	3.996	4.005	3.996	3.986	4.010	4.004	3.993	4.011	4.007
Calculated WoEnFs									
Wo	0.30	51.3	0.91	40.0	0.70	38.2	0.30	39.0	0.40
En	78.2	47.0	79.2	49.8	76.7	48.3	77.8	49.8	78.3
Fs	21.5	1.68	19.9	10.2	22.6	13.4	21.9	11.2	21.3
Lindsley WoEnFs									
Wo	0.30	37.2	0.92	34.4	0.71	33.6	0.31	34.2	0.40
En	78.7	61.5	79.8	54.9	77.5	53.0	78.4	55.6	79.1
Fs	21.0	1.39	19.3	10.8	21.8	13.4	21.3	10.2	20.5

Meteorite	Bjurböle	Bjurböle	Bjurböle	Bjurböle	Bjurböle	Bjurböle	Tennasilm	Tennasilm	Tennasilm
Type/Shock	L4, S1	L4, S1	L4, S1	L4, S1	L4, S1	L4, S1	L4, S3	L4, S3	L4, S3
Mineral	augite	opx	augite	opx	opx	opx	augite	opx	opx
Point	cpx9	opx9	cpx10	opx10	opx11	opx12	cpx1	opx1a	opx1b
SiO_2	53.8	55.5	53.3	55.3	55.3	52.5	53.7	54.8	55.1
TiO_2	0.28	<0.02	0.69	0.08	0.09	0.25	0.53	0.23	0.21
Al_2O_3	0.32	0.46	0.83	0.11	0.10	5.31	0.64	0.15	0.15
Cr_2O_3	0.69	0.34	0.56	0.11	0.07	1.19	0.77	0.12	0.15
MgO	16.4	28.4	16.9	29.0	29.1	28.1	16.4	28.7	28.7
CaO	22.8	0.81	20.9	0.24	0.25	2.42	22.3	1.05	0.65
MnO	0.21	0.49	0.23	0.42	0.44	0.29	0.19	0.43	0.48
FeO	4.60	13.1	5.19	13.8	14.2	9.53	4.47	13.7	14.0
Na_2O	0.49	0.02	0.43	<0.02	<0.02	0.03	0.53	0.04	<0.02
Total	99.63	99.16	98.92	98.99	99.45	99.61	99.47	99.18	99.38
# of Oxygens	6	6	6	6	6	6	6	6	6
Si	1.983	1.996	1.971	1.995	1.989	1.865	1.977	1.980	1.984
Ti	0.008	0.000	0.019	0.002	0.003	0.007	0.015	0.006	0.006
Al	0.014	0.019	0.036	0.005	0.004	0.222	0.028	0.007	0.006
Cr	0.020	0.010	0.016	0.003	0.002	0.033	0.023	0.003	0.004
Mg	0.900	1.522	0.930	1.558	1.559	1.487	0.899	1.544	1.542
Ca	0.901	0.031	0.828	0.009	0.010	0.092	0.880	0.041	0.025
Mn	0.006	0.015	0.007	0.013	0.014	0.009	0.006	0.013	0.015
Fe^{2+}	0.142	0.394	0.161	0.415	0.426	0.283	0.138	0.414	0.422
Na	0.035	0.001	0.031	0.001	0.001	0.002	0.038	0.003	0.001
Total	4.009	3.988	3.999	3.999	4.005	4.000	4.004	4.011	4.005
Calculated WoEnFs									
Wo	46.2	1.58	43.0	0.45	0.47	4.92	45.8	2.04	1.25
En	46.2	77.6	48.3	78.1	77.6	79.5	46.7	76.7	76.9
Fs	7.59	20.8	8.72	21.4	21.9	15.6	7.49	21.2	21.8
Lindsley WoEnFs									
Wo	44.9	1.61	40.6	0.46	0.48	5.31	43.0	2.07	1.26
En	48.4	78.2	50.6	78.6	78.4	79.7	49.6	77.5	77.6
Fs	6.77	20.2	8.77	20.9	21.2	15.0	7.44	20.4	21.2

Meteorite Type/Shock	Tennasilm L4, S3	Tennasilm L4, S3	Tennasilm L4, S3	Tennasilm L4, S3	Tennasilm L4, S3	Tennasilm L4, S3	Tennasilm L4, S3	Tennasilm L4, S3	Tennasilm L4, S3
Mineral	augite	opx	augite	opx	augite	pigeonite	augite	opx	augite
Point	cpx2	opx2	cpx3	opx3	cpx4	opx4	cpx5	opx5	cpx6
SiO_2	54.3	55.0	54.1	55.5	54.1	54.8	53.8	55.4	53.6
TiO_2	0.38	0.21	0.39	0.18	0.46	0.23	0.44	0.16	0.45
Al_2O_3	0.42	0.17	0.49	0.16	0.49	0.20	0.50	0.11	0.48
Cr_2O_3	0.52	0.11	0.78	0.16	0.64	0.16	0.74	0.09	0.79
MgO	19.6	29.0	16.7	28.9	16.6	27.1	16.3	28.9	16.5
CaO	16.7	0.67	22.5	0.73	22.5	3.7	21.9	0.73	21.9
MnO	0.29	0.49	0.25	0.45	0.20	0.39	0.21	0.42	0.21
FeO	6.67	14.0	4.40	13.8	4.32	12.6	5.23	13.8	4.96
Na_2O	0.43	<0.02	0.49	<0.02	0.50	0.11	0.49	<0.02	0.55
Total	99.38	99.57	99.99	99.82	99.72	99.34	99.72	99.63	99.43
# of Oxygens	6	6	6	6	6	6	6	6	6
Si	1.988	1.979	1.980	1.988	1.984	1.983	1.982	1.989	1.978
Ti	0.011	0.006	0.011	0.005	0.013	0.006	0.012	0.004	0.012
Al	0.018	0.007	0.021	0.007	0.021	0.009	0.022	0.005	0.021
Cr	0.015	0.003	0.023	0.004	0.019	0.005	0.022	0.002	0.023
Mg	1.069	1.554	0.909	1.542	0.906	1.461	0.897	1.547	0.909
Ca	0.656	0.026	0.883	0.028	0.884	0.145	0.865	0.028	0.865
Mn	0.009	0.015	0.008	0.014	0.006	0.012	0.006	0.013	0.006
Fe^{2+}	0.204	0.420	0.135	0.413	0.133	0.380	0.161	0.414	0.153
Na	0.030	0.001	0.035	0.001	0.036	0.007	0.035	0.000	0.039
Total	4.000	4.011	4.005	4.002	4.002	4.008	4.002	4.002	4.006
Calculated WoEnFs									
Wo	33.8	1.29	45.6	1.40	45.8	7.26	44.8	1.40	44.7
En	55.2	77.1	47.0	77.2	47.0	73.1	46.5	77.3	47.0
Fs	11.0	21.6	7.39	21.4	7.21	19.6	8.66	21.3	8.23
Lindsley WoEnFs									
Wo	35.6	1.31	43.5	1.42	43.4	8.40	42.3	1.41	42.8
En	54.1	78.0	49.7	77.8	49.5	73.0	49.1	77.8	49.6
Fs	10.9	20.7	6.88	20.8	7.16	18.6	8.64	20.8	7.59

Appendix E: (continued)

Meteorite	Tennasilm	Tennasilm	Tennasilm	Tennasilm	Tennasilm	Ausson	Ausson	Ausson	Ausson
Type/Shock	L4, S3	L4, S3	L4, S3	L4, S3	L4, S3	L5, S2	L5, S2	L5, S2	L5, S2
Mineral	opx	augite	opx	augite	opx	augite	opx	augite	opx
Point	opx6	cpx7	opx7	cpx8	opx8	cpx1	opx1	cpx2	opx2
SiO_2	55.4	54.1	55.6	54.0	55.3	54.1	55.8	54.2	56.0
TiO_2	0.21	0.41	0.16	0.45	0.18	0.66	0.13	0.54	0.17
Al_2O_3	0.14	0.44	0.12	0.50	0.16	0.71	0.16	0.81	0.16
Cr_2O_3	0.10	0.66	0.08	0.70	0.07	0.77	0.13	0.87	0.08
MgO	29.1	16.6	28.9	16.5	28.8	16.5	30.4	16.6	30.8
CaO	0.50	22.4	0.65	22.5	0.65	22.8	0.63	22.6	0.72
MnO	0.50	0.22	0.52	0.20	0.48	0.23	0.51	0.19	0.45
FeO	14.0	4.38	13.7	4.27	13.7	3.09	10.8	3.28	10.7
Na_2O	0.02	0.50	≤0.02	0.51	≤0.02	0.55	0.03	0.57	0.02
Total	100.03	99.75	99.73	99.67	99.37	99.33	98.56	99.61	99.13
# of Oxygens	6	6	6	6	6	6	6	6	6
Si	1.984	1.986	1.993	1.984	1.990	1.983	1.996	1.983	1.992
Ti	0.006	0.011	0.004	0.013	0.005	0.018	0.003	0.015	0.005
Al	0.006	0.019	0.005	0.022	0.007	0.030	0.007	0.035	0.007
Cr	0.003	0.019	0.002	0.020	0.002	0.022	0.004	0.025	0.002
Mg	1.555	0.907	1.542	0.904	1.545	0.903	1.623	0.905	1.634
Ca	0.019	0.883	0.025	0.885	0.025	0.894	0.024	0.884	0.027
Mn	0.015	0.007	0.016	0.006	0.015	0.007	0.016	0.006	0.013
Fe^{2+}	0.418	0.134	0.412	0.131	0.414	0.095	0.322	0.100	0.319
Na	0.001	0.035	0.001	0.036	0.001	0.039	0.002	0.040	0.001
Total	4.007	4.001	4.000	4.001	4.004	3.991	3.997	3.993	4.000
Calculated WoEnFs									
Wo	0.95	45.7	1.25	46.0	1.25	47.1	1.21	46.6	1.35
En	77.5	47.0	77.3	46.9	77.3	47.6	81.8	47.8	82.0
Fs	21.6	7.30	21.5	7.11	21.5	5.37	17.0	5.59	16.7
Lindsley WoEnFs									
Wo	0.96	43.4	1.27	43.3	1.26	43.6	1.22	43.0	1.37
En	78.1	49.5	77.9	49.6	77.9	51.0	82.4	51.4	82.5
Fs	20.9	7.15	20.8	7.18	20.9	5.37	16.4	5.68	16.1

Appendix E: (continued)

Meteorite	Ausson	Ausson	Ausson	Ausson	Ausson	Ausson	Ausson	Ausson	Ausson
Type/Shock	L5, S2	L5, S2	L5, S2	L5, S2	L5, S2	L5, S2	L5, S2	L5, S2	L5, S2
Mineral	augite	opx	augite	opx	augite	opx	augite	opx	opx
Point	cpx3	opx3	cpx4	opx4	cpx5	opx5	cpx6	opx6	opx7
SiO_2	54.2	55.7	54.0	56.1	54.5	56.5	54.0	55.3	55.8
TiO_2	0.38	0.21	0.43	0.12	0.52	0.21	0.55	0.10	0.21
Al_2O_3	0.48	0.23	0.73	0.16	0.73	0.21	0.69	0.16	0.21
Cr_2O_3	0.68	0.14	0.78	0.11	0.77	0.09	0.79	0.10	0.10
MgO	17.4	30.6	16.9	31.2	16.7	30.8	16.5	31.0	30.7
CaO	21.9	0.80	22.1	0.68	22.3	0.56	22.2	0.71	0.69
MnO	0.23	0.54	0.24	0.44	0.25	0.44	0.23	0.50	0.45
FeO	3.41	10.7	3.37	10.4	3.19	10.5	3.38	11.0	10.9
Na_2O	0.47	≤0.02	0.56	0.03	0.61	0.02	0.55	≤0.02	≤0.02
Total	99.06	98.96	99.05	99.37	99.66	99.33	98.91	98.86	99.09
# of Oxygens	6	6	6	6	6	6	6	6	6
Si	1.989	1.987	1.984	1.990	1.990	2.002	1.988	1.978	1.987
Ti	0.011	0.006	0.012	0.003	0.014	0.006	0.015	0.003	0.006
Al	0.021	0.010	0.032	0.007	0.031	0.009	0.030	0.007	0.009
Cr	0.020	0.004	0.023	0.003	0.022	0.003	0.023	0.003	0.003
Mg	0.951	1.628	0.924	1.650	0.910	1.624	0.906	1.651	1.632
Ca	0.861	0.031	0.872	0.026	0.873	0.021	0.877	0.027	0.026
Mn	0.007	0.016	0.008	0.013	0.008	0.013	0.007	0.015	0.014
Fe^{2+}	0.105	0.318	0.104	0.310	0.097	0.310	0.104	0.330	0.323
Na	0.033	0.000	0.040	0.002	0.043	0.001	0.039	0.001	0.001
Total	3.998	4.000	3.999	4.004	3.988	3.989	3.989	4.015	4.001
Calculated WoEnFs									
Wo	44.8	1.56	45.7	1.30	46.2	1.07	46.3	1.33	1.30
En	49.4	81.7	48.4	82.5	48.2	82.5	47.8	81.6	81.8
Fs	5.82	16.8	5.87	16.2	5.56	16.4	5.86	17.1	16.9
Lindsley WoEnFs									
Wo	42.1	1.58	42.5	1.32	42.6	1.08	42.7	1.37	1.32
En	52.2	82.3	51.7	83.2	51.9	83.1	51.4	82.8	82.4
Fs	5.76	16.1	5.82	15.5	5.53	15.9	5.90	15.8	16.3

Meteorite	Ausson	Ausson	Ausson	Ausson	Ausson	Ausson	Ausson	Ausson	Ausson
Type/Shock	L5, S2	L5, S2	L5, S2	L5, S2	L5, S2	L5, S2	L5, S2	L5, S2	L5, S2
Mineral	opx	opx	opx	opx	opx	opx	opx	opx	opx
Point	opx8	opx9	opx10	opx11	opx12	opx13	opx14	opx15	opx16
SiO_2	56.1	56.1	55.5	56.1	55.6	56.3	56.2	56.0	55.7
TiO_2	0.12	0.11	0.14	0.14	0.19	0.15	0.19	0.15	0.13
Al_2O_3	0.12	0.16	0.14	0.17	0.21	0.15	0.19	0.23	0.17
Cr_2O_3	0.11	0.07	0.12	0.13	0.50	0.10	0.12	0.08	0.12
MgO	30.9	30.7	31.3	31.0	30.5	30.9	30.9	30.9	31.0
CaO	0.67	0.71	0.71	0.66	0.64	0.61	0.62	0.60	0.70
MnO	0.47	0.47	0.42	0.52	0.49	0.52	0.47	0.47	0.47
FeO	10.6	10.8	10.7	10.9	11.0	10.9	11.0	11.0	10.8
Na_2O	0.02	<0.02	0.03	0.02	<0.02	0.02	<0.02	0.03	0.02
Total	99.13	99.08	98.98	99.58	99.21	99.59	99.66	99.37	99.11
# of Oxygens	6	6	6	6	6	6	6	6	6
Si	1.994	1.995	1.979	1.988	1.983	1.994	1.990	1.988	1.985
Ti	0.003	0.003	0.004	0.004	0.005	0.004	0.005	0.004	0.003
Al	0.005	0.007	0.006	0.007	0.009	0.006	0.008	0.009	0.007
Cr	0.003	0.002	0.003	0.004	0.014	0.003	0.003	0.002	0.003
Mg	1.638	1.631	1.661	1.638	1.622	1.630	1.628	1.635	1.645
Ca	0.026	0.027	0.027	0.025	0.024	0.023	0.024	0.023	0.027
Mn	0.014	0.014	0.013	0.015	0.015	0.016	0.014	0.014	0.014
Fe^{2+}	0.315	0.320	0.318	0.323	0.329	0.321	0.326	0.326	0.321
Na	0.001	0.001	0.002	0.001	0.000	0.001	0.001	0.002	0.002
Total	3.999	4.000	4.013	4.005	4.001	3.998	3.999	4.003	4.007
Calculated WoEnFs									
Wo	1.30	1.36	1.34	1.25	1.21	1.16	1.20	1.15	1.35
En	82.2	81.9	82.3	81.9	81.5	81.9	81.7	81.8	82.0
Fs	16.5	16.8	16.4	16.9	17.3	16.9	17.1	17.0	16.7
Lindsley WoEnFs									
Wo	1.32	1.37	1.37	1.26	1.23	1.17	1.22	1.17	1.37
En	82.8	82.5	83.3	82.5	82.1	82.6	82.3	82.6	82.9
Fs	15.9	16.2	15.3	16.2	16.7	16.3	16.5	16.3	15.8

Appendix E: (continued)

Meteorite	Jhung	Jhung	Jhung	Jhung	Jhung	Jhung	Jhung	Jhung	Jhung
Type/Shock	L5, S3	L5, S3	L5, S3	L5, S3	L5, S3	L5, S3	L5, S3	L5, S3	L5, S3
Mineral	augite	opx	augite	augite	augite	opx	augite	opx	augite
Point	cpx1	opx1	cpx2a	cpx2b	cpx2c	opx2	cpx3	opx3	cpx4a
SiO_2	54.0	55.0	53.6	53.9	53.4	55.6	52.9	55.4	53.6
TiO_2	0.47	0.19	0.53	0.46	0.40	0.12	0.43	0.21	0.43
Al_2O_3	0.46	0.17	0.51	0.52	0.46	0.08	0.46	0.17	0.51
Cr_2O_3	0.64	0.11	0.76	0.75	0.65	0.13	0.66	0.12	0.78
MgO	16.6	29.2	16.5	16.5	16.9	28.8	18.0	28.8	16.5
CaO	22.5	0.67	21.8	22.4	21.9	0.84	20.4	0.59	21.9
MnO	0.19	0.45	0.22	0.24	0.25	0.46	0.22	0.47	0.28
FeO	4.65	13.8	5.32	4.70	5.11	13.9	6.05	13.8	5.37
Na_2O	0.48	0.03	0.53	0.52	0.48	<0.02	0.51	<0.02	0.55
Total	100.01	99.57	99.74	99.97	99.62	99.93	99.57	99.56	99.90
# of Oxygens	6	6	6	6	6	6	6	6	6
Si	1.980	1.977	1.974	1.979	1.971	1.992	1.954	1.988	1.975
Ti	0.013	0.005	0.015	0.013	0.011	0.003	0.012	0.006	0.012
Al	0.020	0.007	0.022	0.022	0.020	0.004	0.020	0.007	0.022
Cr	0.019	0.003	0.022	0.022	0.019	0.004	0.019	0.003	0.023
Mg	0.906	1.563	0.905	0.901	0.928	1.538	0.991	1.544	0.903
Ca	0.885	0.026	0.862	0.879	0.867	0.032	0.806	0.023	0.862
Mn	0.006	0.014	0.007	0.007	0.008	0.014	0.007	0.014	0.009
Fe^{2+}	0.143	0.416	0.164	0.144	0.157	0.415	0.187	0.415	0.165
Na	0.034	0.002	0.038	0.037	0.034	0.001	0.037	0.000	0.039
Total	4.006	4.013	4.009	4.004	4.015	4.003	4.033	4.000	4.010
Calculated WoEnFs									
Wo	45.6	1.29	44.5	45.5	44.2	1.60	40.5	1.15	44.5
En	46.7	77.4	46.7	46.7	47.3	76.9	49.8	77.4	46.6
Fs	7.68	21.3	8.82	7.82	8.42	21.5	9.74	21.5	8.97
Lindsley WoEnFs									
Wo	43.8	1.32	42.6	43.3	43.5	1.62	41.1	1.17	42.8
En	49.0	78.4	49.1	49.3	49.3	77.5	51.3	77.9	49.1
Fs	7.25	20.3	8.25	7.39	7.18	20.9	7.61	20.9	8.05

Appendix E: (continued)

Meteorite	Jhung	Jhung	Jhung	Jhung	Jhung	Jhung	Jhung	Jhung	Jhung
Type/Shock	L5, S3	L5, S3	L5, S3	L5, S3	L5, S3	L5, S3	L5, S3	L5, S3	L5, S3
Mineral	augite	augite	opx	augite	augite	opx	augite	opx	opx
Point	cpx4b	cpx 4c	opx4	cpx5a	cpx5b	opx5	cpx6	opx6a	opx6b
SiO_2	54.5	53.9	55.2	53.5	53.8	55.6	54.1	55.2	55.6
TiO_2	0.48	0.47	0.19	0.57	0.56	0.17	0.48	0.22	0.11
Al_2O_3	1.79	0.71	0.17	0.73	0.59	0.17	0.51	0.16	0.12
Cr_2O_3	0.71	0.78	0.09	0.97	0.77	0.07	0.77	0.16	0.12
MgO	15.6	16.4	28.9	16.4	16.5	28.6	16.3	28.8	28.7
CaO	20.8	21.7	0.59	21.7	22.5	0.75	22.0	0.96	0.88
MnO	0.17	0.24	0.48	0.23	0.19	0.51	0.25	0.49	0.46
FeO	4.41	5.01	13.7	5.03	4.57	13.7	4.83	13.6	13.6
Na_2O	0.92	0.63	≤0.02	0.57	0.52	0.03	0.54	≤0.02	≤0.02
Total	99.38	99.85	99.32	99.61	99.98	99.55	99.77	99.61	99.47
# of Oxygens	6	6	6	6	6	6	6	6	6
Si	1.993	1.978	1.987	1.970	1.973	1.996	1.987	1.985	1.996
Ti	0.013	0.013	0.005	0.016	0.015	0.005	0.013	0.006	0.003
Al	0.077	0.031	0.007	0.032	0.025	0.007	0.022	0.007	0.005
Cr	0.021	0.023	0.002	0.028	0.022	0.002	0.022	0.005	0.004
Mg	0.851	0.898	1.551	0.898	0.903	1.529	0.894	1.541	1.534
Ca	0.817	0.856	0.023	0.857	0.883	0.029	0.864	0.037	0.034
Mn	0.005	0.007	0.015	0.007	0.006	0.015	0.008	0.015	0.014
Fe^{2+}	0.135	0.154	0.411	0.155	0.140	0.412	0.148	0.409	0.408
Na	0.066	0.045	0.001	0.040	0.037	0.002	0.038	0.001	0.000
Total	3.978	4.005	4.002	4.003	4.004	3.997	3.996	4.006	3.998
Calculated WoEnFs									
Wo	45.2	44.7	1.15	44.7	45.7	1.46	45.1	1.85	1.71
En	47.1	46.9	77.6	46.8	46.7	77.0	46.7	77.0	77.1
Fs	7.74	8.41	21.3	8.45	7.56	21.5	8.15	21.2	21.2
Lindsley WoEnFs									
Wo	39.6	42.1	1.16	41.9	48.0	1.48	42.1	1.87	1.73
En	52.1	49.9	78.2	50.0	45.6	77.6	49.7	77.5	77.6
Fs	8.27	8.05	20.6	8.18	7.00	20.9	8.22	20.6	20.6

Appendix E: (continued)

Meteorite	Jhung	Jhung	Jhung	Jhung	Jhung	Jhung	Kingfisher	Kingfisher	Kingfisher
Type/Shock	L5, S3	L5, S3	L5, S3	L5, S3	L5, S3	L5, S3	L5, S6	L5, S6	L5, S6
Mineral	augite	opx	augite	opx	augite	opx	opx	augite	opx
Point	cpx7	opx7	cpx8	opx8	cpx9	opx9	cpx1a	cpx1b	opx1
SiO_2	54.1	55.4	53.6	55.1	53.5	55.4	54.5	53.5	55.2
TiO_2	0.48	0.17	0.47	0.17	0.37	0.19	0.23	0.46	0.14
Al_2O_3	0.51	0.14	0.49	0.15	0.46	0.18	0.22	0.50	0.16
Cr_2O_3	0.77	0.08	0.73	0.09	0.78	0.16	0.23	0.81	0.13
MgO	16.3	29.0	16.9	28.7	16.5	28.8	28.4	16.7	28.8
CaO	22.0	0.73	21.8	0.68	21.9	0.70	1.54	21.9	0.75
MnO	0.25	0.53	0.25	0.48	0.25	0.45	0.47	0.22	0.46
FeO	4.83	13.5	5.23	14.0	5.32	13.8	13.2	4.66	13.2
Na_2O	0.54	<0.02	0.51	<0.02	0.56	<0.02	0.04	0.65	<0.02
Total	99.77	99.56	99.97	99.46	99.71	99.67	98.83	99.27	98.85
# of Oxygens	6	6	6	6	6	6	6	6	6
Si	1.987	1.988	1.970	1.986	1.974	1.989	1.976	1.975	1.993
Ti	0.013	0.005	0.013	0.005	0.010	0.005	0.006	0.013	0.004
Al	0.022	0.006	0.021	0.006	0.020	0.008	0.009	0.022	0.007
Cr	0.022	0.002	0.021	0.003	0.023	0.004	0.007	0.024	0.004
Mg	0.894	1.553	0.924	1.542	0.909	1.539	1.535	0.917	1.548
Ca	0.864	0.028	0.859	0.026	0.866	0.027	0.060	0.865	0.029
Mn	0.008	0.016	0.008	0.015	0.008	0.014	0.014	0.007	0.014
Fe^{2+}	0.148	0.406	0.161	0.422	0.164	0.415	0.401	0.144	0.400
Na	0.038	0.000	0.036	0.000	0.040	0.000	0.003	0.046	0.001
Total	3.996	4.004	4.013	4.005	4.014	4.001	4.011	4.013	3.998
Calculated WoEnFs									
Wo	45.1	1.40	44.0	1.30	44.5	1.35	2.99	44.7	1.46
En	46.7	77.5	47.3	76.9	46.7	77.1	76.4	47.4	77.8
Fs	8.15	21.1	8.66	21.8	8.83	21.5	20.6	7.81	20.8
Lindsley WoEnFs									
Wo	42.1	1.41	42.9	1.31	43.3	1.37	3.05	43.1	1.47
En	49.7	78.2	49.5	77.5	49.1	77.7	77.2	50.2	78.3
Fs	8.22	20.4	7.61	21.2	7.61	20.9	19.8	6.73	20.2

Meteorite	Kingfisher	Kingfisher	Kingfisher	Kingfisher	Kingfisher	Kingfisher	Long Island	Long Island	Long Island
Type/Shock	L5, S6	L5, S6	L5, S6	L5, S6	L5, S6	L5, S6	L6, S4	L6, S4	L6, S4
Mineral	augite	opx	augite	opx	opx	opx	augite	augite	opx
Point	cpx2	opx2	cpx3	opx3	opx4	opx5	cpx1a	cpx1b	opx1
SiO_2	52.3	54.7	53.2	55.1	54.9	54.1	52.8	53.2	54.8
TiO_2	0.61	0.23	0.46	0.12	0.16	0.18	0.43	0.45	0.17
Al_2O_3	0.84	0.22	0.47	0.11	0.16	0.19	0.53	0.51	0.16
Cr_2O_3	0.94	0.21	1.01	0.09	0.12	0.09	0.72	0.80	0.13
MgO	16.3	28.3	16.5	28.8	28.8	27.7	15.7	16.2	28.6
CaO	21.3	0.97	20.5	0.97	0.98	0.87	21.8	21.9	0.90
MnO	0.24	0.44	0.30	0.40	0.47	0.49	0.22	0.23	0.45
FeO	5.41	13.6	5.79	13.3	13.4	14.9	5.80	4.81	13.8
Na_2O	0.68	0.03	0.66	<0.02	0.04	0.03	0.51	0.55	0.02
Total	98.62	98.67	98.92	98.90	99.08	98.56	98.59	98.69	98.95
# of Oxygens	6	6	6	6	6	6	6	6	6
Si	1.954	1.985	1.977	1.991	1.984	1.979	1.976	1.979	1.984
Ti	0.017	0.007	0.013	0.003	0.004	0.005	0.012	0.013	0.005
Al	0.037	0.010	0.021	0.005	0.007	0.008	0.023	0.022	0.007
Cr	0.028	0.006	0.030	0.003	0.003	0.003	0.021	0.023	0.004
Mg	0.908	1.530	0.915	1.549	1.551	1.509	0.877	0.898	1.541
Ca	0.852	0.038	0.817	0.038	0.038	0.034	0.874	0.874	0.035
Mn	0.007	0.014	0.009	0.012	0.014	0.015	0.007	0.007	0.014
Fe^{2+}	0.169	0.413	0.180	0.402	0.405	0.457	0.181	0.150	0.417
Na	0.049	0.002	0.048	0.001	0.002	0.002	0.037	0.039	0.001
Total	4.021	4.003	4.010	4.004	4.008	4.012	4.008	4.005	4.008
Calculated WoEnFs									
Wo	44.0	1.88	42.5	1.90	1.89	1.69	45.1	45.3	1.74
En	46.9	76.7	47.6	77.4	77.2	74.9	45.2	46.6	76.8
Fs	9.09	21.4	9.84	20.7	20.9	23.4	9.70	8.14	21.5
Lindsley WoEnFs									
Wo	42.9	1.90	40.1	1.92	1.92	1.72	43.5	43.1	1.77
En	49.7	77.2	50.7	77.9	78.0	75.8	47.6	49.3	77.4
Fs	7.44	20.9	9.15	20.2	20.0	22.5	8.95	7.68	20.8

Meteorite	Long Island	Long Island	Long Island	Long Island	Long Island	Long Island	Long Island	Long Island	Long Island
Type/Shock	L6, S4	L6, S4	L6, S4	L6, S4	L6, S4	L6, S4	L6, S4	L6, S4	L6, S4
Mineral	augite	opx	augite	opx	augite	opx	augite	opx	augite
Point	cpx2	opx2	cpx3	opx3	cpx4	opx4	cpx5	opx5	cpx6
SiO_2	53.4	54.8	53.6	54.6	52.5	55.1	53.2	54.5	53.2
TiO_2	0.48	0.18	0.45	0.20	0.43	0.20	0.43	0.17	0.41
Al_2O_3	0.50	0.16	0.49	0.14	0.48	0.16	0.49	0.17	0.51
Cr_2O_3	0.67	0.13	0.82	0.06	0.80	0.15	0.84	0.12	0.75
MgO	16.1	28.4	16.4	28.5	16.1	28.7	16.3	28.7	16.4
CaO	22.4	0.84	21.4	1.11	21.7	0.65	21.7	0.75	22.1
MnO	0.20	0.43	0.22	0.48	0.22	0.52	0.24	0.55	0.17
FeO	4.18	13.8	4.85	13.6	6.14	14.0	5.13	13.7	4.90
Na_2O	0.53	≤0.02	0.54	≤0.02	0.50	≤0.02	0.56	≤0.02	0.51
Total	98.49	98.81	98.77	98.68	98.85	99.44	98.85	98.70	98.90
# of Oxygens	6	6	6	6	6	6	6	6	6
Si	1.985	1.986	1.987	1.983	1.963	1.984	1.976	1.978	1.974
Ti	0.013	0.005	0.013	0.005	0.012	0.005	0.012	0.005	0.012
Al	0.022	0.007	0.021	0.006	0.021	0.007	0.022	0.007	0.022
Cr	0.020	0.004	0.024	0.002	0.024	0.004	0.025	0.003	0.022
Mg	0.893	1.537	0.906	1.540	0.895	1.543	0.902	1.555	0.906
Ca	0.893	0.032	0.851	0.043	0.871	0.025	0.866	0.029	0.880
Mn	0.006	0.013	0.007	0.015	0.007	0.016	0.008	0.017	0.005
Fe^{2+}	0.130	0.420	0.150	0.414	0.192	0.422	0.160	0.417	0.152
Na	0.038	0.000	0.039	0.000	0.036	0.000	0.040	0.001	0.037
Total	4.000	4.004	3.998	4.008	4.021	4.006	4.011	4.012	4.010
Calculated WoEnFs									
Wo	46.5	1.60	44.5	2.14	44.3	1.25	44.7	1.44	45.3
En	46.5	76.8	47.3	76.5	45.5	76.9	46.6	77.1	46.6
Fs	7.08	21.6	8.20	21.3	10.1	21.8	8.68	21.5	8.08
Lindsley WoEnFs									
Wo	43.7	1.62	41.4	2.17	43.6	1.26	42.8	1.47	43.8
En	49.2	77.3	50.3	77.3	47.5	77.6	49.3	78.1	49.0
Fs	7.16	21.1	8.33	20.5	8.87	21.1	7.92	20.4	7.29

Appendix E: (continued)

Meteorite	Long Island	Long Island	Long Island	Long Island	Long Island	Tenham	Tenham	Tenham	Tenham
Type/Shock	L6, S4	L6, S4	L6, S4	L6, S4	L6, S4	L6, S4	L6, S4	L6, S4	L6, S4
Mineral	opx	augite	opx	augite	opx	augite	opx	augite	opx
Point	opx6	cpx7	opx7	cpx8	opx8	cpx1	opx1	cpx2	opx2
SiO_2	54.6	53.1	54.3	53.4	54.8	52.8	54.8	53.2	54.7
TiO_2	0.22	0.44	0.21	0.50	0.13	0.47	0.16	0.42	0.24
Al_2O_3	0.18	0.50	0.20	0.51	0.16	0.53	0.16	0.52	0.17
Cr_2O_3	0.15	0.65	0.11	0.71	0.11	0.89	0.13	0.86	0.09
MgO	28.5	16.3	28.3	16.3	28.5	16.4	28.8	16.4	29.0
CaO	0.91	22.0	0.74	21.9	0.80	21.8	0.80	21.6	0.65
MnO	0.47	0.17	0.47	0.24	0.45	0.23	0.51	0.24	0.47
FeO	13.7	4.76	14.3	5.08	13.6	4.81	13.3	4.83	13.5
Na_2O	<0.02	0.50	<0.02	0.49	<0.02	0.58	0.03	0.59	<0.02
Total	98.65	98.51	98.65	99.11	98.57	98.52	98.70	98.56	98.77
# of Oxygens	6	6	6	6	6	6	6	6	6
Si	1.982	1.978	1.977	1.977	1.988	1.969	1.986	1.979	1.979
Ti	0.006	0.012	0.006	0.014	0.004	0.013	0.004	0.012	0.007
Al	0.008	0.022	0.009	0.022	0.007	0.024	0.007	0.023	0.007
Cr	0.004	0.019	0.003	0.021	0.003	0.026	0.004	0.025	0.003
Mg	1.540	0.907	1.538	0.901	1.544	0.912	1.554	0.909	1.567
Ca	0.035	0.879	0.029	0.870	0.031	0.871	0.031	0.859	0.025
Mn	0.015	0.005	0.014	0.007	0.014	0.007	0.016	0.008	0.014
Fe^{2+}	0.415	0.148	0.437	0.157	0.412	0.150	0.402	0.150	0.407
Na	0.000	0.036	0.001	0.035	0.000	0.042	0.002	0.042	0.000
Total	4.005	4.006	4.014	4.004	4.003	4.014	4.006	4.007	4.010
Calculated WoEnFs									
Wo	1.75	45.3	1.44	45.0	1.55	44.9	1.55	44.6	1.26
En	76.8	46.8	76.2	46.6	77.2	47.0	77.6	47.2	77.8
Fs	21.4	7.89	22.3	8.48	21.3	8.11	20.9	8.19	20.9
Lindsley WoEnFs									
Wo	1.77	43.8	1.47	42.9	1.57	43.2	1.58	42.4	1.28
En	77.5	49.1	77.1	49.0	77.7	49.7	78.4	50.1	78.6
Fs	20.8	7.19	21.5	8.06	20.7	7.09	20.1	7.54	20.2

Appendix E: (continued)

Meteorite	Tenham	Tenham	Tenham	Tenham	Tenham	Tenham	Tenham	Tenham	Tenham
Type/Shock	L6, S4	L6, S4	L6, S4	L6, S4	L6, S4	L6, S4	L6, S4	L6, S4	L6, S4
Mineral	augite	opx	augite	opx	augite	opx	augite	opx	augite
Point	cpx3	opx3	cpx4	opx4	cpx5	opx5	cpx6	opx6	cpx7
SiO_2	53.4	54.8	53.0	54.4	53.8	54.9	54.0	55.4	53.9
TiO_2	0.48	0.18	0.52	0.20	0.49	0.21	0.48	0.17	0.52
Al_2O_3	0.59	0.18	0.58	0.17	0.52	0.19	0.51	0.17	0.51
Cr_2O_3	0.90	0.08	0.78	0.13	0.85	0.10	0.88	0.09	0.77
MgO	16.5	28.9	16.2	29.1	16.4	28.2	16.4	28.5	16.2
CaO	21.8	0.77	21.8	0.62	21.6	0.71	21.4	0.75	21.9
MnO	0.22	0.53	0.22	0.51	0.24	0.49	0.22	0.50	0.21
FeO	4.60	13.2	4.98	13.8	5.15	14.2	5.20	13.7	4.75
Na_2O	0.59	0.03	0.53	0.02	0.60	<0.02	0.57	<0.02	0.55
Total	99.08	98.71	98.69	99.02	99.75	99.00	99.64	99.27	99.42
# of Oxygens	6	6	6	6	6	6	6	6	6
Si	1.975	1.984	1.973	1.971	1.981	1.988	1.987	1.994	1.987
Ti	0.013	0.005	0.015	0.006	0.014	0.006	0.013	0.005	0.014
Al	0.026	0.008	0.025	0.007	0.023	0.008	0.022	0.007	0.022
Cr	0.026	0.002	0.023	0.004	0.025	0.003	0.026	0.003	0.022
Mg	0.911	1.560	0.901	1.573	0.899	1.522	0.897	1.531	0.892
Ca	0.865	0.030	0.870	0.024	0.853	0.027	0.845	0.029	0.866
Mn	0.007	0.016	0.007	0.016	0.008	0.015	0.007	0.015	0.007
Fe^{2+}	0.142	0.400	0.155	0.418	0.158	0.430	0.160	0.412	0.146
Na	0.043	0.002	0.038	0.002	0.043	0.001	0.040	0.001	0.039
Total	4.007	4.007	4.007	4.019	4.003	4.001	3.997	3.997	3.996
Calculated WoEnFs									
Wo	44.9	1.49	45.0	1.18	44.5	1.37	44.3	1.44	45.3
En	47.3	77.8	46.6	77.5	46.9	76.3	47.0	77.0	46.7
Fs	7.76	20.8	8.39	21.4	8.65	22.3	8.74	21.5	7.99
Lindsley WoEnFs									
Wo	42.6	1.52	43.0	1.21	41.7	1.39	41.0	1.46	42.2
En	50.3	78.6	49.2	78.7	49.9	76.9	50.1	77.6	49.7
Fs	7.08	19.9	7.77	20.1	8.45	21.7	8.94	20.9	8.14

Appendix E: (continued)

Meteorite	Tenham	Tenham	Tenham	Tenham	Tenham	Fisher	Fisher	Fisher	Fisher
Type/Shock	L6, S4	L6, S4	L6, S4	L6, S4	L6, S4	L6, S5	L6, S5	L6, S5	L6, S5
Mineral	opx	augite	opx	augite	opx	augite	opx	opx	augite
Point	opx7	cpx8	opx8	cpx9	opx9	cpx1	opx1a	opx1b	cpx2a
SiO_2	55.4	53.4	55.3	53.7	55.2	53.4	55.1	55.0	53.7
TiO_2	0.21	0.52	0.19	0.45	0.21	0.49	0.21	0.18	0.43
Al_2O_3	0.16	0.52	0.15	0.53	0.19	0.49	0.17	0.17	0.60
Cr_2O_3	0.10	0.86	0.08	0.86	0.10	0.77	0.12	0.09	0.67
MgO	28.5	16.2	28.6	16.3	28.4	16.5	29.1	28.7	16.4
CaO	0.77	21.3	0.75	21.5	0.79	21.8	0.74	0.71	22.2
MnO	0.45	0.18	0.43	0.24	0.44	0.24	0.46	0.45	0.20
FeO	13.7	5.30	13.9	5.08	13.8	4.70	13.6	13.9	4.41
Na_2O	0.02	0.60	0.04	0.56	0.02	0.52	≤0.02	≤0.02	0.58
Total	99.31	98.92	99.44	99.18	99.15	98.88	99.46	99.20	99.26
# of Oxygens	6	6	6	6	6	6	6	6	6
Si	1.994	1.983	1.991	1.985	1.991	1.980	1.982	1.985	1.981
Ti	0.006	0.015	0.005	0.013	0.006	0.014	0.006	0.005	0.012
Al	0.007	0.023	0.006	0.023	0.008	0.021	0.007	0.007	0.026
Cr	0.003	0.025	0.002	0.025	0.003	0.022	0.003	0.003	0.020
Mg	1.531	0.896	1.534	0.897	1.529	0.910	1.558	1.545	0.903
Ca	0.030	0.846	0.029	0.852	0.031	0.865	0.028	0.028	0.879
Mn	0.014	0.006	0.013	0.008	0.013	0.008	0.014	0.014	0.006
Fe^{2+}	0.412	0.165	0.417	0.157	0.417	0.146	0.408	0.419	0.136
Na	0.002	0.043	0.003	0.040	0.001	0.037	0.000	0.001	0.041
Total	3.997	4.000	4.001	3.999	3.999	4.003	4.006	4.007	4.004
Calculated WoEnFs									
Wo	1.49	44.2	1.45	44.5	1.54	44.8	1.39	1.40	45.7
En	77.1	46.9	77.0	46.9	76.8	47.2	77.6	77.0	46.9
Fs	21.4	8.91	21.6	8.61	21.6	7.98	21.0	21.6	7.38
Lindsley WoEnFs									
Wo	2.71	41.1	1.46	41.3	1.55	42.5	1.41	1.41	43.4
En	76.7	49.8	77.5	49.9	77.3	49.9	78.2	77.7	49.6
Fs	20.9	9.08	21.1	8.75	21.1	7.67	20.3	20.9	6.98

Meteorite	Fisher	Fisher	Fisher	Fisher	Fisher	Fisher	Fisher	Fisher	Fisher
Type/Shock	L6, S5	L6, S5	L6, S5	L6, S5	L6, S5	L6, S5	L6, S5	L6, S5	L6, S5
Mineral	augite	opx	augite	augite	opx	augite	opx	augite	opx
Point	cpx2b	opx2	cpx3a	cpx3b	opx3	cpx4	opx4	cpx5	opx5
SiO_2	53.7	55.1	53.7	53.6	55.2	53.7	54.9	52.2	54.9
TiO_2	0.41	0.19	0.49	0.47	0.19	0.47	0.18	0.49	0.22
Al_2O_3	0.47	0.16	0.57	0.58	0.16	0.50	0.16	0.51	0.16
Cr_2O_3	0.76	0.15	0.82	0.70	0.07	0.83	0.04	0.79	0.10
MgO	16.2	28.6	16.4	16.2	28.7	16.5	29.0	16.0	28.8
CaO	21.8	0.75	21.7	21.6	0.72	21.8	0.68	21.2	0.61
MnO	0.20	0.47	0.26	0.20	0.49	0.23	0.47	0.23	0.50
FeO	4.59	13.8	4.71	5.10	13.9	4.98	13.6	7.06	13.8
Na_2O	0.55	<0.02	0.56	0.56	0.03	0.57	<0.02	0.57	0.02
Total	98.76	99.22	99.17	99.10	99.42	99.55	99.10	99.09	99.02
# of Oxygens	6	6	6	6	6	6	6	6	6
Si	1.990	1.989	1.982	1.984	1.987	1.979	1.982	1.956	1.984
Ti	0.012	0.005	0.014	0.013	0.005	0.013	0.005	0.014	0.006
Al	0.021	0.007	0.025	0.025	0.007	0.022	0.007	0.023	0.007
Cr	0.022	0.004	0.024	0.020	0.002	0.024	0.001	0.023	0.003
Mg	0.898	1.536	0.902	0.896	1.540	0.905	1.562	0.892	1.550
Ca	0.868	0.029	0.859	0.857	0.028	0.862	0.026	0.851	0.023
Mn	0.006	0.014	0.008	0.006	0.015	0.007	0.014	0.007	0.015
Fe^{2+}	0.142	0.416	0.146	0.158	0.420	0.153	0.412	0.221	0.416
Na	0.040	0.001	0.040	0.040	0.002	0.041	0.000	0.041	0.002
Total	3.999	4.001	4.000	3.999	4.006	4.006	4.009	4.028	4.006
Calculated WoEnFs									
Wo	45.4	1.45	44.9	44.7	1.40	44.7	1.29	43.2	1.15
En	46.9	77.0	47.1	46.7	76.9	47.0	77.6	45.3	77.3
Fs	7.73	21.6	8.04	8.56	21.7	8.30	21.2	11.6	21.5
Lindsley WoEnFs									
Wo	42.3	1.47	41.8	41.9	1.42	42.5	1.31	43.1	1.16
En	49.8	77.5	50.1	49.4	77.6	49.7	78.4	47.0	78.0
Fs	7.88	21.0	8.11	8.66	21.0	7.81	20.3	9.86	20.8

Meteorite	Fisher	Kyushu	Kyushu	Kyushu	Kyushu	Kyushu	Kyushu	Kyushu	Kyushu
Type/Shock	L6, S5	L6, S5	L6, S5	L6, S5	L6, S5	L6, S5	L6, S5	L6, S5	L6, S5
Mineral	augite	augite	opx	augite	opx	augite	opx	augite	augite
Point	cpx6	cpx1	opx1	cpx2	opx2	cpx3	opx3	cpx4a	cpx4b
SiO_2	53.4	53.4	54.8	52.8	54.9	53.3	55.2	53.5	53.8
TiO_2	0.50	0.47	0.21	0.49	0.19	0.44	0.20	0.49	0.51
Al_2O_3	0.51	0.51	0.16	0.53	0.15	0.46	0.16	0.51	0.51
Cr_2O_3	0.81	0.82	0.14	0.88	0.11	0.72	0.14	0.78	0.86
MgO	16.5	16.6	28.7	16.6	28.7	17.0	28.9	16.4	16.4
CaO	22.0	21.7	0.80	21.5	0.53	21.8	0.84	21.7	21.5
MnO	0.21	0.21	0.48	0.24	0.43	0.27	0.46	0.24	0.26
FeO	4.98	5.12	13.8	5.35	13.9	4.62	13.9	4.95	5.11
Na_2O	0.56	0.59	0.02	0.57	<0.02	0.46	0.02	0.55	0.59
Total	99.46	99.48	99.03	98.90	98.89	98.99	99.89	99.16	99.48
# of Oxygens	6	6	6	6	6	6	6	6	6
Si	1.971	1.972	1.982	1.966	1.986	1.972	1.981	1.979	1.983
Ti	0.014	0.013	0.006	0.014	0.005	0.012	0.006	0.013	0.014
Al	0.022	0.022	0.007	0.023	0.006	0.020	0.007	0.022	0.022
Cr	0.024	0.024	0.004	0.026	0.003	0.021	0.004	0.023	0.025
Mg	0.910	0.916	1.547	0.918	1.549	0.938	1.548	0.906	0.899
Ca	0.870	0.859	0.031	0.855	0.021	0.863	0.032	0.861	0.849
Mn	0.007	0.006	0.015	0.007	0.013	0.009	0.014	0.008	0.008
Fe^{2+}	0.154	0.158	0.416	0.166	0.420	0.143	0.417	0.153	0.157
Na	0.040	0.042	0.001	0.041	0.000	0.033	0.001	0.039	0.042
Total	4.012	4.012	4.009	4.016	4.003	4.011	4.010	4.004	3.999
Calculated WoEnFs									
Wo	44.8	44.3	1.54	43.9	1.05	44.2	1.59	44.7	44.4
En	46.9	47.2	77.0	47.2	77.3	48.0	77.0	47.0	47.0
Fs	8.29	8.46	21.5	8.89	21.6	7.78	21.4	8.35	8.63
Lindsley WoEnFs									
Wo	43.2	42.8	1.57	42.5	1.06	42.9	1.62	42.4	41.3
En	49.4	49.8	77.7	49.7	77.9	50.3	77.7	49.7	50.1
Fs	7.44	7.50	20.7	7.84	21.1	6.81	20.7	7.85	8.69

Appendix E: (continued)

Meteorite	Kyushu	Kyushu	Kyushu	Kyushu	Kyushu	Kyushu
Type/Shock	L6, S5	L6, S5	L6, S5	L6, S5	L6, S5	L6, S5
Mineral	opx	augite	augite	opx	opx	opx
Point	opx4	cpx5a	cpx5b	opx5	opx6	opx7
SiO_2	55.2	53.7	53.6	55.2	54.5	54.4
TiO_2	0.20	0.47	0.44	0.23	0.21	0.20
Al_2O_3	0.18	0.45	0.50	0.14	0.23	0.17
Cr_2O_3	0.14	0.70	0.63	0.12	0.14	0.06
MgO	28.6	16.8	16.5	28.5	28.1	28.9
CaO	0.84	22.0	22.1	0.77	1.60	0.73
MnO	0.41	0.28	0.25	0.50	0.47	0.44
FeO	13.7	4.47	4.40	14.1	13.7	13.8
Na_2O	0.03	0.47	0.52	≤0.02	0.04	≤0.02
Total	99.28	99.29	98.98	99.63	99.03	98.71
# of Oxygens	6	6	6	6	6	6
Si	1.988	1.979	1.984	1.986	1.978	1.975
Ti	0.006	0.013	0.012	0.006	0.006	0.005
Al	0.007	0.020	0.022	0.006	0.010	0.007
Cr	0.004	0.020	0.018	0.003	0.004	0.002
Mg	1.538	0.924	0.908	1.530	1.517	1.565
Ca	0.032	0.868	0.876	0.029	0.062	0.028
Mn	0.012	0.009	0.008	0.015	0.015	0.013
Fe^{2+}	0.412	0.138	0.136	0.425	0.417	0.418
Na	0.002	0.034	0.037	0.001	0.003	0.000
Total	4.001	4.005	4.001	4.001	4.012	4.013
Calculated WoEnFs						
Wo	1.60	44.8	45.4	1.45	3.08	1.38
En	77.1	47.7	47.1	76.5	75.4	77.3
Fs	21.3	7.58	7.47	22.0	21.5	21.3
Lindsley WoEnFs						
Wo	1.62	42.9	43.2	1.47	3.1	1.42
En	77.6	50.1	49.7	77.1	76.3	78.3
Fs	20.8	7.00	7.17	21.4	20.5	20.3

Meteorite	ALH85045	ALH85045	ALH85045	ALH85045	ALH85045	ALH85045	ALH85045	ALH85045
Type/Shock	L3, S2	L3, S2	L3, S2	L3, S2	L3, S2	L3, S2	L3, S2	L3, S2
Mineral	troilite	kamacite	troilite	kamacite	troilite	kamacite	troilite	kamacite
Point	SM1	MS1	SM2	MS2	SM3	MS3	SM4	MS4
P	0.00	0.00	0.00	0.00	0.00	0.00	<0.03	<0.03
S	36.2	0.04	36.2	0.04	36.2	0.05	36.2	0.02
Fe	62.7	93.0	63.0	94.6	62.3	94.4	62.9	92.9
Co	0.00	0.85	0.00	0.77	<0.06	0.79	0.00	0.73
Ni	<0.04	4.42	0.06	3.79	0.05	5.31	0.10	4.55
Total	98.94	98.30	99.24	99.17	98.59	100.52	99.11	98.23
Normalized Atomic Concentration								
P	0.00	0.00	0.00	0.00	0.00	0.00	0.00	0.00
S	50.1	0.07	50.0	0.06	50.3	0.09	50.0	0.04
Fe	49.8	94.8	50.0	95.6	49.7	94.1	49.9	94.8
Co	0.00	0.82	0.00	0.74	0.00	0.75	0.00	0.71
Ni	0.00	4.29	0.04	3.64	0.04	5.03	0.07	4.41
Total	99.98	100.00	100.00	100.00	99.99	100.00	99.99	99.98

Meteorite	ALH85045	ALH85045	ALH85045	ALH85045	ALH85045	ALH85045	ALH85045	ALH85045
Type/Shock	L3, S2	L3, S2	L3, S2	L3, S2	L3, S2	L3, S2	L3, S2	L3, S2
Mineral	troilite	kamacite	troilite	tetrataenite	troilite	taenite	troilite	kamacite
Point	SM5	MS5	SM6	MS6	SM7	MS7	SM8	MS8
P	0.00	0.00	0.00	<0.03	0.00	0.00	0.00	0.00
S	36.3	0.04	36.3	0.06	36.4	0.03	36.2	0.04
Fe	63.1	93.0	62.6	47.4	63.3	59.2	62.8	94.2
Co	0.00	0.81	0.00	0.08	0.06	0.12	<0.06	0.72
Ni	<0.04	4.87	0.06	51.3	0.22	39.1	0.12	4.06
Total	99.46	98.70	98.95	98.86	99.96	98.46	99.11	99.02
Normalized Atomic Concentration								
P	0.00	0.00	0.00	0.00	0.00	0.00	0.00	0.00
S	50.1	0.06	50.2	0.10	50.0	0.05	50.0	0.08
Fe	49.9	94.5	49.7	49.2	49.8	61.3	49.9	95.3
Co	0.00	0.78	0.00	0.08	0.04	0.12	0.00	0.69
Ni	0.00	4.71	0.05	50.6	0.16	38.5	0.09	3.91
Total	99.99	100.00	100.00	99.97	100.00	100.00	99.99	100.00

Meteorite	ALH85045	ALH85045	ALH85045	ALH85045	ALH85045	ALH85045	LEW86204	LEW86204
Type/Shock	L3, S2	L3, S2	L3, S2	L3, S2	L3, S2	L3, S2	L4, S3	L4, S3
Mineral	troilite	kamacite	troilite	kamacite	troilite	tetrataenite	troilite	taenite
Point	SM9	MS9	SM10	MS10	SM11	MS11	SM1	MS1
P	0.00	<0.03	0.00	<0.03	0.03	0.00	<0.03	0.00
S	36.2	0.02	35.6	0.02	35.9	0.02	36.4	0.03
Fe	63.0	92.7	63.0	92.9	62.9	47.8	62.7	65.2
Co	0.00	0.80	0.00	0.80	0.00	0.08	0.00	0.16
Ni	<0.04	5.67	0.04	5.20	0.20	50.3	0.18	33.3
Total	99.20	99.20	98.67	98.91	98.99	98.25	99.31	98.68
Normalized Atomic Concentration								
P	0.00	0.00	0.00	0.00	0.04	0.00	0.00	0.00
S	50.0	0.04	49.6	0.03	49.7	0.04	50.2	0.06
Fe	50.0	93.7	50.4	94.2	50.1	49.9	49.7	67.1
Co	0.00	0.77	0.00	0.77	0.00	0.08	0.00	0.15
Ni	0.00	5.45	0.03	5.01	0.15	50.0	0.14	32.7
Total	99.99	99.98	100.00	99.97	100.00	100.00	99.97	100.00

Meteorite	LEW86204	LEW86204	LEW86204	LEW86204	LEW86204	LEW86204	LEW86204	LEW86204
Type/Shock	L4, S3	L4, S3	L4, S3	L4, S3	L4, S3	L4, S3	L4, S3	L4, S3
Mineral	troilite	tetrataenite	troilite	kamacite	troilite	kamacite	troilite	tetrataenite
Point	SM2	MS2	SM3	MS3	SM4	MS4	SM5	MS5
P	<0.03	0.00	0.00	<0.03	<0.03	0.05	0.03	0.05
S	36.3	0.04	36.3	<0.02	36.4	<0.02	36.7	0.03
Fe	62.6	46.3	63.2	93.5	62.8	93.3	62.2	49.3
Co	0.00	0.06	<0.06	0.55	<0.06	0.63	0.00	0.11
Ni	0.08	53.2	0.04	5.49	<0.04	5.11	0.10	49.7
Total	98.96	99.56	99.46	99.55	99.18	99.07	99.03	99.24
Normalized Atomic Concentration								
P	0.00	0.00	0.00	0.00	0.00	0.09	0.04	0.09
S	50.2	0.07	50.0	0.00	50.2	0.00	50.6	0.05
Fe	49.7	47.7	50.0	94.2	49.7	94.4	49.2	50.9
Co	0.00	0.06	0.00	0.53	0.00	0.60	0.00	0.11
Ni	0.06	52.2	0.03	5.26	0.03	4.92	0.08	48.8
Total	99.98	100.00	99.97	99.95	99.96	99.98	100.00	100.00

Meteorite	LEW86204	LEW86204	LEW86204	LEW86204	LEW86204	LEW86204	LEW86204	LEW86204
Type/Shock	L4, S3	L4, S3	L4, S3	L4, S3	L4, S3	L4, S3	L4, S3	L4, S3
Mineral	troilite	tetrataenite	troilite	kamacite	troilite	tetrataenite	troilite	tetrataenite
Point	SM6	MS6	SM7	MS7	SM8	MS8	SM9	MS9
P	0.00	0.00	0.00	0.00	0.00	0.00	<0.03	<0.03
S	36.4	0.02	36.2	0.02	36.4	0.07	36.3	0.05
Fe	62.9	47.8	63.5	94.3	63.1	45.7	62.9	51.1
Co	<0.06	0.10	0.00	0.57	0.00	0.06	0.00	0.09
Ni	0.15	50.9	<0.04	5.08	0.10	53.1	0.25	48.2
Total	99.49	98.80	99.72	100.00	99.66	98.93	99.41	99.50
Normalized Atomic Concentration								
P	0.00	0.00	0.00	0.00	0.00	0.00	0.00	0.00
S	50.1	0.04	49.8	0.04	50.1	0.12	50.0	0.10
Fe	49.7	49.6	50.1	94.6	49.8	47.4	49.8	52.6
Co	0.00	0.09	0.00	00.54	0.00	0.06	0.00	0.09
Ni	0.11	50.2	0.00	04.84	0.08	52.4	0.19	47.2
Total	99.98	100.00	99.98	100.00	100.00	100.00	99.97	99.99

Meteorite	QUE90201	QUE90201	QUE90201	QUE90201	QUE90201	QUE90201	QUE90201	QUE90201
Type/Shock	L5, S3	L5, S3	L5, S3	L5, S3	L5, S3	L5, S3	L5, S3	L5, S3
Mineral	troilite	taenite	troilite	taenite	troilite	taenite	troilite	taenite
Point	SM1	MS1	SM2	MS2	SM3	MS3	SM4	MS4
P	0.00	0.00	0.04	0.00	<0.03	0.00	<0.03	0.00
S	36.5	0.02	36.1	0.03	36.0	<0.02	36.4	0.04
Fe	62.5	75.0	63.2	75.3	63.0	76.1	63.0	75.5
Co	<0.06	1.01	<0.06	1.04	<0.06	1.02	0.00	1.07
Ni	0.07	22.8	0.19	22.2	0.12	22.0	0.06	22.2
Total	99.07	98.78	99.47	98.54	99.18	99.15	99.47	98.87
Normalized Atomic Concentration								
P	0.00	0.00	0.05	0.00	0.00	0.00	0.00	0.00
S	50.4	0.04	49.8	0.05	49.8	0.00	50.2	0.06
Fe	49.5	76.8	50.0	77.2	50.0	77.7	49.8	77.3
Co	0.00	0.98	0.00	1.01	0.00	0.99	0.00	1.04
Ni	0.05	22.2	0.14	21.7	0.09	21.3	0.05	21.6
Total	99.98	100.00	99.98	100.00	99.94	99.98	99.98	100.00

Meteorite	QUE90201	QUE90201	QUE90201	QUE90201	QUE90201	QUE90201	QUE90201	QUE90201
Type/Shock	L5, S3	L5, S3	L5, S3	L5, S3	L5, S3	L5, S3	L5, S3	L5, S3
Mineral	troilite	taenite	troilite	taenite	troilite	kamacite	troilite	taenite
Point	SM5	MS5	SM6	MS6	SM7	MS7	SM8	MS8
P	<0.03	<0.03	<0.03	<0.03	0.00	0.04	<0.03	0.00
S	36.5	0.04	36.0	0.04	36.7	0.04	36.3	0.02
Fe	62.9	75.5	62.9	75.3	62.3	89.3	62.7	75.7
Co	0.00	1.12	<0.06	1.06	0.08	3.08	<0.06	1.00
Ni	0.07	22.4	0.09	22.3	0.11	7.10	0.06	22.4
Total	99.52	99.08	98.91	98.72	99.17	99.55	99.06	99.11
Normalized Atomic Concentration								
P	0.00	0.00	0.00	0.00	0.00	0.08	0.00	0.00
S	50.3	0.07	49.9	0.07	50.6	0.06	50.2	0.03
Fe	49.7	77.1	50.0	77.1	49.3	90.1	49.7	77.2
Co	0.00	1.08	0.00	1.02	0.06	2.95	0.00	0.96
Ni	0.05	21.7	0.07	21.8	0.08	6.81	0.04	21.8
Total	99.99	99.97	99.96	99.97	100.00	100.00	99.95	100.00

Meteorite	GRO85209	GRO85209	GRO85209	GRO85209	GRO85209	GRO85209	GRO85209	GRO85209
Type/Shock	L6, S3	L6, S3	L6, S3	L6, S3	L6, S3	L6, S3	L6, S3	L6, S3
Mineral	troilite	kamacite	troilite	kamacite	troilite	taenite	troilite	kamacite
Point	SM1	MS1	SM2	MS2	SM3	MS3	SM4	MS4
P	0.00	0.00	0.00	0.03	<0.03	0.00	0.00	0.00
S	35.7	0.02	36.4	0.02	36.3	0.00	35.8	<0.02
Fe	63.1	92.8	63.0	93.2	63.1	52.4	61.4	93.8
Co	<0.06	1.19	<0.06	1.18	<0.06	0.27	0.00	1.27
Ni	<0.04	5.09	<0.04	5.21	0.36	46.9	0.25	4.38
Total	98.78	99.09	99.38	99.69	99.72	99.62	97.40	99.46
Normalized Atomic Concentration								
P	0.00	0.00	0.00	0.06	0.00	0.00	0.00	0.00
S	49.6	0.04	50.2	0.03	49.9	0.00	50.3	0.00
Fe	50.3	93.9	49.8	93.8	49.8	53.9	49.5	94.6
Co	0.00	1.14	0.00	1.12	0.00	0.27	0.00	1.21
Ni	0.00	4.90	0.00	4.99	0.27	45.9	0.20	4.20
Total	99.95	100.00	99.96	100.00	99.96	100.00	100.00	99.99

Meteorite	GRO85209	GRO85209	GRO85209	GRO85209	GRO85209	GRO85209	GRO85209	GRO85209
Type/Shock	L6, S3	L6, S3	L6, S3	L6, S3	L6, S3	L6, S3	L6, S3	L6, S3
Mineral	troilite	tetrataenite	troilite	tetrataenite	troilite	tetrataenite	troilite	taenite
Point	SM5	MS5	SM6	MS6	SM7	MS7	SM8	MS8
P	0.00	0.00	<0.03	<0.03	0.00	<0.03	<0.03	0.00
S	36.2	0.05	36.6	0.03	36.5	0.03	36.2	0.03
Fe	62.1	48.6	62.0	45.4	62.5	49.2	62.7	59.4
Co	0.00	0.14	<0.06	0.11	0.00	0.20	<0.06	0.27
Ni	0.09	50.1	0.09	54.3	0.08	50.0	0.21	40.5
Total	98.37	98.85	98.70	99.77	99.12	99.50	99.14	100.25
Normalized Atomic Concentration								
P	0.00	0.00	0.00	0.00	0.00	0.00	0.00	0.00
S	50.32	0.10	50.7	0.05	50.4	0.06	50.0	0.05
Fe	49.62	50.38	49.2	46.7	49.5	50.7	49.8	60.5
Co	0.00	0.14	0.00	0.11	0.00	0.20	0.00	0.26
Ni	0.07	49.39	0.07	53.1	0.06	49.0	0.16	39.2
Total	100.00	100.00	99.96	99.96	100.00	99.96	99.99	100.00

Meteorite	GRO85209	GRO85209	Hallingeberg	Hallingeberg	Hallingeberg	Hallingeberg	Hallingeberg	Hallingeberg
Type/Shock	L6, S3	L6, S3	L3, S3	L3, S3	L3, S3	L3, S3	L3, S3	L3, S3
Mineral	troilite	taenite	troilite	taenite	troilite	tetrataenite	troilite	kamacite
Point	SM9	MS9	SM1	MS1	SM3	MS3	SM4	MS4
P	0.00	0.00	0.00	<0.03	<0.03	0.00	0.00	0.00
S	36.2	0.03	36.1	0.05	36.4	0.04	36.4	0.02
Fe	62.6	52.8	62.7	78.6	63.0	49.9	62.8	93.8
Co	0.00	0.26	<0.06	0.62	0.00	0.19	0.00	0.72
Ni	0.23	46.9	0.23	20.7	0.14	48.6	<0.04	5.29
Total	99.04	99.94	98.99	100.04	99.56	98.80	99.19	99.84
Normalized Atomic Concentration								
P	0.00	0.00	0.00	0.00	0.00	0.00	0.00	0.00
S	50.1	0.06	50.0	0.09	50.1	0.08	50.2	0.03
Fe	49.7	54.0	49.8	79.4	49.8	51.8	49.7	94.2
Co	0.00	0.25	0.00	0.59	0.00	0.18	0.00	0.69
Ni	0.18	45.7	0.18	19.9	0.11	48.0	0.00	5.06
Total	100.00	100.00	99.98	99.99	99.98	100.00	99.97	100.00

Meteorite	Hallingeberg	Hallingeberg	Hallingeberg	Hallingeberg	Hallingeberg	Hallingeberg	Hallingeberg	Hallingeberg
Type/Shock	L3, S3	L3, S3	L3, S3	L3, S3	L3, S3	L3, S3	L3, S3	L3, S3
Mineral	troilite	kamacite	troilite	kamacite	troilite	kamacite	troilite	kamacite
Point	SM5	MS5	SM6	MS6	SM8	MS8	SM9	MS9
P	0.00	0.00	<0.03	<0.03	0.00	0.00	0.00	0.00
S	36.4	0.03	36.6	0.02	36.5	0.00	36.1	0.36
Fe	63.1	95.6	63.2	96.2	63.0	95.8	63.1	92.6
Co	<0.06	0.67	0.00	0.77	0.00	0.71	<0.06	0.72
Ni	<0.04	2.86	<0.04	3.11	<0.04	2.75	0.06	3.23
Total	99.48	99.18	99.84	100.13	99.53	99.27	99.27	96.89
Normalized Atomic Concentration								
P	0.00	0.00	0.00	0.00	0.00	0.00	0.00	0.00
S	50.1	0.05	50.2	0.04	50.2	0.00	49.8	0.64
Fe	49.8	96.6	49.8	96.3	49.7	96.7	50.1	95.5
Co	0.00	0.64	0.00	0.73	0.00	0.68	0.00	0.70
Ni	0.00	2.74	0.00	2.96	0.00	2.64	0.05	3.17
Total	99.97	100.00	99.98	99.97	99.98	99.99	99.99	100.00

Meteorite	Hallingeberg	Hallingeberg	Hallingeberg	Hallingeberg	Hallingeberg	Hallingeberg	Hallingeberg	Hallingeberg
Type/Shock	L3, S3	L3, S3	L3, S3	L3, S3	L3, S3	L3, S3	L3, S3	L3, S3
Mineral	troilite	kamacite	troilite	kamacite	troilite	tetrataenite	troilite	kamacite
Point	SM10	MS10	SM11	MS11	SM13	MS13	SM14	MS14
P	0.00	<0.03	<0.03	0.00	0.00	<0.03	<0.03	<0.03
S	36.8	0.03	36.5	0.00	36.8	0.05	36.4	0.04
Fe	63.3	95.1	63.4	93.8	63.4	49.5	62.9	96.6
Co	<0.06	0.74	0.00	0.67	<0.06	0.08	<0.06	0.89
Ni	0.13	5.33	0.06	5.36	0.38	50.7	<0.04	2.66
Total	100.24	101.21	99.97	99.84	100.53	100.34	99.30	100.21
Normalized Atomic Concentration								
P	0.00	0.00	0.00	0.00	0.00	0.00	0.00	0.00
S	50.2	0.05	50.1	0.00	50.1	0.09	50.1	0.07
Fe	49.7	94.2	49.9	94.2	49.6	50.6	49.8	96.5
Co	0.00	0.69	0.00	0.64	0.00	0.08	0.00	0.85
Ni	0.09	5.02	0.04	5.12	0.29	49.2	0.03	2.53
Total	99.98	99.97	99.98	99.99	99.99	99.98	99.96	99.97

Meteorite	Bjurböle	Bjurböle	Bjurböle	Bjurböle	Bjurböle	Bjurböle	Bjurböle	Bjurböle
Type/Shock	L4, S1	L4, S1	L4, S1	L4, S1	L4, S1	L4, S1	L4, S1	L4, S1
Mineral	troilite	tetrataenite	troilite	taenite	troilite	kamacite	troilite	taenite
Point	SM2	MS2	SM3	MS3	SM4	MS4	SM7	MS7
P	0.00	<0.03	0.00	0.00	0.00	0.00	0.00	0.00
S	36.5	0.03	36.8	0.03	36.8	0.00	36.7	0.03
Fe	62.0	48.4	62.3	63.3	61.9	93.8	62.6	63.8
Co	0.00	0.14	<0.06	0.39	0.06	1.10	<0.06	0.30
Ni	0.11	50.0	0.11	35.1	0.16	5.38	0.12	34.9
Total	98.64	98.62	99.16	98.80	98.85	100.28	99.38	99.06
Normalized Atomic Concentration								
P	0.00	0.00	0.00	0.00	0.00	0.00	0.00	0.00
S	50.6	0.06	50.7	0.05	50.8	0.00	50.5	0.05
Fe	49.3	50.3	49.2	65.2	49.1	93.8	49.4	65.5
Co	0.00	0.14	0.00	0.38	0.05	1.05	0.00	0.29
Ni	0.08	49.5	0.08	34.4	0.12	5.12	0.09	34.1
Total	100.00	99.97	99.97	100.00	100.00	100.00	99.98	100.00

Meteorite	Bjurböle	Bjurböle	Bjurböle	Bjurböle	Bjurböle	Bjurböle	Bjurböle	Bjurböle
Type/Shock	L4, S1	L4, S1	L4, S1	L4, S1	L4, S1	L4, S1	L4, S1	L4, S1
Mineral	troilite	tetrataenite	troilite	taenite	troilite	tetrataenite	troilite	taenite
Point	SM8	MS8	SM10	MS10	SM11	MS11	SM12	MS12
P	0.00	<0.03	<0.03	0.00	0.00	0.03	0.00	0.04
S	36.9	0.02	36.3	<0.02	36.8	<0.02	36.2	0.03
Fe	62.6	47.3	62.6	53.3	62.2	48.0	63.1	53.0
Co	<0.06	0.13	<0.06	0.15	<0.06	0.13	<0.06	0.21
Ni	0.20	52.0	0.15	45.7	0.20	51.0	0.14	46.8
Total	99.68	99.41	99.11	99.20	99.23	99.11	99.53	100.13
Normalized Atomic Concentration								
P	0.00	0.00	0.00	0.00	0.00	0.05	0.00	0.07
S	50.6	0.03	50.2	0.00	50.7	0.00	49.9	0.06
Fe	49.3	48.8	49.7	55.0	49.2	49.6	49.9	54.2
Co	0.00	0.13	0.00	0.15	0.00	0.13	0.00	0.21
Ni	0.15	51.1	0.11	44.9	0.15	50.2	0.11	45.5
Total	99.99	99.99	99.96	99.99	99.99	99.98	99.99	100.00

Meteorite	Bjurböle	Bjurböle	Ausson	Ausson	Ausson	Ausson	Ausson	Ausson
Type/Shock	L4, S1	L4, S1	L5, S2	L5, S2	L5, S2	L5, S2	L5, S2	L5, S2
Mineral	troilite	taenite	troilite	kamacite	troilite	kamacite	troilite	kamacite
Point	SM13	MS13	SM1	MS1	SM2	MS2	SM3	MS3
P	0.00	0.00	0.00	0.00	<0.03	0.03	0.00	<0.03
S	36.5	0.06	36.7	0.00	36.7	<0.02	36.7	0.02
Fe	62.4	55.3	62.1	93.3	62.6	93.2	62.4	94.4
Co	0.00	0.31	0.00	0.55	<0.06	0.54	0.00	0.48
Ni	0.16	43.0	0.05	6.37	0.04	6.45	<0.04	6.11
Total	99.07	98.67	98.91	100.18	99.35	100.17	99.14	100.96
Normalized Atomic Concentration								
P	0.00	0.00	0.00	0.00	0.00	0.05	0.00	0.00
S	50.5	0.12	50.7	0.00	50.5	0.00	50.6	0.03
Fe	49.4	57.2	49.2	93.4	49.5	93.3	49.4	93.7
Co	0.00	0.30	0.00	0.52	0.00	0.51	0.00	0.46
Ni	0.12	42.4	0.04	6.07	0.03	6.14	0.00	5.77
Total	99.99	100.00	100.00	100.00	99.98	99.98	99.98	99.97

Meteorite	Ausson	Ausson	Ausson	Ausson	Ausson	Ausson	Kingfisher	Kingfisher
Type/Shock	L5, S2	L5, S2	L5, S2	L5, S2	L5, S2	L5, S2	L5, S6	L5, S6
Mineral	troilite	taenite	troilite	tetrataenite	troilite	kamacite	troilite	taenite
Point	SM4	MS4	SM5	MS5	SM6	MS6	SM4	MS4
P	<0.03	0.00	0.00	0.04	<0.03	<0.03	0.00	0.00
S	36.9	0.02	36.8	0.02	36.6	<0.02	37.7	<0.02
Fe	62.6	70.8	62.8	47.3	62.1	92.1	58.0	75.5
Co	<0.06	0.16	0.00	0.14	0.00	0.51	<0.06	0.38
Ni	0.07	28.7	<0.04	51.5	0.05	6.44	2.10	22.4
Total	99.58	99.75	99.64	99.03	98.75	99.10	97.81	98.27
Normalized Atomic Concentration								
P	0.00	0.00	0.00	0.07	0.00	0.00	0.00	0.00
S	50.6	0.04	50.5	0.04	50.6	0.00	52.2	0.00
Fe	49.3	72.0	49.5	49.0	49.3	93.3	46.2	77.7
Co	0.00	0.15	0.00	0.14	0.00	0.49	0.00	0.37
Ni	0.05	27.8	0.00	50.8	0.04	6.20	1.59	21.9
Total	99.94	99.99	99.98	100.00	99.98	99.95	99.99	99.98

Meteorite	Kingfisher	Kingfisher	Long Island	Long Island	Long Island	Long Island	Long Island	Long Island
Type/Shock	L5, S6	L5, S6	L6, S4	L6, S4	L6, S4	L6, S4	L6, S4	L6, S4
Mineral	troilite	taenite	troilite	tetrataenite	troilite	taenite	troilite	kamacite
Point	SM5	MS5	SM2	MS2	SM4	MS4	SM5	MS5
P	<0.03	0.00	<0.03	0.00	0.00	0.00	0.00	0.00
S	36.2	<0.02	37.0	0.00	37.3	0.02	37.3	0.03
Fe	59.8	70.5	61.0	47.8	62.0	61.0	62.1	93.5
Co	<0.06	0.26	<0.06	0.13	<0.06	0.45	<0.06	0.81
Ni	2.80	27.9	0.51	50.9	0.14	36.7	0.14	5.37
Total	98.79	98.66	98.50	98.80	99.44	98.10	99.52	99.72
Normalized Atomic Concentration								
P	0.00	0.00	0.00	0.00	0.00	0.00	0.00	0.00
S	50.2	0.00	51.2	0.00	51.1	0.04	51.1	0.06
Fe	47.6	72.4	48.4	49.6	48.8	63.3	48.8	94.0
Co	0.00	0.25	0.00	0.12	0.00	0.44	0.00	0.77
Ni	2.12	27.3	0.39	50.3	0.10	36.2	0.11	5.14
Total	99.94	99.99	99.96	100.00	99.98	100.00	99.99	100.00

Meteorite	Shaw	Shaw	Shaw	Shaw	Shaw	Shaw	Shaw	Shaw
Type/Shock	L7, brec.	L7, brec.	L7, brec.	L7, brec.	L7, brec.	L7, brec.	L7, brec.	L7, brec.
Mineral	troilite	taenite	troilite	taenite	troilite	taenite	troilite	taenite
Point	SM2	MS2	SM4	MS4	SM5	MS5	SM6	MS6
P	<0.03	0.05	<0.03	0.00	0.00	0.00	0.00	0.00
S	34.9	0.03	37.1	0.05	36.0	0.03	36.2	<0.02
Fe	62.7	80.3	62.4	83.4	58.4	85.9	62.6	83.0
Co	0.00	0.56	0.00	0.77	0.40	0.58	0.00	0.70
Ni	0.10	18.1	0.45	16.0	3.83	12.6	0.10	16.3
Total	97.69	99.07	99.91	100.25	98.63	99.06	98.94	100.02
Normalized Atomic Concentration								
P	0.00	0.08	0.00	0.00	0.00	0.00	0.00	0.00
S	49.1	0.06	50.7	0.09	50.1	0.05	50.2	0.00
Fe	50.8	81.8	49.0	83.8	46.6	87.3	49.8	83.7
Co	0.00	0.54	0.00	0.74	0.30	0.55	0.00	0.67
Ni	0.08	17.5	0.34	15.3	2.92	12.1	0.07	15.6
Total	99.98	100.00	99.98	100.00	100.00	100.00	100.00	99.98

Meteorite	Kyushu	Kyushu	Kyushu	Kyushu	Kyushu	Kyushu	Kyushu	Kyushu
Type/Shock	L6, S5	L6, S5	L6, S5	L6, S5	L6, S5	L6, S5	L6, S5	L6, S5
Mineral	troilite	taenite	troilite	kamacite	troilite	taenite	troilite	taenite
Point	SM2	MS2	SM3	MS3	SM4	MS4	SM5	MS5
P	0.00	0.00	<0.03	<0.03	0.04	0.00	<0.03	0.00
S	36.4	0.03	36.8	<0.02	36.7	0.05	36.6	0.05
Fe	61.9	66.7	62.3	91.8	61.7	58.7	62.0	67.8
Co	0.00	0.24	0.00	0.63	0.00	0.21	0.00	0.16
Ni	<0.04	32.9	0.07	6.78	0.11	39.4	0.05	30.6
Total	98.34	99.88	99.21	99.17	98.53	98.35	98.62	98.62
Normalized Atomic Concentration								
P	0.00	0.00	0.00	0.00	0.05	0.00	0.00	0.00
S	50.6	0.06	50.7	0.00	50.8	0.10	50.6	0.08
Fe	49.4	67.9	49.3	92.8	49.1	60.8	49.3	69.8
Co	0.00	0.24	0.00	0.60	0.00	0.21	0.00	0.15
Ni	0.00	31.9	0.06	6.52	0.08	38.9	0.04	30.0
Total	99.98	100.00	99.98	99.95	100.00	100.00	99.97	100.00

Meteorite	Kyushu	Kyushu	Kyushu	Kyushu	McKinney	McKinney	McKinney	McKinney
Type/Shock	L6, S5	L6, S5	L6, S5	L6, S5	L4, S6	L4, S6	L4, S6	L4, S6
Mineral	troilite	kamacite	troilite	taenite	troilite	taenite	troilite	taenite
Point	SM6	MS6	SM7	MS7	SM3	MS3	SM4	MS4
P	0.00	0.00	0.00	<0.03	0.00	0.03	0.03	0.05
S	36.4	0.02	36.5	0.02	36.6	0.05	36.3	0.06
Fe	62.7	91.3	61.5	62.4	62.5	87.6	61.6	85.3
Co	<0.06	0.78	<0.06	0.11	<0.06	0.73	<0.06	0.68
Ni	<0.04	6.90	<0.04	35.6	0.16	11.1	0.34	13.4
Total	99.17	99.02	97.99	98.10	99.30	99.50	98.29	99.54
Normalized Atomic Concentration								
P	0.00	0.00	0.00	0.00	0.00	0.06	0.04	0.09
S	50.3	0.04	50.8	0.03	50.4	0.09	50.5	0.11
Fe	49.7	92.6	49.2	64.7	49.4	88.5	49.2	86.2
Co	0.00	0.75	0.00	0.11	0.00	0.70	0.00	0.65
Ni	0.00	6.65	0.00	35.1	0.12	10.7	0.26	12.9
Total	99.96	100.00	99.97	99.97	99.97	100.00	99.97	100.00

Meteorite	McKinney	McKinney	McKinney	McKinney	Y75097	Y75097	Y75097	Y75097
Type/Shock	L4, S6	L4, S6	L4, S6	L4, S6	breccia	breccia	breccia	breccia
Mineral	troilite	taenite	troilite	taenite	troilite	taenite	troilite	taenite
Point	SM5	MS5	SM6	MS6	SM1	MS1	SM2	MS2
P	<0.03	0.06	<0.03	0.08	0.00	0.00	<0.03	0.00
S	36.6	0.20	36.4	0.08	35.9	0.05	36.5	0.10
Fe	61.5	88.0	62.1	89.2	61.5	58.5	61.9	61.5
Co	0.00	0.60	0.00	0.59	0.00	0.67	0.06	0.48
Ni	0.77	10.7	0.13	9.23	0.17	39.7	0.04	36.1
Total	98.84	99.61	98.61	99.20	97.54	98.92	98.43	98.20
Normalized Atomic Concentration								
P	0.00	0.11	0.00	0.14	0.00	0.00	0.00	0.00
S	50.6	0.34	50.5	0.15	50.3	0.09	50.6	0.19
Fe	48.8	88.7	49.4	90.3	49.5	60.3	49.3	63.7
Co	0.00	0.57	0.00	0.57	0.00	0.65	0.04	0.47
Ni	0.58	10.3	0.10	8.88	0.13	39.0	0.03	35.6
Total	99.98	100.00	99.98	100.00	100.00	100.00	99.97	100.00

Meteorite	Y75097	Y75097	Y75097	Y75097	Y75097	Y75097	Y793241	Y793241
Type/Shock	breccia	breccia	breccia	breccia	breccia	breccia	breccia	breccia
Mineral	troilite	taenite	troilite	taenite	troilite	taenite	troilite	taenite
Point	SM3	MS3	SM4	MS4	SM5	MS5	SM1	MS1
P	<0.03	0.00	0.00	<0.03	0.00	<0.03	0.00	0.04
S	36.3	<0.02	36.7	0.02	36.4	0.09	36.5	0.00
Fe	61.9	64.9	62.1	53.9	62.5	60.1	62.9	50.8
Co	0.00	0.50	<0.06	0.06	<0.06	0.34	0.00	0.15
Ni	0.07	33.4	0.08	44.4	0.07	38.1	0.12	47.9
Total	98.29	98.79	98.86	98.41	99.03	98.63	99.52	98.94
Normalized Atomic Concentration								
P	0.00	0.00	0.00	0.00	0.00	0.00	0.00	0.07
S	50.5	0.00	50.7	0.04	50.3	0.16	50.3	0.00
Fe	49.5	66.8	49.2	56.0	49.6	62.0	49.6	52.6
Co	0.00	0.49	0.00	0.06	0.00	0.33	0.00	0.15
Ni	0.05	32.7	0.06	43.9	0.06	37.5	0.09	47.2
Total	99.99	99.99	100.00	99.99	99.98	99.98	100.00	100.00

Meteorite	Y793241	Y793241	EET87555	EET87555	EET87555	EET87555	EET87555	EET87555
Type/Shock	breccia	breccia	breccia	breccia	breccia	breccia	breccia	breccia
Mineral	troilite	tetrataenite	troilite	kamacite	troilite	taenite	troilite	kamacite
Point	SM2	MS2	SM1	MS1	SM3	MS3	SM4	MS4
P	0.00	<0.03	0.00	0.00	0.00	0.00	0.00	<0.03
S	36.5	0.18	35.9	0.09	36.5	0.02	36.6	0.05
Fe	62.1	46.4	62.4	91.3	63.1	72.7	62.9	90.4
Co	<0.06	0.16	0.00	0.80	0.00	0.36	0.06	1.13
Ni	0.37	52.6	0.13	7.07	0.07	26.4	0.04	7.16
Total	98.96	99.29	98.35	99.22	99.67	99.47	99.61	98.77
Normalized Atomic Concentration								
P	0.00	0.00	0.00	0.00	0.00	0.00	0.00	0.00
S	50.4	0.33	50.0	0.17	50.1	0.04	50.3	0.09
Fe	49.3	47.9	49.9	92.3	49.8	74.0	49.6	91.9
Co	0.00	0.15	0.00	0.76	0.00	0.35	0.04	1.09
Ni	0.28	51.6	0.10	6.80	0.05	25.6	0.03	6.92
Total	99.99	99.96	100.00	100.00	100.00	100.00	100.00	99.98

Meteorite	EET87555	EET87555	EET87555	EET87555
Type/Shock	breccia	breccia	breccia	breccia
Mineral	troilite	kamacite	troilite	taenite
Point	SM5	MS5	SM6	MS6
P	0.00	0.00	0.00	0.00
S	36.6	0.00	35.8	0.03
Fe	62.7	90.3	62.5	81.2
Co	<0.06	1.07	<0.06	0.60
Ni	0.19	7.02	0.29	17.1
Total	99.43	98.36	98.55	98.86
Normalized Atomic Concentration				
P	0.00	0.00	0.00	0.00
S	50.3	0.00	49.8	0.05
Fe	49.5	92.1	50.0	82.8
Co	0.00	1.04	0.00	0.58
Ni	0.14	6.82	0.22	16.6
Total	99.98	100.00	99.99	100.00

APPENDIX F: Fortran Code for the Thermal Model

The following listing is the source code used to calculate the time-temperature-depth curves in this work. This code was modified from a Fortran program written by M. Miyamoto in 1978. The main program passes a time value to the subroutine 'TAL' which returns the corresponding temperature increment. Parameters used to generate the present model were listed in chapter 5 of this study. Close adherence must be made to the unit conversions in the comments portion of the program.

```
      PROGRAM ONIONSHL
      IMPLICIT REAL*8(A-H,O-Z)
      CHARACTER*30 TEXTNAME
      EXTERNAL FUNCA
      COMMON/MM/CRH,ART,RFC,TI,RA,AKAP
      COMMON/MM2/ALPHA(500),RAA,RH,PAI,ICNT,NF


C     ALPHA(N)    IS DEPENDENT ON RAA (RADIUS OF BODY) & h
C     RA=         RADIUS OF BODY IN KM
C     ART=        26Al/27Al
C     CRH=        RATIO OF BULK Al TO BULK Al IN H CHONDRITES
C     DENS=       DENSITY OF PARENT BODY
C     TI=         INITIAL AND SURFACE TEMPERATURE
C     RH=         EMISSIVITY
C     AH=         HEAT GENERATION IN ERG/CM**3.SEC
C     AK=         THERMAL CONDUCTIVITY IN ERG/CM.SEC.DEG
C     AKAP=       DIFFUSIVITY IN CM**2/SEC
C     RKM=        DISTANCE FROM CENTER IN KM
C     RFC=        FRACTION OF DEPTH FROM CENTER
C     TEMP=       TEMPERATURE IN K
C     TIME=       TIME IN SEC
```

```
      WRITE(*,'(/A\)') 'NAME OF TEXT FILE-->'
      READ(*,'(A)') TEXTNAME
      OPEN (100,FILE=TEXTNAME,STATUS='NEW')
      WRITE (*,'(/A\)')'RADIUS OF THE BODY (RA)-->'
      READ (*,'(bn,f5.2)') RA
      WRITE (*,'(/A\)')'RADIUS OF THE SHELL (RFC)-->'
      READ (*,'(bn,f5.2)') RRR
      RFC = RRR/RA

      WRITE (*,'(//A)') 'WORKING...'
      WRITE (*,'(A)') 'PRINT ORDER time THEN temperature'
      TI = 180.0
      AKAP = 7.0D-3
      CRH = 12.2D0/11.3D0
      DO 1 I=1,2500
      AA = (1.00285**I)*9.0D4
      BB = AA*3.1536D7
      CC=0.0D0
      CALL TAL(BB,CC)
      AKAP = 3.77D-3 + 1.16/CC
      WRITE(*,4) AA,CC
      WRITE(100,'(D15.10,1X,D15.10)') AA,CC
      AA = 0.0D0
1     CONTINUE
4     FORMAT(D15.10,10X,D15.10)
      CLOSE(100)
      PAUSE
      END


      SUBROUTINE TAL(TIME,TEMP)
      IMPLICIT REAL*8(A-H,O-Z)
      EXTERNAL FUNCA
      COMMON/MM/CRH,ART,RFC,TI,RA,AKAP
```

```
      COMMON/MM2/ALPHA(500),RAA,RH,PAI,ICNT,NF
      EPS=1.0
      PAI=3.1415926535897932D00
      NF=500
      RH=0.01D0
      ART=1.0D-5
      RAA=RA*1.0D5
      R=RFC*RAA
      ICNT=ICNT+1
      IF(ICNT.GT.1) GO TO 100
      CALL ROOTS
100   CONTINUE
      DENS=3.61
      AH=115.0*CRH*ART*DENS/3.1536
      AK=1.98D5
      ALMD=(9.63D-7)/3.1536D7
      RA2=RAA*RAA
      ALK=ALMD/AKAP
      TMPA=((2.0D0)*RH*RA2*AH)/(R*AK)
200   TIMS=TIME
      SUM=0.0D1
      TMPD=(-1.0D0)*ALMD*TIMS
      IF(TMPD.GT.-80.0) GO TO 210
      TMPB=0.0
      GO TO 220
210   TMPB=EXP(TMPD)
220   CONTINUE
      TMP7B=10000.
      DO 300 N=1,NF
      ALPH2=ALPHA(N)**2
      TMP1=SIN(R*ALPHA(N))/SIN(RAA*ALPHA(N))
      TMP2=1.0D0-ALK/ALPH2
      TMP3=ALPH2*(RA2*ALPH2+RA2*RH*RH-RAA*RH)
      TMPC=-1.0D0*AKAP*ALPH2*TIMS
```

```
      IF(TMPC.GT.-80.0) GO TO 240
      TMP4=TMPB
      GO TO 250
240   TMP4=TMPB-EXP(TMPC)
250   TMP5=TMP4/(TMP2*TMP3)
      TMP6=TMPA*TMP1*TMP5
      SUM=SUM+TMP6
      TMP7=ABS(TMP6)
      IF(TMP7.LT.1.0.AND.TMP7B.LT.1.0) GO TO 400
      TMP7B=TMP7
300   CONTINUE
      WRITE(*,30)
30    FORMAT('TEMPERATURE DID NOT CONVERGE')
400   TEMP=SUM+TI
1000  RETURN
      END

      SUBROUTINE ROOTS
      IMPLICIT REAL*8(A-H,O-Z)
      EXTERNAL FUNCA
      COMMON/MM2/ALPHA(500),RAA,RH,PAI,ICNT,NF,RFC,TI,RA,AKAP
      EPS=1.0D-15
      DO 250 N=1,NF
      XB=FLOAT(N)*PAI-1.0D-12
      XA=XB-1.0D+0
150   L=100
      CALL DNLBIT(X,FUNCA,XA,XB,EPS,L,IERR)
      IF(IERR.LE.1) GO TO 200
      IF (IERR.EQ.2) WRITE(9,10)
      IF (IERR.EQ.1) WRITE(9,12)
10    FORMAT('INITIAL VALUE ERROR')
12    FORMAT('NOT CONVERGED ALPHA(N)')
      GO TO 300
200   ALPHA(N)=X/RAA
```

```
250   CONTINUE
      RETURN
300   STOP
      END

      REAL*8 FUNCTION FUNCA(X)
      IMPLICIT REAL*8(A-H,O-Z)
      COMMON/MM2/ALPHA(500),RAA,RH,PAI,ICNT,NF,RFC,TI,RA,AKAP
      FUNCA=X/TAN(X)+RAA*RH-1.0D0
      RETURN
      END
      SUBROUTINE  DNLBIT(X,FUNCT,XL,XR,EPS,ITEND,IER)
      IMPLICIT REAL*8(A-H,O-Z)
      IER = 0
      X   = XL
      FL  = FUNCT(X)
      IF( FL ) 100,555,100
100   X   = XR
      FR  = FUNCT(X)
      IF( FR ) 110,555,110
110   IF( FL*FR ) 130,555,120
120   X   = (XL+XR)*.5D+0
      IER = 2
      WRITE(*,620)
      RETURN

130   DO  250 N=1,ITEND
      X   = (XL+XR)*0.5D0
      F   = FUNCT(X)
      IF( F ) 140,555,140
140   IF( F *FL ) 150,555,160
150   XR  = X
      FR  = F
      GO TO 170
```

```
160   XL   = X
      FL   = F
170   DF   = FL-FR
      DX   = (XR-XL)*FL
      DX   = DX/DF
      X    = XL+DX
      F    = FUNCT(X)
      IF( F ) 175,555,175
175   IF( FL*F ) 180,190,190
180   XR   = X
      FR   = F
      GO TO 200
190   XL   = X
      FL   = F
200   DX   = XR-XL
      IF( ABS(X).LE.1.0D0 ) GO TO 210
      DX   = DX/X
210   CONTINUE
      IF( ABS(DX)-EPS) 555,555,250
220   X    = XR
      IF( ABS(FR)-1.0D-12 ) 555,555,230
230   X    = XL
      IF( ABS(FL)-1.0D-12 ) 555,555,250
250   CONTINUE
      IER = 1
555   RETURN
620   FORMAT('(SUBR. DNLBIT) NO CALCULATION FOR F(XL).F(XR) > 0')
      END
```

VITA

Marvin Edward Bennett III was born in Mason, West Virginia on July 1, 1957. He received a Degree of Bachelor of Sciences with a major in Geology from Marshall University, W.V. in 1979 and a Degree of Master of Sciences with an emphasis in Geochemistry from Stephen F. Austin State University, Tx. in 1986. Between 1982 and 1989 he was employed as an Instructor of Geology at Centenary College in Shreveport, La. In August, 1989 he entered the University of Tennessee, Knoxville and in May, 1995 received the Degree of Doctor of Philosophy in Geology.